Growth of Carbon Nanotubes on Electrospun Cellulose Fibres for High Performance Supercapacitors and Carbon Fibre Composites

Submitted by Qiang Li to the University of Exeter

as a thesis for the degree of

Doctor of Philosophy in Engineering

In September 2018

I certify that all material in this thesis which is not my own work has been identified and that no material has previously been submitted and approved for the award of a degree by this or any other University.

Signature: ……**Qiang Li**……..

Abstract

The production of cellulose derived hybrid carbon nanofibre (CNF)/carbon nanotubes (CNTs) electrodes for the fabrication of supercapacitors and carbon fibre composites was investigated. The CNTs were grown via a floating catalyst chemical vapor deposition (CVD) method on the top surface of electrospun cellulose derived CNFs. These CNF and CNF/CNTs samples were then used as electrodes to produce liquid electrolyte-based supercapacitors. The growth of CNTs leads to an improvement of electrochemical performance compared to the plain CNFs. This improvement is due to the grown CNTs enlarging the reactive sites through enhanced surface area and porosity, and thereby increasing the conductivity of the system.

CNTs have been also grown onto CNFs containing ferrocene and SiC particles. Composites were fabricated by combining the fibres and CNTs grown fibres with model polymers. The stress transfer properties of these materials have been estimated using an in situ Raman spectroscopic method by observing the shift of the Raman band during the tensile deformation of model polymer composites. Using this method, the elastic modulus of CNF/SiC/CNTs fibres has been estimated to be 208 ± 26 GPa. No shifts in the peak positions of bands relating to the carbon structure were obtained for in situ Raman spectroscopic studies of the CNF/CNTs fibres made from the ferrocene embedded fibres. This was thought to be due to the low yield of CNTs on the surface of the fibres.

Furthermore, CNF/CNTs electrode-based structural supercapacitors, combining a solid electrolyte with the carbonized fibres, have been produced. These CNF/CNTs electrodes have a better capacitive performance than the plain CNF

electrodes. There was a decrease in this performance with increased curing time of the resin, from 2 to 24 h, due to a lack of charge carrier mobility in the latter samples. A Raman spectroscopic study of the deformation of the carbon structures showed that the G-band shift towards a lower wavenumber position for the CNF and CNF/CNTs samples processed at a carbonization temperature of 2000 °C. Moduli of these fibres were estimated to be ~145 GPa and ~271 GPa, respectively, suggesting the growth of CNTs not only enhances the capacitive performance but also the mechanical properties of the structural supercapacitors. No Raman bend shift was found for the CNFs and CNF/CNTs samples processed below a carbonization temperature of 2000 °C, e.g. 900 °C and 1500 °C. This is because the graphitic structures are not well developed at carbonization temperatures below 1500 °C.

Table of Contents

List of Figures

List of Tables

List of Abbreviations

ACFs	Activated carbon fibres
ACN	Acetonitrile
ACNFs	Activated carbon nanofibres
ACs	Activated carbons
BET	Brunauer-Emmett-Teller
BJH	Barrett-Joyner-Halenda
CA	Cellulose acetate
CAG	Carbon aerogel
CEW	CHI600C electrochemical workstation
CNF	Carbon nanofibre
CNTs	Carbon nanotubes
CV	Cyclic voltammetry
CVD	Chemical vapour deposition
DCM	Dichloromethane
DMAc	dimethylacetamide
DMF	N, N-dimethylformamide
DP	Degree of polymerization
EDL	Electrical double layer
EDLC	Electrical double layer capacitor
EIS	Electrochemical impedance spectra
EMITFSI	1-ethyl-3-methylimidazolium bis(trifluoromethylsulfonyl) imide
FTIR	Fourier transform infrared spectroscopy
FWHM	Full width at half maximum
GCD	Galvanostatic charge/discharge

IHP	Inner Helmholtz plane
IL	Ionic liquid
LOI	Lateral order index
MeOH	Methanol
MWCNTs	Multi-walled carbon nanotubes
NLDFT	Non-local Density Functional Theory
OHP	Outer Helmholtz plane
PAN	Polyacrylonitrile
PANI	Polyaniline
PC	Propylene carbonate
PEGDGE	Poly(ethylene glycol) diglycidyl ether
PMMA	Poly(methyl methacrylate)
SAED	Selective area electron diffraction
SEM	Scanning electron microscope
SOHIO	Standard Oil of Ohio
SWCNTs	Single-walled carbon nanotubes
TCI	Total crystalline index
TEM	Transmission electron microscopy
$TEMABF_4$	Triethylmethylammonium tetrafluoroborate
TETA	Triethylenetetramine
TGA	Thermogravimetric analysis
TK	Tuinstra-Koenig
UAVs	Unmanned aerial vehicles
VLS	Vapour-liquid-solid
VSS	Vapor-solid-solid

List of Publications

Li, Q., Deng, L., Kim, J.-K., Zhu, Y. Q., Holmes, S. M., Perez-Page, M., & Eichhorn, S. J. (2017). Growth of Carbon Nanotubes on Electrospun Cellulose Fibers for High Performance Supercapacitors. ***Journal of The Electrochemical Society****, 164*(13), A3220-A3228. doi:10.1149/2.1181713jes

Li, Q., Zhu, Y. Q., & Eichhorn, S. J. (2018). Structural supercapacitors using a solid resin electrolyte with carbonized electrospun cellulose/carbon nanotube electrodes. ***Journal of Materials Science****, 53*(20), 14598-14607. doi:10.1007/s10853-018-2665-x

Li, Q., Zhu, Y. Q., & Eichhorn, S. J. Carbonized Electrospun Cellulose Composite Nanofibres Containing Silicon Carbide Nanoparticles, ***Composites Part A****,* submitted*.*

Acknowledgements

I would like to express my sincere gratitude to my PhD supervisors, Prof. Stephen Eichhorn and Prof. Yanqiu Zhu, for their consistent guidance, encouragement, and inspiration throughout my PhD study. I would also like to thank the Chinese Scholarship Council and the University of Exeter for funding a PhD studentship for me.

I am grateful to all the colleagues I have been working with in my research group: Dr Nandula Wanasekara, Dr Rinat Nigmatullin, Dr Anna Lewandowska, Dr James Beard, Dr Hewson Daniel, Nor Hanifawati Inai, Masitah Abu Kassim, Joe Morgan, Caterina Palange. They have been sharing their fascinating expertise and experiences, which are of great value for me.

My keen appreciation goes to Prof. Kim Jang-Kyo, who gave me the chance to work with his group during my internship in the Hong Kong University of Science and Technology (HKUST). I am also grateful to Dr Libo Deng (Shen Zhen University) for his guidance on the electrospinning and electrochemical tests. Thanks to Dr Binling Chen for helping me to improve my experimental skills and solidify my fundamentals, and his keen support and encouragement throughout my PhD study and followed paper writing period. I would like to thank Prof. Stuart Holmes, Dr M. Perez-Page (University of Manchester), Dr Yongde Xia, Zheng Huang, and Mian Zahid Hussain for performing BET analysis and all the helpful discussions. Thanks to Dr Yat-Tarng (Tommy) Shyng for his help with FTIR measurements and helpful discussions on in situ Raman spectroscopy studies.

I would also like to thank Dr Hong Chang, Dr Bahareh Yazdani, and Dr Judith Bannerman for their comprehensive training and assistance with imaging suite

facilities (SEM, TEM, XRD, etc.). Thanks to Dr Ellen Green for her assistance on the Raman measurements, and thanks to Dr Sakineh Chabi, Dr Zhuxian Yang, Yu Chen, Pablo Martinez Pancorbo, Dr Nannan Wang for their assistance on performing CVD.

I deeply appreciate my parents who have been supporting me and encouraging me all the time. At last, but not the least, I would like to give my great thanks to my wife and daughter for loving and inspiring me.

Chapter 1 Introduction

This chapter is an introduction to the thesis, which reports research into electrospun cellulose derived carbon fibres for the fabrication of composites and supercapacitors. This chapter starts with a general introduction, followed by objectives, and finally a brief description of the structure for the thesis.

1.1 General Introduction

Carbon fibres have been widely used in applications such as military and civil aircraft, unmanned aerial vehicles (UAVs), space launchers, satellites, building structures, and automotive applications due to their high specific strength and stiffness (Jacob, 2014; Noisternig, 2000; Soutis, 2005). These fibres have also found applications in energy storage devices because of their excellent electrical properties (Chen, 2016). Most of the commercial carbon fibres are produced from oil-based precursors such as polyacrylonitrile (PAN), which is thought to be unsustainable and expensive (Dumanlı & Windle, 2012; Hassan, Schiermeister, & Staiger, 2015). The rapid increasing demands on the use of carbon fibres in the global market have stimulated the discovery of alternative precursor materials. Cellulose fibres stand out as a precursor for the production of carbon fibres. They have huge potential to complement PAN precursors because they are inexpensive, renewable, highly crystalline and abundant in nature (Frank, Steudle, Ingildeev, Sporl, & Buchmeiser, 2014). Electrospinning is a simple and continuous approach to generate polymer nanofibres with large surface to volume ratios (Sun *et al.*, 2014). Compared to traditional carbon fibres, electrospun polymer fibres, subsequently pyrolyzed to carbon nanofibres (CNFs) are competitive candidates for the fabrication of electrodes and composites owing

to their relatively high surface area, pore size distribution, high electrical conductivity, excellent cyclic stability, and good mechanical properties (Salanne *et al.*, 2016).

Supercapacitors are particular promising energy storage devices when compared to lithium-ion batteries and fuel cells owing to their high power density, fast charge/discharge mobility, and good lifecycle stability (Yu, Tetard, Zhai, & Thomas, 2015). Carbon nanotubes (CNTs) have been intensively investigated as additives for the production of supercapacitors (Miao *et al.*, 2016; Wang, Song*, et al.*, 2015; Yu *et al.*, 2016; Zheng, Cai, Ma, & Gong, 2015). Because of their small diameters and relatively high conductivity, their incorporation with CNFs have a potential to achieve enhanced capacitive performance for supercapacitor electrodes. Electrospun CNFs have been previously reported for the fabrication of supercapacitor electrodes (Deng, Young, Kinloch, Abdelkader*, et al.*, 2013). In the current research, this approach has been extended to study the in situ growth of CNTs on the CNFs via a chemical vapour deposition (CVD) technique. This approach was used to further improve the capacitive performance of electrospun CNF electrodes.

Stress transfer ability between carbon fibres and matrix is one of the most important interfacial properties in composites. An interface with high stress transfer efficiency allows a great amount of applied stress to be transferred to the reinforcing phase. The stress transfer depends on the interfacial shear stress between the fibre and the matrix (Schadler, Giannaris, & Ajayan, 1998). Qian *et al.* have evaluated the in-plane shear properties of carbon aerogel modified carbon fibre fabric-based structural supercapacitors using the ASTM standard D3518 (Qian, Kucernak, Greenhalgh, Bismarck, & Shaffer, 2013). Over the years

Raman spectroscopy has been successfully applied to evaluate mechanical properties of carbon materials by the observation of the shift in the position of characteristic bands when the materials are deformed (Papageorgiou, Kinloch, & Young, 2017). This technique was initially developed by Young and co-workers for the deformation of carbon fibres (Huang & Young, 1995). Since then, it has been applied to investigate the mechanical properties of other carbon materials such as CNTs (Prabhakaran, Stephen, & Robert, 2007) and graphene (Mohiuddin, Lombardo, Nair, Bonetti, Savini, Jalil, Bonini, Basko, Galiotis, Marzari*, et al.*, 2009). The Raman shift arises from the change of vibrational frequencies of the normal modes when deformation is applied (Schadler *et al.*, 1998). It is believed that higher stress transfer from the matrix to the carbon fibres results in a larger Raman band shift (Xu, Loomis, Bradshaw, & Panchapakesan, 2012). Raman spectroscopy also has been reported as a technique to estimate the mechanical stiffness of CNFs produced from electrospun precursors (Deng, Young, Kinloch, Zhu, & Eichhorn, 2013). The growth of CNTs on the surface of CNFs has been used to enhance the interfacial strength with a matrix in a composite (Sharma & Lakkad, 2011).

In the present study, CNF/CNTs are fabricated using a new approach. This approach involves embedding ferrocene powders and SiC nanoparticles directly into cellulose derived CNFs during the electrospinning process. CNTs are then grown on the surface of these CNF composites using a CVD technique. The stress transfer from the matrix to the CNF/CNTs is then investigated using a Raman spectroscopic technique. Furthermore, since the CNF/CNTs combine both conductive and high mechanical properties (stiffness, strength), their potential as candidates for supercapacitor electrodes is discussed. Development

of structural supercapacitors using the CNF/CNTs electrodes is then explored. In the absence of a traditional liquid electrolyte, structural supercapacitors generally utilize a solid electrolyte to allow them to simultaneously resist mechanical stresses and store electrochemical energy (Deka, Hazarika, Kim, Park, & Park, 2017). Raman spectroscopy is used to assess the mechanical properties of these fibres, and their appropriateness for a structural supercapacitor.

1.2 Objectives

The aim of this study is to investigate the capacitive performance and mechanical properties of CNTs grown electrospun cellulose derived CNFs. A number of objectives have been addressed:

- To produce electrospun cellulose fibres derived CNFs, and grow CNTs on their surface via a CVD technique to make CNF/CNT composite electrodes. Electrochemical properties for the CNFs and CNF/CNTs-based electrodes are then estimated.
- To produce cellulose composite fibres by embedding SiC into cellulose fibres via electrospinning, followed by growing CNTs on these composite fibres. To evaluate the availability of SiC as reinforcing elements for a carbon fibre composite. The stress transfer properties of these composites are then estimated.
- To grow CNTs directly from embedded ferrocene catalysts in CNFs, and to evaluate the mechanical properties of the CNF/CNTs.
- To investigate how the growth of CNTs on the CNF electrodes in structural supercapacitors improve their electrochemical and the stress transfer properties.

1.3 Structure of Thesis

- Chapter 1 is a general introduction to electrospun cellulose derived CNFs-based supercapacitors and carbon fibre composites, the objectives, and structure for this project.
- Chapter 2 contains a literature review of supercapacitors and their performance. This review also includes an introduction to the production of carbon fibres from electrospun cellulose fibre precursors. This is followed by an introduction to carbon fibre and CNT electrodes, three types of electrolytes, and finally mechanical tests for CNF/CNTs via in situ Raman spectroscopic approaches.
- Chapter 3 reports on electrospun CNF/CNT fibres for the fabrication of liquid electrolyte-based supercapacitors.
- Chapter 4 reports the growth of CNTs on electrospun CNF/SiC fibres for the fabrication of reinforcing materials for producing carbon fibre composites.
- Chapter 5 presents the direct growth of CNTs on the surface of electrospun CNF/ferrocene fibres.
- Chapter 6 presents the fabrication of CNF/CNT electrodes-based structural supercapacitors with an evaluation of their electrochemical and mechanical performance.
- Chapter 7 gives conclusions and suggestions for future work.

1.4 References

Chen, J. Y. (2016). *Activated Carbon Fiber and Textiles*: Elsevier Science.

Deka, B. K., Hazarika, A., Kim, J., Park, Y. B., & Park, H. W. (2017). Recent development and challenges of multifunctional structural supercapacitors for automotive industries. *International Journal of Energy Research, 41*(10), 1397-1411. doi:10.1002/er.3707

Deng, L., Young, R. J., Kinloch, I. A., Abdelkader, A. M., Holmes, S. M., De Haro-Del Rio, D. A., & Eichhorn, S. J. (2013). Supercapacitance from cellulose and carbon nanotube nanocomposite fibers. *ACS Appl Mater Interfaces, 5*(20), 9983-9990. doi:10.1021/am403622v

Deng, L. B., Young, R. J., Kinloch, I. A., Zhu, Y. Q., & Eichhorn, S. J. (2013). Carbon nanofibres produced from electrospun cellulose nanofibres. *Carbon, 58*, 66-75. doi:10.1016/j.carbon.2013.02.032

Dumanlı, A. G., & Windle, A. H. (2012). Carbon fibres from cellulosic precursors: a review. *Journal of Materials Science, 47*(10), 4236-4250. doi:10.1007/s10853-011-6081-8

Frank, E., Steudle, L. M., Ingildeev, D., Sporl, J. M., & Buchmeiser, M. R. (2014). Carbon fibers: precursor systems, processing, structure, and properties. *Angew Chem Int Ed Engl, 53*(21), 5262-5298. doi:10.1002/anie.201306129

Hassan, M. M., Schiermeister, L., & Staiger, M. P. (2015). Sustainable Production of Carbon Fiber: Effect of Cross-Linking in Wool Fiber on Carbon Yields and Morphologies of Derived Carbon Fiber. *ACS Sustainable Chemistry & Engineering, 3*(11), 2660-2668. doi:10.1021/acssuschemeng.5b00994

Huang, Y., & Young, R. J. (1995). Effect of Fiber Microstructure Upon the Modulus of Pan-and Pitch-Based Carbon-Fibers. *Carbon, 33*(2), 97-107. doi:10.1016/0008-6223(94)00109-D

Jacob, A. (2014). Carbon fibre and cars – 2013 in review. *Reinforced Plastics, 58*(1), 18-19. doi:10.1016/s0034-3617(14)70036-0

Miao, F. J., Shao, C. L., Li, X. H., Wang, K. X., Lu, N., & Liu, Y. C. (2016). Electrospun Carbon Nanofibers/Carbon Nanotubes/Polyaniline Ternary Composites with Enhanced Electrochemical Performance for Flexible Solid-State Supercapacitors. *Acs Sustainable Chemistry & Engineering, 4*(3), 1689-1696. doi:10.1021/acssuschemeng.5b01631

Mohiuddin, T. M. G., Lombardo, A., Nair, R. R., Bonetti, A., Savini, G., Jalil, R., . . . Ferrari, A. C. (2009). Uniaxial strain in graphene by Raman spectroscopy:Gpeak splitting, Grüneisen parameters, and sample orientation. *Physical Review B, 79*(20), 205433. doi:10.1103/PhysRevB.79.205433

Noisternig, J. F. (2000). Carbon fibre composites as stay cables for bridges. *Applied Composite Materials, 7*(2-3), 139-150. doi:10.1023/A:1008946132034

Papageorgiou, D. G., Kinloch, I. A., & Young, R. J. (2017). Mechanical properties of graphene and graphene-based nanocomposites. *Progress in Materials Science, 90*, 75-127. doi:10.1016/j.pmatsci.2017.07.004

Prabhakaran, K., Stephen, J. E., & Robert, J. Y. (2007). Deformation of isolated single-wall carbon nanotubes in electrospun polymer nanofibres. *Nanotechnology, 18*(23), 235707. doi:10.1088/0957-4484/18/23/235707

Qian, H., Kucernak, A. R., Greenhalgh, E. S., Bismarck, A., & Shaffer, M. S. (2013). Multifunctional structural supercapacitor composites based on carbon aerogel modified high performance carbon fiber fabric. *ACS Appl Mater Interfaces, 5*(13), 6113-6122. doi:10.1021/am400947j

Salanne, M., Rotenberg, B., Naoi, K., Kaneko, K., Taberna, P. L., Grey, C. P., . . . Simon, P. (2016). Efficient storage mechanisms for building better supercapacitors. *Nature Energy, 1*, 16070. doi:10.1038/Nenergy.2016.70

Schadler, L. S., Giannaris, S. C., & Ajayan, P. M. (1998). Load transfer in carbon nanotube epoxy composites. *Applied Physics Letters, 73*(26), 3842-3844. doi:10.1063/1.122911

Sharma, S. P., & Lakkad, S. C. (2011). Effect of CNTs growth on carbon fibers on the tensile strength of CNTs grown carbon fiber-reinforced polymer matrix composites. *Composites Part a-Applied Science and Manufacturing, 42*(1), 8-15. doi:10.1016/j.compositesa.2010.09.008

Soutis, C. (2005). Fibre reinforced composites in aircraft construction. *Progress in Aerospace Sciences, 41*(2), 143-151. doi:10.1016/j.paerosci.2005.02.004

Sun, B., Long, Y. Z., Zhang, H. D., Li, M. M., Duvail, J. L., Jiang, X. Y., & Yin, H. L. (2014). Advances in three-dimensional nanofibrous macrostructures via electrospinning. *Progress in Polymer Science, 39*(5), 862-890. doi:10.1016/j.progpolymsci.2013.06.002

Wang, T., Song, D. F., Zhao, H., Chen, J. Y., Zhao, C. H., Chen, L. L., . . . Xie, E. Q. (2015). Facilitated transport channels in carbon nanotube/carbon nanofiber hierarchical composites decorated with manganese dioxide for flexible supercapacitors. *Journal of Power Sources, 274*, 709-717. doi:10.1016/j.jpowsour.2014.10.102

Xu, P., Loomis, J., Bradshaw, R. D., & Panchapakesan, B. (2012). Load transfer and mechanical properties of chemically reduced graphene reinforcements in polymer composites. *Nanotechnology, 23*(50), 505713. doi:10.1088/0957-4484/23/50/505713

Yu, J., Lu, W., Pei, S., Gong, K., Wang, L., Meng, L., . . . Chou, T. W. (2016). Omnidirectionally Stretchable High-Performance Supercapacitor Based on Isotropic Buckled Carbon Nanotube Films. *ACS Nano, 10*(5), 5204-5211. doi:10.1021/acsnano.6b00752

Yu, Z. N., Tetard, L., Zhai, L., & Thomas, J. (2015). Supercapacitor electrode materials: nanostructures from 0 to 3 dimensions. *Energy & Environmental Science, 8*(3), 702-730. doi:10.1039/c4ee03229b

Zheng, Q., Cai, Z., Ma, Z., & Gong, S. (2015). Cellulose nanofibril/reduced graphene oxide/carbon nanotube hybrid aerogels for highly flexible and all-solid-state supercapacitors. *ACS Appl Mater Interfaces, 7*(5), 3263-3271. doi:10.1021/am507999s

Chapter 2 Background and Literature Review

2.1 History of supercapacitors

Over 200 years ago in 1745, German physicist Ewald Georg von Kleist first found charges could be stored by applying a high voltage via a nail to a hand-held glass jar of alcohol (Keithley, Instrumentation, & Society, 1999). In this earliest capacitor, Von Kleist's hand and water acted as conductors and the glass jar as a dielectric. In 1746, a similar jar, called a Leyden jar was invented by Dutch physicist Pieter van Musschenbroek (Brusso & Chaparala, 2014). The mechanism of the capacitor was investigated later by Benjamin Franklin and concluded that the charges were being stored in the glass. Since late 19th century, instead of glass, non-conductive materials such as porcelain, paper, and mica were used as a dielectric for early capacitors. The big breakthrough was made by the invention of the electrolytic capacitor using aluminium as electrodes with a neutral or alkaline electrolyte by Charles Pollak (Both, 2015). This capacitor was later patented in 1896 (Charles, 1896). In 1957 the first double layer capacitor was invented by H. Becker, who developed the supercapacitor with porous carbon as the electrode material (Becker, 1957). In 1966, Standard Oil of Ohio (SOHIO) developed supercapacitors (Rightmire, 1966) and licensed the technology to NEC, who commercialized them in 1978 for backup power for computer memory (Schindall, 2007). Since then, the market for supercapacitors has grown slowly until Panasonic branded a supercapacitor called Goldcaps (Faisal, Rahman, & Asmatulu, 2016). The market for supercapacitors expanded very rapidly during the last three decades. More and more companies such as Maxwell Technologies, APowerCap, SPS, and Skeleton have been extensively developing the supercapacitor market for a wide range of applications such as

aviation, military, automotive, bus/tram, railway, buses, etc. Sales of supercapacitors were about 400 million US dollars in 2016 and were estimated to grow to 800 million to 1 billion US dollars by 2026 (Ghaffarzadeh, 2016).

2.2 Basis of supercapacitors

A conventional parallel-plate capacitor is a device that consists of two conductive plates separated by a non-conductive region to store electrical energy in an electric field, as shown in Figure 2.1. The non-conductive region can be either a vacuum or an electrical insulator material, known as the dielectric.

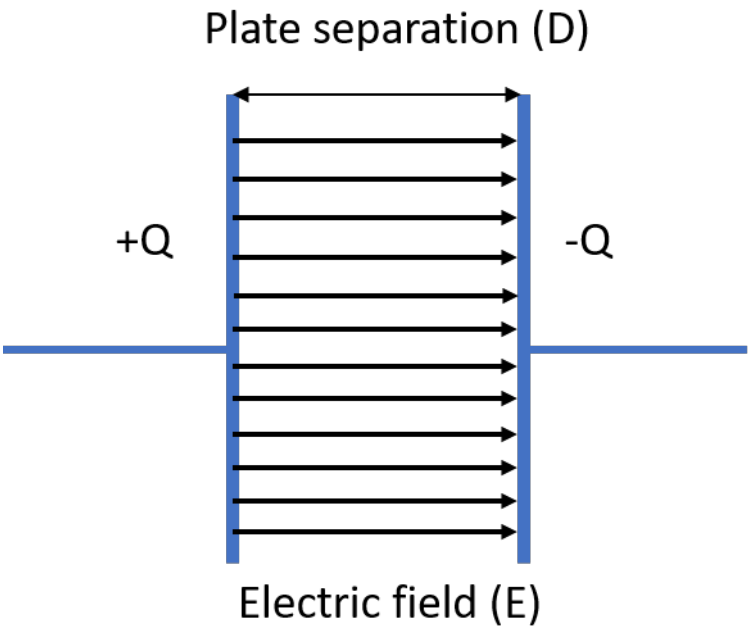

Figure 2.1 Schematic of a conventional parallel-plate dielectric capacitor.

As a voltage is applied to induce a potential difference, e.g. connecting a capacitor to a battery, equal charges (Q) travel to the surfaces of each opposite conductor without moving through the dielectric (Deshpande, 2014). In this case, net positive charges are stored on one terminal and net negative charges are

stored on the other terminal, resulting in an electric field to store energy in the capacitor. Capacitance, C is the ability of a capacitor to store electric charges, defined as the ratio of stored positive or negative charge Q to the applied voltage V according to the equation

$$C = \frac{Q}{V} \qquad (2.1)$$

The International System of Units of capacitance is the farad (F). A capacitance of one farad means that one coulomb of charge on each conductor generates a voltage of one volt between its plates (Deshpande, 2014).

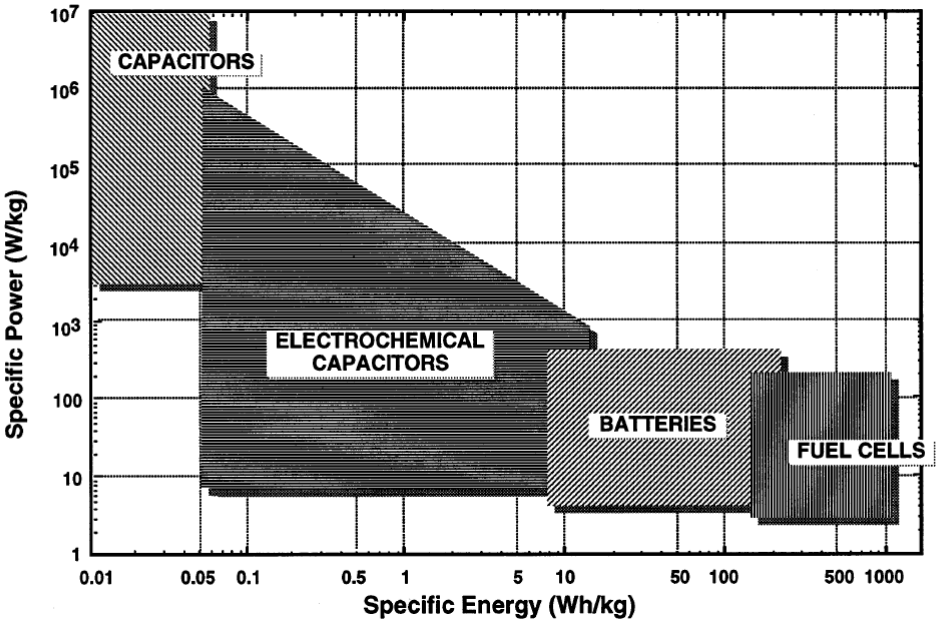

Figure 2.2 Sketch of Ragone plot for specific energy and power capabilities of capacitors, electrochemical capacitors (supercapacitors), batteries and fuel cells. Taken from (Kotz & Carlen, 2000).

Compared to conventional parallel-plate capacitors, supercapacitors are electrochemical energy storage devices that do not use a solid or a vacuum

dielectric, but the electrostatic double-layer effect or faradaic redox reactions with charge-transfer to store energy (Wang, Zhang, & Zhang, 2012). The so-called Ragone plot is a diagram that presents the specific energy and specific power for four typical energy storage and conversion devices, as shown in Figure 2.2 (Kotz & Carlen, 2000). From the Ragone plot, one can see that supercapacitors have higher specific power in comparison to batteries and fuel cells, although the specific energy of supercapacitors is in the middle range of the four types of energy storage devices (capacitors, supercapacitors, fuel cells, and batteries). Supercapacitors can be therefore combined with batteries and capacitors to construct a hybrid system for optimization of the overall performance of the device in terms of specific energy and specific power. Furthermore, the application of supercapacitors can complement the drawbacks of other power sources such as low life cycles in batteries and low energy density in fuel cells. A comparison of supercapacitors with other energy storage devices is shown in Table 2.1 (Pandolfo & Hollenkamp, 2006).

Table 2.1 Comparison of the performance of electrolytic capacitors, supercapacitors, and batteries. Taken from (Pandolfo & Hollenkamp, 2006).

Characteristic	Capacitor	Supercapacitor	Battery
Specific energy (W h kg^{-1})	< 0.1	1 - 10	10 - 100
Specific power (W h kg^{-1})	> 10000	500 - 10000	< 1000
Discharge time	10^{-6} – 10^{-3}	s to min	0.3 – 3 h
Charge time	10^{-6} – 10^{-3}	s to min	1 – 5 h
Cycle - life	Almost infinite	> 500000	About 1000

In general, supercapacitors can be classified into two types; namely the electrical double layer capacitor (EDLC) and the pseudocapacitor (Wang *et al.*, 2012). An EDLC stores energy by accumulating the electrostatic charges at the electrodes/electrolyte interface while the pseudo-capacitance is developed from the fast and reversible surface redox processes.

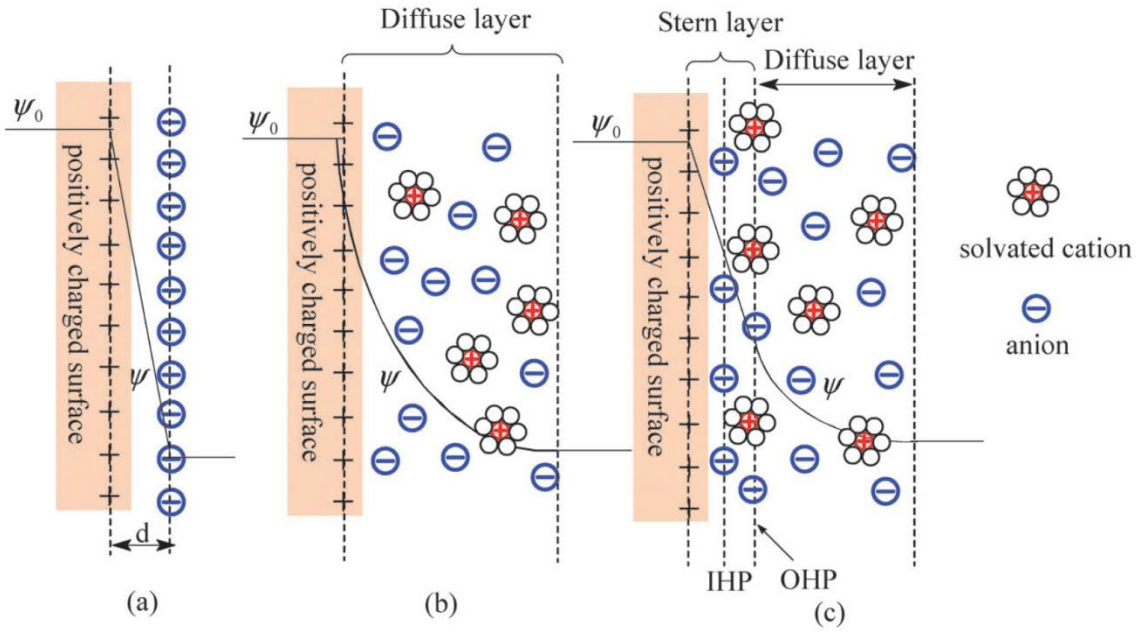

Figure 2.3 Models of the electrical double layer (EDL) at a positively charged surface: (a) the Helmholtz model, (b) the Gouy–Chapman model, and (c) the Stern model with the inner Helmholtz plane (IHP) and outer Helmholtz plane (OHP) and diffuse layer. Taken from (Zhang & Zhao, 2009).

As illustrated in Figure 2.3a, the EDLC model was first introduced and modelled by von Helmholtz, who considered that the electrical charges are stored in a so-called double-layer model, which is very similar to the conventional parallel-plate capacitor (Helmholtz, 1853; Zhang & Zhao, 2009). In the Helmholtz model, a solid electrode is brought into a liquid electrolyte. By applying a voltage an interface is

built up between the two phases (electrodes and electrolyte) during which the electrodes repel the same charged ions while absorbing counter ions to their surfaces (Wang *et al.*, 2012). As a consequence, two layers of opposite charges form at the interface between the electrodes and the electrolyte, separated by a molecular dielectric (Wang *et al.*, 2012). This model was further modified by Gouy and Chapman, and Stern and Geary, who suggested the co-existence of two regions with different ionic concentrations, namely a diffuse layer and a Stern layer or compact layer, as shown in Figure 2.3b and c (Chapman, 1913; Gouy, 1910; Stern, 1924; Zhang & Zhao, 2009). In the diffuse layer, electrolyte ions (both cations and anions) are distributed in the electrolyte solution, driven by thermal motion (Serp & Machado, 2015). The Stern layer however consists of two sublayers, referred as the inner Helmholtz plane (IHP) that is the molecular dielectric (monolayer of solvent molecules) in the Helmholtz model, and the outer Helmholtz plane (OHP) that is contributed by solvated counterions that are opposite to the charges on the surfaces of the electrodes (Zhang & Zhao, 2009). The IHP is closed to the solid electrodes while the OHP is adjacent to the diffuse region (Zhang & Zhao, 2009). In this case, the number of charges in the electrode is equal to that of the counter-charges in the OHP. Therefore, the double-layer charges form a static electric field within the layer of the solvent molecules in the IHP. This extremely short separation distance between double layers contributes to the much higher energy storage in EDLCs than for conventional parallel-plate capacitors. There is no transfer of charge between the electrode and the electrolyte, which implies that the overall electrolyte concentration remains constant during the charging and discharging processes. Therefore, the forces that cause the adhesion are not chemical bonds but physical forces (e.g. electrostatic forces).

Pseudocapacitors have a completely different energy storage mechanism compared to EDLCs. Pseudocapacitors are based on reversible and fast Faradaic reactions between the electrolyte and the electrode. The Faradaic reaction, also referred to as a redox reaction, can cause charge transfer across the double layer. Conway concluded the mechanisms underlying the function of pseudocapacitors are underpotential deposition, redox pseudocapacitance and intercalation pseudocapacitance (Augustyn, Simon, & Dunn, 2014; Conway, 2013). Electrode materials that are commonly used in pseudocapacitors are RuO_2 (Trasatti & Buzzanca, 1971), MnO_2, (Chen, Zhu, Wu, Han, & Wang, 2010), and Co_3O_4 (Xia *et al.*, 2011). It has been shown that pseudocapacitors have advantages of widening the working voltage window, achieving a higher specific capacitance, and having a higher energy density than EDLCs (Wang *et al.*, 2012). However, they generally have lower power densities due to lower electrical conductivity and poor stability during charging and discharging cycling in the redox reactions (Wang *et al.*, 2012).

2.3 The performance of supercapacitors

Due to the limitation of the surface area of the electrodes and the long distance of the electrode separation, the capacitance of conventional capacitors is much lower in comparison to EDLCs. For a parallel-plate conventional capacitor, capacitance C is directly proportional to the surface area A of each electrode and inversely proportional to the distance D between the electrodes (Salanne *et al.*, 2016) according to the equation

$$\mathrm{C} = \varepsilon_0 \varepsilon_\mathrm{r} \frac{\mathrm{A}}{\mathrm{D}} \qquad (2.2)$$

where ε_0 is the dielectric constant (or "permittivity of free space") and ε_r is the dielectric constant of the insulating material between the electrodes. Equation 2.2 can also be applied to EDLCs. The distance D in EDLCs is however the thickness of the molecular dielectric in IHP, which is highly dependent on the concentration of the electrolyte and the size of the ions in the electrolyte. This thickness is normally in the order of 5 – 10 Å (Kotz & Carlen, 2000), much lower than for a parallel-plate capacitor. From Equation 2.2, a smaller D will give a very high capacitance. This is the main reason why EDLCs have a larger capacitance than conventional capacitors. However, for porous electrode-based supercapacitors, not all the pores act as host sites for ions in the electrolyte and therefore the capacitance and the specific surface area do not have a strictly linear relationship (Barbieri, Hahn, Herzog, & Kotz, 2005). This lack of a linear relationship has been proven experimentally (Barbieri *et al.*, 2005; Gamby, Taberna, Simon, Fauvarque, & Chesneau, 2001).

EDLCs can be considered to be a combination of two series of connected capacitors, as illustrated in Figure 2.4. The total capacitance (C_T) can be calculated using the equation (Pandolfo & Hollenkamp, 2006)

$$\frac{1}{C_T} = \frac{1}{C_p} + \frac{1}{C_n} \qquad (2.3)$$

where C_p and C_n are the capacitances of the positive and negative electrodes, respectively. For an EDLC with a symmetric configuration that contains identical electrodes on both sides, $C_p = C_n$, and thus by equation 2.3, the total capacitance C_T can be calculated to be half of either C_p or C_n (Wang *et al.*, 2012). While in an asymmetric EDLC, in which two different electrodes are constructed on both

sides, the C_T as half of either electrode's capacitance is not applied (Wang *et al.*, 2012). It should be noted that for symmetric EDLCs, the capacitance that is calculated for a single electrode is always 4 times of that calculated for a complete capacitor (Suss *et al.*, 2015). This is because the complete capacitor has doubled in weight and is half the capacitance than that of a single electrode.

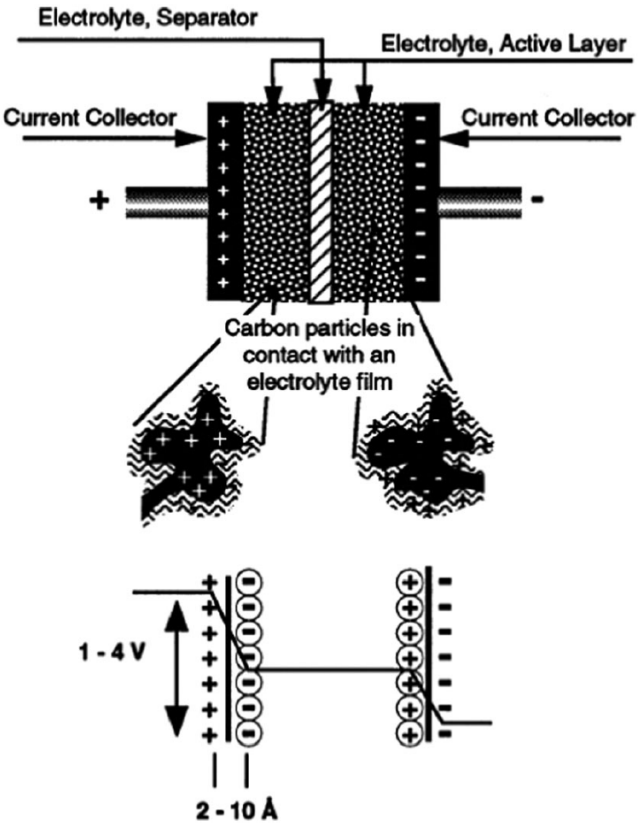

Figure 2.4 Principles of an EDLC and an illustration of the potential drop at the electrode/electrolyte interface. Taken from (Wang *et al.*, 2012).

The two primary attributes of an EDLC are its energy density and power density. For either measurement, the density can be calculated as a quantity per unit mass, per unit area, or per unit volume. The energy E and power P can be obtained by using the equations

$$E = \frac{1}{2}CV^2 \qquad (2.4)$$

and

$$P = \frac{V^2}{4R_s} \qquad (2.5)$$

where R_s is the equivalent series resistance of the capacitor (in ohms), V is the cell voltage (in volts), and C is the capacitance (in Farads). From the above equations, in general, the power density and energy density are directly determined by the R_s, V, and C values. R_s is the internal resistance that is associated with the resistance of the electrodes, the electrolyte, and the contact resistance between the electrodes and collectors. Specifically, to increase the energy density, one aims to increase the values of V and C. To increase the power density, the value of V should be increased or R_s should be reduced. V is highly dependent on the type of aqueous electrolyte used. For example, the voltage window of an EDLC is about 1 V when using carbon-based electrode materials with aqueous electrolytes, whereas the voltage window changes to 3 - 3.5 V when using organic electrolytes (Wang *et al.*, 2012). Furthermore, the increase in the capacitance of an EDLC can be achieved by carefully selecting the electrode materials with optimized structures.

2.4 Structural supercapacitors

Structural supercapacitors rely on the combination of high mechanical properties and electrocapacitive performance of the materials used for their construction. The main component of a structural supercapacitor is the electrode material, which should possess both sufficient electrical conductivity and high mechanical

properties. As laminated carbon fibre composites have a similar architecture to structural supercapacitors, woven carbon fibres have been chosen as electrodes for the fabrication of structural supercapacitors in recent years (Javaid *et al.*, 2016; Qian, Diao*, et al.*, 2013). Activation has become a common method to increase the surface area of carbon fibre electrodes, and to develop the distribution of porosity. Qian, Diao*, et al.* (2013) reported KOH activation as an effective way to increase the specific surface area and capacitance of carbon fibre electrodes for structural supercapacitors, simultaneously being able to maintain their mechanical properties. In addition, Qian, Kucernak*, et al.* (2013) designed a novel structure of electrodes by embedding carbon fibres in a carbon aerogel (CAG). These CAG modified carbon fibre electrodes increase in their surface area compared to plain carbon fibres, leading to an enhanced electrode capacitance (by 100 times) with an increased shear strength (by 4.5 times). More recently, Hudak, Schlichting, and Eisenbeiser (2017) reported the fabrication of structural supercapacitors with multi-walled carbon nanotubes (MWCNT) impregnated carbon fibre electrodes. Compared to plain carbon fibre supercapacitors in a two-electrode system, the incorporation of MWCNTs resulted in a significant increase in their specific capacitance from 3.3 - 4.7 mF g^{-1} to an average value of 125 mF g^{-1} (Hudak *et al.*, 2017). Meanwhile, the flexural strength and modulus of MWCNT impregnated carbon fibre electrode-based supercapacitors were reported to be 21 MPa and 2.9 GPa, respectively (Hudak *et al.*, 2017). This study also involved a three-electrode system, in which the capacitance of MWCNTs or electrochemical functionalization impregnated carbon fibres could reach 3 F g^{-1}, much higher than that of the two-electrode system (Hudak *et al.*, 2017). In addition to carbon fibre electrodes, graphene has also been previously

demonstrated to be a good electrode candidate for structural supercapacitors (Xu & Zhang, 2017).

Most industrial polymers are non-conductive, and therefore some conductive ingredients such as ionic liquids (IL) and salts are typically added to these polymer materials to make solid electrolytes (Deka *et al.*, 2017). It is believed that an increased concentration of IL in solid electrolytes could result in an increased ionic conductivity but reduced mechanical properties (Javaid *et al.*, 2016). Thus, in real applications, the concentration of IL in the electrolyte matrix should be adjusted to balance the multifunctionality of the structural supercapacitors.

2.5 Electrospun cellulose fibre derived carbon fibres

2.5.1 Introduction to cellulose fibres

Cellulose is one of the most abundant biomass materials in the world. It has a general formula $(C_6H_{10}O_5)_n$, and is a linear polymer therefore of anhydroglucose units (Dumanlı & Windle, 2012). Cellulose can be biosynthesized from a large variety of plants such as wood, hemp, flax, and cotton. It can be also obtained from bacterial and sea creatures such as tunicates. Cellulose is a linear homopolysaccharide that consists of repeated β-D-glucopyranose units linked via (1→4) glycosidic linkages (Sjostrom, 2013). The length of the cellulose chains is highly dependent on the source e.g. the degree of polymerization (DP) for wood derived native cellulose is around 10000 glucopyranose units and the DP for cotton derived native cellulose is around 15000 (Siqueira, Bras, & Dufresne, 2010). Cellulose fibres are considered to be formed by the aggregation of cellulose microfibrils, which are bundles of cellulose molecules linked laterally and stabilized by strong intra- and inter-molecular hydrogen bonds. These

hydrogen bonds firmly hold the adjacent cellulose molecule chains side-by-side to giving the structure high tensile strength. These hydrogen bonds are formed between O(6) to O(2)H and O(3)H groups, as shown in Figure 2.5 (Sjostrom, 2013). The microfibrils are 2 - 20 nm in length and they consist of alternated crystalline regions and amorphous regions (Azizi Samir, Alloin, & Dufresne, 2005).

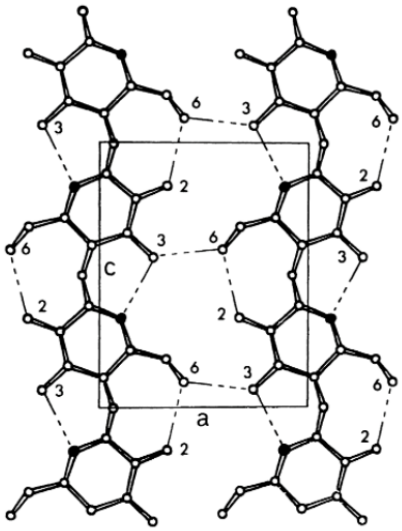

Figure 2.5 Projection of the a-c crystallographic plane in cellulose I with numbered atoms and the hydrogen bonding network (dotted lines). Taken from (Sjostrom, 2013).

In general, cellulose is found in two forms; either native or regenerated cellulose. Native cellulose, also referred as cellulose I, is the crystalline form that can be found in nature. Cellulose I itself has two different crystalline forms, namely I_α and I_β (Atalla & Vanderhart, 1984). Most sources of cellulose I have mixtures of these two allomorphs. The percentage of these two allomorphs is dependent on the origin of the material, e.g. I_α is predominant in bacterial celluloses, while tunicate is I_β rich (Eichhorn *et al.*, 2010). Regenerated cellulose, namely cellulose II, has antiparallel chains as opposed to the parallel chains in

cellulose I. It is believed that cellulose II has the same hydrogen bonds within the chains in the a-c plane as in cellulose I (Sjostrom, 2013). However, cellulose II has two additional hydrogen bonds between the corner chain and the centre chain compared to cellulose I (Figure 2.6) (Sjostrom, 2013). This results in a more thermodynamically stable cellulose II structure than cellulose I (Sjostrom, 2013).

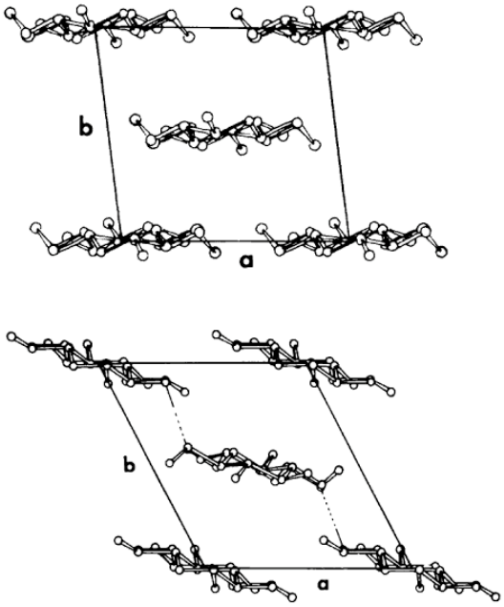

Figure 2.6 Axial projections of the structures of cellulose I (top) and cellulose II (bottom). Taken from (Sjostrom, 2013).

2.5.2 The basics of electrospinning

Electrospinning is a method that has been used to generate fibres from polymer solutions or melts by means of electrostatic forces (Zhang, Kang, Tarascon, & Kim, 2016). The fibres produced by electrospinning can be continuous ultrafine nanofibres, although micron-sized fibres are also possible. Because of the nanoscale diameter of the fibres, they provide a larger surface area to volume

ratios than materials obtained from other traditional spinning methods (Ramakrishna *et al.*, 2006).

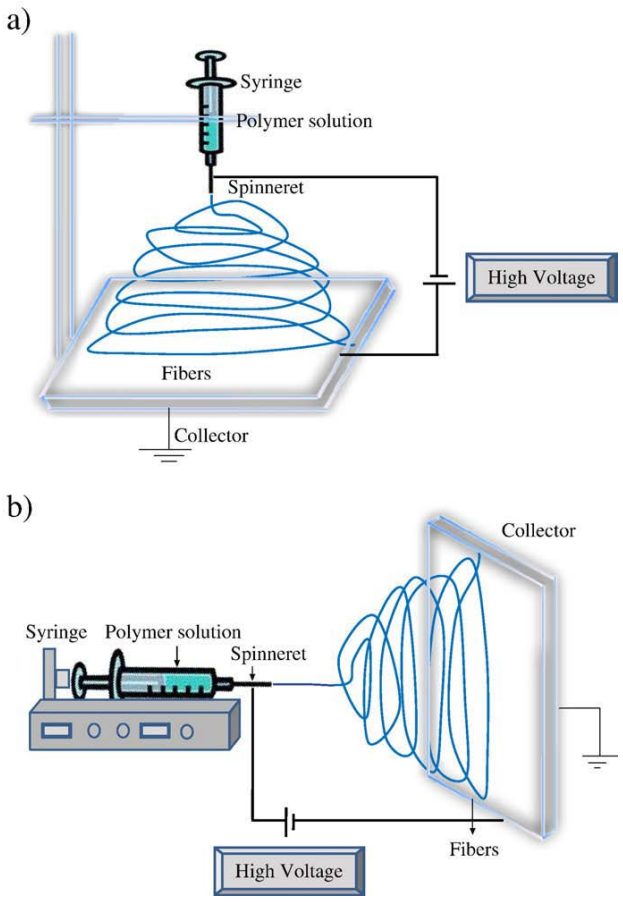

Figure 2.7 Schematic of a typical electrospinning apparatus; (a) typical vertical set up and (b) a horizontal set up. Taken from (Bhardwaj & Kundu, 2010).

As can be seen from Figure 2.7, a typical basic electrospinning apparatus consists of three major parts; namely a high voltage power supply, a spinneret and an earthed or charged collector (Zhang *et al.*, 2016). Specifically, the spinneret can be a pipette tip (metallic needle or other tube tips) connected to a syringe pump, in which the polymer solution is inserted before electrospinning takes place. The polymer solution is prepared via dissolving polymer powder or liquid in a solvent before introduction into a syringe pump. In most cases,

electrospinning is conducted in a chamber with a ventilation system to prevent problems caused by emitting unpleasant or toxic vapour from the volatile polymer solution.

The process of electrospinning typically starts with a polymer solution droplet being held by surface tension at the end of spinneret tip, a certain distance from a metallic collector in ambient conditions without the presence of a voltage. When a high voltage ranging from 1 to 30 kV is applied to the needle, an electric field is accordingly generated, and in turn, an electric charge is induced and evenly distributed on the surface of the polymer solution droplet. Theoretically, the droplet at the nozzle of the spinneret with the electric charges has two types of electrostatic forces. One force is the electrostatic repulsion existing between the surface charges. The other is the Coulombic force induced by the external electric field. The combined influence of these two forces distorts the polymer solution droplet into a conical shape called the Taylor cone (Taylor, 1969). In accordance with the cone-jet regime, the appearance of the Taylor cone is considered as the initiation of the formation of the fibres. Once the electrostatic forces exceed a critical value, the repulsive electrical forces are able to overcome the surface tension to allow a charged jet of the solution to eject from the tip of the Taylor cone (Bhardwaj & Kundu, 2010). The formation and acceleration of the fluid jet are impacted by the presence of the electric field. It should be noted that the jet is only stable within a short straight-line distance from the tip of the spinneret. This straight electric jet then experiences a stretching and simultaneously an unstable ‘whipping’ zone (Huang, Zhang, Kotaki, & Ramakrishna, 2003). As the electrified jet is further stretched and elongated within the whipping zone, a long and thin thread is finally formed, during which the solvent of the polymer solution

evaporates, leaving solid polymer in the jet. The whole process leads to the reduction of the diameter of the liquid jet from hundreds of micrometres to as small as several nanometres. These ultrathin fibres are finally collected via a grounded metallic collector. Due to the whipping process, the nanofibres are normally randomly oriented using this basic setup.

2.5.3 Control of the morphology of electrospun fibres

The working parameters are of importance in the process of electrospinning to control a variety of properties of fibres. These properties include the morphologies, diameters and also mechanical properties. The appearance of beads in electrospun fibres is one of the common but unwanted problems of the process. Beads are thought to be defect structures because they disturb the unique properties of electrospun fibres and decrease the surface area to volume ratio (Demir, Yilgor, Yilgor, & Erman, 2002). It has been found that surface tension is the main driving force behind the formation of beads. Surface tension forces the liquid jet to form spherical droplets at the end of the spinneret by minimizing the surface area (Li & Xia, 2004). On the other hand, the electrostatic forces tend to increase the surface area of droplets, leading to the reduction of diameters to form a bead-free jet (Li & Xia, 2004). Also, viscoelastic forces favour slow changes in the jet shape and resist the formation of beads on the surface of fibres (Li & Xia, 2004). Thus, in order to prevent the formation of the beads, actions should be taken to afford a suitable net force to make surface tension smaller than the other two forces. Theoretically, viscoelastic forces are determined by the solution viscosity. It is hard to obtain smooth fibres in a solution with a very low viscosity. By increasing the solution viscosity, the density of the beads decreases, or they disappear completely. This is because chain entanglement increases with

an increase in the viscosity, which can be achieved by increasing the solution concentration (Tungprapa *et al.*, 2007). However, very high solution viscosities can result in difficulties in creating a jet from the Taylor-cone (Beachley & Wen, 2009). The concentration of the solution can also influence the density of the beads due to a close relationship between concentration and viscosity; normally a higher solution concentration leads to a higher viscosity (Tungprapa *et al.*, 2007). In general, a sufficiently low concentration of polymer solution results in a breakdown the charged jet into small droplets, leading to electrospraying instead of electrospinning (Costa, Bretas, & Gregorio, 2010). An increase in the polymer concentration leads to the formation of beads along the fibre lengths. When the concentration reaches an optimum value, smooth nanoscale fibres without beads can be obtained. In previous research on producing cellulose acetate with a DMAc/acetone solution, beads were removed by increasing the concentration from 12.5 to 15 wt.% (Liu & Hsieh, 2002). In addition to controlling the solution parameters to remove beads from spun fibres, the spinning voltage can also be an important factor for this purpose. Recent research has reported that the shape of the droplet on top of the spinneret can be changed by increasing the voltage (Deitzel, Kleinmeyer, Harris, & Beck Tan, 2001). In this case, the reason for the formation of beads arises from the movement of the initial jet at the syringe tip when increasing the voltage. This instability then gives rise to the formation of a high density of beads along the electrospun fibres (Deitzel, Kleinmeyer, Harris, & Tan, 2001). Other research has however found the opposite result when electrospinning nanofibres from a poly(desaminotyrosyl-tyrosine ethyl ester carbonate) solution at two different concentrations (15% and 20% w/v). Smooth fibres were obtained by increasing the electrostatic field strengths from 10 - 15

kV/10 cm to 20 - 25 kV/10 cm (Meechaisue, Dubin, Supaphol, Hoven, & Kohn, 2006).

2.5.4 Production of cellulose fibres from electrospun cellulose acetate fibres

Cellulose II can be converted from the less stable cellulose I structure by two approaches, namely regeneration and mercerization. Regeneration is a process to precipitate cellulose out of solutions by dilution in water, while mercerization involves swelling cellulose I in an alkali solution to accomplish the conversion (Kolpak, Weih, & Blackwell, 1978). It is believed that the processing of cellulose is difficult in general as this natural polymer does not melt or dissolve in usual solvents due to its strong intermolecular hydrogen bonds (Bodvik *et al.*, 2010). Others however have asserted that the low aqueous solubility of cellulose is because the cellulose is significant amphiphilic (Medronho, Romano, Miguel, Stigsson, & Lindman, 2012).

Regenerated cellulose fibres can also be obtained from electrospinning of cellulose derivatives, such as cellulose acetate (CA). Cellulose acetate (CA) is the acetate ester of cellulose, which has been used as the material for the preparation of semipermeable membranes (Makhija & Vavia, 2003), cigarette filters (Harris, 2011), highly absorbent nappies (Konwarh, Karak, & Misra, 2013) amongst many other applications. Many solvent systems are capable of dissolving CA to make an electrospun solution. The solvent system can be either single or mixed. Single solvent systems consist of acetone, chloroform, N, N-dimethylformamide (DMF), dichloromethane (DCM), formic acid, methanol (MeOH) and pyridine (Tungprapa *et al.*, 2007). Mixed binary solvent systems comprise of acetone/dimethylacetamide (DMAc), chloroform/MeOH, and

DCM/MeOH (Tungprapa *et al.*, 2007). Among these electrospun solutions for electrospinning CA, the acetone/DMAc system has gained particular interest. Numerous groups have successfully produced pure CA fibres from this mixed solvent system (Liu & Tang, 2006; Tarus, Fadel, Al-Oufy, & El-Messiry, 2016; Tian *et al.*, 2011). It should be noted that neither acetone nor DMAc alone enables the continuous production of fibres (Liu & Hsieh, 2002). For instance, short and beaded fibres were obtained by electrospinning of 5 and 8% (*w*/*w*) CA solutions in acetone, possibly because of the low shear viscosity of the solution (Jaeger, Bergshoef, Batlle, Schönherr, & Julius Vancso, 1998). On the other hand, continuous electrospun fibres with diameters of 100 nm - 1 um were achieved by using a binary mixture solvent of 12.5 - 20% (*w*/*w*) CA in 2:1 acetone/DMAc (Liu & Tang, 2006). Similarly, another study pointed out that cylindrical shaped electrospun fibres were obtained by using an acetone/DMAc (2:1 w/w) solvent system (Rodriguez, Gatenholm, & Renneckar, 2012). It is further noted that there is an interesting power law relationship of 0.26 between the solution flow rate and the CA fibre size for 17% CA in acetone/DMAc (2:1 w/w). Other ratios of acetone/DMAc have been found to be capable of producing smooth electrospun fibres e.g. 16% (w/v) CA in 1:1, 2:1, and 3:1 (v/v) acetone/DMAc, and 14, 16, 18, 20% (w/v) CA in 2:1 (v/v) acetone-DMAc (Tungprapa *et al.*, 2007).

Deacetylation is used to convert electrospun CA fibres into cellulose fibres. Deacetylation of CA membranes has been achieved by either NaOH/ethanol or NaOH/water treatments (Callegari, Tyomkin, Kornev, Neimark, & Hsieh, 2011; Han, Youk, Min, Kang, & Park, 2008; Khatri, Wei, Kim, & Kim, 2012; Liu & Hsieh, 2002).

A typical deacetylation reaction of CA and NaOH has been given by (He, 2017) as

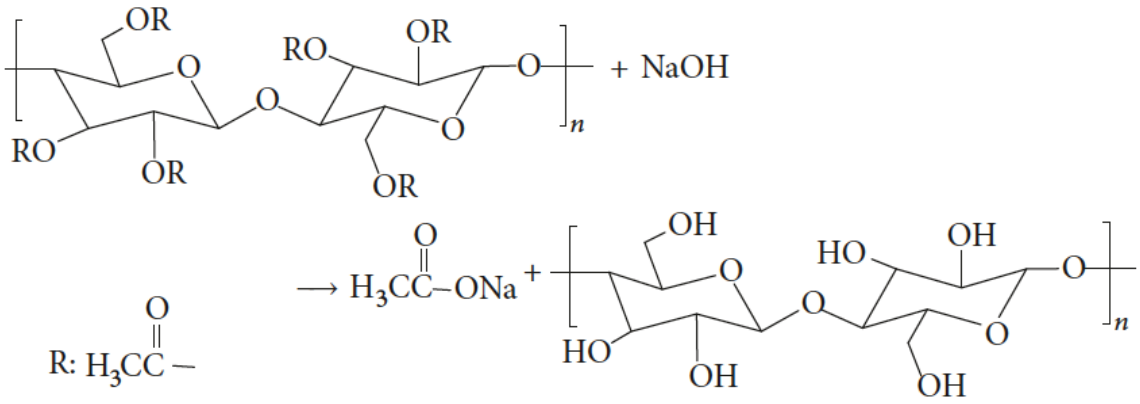

Very recently, a so-called ultrasonic-assisted deacetylation was developed on the basis of NaOH deacetylation to convert electrospun CA nanofibres into cellulose nanofibres (Ahmed *et al.*, 2017). In addition to NaOH, other chemical agents for deacetylation have been utilized, such as fluorination (Kim & Lee, 2016).

2.5.5 Carbon nanofibres generated from electrospun cellulose fibres

2.5.5.1 General introduction to carbon nanofibres

Carbon nanofibres are sp^2 carbon-based linear filaments with a nano-scale diameter. They possess several unique properties, such as high specific area, flexibility, high mechanical strength, and high electrical conductivity. The combination of carbon nanofibres with a matrix material enables the fabrication of high-performance composites. These composites afford good toughness and strength for potential use in the automobile and aerospace industries (Barcena, Coleto, Zhang, Hilmas, & Fahrenholtz, 2010; Khanna & Bakshi, 2009). Carbon nanofibres are different from traditional filaments of the same material in terms of their diameter and structure. Traditional carbon fibres are typically prepared from

precursors such as polyacrylonitrile (PAN), pitch or cellulose by heat treatment including stabilization, carbonization and graphitization.

The production of carbon nanofibres (CNFs) can be achieved by two approaches, electrospinning (Kim & Yang, 2003) and chemical vapour deposition (CVD) (Gao, Pandey, Turner, Westgate, & Sammakia, 2012). In the case of the CVD method, the direct growth of carbon nanofibres can be accomplished by feeding a carbon source over metallic nanoparticles in a heated chamber, which is very similar to the process of growing carbon nanotubes (CNTs). Figure 2.8 gives a schematic and the mechanism of nanofibre formation. Hydrocarbon molecules are decomposed into carbon atoms which then interact with the surface of the metal particles. The carbon atoms are then dissolved into bulk metal particles or are diffused onto their surface. Finally, precipitation of carbon atoms takes place in the form of carbon nanofibres (De Jong & Geus, 2007).

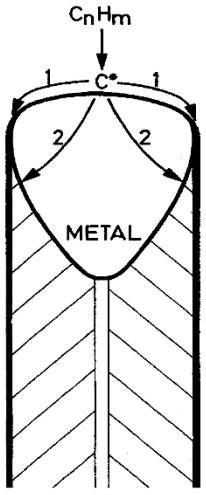

Figure 2.8 Schematic of the metal-catalysed growth of carbon nanofibres from gaseous hydrocarbons; the arrows represent traveling routes of carbon atoms. Taken from (De Jong & Geus, 2007).

Generally, the precipitation of carbon atoms only takes place on certain facets of the catalyst particles (Jiang, 2014). The structures and morphologies of CNFs are highly influenced by the morphology and chemical state of the catalysts (Jiang, 2014). For example, fishbone-type fibres result from the precipitation of carbon atoms onto Ni (111) metal particles, which are normally epitaxial (De Jong & Geus, 2007). The morphology of these particles is shown in Figure 2.9. It is noted that the parallel fibres resulting from this process are often referred to as carbon nanotubes, which are characterised by an entire hollow structure along the tube direction (De Jong & Geus, 2007). These are distinctive compared to carbon nanofibres, which have regularly stacked, truncated conical or planar layers along the filament length (Oberdorster, Castranova, Asgharian, & Sayre, 2015).

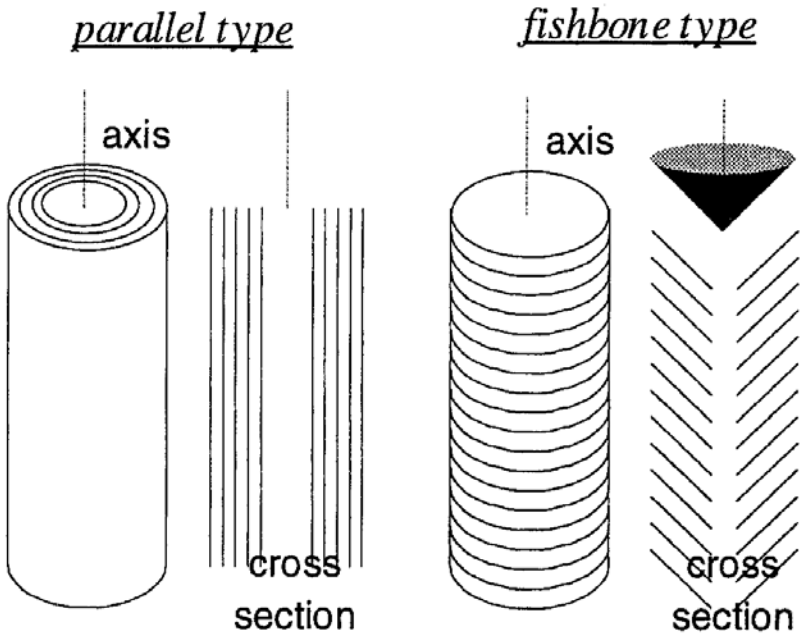

Figure 2.9 The structure and cross-sections of parallel (left) and fishbone type (right) carbon nanofibres from TEM images. Taken from (De Jong & Geus, 2007).

In addition to the traditional CVD approach, the fabrication of carbon nanofibres can also be achieved by electrospinning with the right polymer solution, followed

by thermal treatment in an inert atmosphere (Deng, Young, Kinloch, Zhu*, et al.*, 2013). The thermal treatment of a cellulosic precursor typically includes two main steps; namely the stabilization of the original fibres in the air at around 300 °C followed by carbonization at 400 - 900 °C (Dumanlı & Windle, 2012). The carbonized nanofibre subsequently undergoes graphitization at a temperature in the range 900 - 3000 °C to produce so-called graphite fibres (Dumanlı & Windle, 2012). In general, several superior properties such as nanosized diameters, high surface area, and thin web morphology of nanofibres are benefited by the application of electrospinning.

2.5.5.2 Production of carbon nanofibres from cellulosic precursors

Cellulose is a glucose-based and linear polymer connected by β-(1-4) glycosidic linkages (Dumanlı & Windle, 2012). The presence of hydroxyl groups in the cellulose structure allows it to form intra- and inter-molecular hydrogen bonds, thereby forming a variety of ordered crystalline arrangements. In accordance with molecular stoichiometry $(C_6H_{10}O_5)_n$, theoretically, the carbon yield in the process of carbonization of cellulose is 44.4% (Morgan, 2005). However, the actual yield is much lower than this theoretical value; it is normally between 10 and 30% (Huang, 2009). This relatively low yield results from the elimination of oxygenated compounds such as carbon monoxide (CO) and carbon dioxide (CO_2) and some other carbon-containing gases during the carbonization process (Huang, 2009). The improvement of the carbon yield from cellulose precursors can be achieved by two approaches; adding suitable chemicals such as impregnants or flame retardants to modify and stabilize the pyrolytic mechanism or pyrolysing cellulose at slow heating rates and dwelling at a low temperature before carbonization (Dumanlı & Windle, 2012).

As illustrated in Figure 2.10, the conversion of cellulose fibre to carbon fibre includes generally four steps: dehydration, depolymerisation, carbonization, and graphitization (Dumanlı & Windle, 2012; Tang & Bacon, 1964). Dehydration and depolymerisation are two major reactions that dominate the pyrolysis of cellulose. The physical desorption of water takes place at 150 ºC prior to dehydration at temperatures in the range 150 - 240 ºC. During dehydration, the elimination of the hydroxyl groups results in the formation of conjugated double bonds. It is noted that both intra or inter molecular dehydration can take place during the dehydration process (Huang, 2009), in which the polymeric structure of cellulose is basically unchanged. Depolymerisation in a temperature range of 240 - 400 ºC is believed to be a major part of thermal degradation, during which the cellulose structure breaks down and the basic structure of the carbon fibres start to form (Tang & Bacon, 1964). One of the main reactions during depolymerisation is the formation of levoglucosan by the thermal scission of the 1,4 glycosidic bonds along the cellulosic chains (Li, Lyons-Hart, Banyasz, & Shafer, 2001). Levoglucosan can further form tar to significantly reduce the carbon yield (Li *et al.*, 2001). It is believed that the formation of levoglucosan is a competitive reaction with dehydration (Huang, 2009). Therefore, the application of slow heating rates at temperatures below the formation temperature of levoglucosan (250 ºC) can be used to increase the carbonization yield (Huang, 2009). Slow pyrolysis is also expected to improve the properties of the final fibres; these properties include porosity and a better microstructure compared to a fast pyrolysis product (Dumanlı & Windle, 2012). Following heat treatment of the structure at temperatures over 400 °C, normally in the range 400 to 900 °C, all the carbonaceous residues aromatize to form graphitic layers (Dumanlı & Windle, 2012). In general, carbonization of cellulose is a process of conversion from a

depolymerised structure into a more ordered carbon structure. Graphitization is performed within a relatively higher temperature range of 900 - 3000 °C to obtain high-modulus fibres via the development of ordering of the single layer graphitic stacks (Dumanlı & Windle, 2012; Tang & Bacon, 1964).

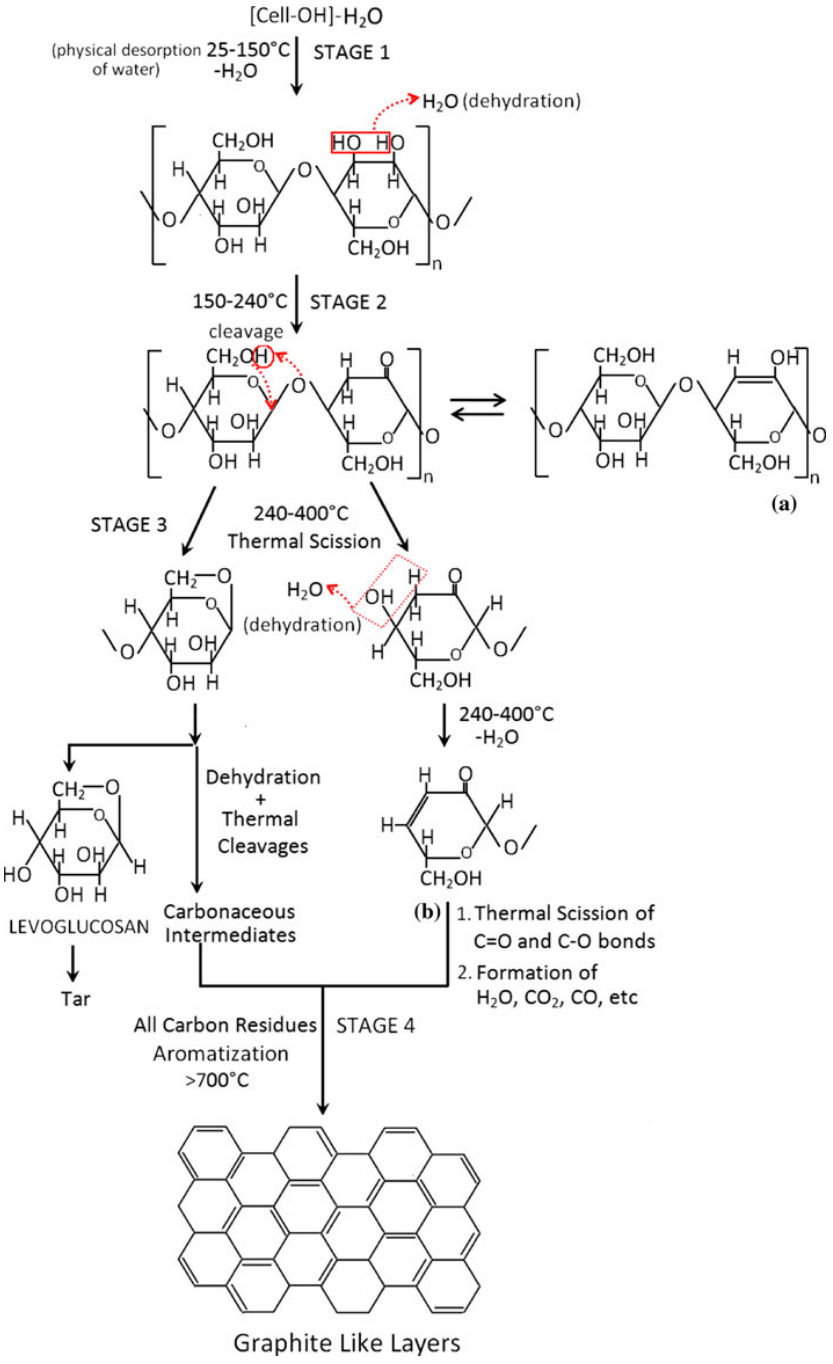

Figure 2.10 Reactions involved in the conversion of cellulose into carbon fibres (Dumanlı & Windle, 2012; Tang & Bacon, 1964).

2.5.6 Electrospinning in the presence of nanomaterials

Nanomaterials such as nanoparticles, nanowires, and molecular species can be directly mixed into the polymer solution for electrospinning to produce nanofibres with the combination of these functional nanomaterials (Li & Xia, 2004). For instance, SBA-15 type ordered mesoporous silica particles have been incorporated into electrospun polyacrylonitrile (PAN) nanofibres (Almuhamed *et al.*, 2014). The specific surface area and pore volume of fibres were found to increase compared with the plain electrospun PAN fibres (Almuhamed *et al.*, 2014). In addition, The incorporation of $Fe(Acc)_3$ into PAN nanofibres via electrospinning was demonstrated by Hou and Reneker (2004). Fe nanoparticles released from Fe salts to catalyse the growth of carbon nanotubes directly onto the surface of carbonized PAN nanofibres. Lu and Hsieh (2010) also reported a doubling of the Young's modulus and tensile strength for electrospun cellulose/0.55 wt.% MWCNT fibres compared to plain cellulose fibres.

2.5.7 Mechanical properties of electrospun cellulose derived carbon nanofibre

The mechanical properties of carbonized cellulose fibres are comparable with conventional micro-sized carbon fibres. Lewandowska, Soutis, Savage, and Eichhorn (2015) have investigated both single fibre tensile testing and Raman shifts recorded from polarized spectra of carbonized and graphitized cellulose fibres (at a temperature of 2000 °C); these experiments were performed to estimate their tensile modulus. The results suggested a modulus of approximately 70 GPa for the graphitized cellulose fibres, which is potentially competitive with E-glass fibres. Similarly, the effective Young's modulus of the CNFs derived from electrospun cellulose fibres was estimated by using in situ

Raman spectroscopy, and found to be highly dependent on the pyrolysis temperature. Modulus was found to increase by 40%, from 60 GPa at a pyrolysis temperature of 1500 °C to 100 GPa at 2200 °C (Deng, Young, Kinloch, Zhu*, et al.*, 2013). The modulus of graphitized skin-core structured cellulose fibres was also investigated using the same in situ Raman and deformation test. Larger shifts were observed for the skin than the core, and therefore, a higher modulus of the skin was assumed compared to the core. The modulus of skin and core were estimated using this method to be 140 GPa and 40 GPa, respectively. (Kong, Deng, Kinloch, Young, & Eichhorn, 2012). Nano-sized cellulose-based CNFs generally have much better mechanical properties compared to micron-sized fibres. This is thought to be due to their much smaller diameters, thereby providing a higher surface area for adhesion and then subsequently stress transfer in a composite material.

2.6 Growth of carbon nanotubes (CNTs)

2.6.1 Crystallographic structure of CNTs

A CNT is an arrangement of sp^2 bonded carbon atoms, which can be visualized as a rolled sheet (or concentric sheets) of graphene. CNTs are normally nanometres in diameter and micrometres to centimetres in length (Aqel, Abou El-Nour, Ammar, & Al-Warthan, 2012). In accordance with the number of concentrically arranged tubes, CNTs are typically divided into two categories; namely single-walled carbon nanotubes (SWCNTs) and multi-walled carbon nanotubes (MWCNTs) (Karimi *et al.*, 2015). To better understand the crystal structure of SWCNTs, it is necessary to introduce another carbon structure, namely graphene. Graphene is a single layer of sp^2 hybridized carbon atoms that are arranged in a honeycomb lattice. The unit cell of CNTs can be defined by the

primitive vectors $\overrightarrow{a_1}$ and $\overrightarrow{a_2}$ along a graphene sheet. Each CNT is defined by the chiral vector, $\overrightarrow{C_h}$ and the chiral angle, θ.

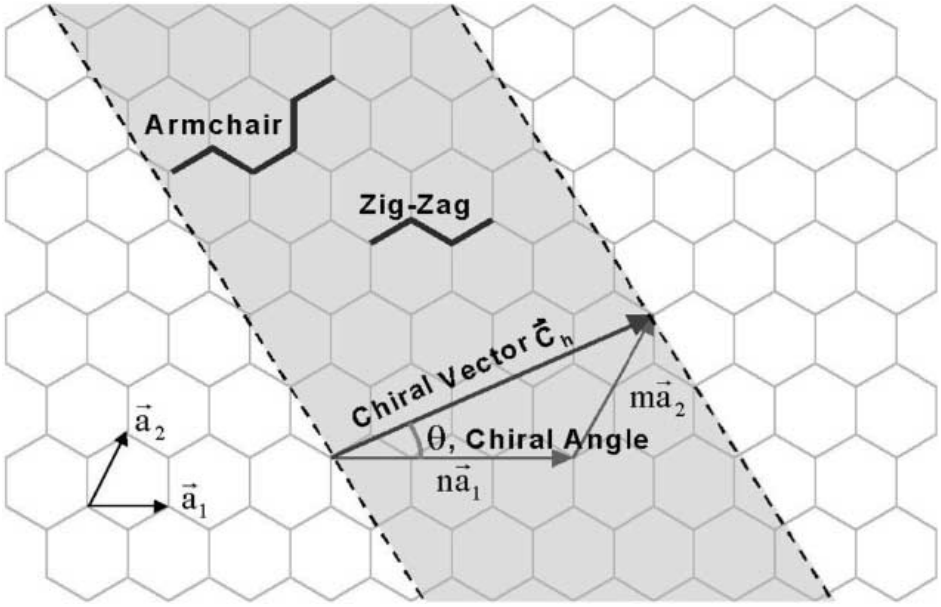

Figure 2.11 Schematic showing how a hexagonal sheet of graphite is rolled to form a carbon nanotube. Taken from (Thostenson, Ren, & Chou, 2001).

In Figure 2.11, the structure of a CNT can be imaged by cutting the graphene sheet along the dotted lines and rolling this sheet to form a tube, and therefore the tip and the tail of the chiral vector are connected to each other. The chiral vector $\overrightarrow{C_h}$ is defined by the equation

$$\overrightarrow{C_h} = n\overrightarrow{a_1} + m\overrightarrow{a_2} \qquad (2.6)$$

where the $\overrightarrow{a_1}$ and $\overrightarrow{a_2}$ are unit vectors, the *n* and *m* are the numbers of steps along the unit vectors of two hexagonal lattices, 0 ≤ *m* ≤ *n*.

The angle *θ* between $\overrightarrow{C_h}$ and $\overrightarrow{a_1}$ is called the chiral angle, and determines the degree of twist in the CNT. The chiral angle *θ* is defined by the equation

$$\cos\theta = \frac{C_h a_1}{|C_h||a_1|} = \frac{2n+m}{2\sqrt{n^2+m^2+nm}} \qquad (2.7)$$

The two limits of chiral angle are 0° and 30°, which refer to zigzag (0°) and armchair (30°) CNTs based on the geometry of the carbon bonds around the circumference of the CNTs, shown in Figure 2.12.

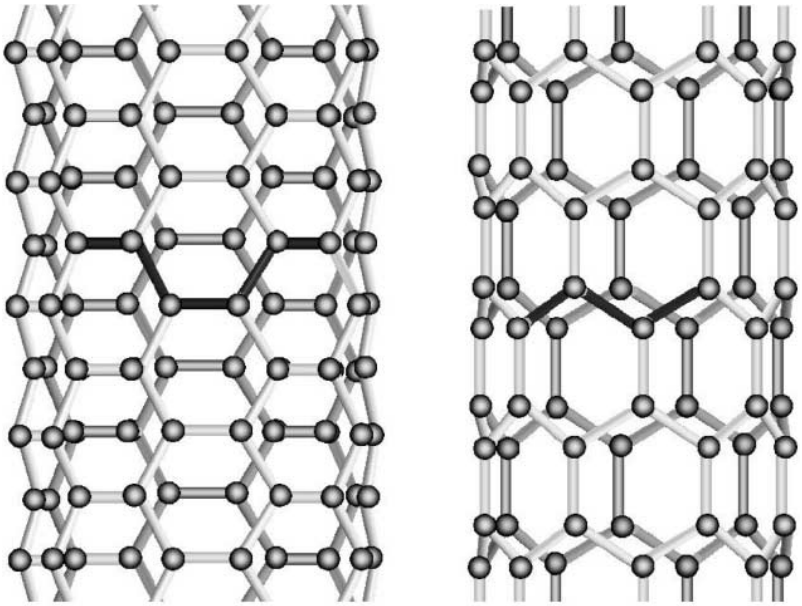

Figure 2.12 Illustrations of the atomic structure of (a) an armchair and (b) a zigzag nanotube. Taken from (Thostenson *et al.*, 2001).

In general, SWCNTs can be also distinguished by three categories depending on the different m and n values,

1. Armchair nanotubes for which $n = m$
2. Zigzag nanotubes for which m = 0
3. Chiral nanotubes ($n \neq m \neq 0$)

The chirality also has a great influence on the material properties of the SWCNTs (Thostenson *et al.*, 2001). In particular, electronic properties are determined by the chirality, leading to them performing as either metallic or semiconducting materials (Yanagi *et al.*, 2010). Semiconducting nanotubes are of interest for applications as photonic devices (Yamashita, Saito, & Choi, 2013), while metallic nanotubes are promising for numerous electronic applications such as nanocircuit components and power transmission cables (Nanot, Haroz, Kim, Hauge, & Kono, 2012).

2.6.2 Growth methods for CNTs

There are three methods for the general synthesis of CNTs; namely an arc-discharge method (Ebbesen & Ajayan, 1992), a laser-vaporization technique (Puretzky *et al.*, 2002), and chemical vapour deposition (CVD) (Cassell, Raymakers, Kong, & Dai, 1999). The first two methods have inherent drawbacks owing to their own operating limitations involving high-power electric arcs and relatively high-temperature conditions. Although a high yield of crystalline CNTs is possible by the arc-discharge method, the resultant materials are highly impure. It is also difficult to grow highly aligned CNTs. A high purity form of CNTs can be successfully grown by a laser-vaporization technique. However, their production yield is very low.

CVD gains its popularity among the techniques for growing CNTs with obvious advantages in terms of low growth temperatures, ease of control and scale up, and relatively low cost. The CVD method is thought of as a standard method to produce CNTs. The CVD process generally needs a high-temperature reaction zone, a hydrocarbon source, and a catalyst material. The hydrocarbon can be in different forms: gas vapour (ethylene or methane (Cheung, Kurtz, Park, & Lieber,

2002), etc.), liquid (benzene (Kamalakaran *et al.*, 2000), alcohol (Maruyama, Kojima, Miyauchi, Chiashi, & Kohno, 2002), etc.), and volatile solid (camphor (Mukul & Yoshinori, 2007), naphthalene (Wang, Shao, & Xue, 2015), etc.). In the case of a vapour hydrocarbon, it can be directly introduced into a high-temperature reactor (at temperatures in the range 600 - 1200 °C), followed by a decomposition to carbon atoms as a precursor of CNTs (Kumar & Ando, 2010). The CNTs thus grow with the presence of the catalysts. While for a liquid or solid hydrocarbon, it is necessary to preheat or directly introduce volatile materials to the high-temperature reaction zone in the CVD to transfer them to vapour. The catalysts can be either pre-located or floated into the reaction zone of CVD reactor. The catalyst vapour liberates catalytic nanoparticles when being pyrolyzed at a suitable temperature. In fact, it is available to control the structure and morphology of CNTs by varying hydrocarbon, catalyst, temperature, pressure, gas flow rate and deposition time.

2.6.3 CNT Catalysts

For growing CNTs, transition metal nanoparticles (Fe, Co, and Ni) are thought to be the most commonly used metallic catalysts due to their high solubility and diffusion rate for carbon atoms at high temperatures (Kumar & Ando, 2010). Besides, Fe, Co, and Ni have stronger adhesion with the grown CNTs than other transition metals. This results in the formation of high-curvature CNTs such as SWCNTs. Further, in a thermal CVD process using C_2H_2 as a carbon source, the growth rate of CNTs for different catalysts is in the order of Ni > Co > Fe. However, higher crystalline CNTs have been obtained by using the Fe catalyst, compared to those grown from Ni or Co catalysts (Lee, Park, & Yu, 2002). The influence of the size of nanoclusters of catalysts on the diameters and structures of CVD-

grown CNTs has been reported; larger catalyst clusters lead to larger CNTs (Cheung *et al.*, 2002). As alternatives to transition metals, solid organometallocenes (ferrocene, cobaltocene and nickelocene) are also proven to be good candidates as CNT catalysts. They can be used for the same function as transition metals owing to their liberation of metal nanoparticles at suitable temperatures. Apart from a number of commonly used transition metals (Fe, Co, Ni), other metallic species such as Al, In, Pt, Ti, Mg, Pd, K, Cs, Na, W, Mn, Mo and Ir have also been reported to grow CNTs by the decomposition of different hydrocarbons (Esconjauregui, Whelan, & Maex, 2009). With recent developments in novel catalysts, many non-metallic species have been found to be used to catalyse CNT growth under specific conditions. It has also been shown that CNTs can be grown from ceramic, semiconductor nanoparticles of SiC, Ge, and Si (Takagi, Hibino, Suzuki, Kobayashi, & Homma, 2007), and nano-sized diamond particles (Takagi, Kobayashi, & Homma, 2009).

2.6.4 Carbon fibre substrate to grow CNTs

The substrate is also of importance for the growth of CNTs in addition to the selection of the carbon source and the catalyst. The material used for the substrate with a certain surface morphology and texture can affect the yield and quality of the grown CNTs. The substrate not only acts as a medium for supporting the catalyst but also interacts with its growth environment. Various substrates that are popular for the CVD process of growing CNTs are silicon (Kumar, Kakamu, Okazaki, & Ando, 2004), silicon carbide (Murakami *et al.*, 2004), quartz (Kitiyanan, Alvarez, Harwell, & Resasco, 2000), silica (Li *et al.*, 1996), and alumina (Hiroshi *et al.*, 2008).

CNF can also be used as a substrate for the growth of CNTs. The methods that used to introduce catalysts to CNF substrates include a floating catalyst approach (Shazed, Suraya, Rahmanian, & Salleh, 2014), grafting the catalyst by simply dipping CNFs into the solution containing the catalyst (Samsur, Rangari, Jeelani, Zhang, & Cheng, 2013) or using a magnetron sputtering method to coat catalysts onto the surfaces of CNFs (Thostenson, Li, Wang, Ren, & Chou, 2002), and encapsulating the catalyst nanoparticles into the CNFs by electrospinning (Hou & Reneker, 2004; Lai, Guo, Wu, Reneker, & Hou, 2008). Among these methods, the floating catalyst approach is the most convenient and size-controllable processing route to make CNF/CNTs. However, the main problems associated with growing CNTs on the surface of CNFs are that:

- the diffusion of catalytic nanoparticles into the carbon substrates may happen during the deposition period, and
- different types of carbon materials may form on the CNF substrates to influence the purity of CNTs because the CNT growth conditions are similar to amorphous carbon or less crystalline CNFs.

2.7 Activated carbon fibre electrodes

Activated carbon fibres (ACFs) are one of the most widely used electrodes for the fabrication of EDLCs. This is because ACFs have a high specific surface area and high electrical conductivity. ACFs, for this purpose, are produced by activation (physical activation or chemical activation) of carbonaceous fibres to make porous structures of electrodes. In the physical activation, carbon precursors are treated by the gases e.g. steam and CO_2 at a high temperature of 700 - 1200 °C (Simon & Gogotsi, 2008). During chemical activation, redox

reactions take place between carbon precursors and chemical agents such as potassium hydroxide (KOH) (Yoon *et al.*, 2004), sodium hydroxide (NaOH) (Xu *et al.*, 2010), and zinc chloride (ZnCl) (Teng & Yeh, 1998). The capacitance of EDLCs are highly dependent on the features of electrodes such as the electrical conductivity, specific surface area, pore size distribution, pore shape and structure, and surface functional groups (Choi & Yoon, 2015). The specific surface area and pore size distribution are two of the essential influencing factors that affect the capacitance of carbon-based EDLCs (Wang *et al.*, 2012), which can be optimized by the activation process (Babel & Jurewicz, 2004).

Among all these activation agents, KOH activation is a well-known chemical activation technique that is used to produce activated carbons. KOH activation is advantageous compared to physical activation because it can be completed at low temperatures, but a high specific surface area can be achieved. Moreover, the micropores and mesopores can be easily developed with a controlled pore size distribution during the KOH activation.

KOH activation is a complex process that contains several consecutive redox reactions as follows (Wang & Kaskel, 2012)

$$6KOH + 2C \rightarrow 2K + 3H_2 + 2K_2CO_3 \quad (2.8)$$

$$K_2CO_3 \rightarrow K_2O + CO_2 \quad (2.9)$$

$$CO_2 + C \rightarrow 2CO \quad (2.10)$$

$$K_2CO_3 + 2C \rightarrow 2K + 3CO \quad (2.11)$$

$$C + K_2O \rightarrow 2K + CO \quad (2.12)$$

The formation of K_2CO_3 initiates from about 400 °C by the reaction of KOH with C atoms that are contained within the carbon fibres (Raymundo-Pinero *et al.*, 2005). When the temperature is elevated to 600 °C, the transition from KOH to K_2CO_3 is fully completed (Lozano-Castello, Calo, Cazorla-Amoros, & Linares-Solano, 2007). K_2CO_3 then decomposes into CO_2 and K_2O when the temperature increases above 700 °C (Raymundo-Pinero *et al.*, 2005), and fully consumes at 800 °C. The CO_2 reacts with C to produce CO at high temperatures. Moreover, the resulting K_2O and K_2CO_3 can further react with carbon to form metallic K at temperatures above 700 °C (Lozano-Castello *et al.*, 2007) (Wang & Kaskel, 2012).

In general, there are three activation mechanisms that can be then concluded from the above reactions. The carbon atoms are consumed by the reaction of potassium compounds (KCO_3, K_2O) with carbon so that this process etches the fibres. As the reactions are redox reactions, this type of activation is also called chemical activation. The formation of CO_2 can also cause gasification of carbon to further develop pores. No redox reaction is included in this type of activation (equation 2.9), so it is called physical activation. Furthermore, the resultant metallic K can intercalate into the carbon lattices, leading to carbon lattice expansion to form pores in the carbon structure. The activation of amorphous CNFs is believed to broaden the starting micropores, from 0.5 to 0.7 - 0.9 nm, and generate new micropores in the range of 1 - 2 nm (Barranco *et al.*, 2010). The modification of the pore size distribution together with an increase in surface oxygen content can lead to a very high capacitance of 255 F g^{-1} in an acidic electrolyte with a high surface area of 1520 m^2 g^{-1} (Barranco *et al.*, 2010). KOH activated viscose fibres as electrodes for the fabrication of supercapacitors have been systematically investigated. With a surface area of 1304 m^2 g^{-1}, specific

capacitance reached a value of 276 F g^{-1} in a 7 M KOH electrolyte (Babel & Jurewicz, 2004). In other work, KOH activation of cellulose-based waste coffee grounds resulted in hierarchically porous carbon nanosheets with a capacitance of 121 F g^{-1} at a current density of 0.5 A g^{-1}, and a high specific surface area of 1945.7 m^2 g^{-1} (Yun *et al.*, 2015). More recently, other precursors of derived activated carbon nanofibres (ACNFs) have been used as electrodes for the production of supercapacitors , e.g. sawdust (Huang, Liu, Zhao, & Chen, 2017), coconut fibres (Yin *et al.*, 2016), waste cotton glove (Wei, Yu, Yang, & Zhang, 2017), and pineapple leaf fibre (Sodtipinta *et al.*, 2017).

2.8 CNT electrodes

CNTs are also good electrodes themselves, or they can be used as an additive to produce electrodes. Their use as a pure electrode material can lead to specific capacitances that range between 15 and 200 F g^{-1}, with surface areas between 120 and 500 m^2 g^{-1} (Liu, Li, Ma, & Cheng, 2010). Normally, CNTs-based supercapacitors have a moderate surface area. They however have high capacitance because of the central canal running along the CNT length, and the entanglement resulting in mesopores within the CNT networks enabling easy access of the electrolyte ions to the electrodes (Frackowiak, Metenier, Bertagna, & Beguin, 2000). For instance, a value of specific capacitance 135 F g^{-1} with a specific surface area below 470 m^2 g^{-1} was obtained for an EDLC by using MWCNTs as an electrode (Frackowiak *et al.*, 2000). In fact, the surface area of CNTs was not as high as the conventional activated carbons (ACs) (normally 1000 - 2000 m^2 g^{-1}), but the capacitance of CNTs-based electrodes was competitive. In other work, the supercapacitors using untreated CNTs also achieved a capacitance of 102 F g^{-1} in a 38 wt.% H_2SO_4 electrolyte with an

average pore size of 9.2 nm and a specific surface area of 430 $m^2 g^{-1}$ (Niu, Sichel, Hoch, Moy, & Tennent, 1997). It was found that a high capacitive performance resulted from the high conductivity of CNTs with extremely low R_S (0.01 Ω). By optimizing the composition of the binder, annealing temperature, type of current collector, charging time, and discharging current density, a high specific capacitance of 180 F g^{-1} was obtained in an SWCNTs-based EDLC with 7.5 N KOH as an electrolyte (An *et al.*, 2001). It is found that the low surface area of pure CNTs can be improved by activation. The electrochemical capacitance of KOH activated CVD grown CNTs can reach 2 times that of untreated CNTs, with 3 times the BET specific surface area and 1.5 times the pore volume improvement after activation (Jiang, Qu, Zhou, Zhang, & Yu, 2002). Notably, KOH activated CNT electrodes that are prepared by catalytic decomposition of acetylene at 450 °C could also achieve a huge increase in their surface area, from 345 to 1670 $m^2 g^{-1}$, almost 5 times higher in comparison to the raw MWCNTs (Raymundo-Pinero *et al.*, 2005). The improvement of the surface area is because lots of defects are generated on the CNT walls, and the CNT walls are separated during the metallic K intercalation process (Raymundo-Pinero *et al.*, 2005). However, high purity MWCNTs produced at 600 °C only gave a surface area of 868 $m^2 g^{-1}$, nearly half of that obtained at 450 °C, indicating less well-ordered CNT walls benefit the development of accessible pores, and in turn improve the capacitive properties (Raymundo-Pinero *et al.*, 2005). The remarkably high specific surface area of activated CNTs is a sign of their potential to apply activated CNTs as electrodes for the fabrication of EDLCs. More recently, KOH activated CNT foams have been used as electrodes for EDLCs; a high specific capacitance of 144 F g^{-1} with a surface area of 1487 $m^2 g^{-1}$ was obtained. This

high capacitance was also considered to be contributed to the generation of a large number of micropores and mesopores during activation (Wang *et al.*, 2017).

2.9 ACNF/CNTs composite electrodes

Both ACNFs and CNTs have been used as electrodes for making EDLCs. The combination of both carbon materials also takes advantages of the properties of both carbon-based materials, which offers potential to make functional supercapacitors, e.g. free-standing supercapacitors with excellent mechanical properties. The production of composite electrodes of CNTs and ACs has been investigated for a long time. In general, AC/CNTs hybrid electrodes can be prepared by the growth of CNTs on ACs with a binder (Jian *et al.*, 2017), mixing ACs and CNTs together with a binder (Taberna, Chevallier, Simon, Plee, & Aubert, 2006), electrophoretic deposition (Huq, Hsieh, & Ho, 2016), or passing a CNTs/ACs pulp through a filter (Xu *et al.*, 2011). The addition of CNTs in AC electrodes has improved the capacitive performance of an AC/carbon black-based EDLC (Zheng, Qian, & Wei, 2012). However, the main problem of using AC powders is that the addition of a binder or other deposition techniques are required, which adversely influences their performance. Instead of ACs, the use of ACNFs as active material films can be directly used in devices. The combination of ACNFs and CNTs is believed to be a good electrode to improve capacitive performance compared to either pure ACNFs or pure CNTs. Similar to the approaches of making AC/CNTs composites, incorporation of CNFs and CNTs can be achieved by the dispersion of CNTs in electrospun polymeric solutions (Deng, Young, Kinloch, Abdelkader*, et al.*, 2013), physically grafting CNTs onto the surface of CNFs (Islam *et al.*, 2016), or growing CNTs on the surface of CNFs (Zhou, Wu, & Fong, 2012). In particular, electrospinning is

thought to be a good approach to fabricate CNFs or CNF/CNTs. This approach has been used to make activated CNF/CNTs composite electrodes by dispersion of CNTs into the electrospun polymeric precursor solution. These electrospun precursors with CNTs are then carbonized and activated to make composite electrodes. These precursors of PAN and cellulose have been demonstrated to have a capacitance of 310 F g^{-1} (Guo *et al.*, 2009), and 160 F g^{-1} (Deng, Young, Kinloch, Abdelkader*, et al.*, 2013), respectively. It is believed that the addition of highly conductive CNTs in the activated electrospun cellulose or PAN-based carbon fibres results in an improved charge transfer in the electrodes, leading to an enhanced specific capacitance. In addition to electrospinning the suspended CNTs solution to make CNF/CNTs composite electrodes, CNTs can be also grown from the surface of electrospun CNFs. Recent studies showed the CVD grown CNTs on electrospun based PAN (Zhou *et al.*, 2012) and cellulose (Kuzmenko *et al.*, 2016) derived carbon fibres have increased the capacitance compared to the pristine spun fibres. However, activation of CNF/CNTs was not performed to further enhance the capacitive performance in the above cases. Furthermore, enhanced capacitive performance could be achieved by introducing MnO_2 fillers in ACNF/CNTs (Zhang *et al.*, 2017) or by incorporation of polyaniline (PANI) into ACNF/CNTs to produce a pseudocapacitor (Li & Chen, 2017).

2.10 Electrolytes for the electrical double layer capacitors (EDLCs)

An electrolyte is also one of the important components in addition to the electrodes because it provides the ions for the formation of the electric double layers in EDLCs. Also, the electrolyte enters both electrodes and the separator materials. Therefore, the electrolyte is required to have a low viscosity, a wide

voltage window, high electrochemical stability, and a high ionic concentration (Wang *et al.*, 2012). It is also required to have a low solvated ionic radius, low resistivity, low volatility, low toxicity, low cost as well as being available with high purity (Wang *et al.*, 2012). In general, electrolytes consist of three types: aqueous, organic, and ionic liquids.

2.10.1 Aqueous electrolytes

Aqueous electrolytes have the advantages of providing lower resistance and higher ionic concentration when compared with organic electrolytes. The commonly used aqueous electrolytes are H_2SO_4, KOH, Na_2SO_4, and NH_4Cl. In general, aqueous electrolytes can achieve EDLCs with higher capacitance and higher power than those made with organic electrolytes (Wang *et al.*, 2012). This is due to the fact that aqueous electrolytes can provide higher ionic concentrations and smaller ionic radius, resulting in more ions being stored in the pores in the electrodes and therefore a higher capacitance. However, the voltage window of an EDLC by using aqueous electrolytes is as low as about 1 V, because the decomposition voltage of water occurs at 1.23 V (Gonzalez, Goikolea, Barrena, & Mysyk, 2016). This voltage window is much narrower than those used for organic electrolytes, which leads to limited energy and power densities. Also, care is required when the aqueous electrolyte is being applied because evaporation of the electrolyte will take place when the supercapacitors are not perfectly sealed. This requires a precise operation to fabricate aqueous electrolyte supercapacitors.

2.10.2 Organic electrolytes

The most important advantage of using organic electrolytes compared to aqueous is that the voltage window can reach as high as 3.5 V (Wang *et al.*, 2012). Organic electrolytes are normally prepared by dissolving salts into solvents. The most commonly used solvents are acetonitrile (ACN) and propylene carbonate (PC). Tetraethylammonium tetrafluoroborate, tetraethylphosphonium tetrafluoroborate, and triethylmethylammonium tetrafluoroborate ($TEMABF_4$) are the most commonly used organic salts for electrolytes (Wang *et al.*, 2012).

2.10.3 Ionic liquid electrolytes

Ionic liquid (IL) gel polymer electrolytes are prepared by mixing the ILs into a polymer matrix to form a mechanically strong, electrochemically and thermally stable, and highly conductive electrolyte. Compared to aqueous and organic electrolytes, the size of the ion in ILs are relatively easier to determine, as there is no solvation shell that is developed by the solvents. IL electrolytes however have relatively low conductivities; typically less than 10 mS cm^{-1} (Galiński, Lewandowski, & Stępniak, 2006). The most commonly used ILs for EDLCs are imidazolium, pyrrolidinium, as well as asymmetric, aliphatic quaternary ammonium salts with anions such as tetrafluoroborate, trifluoromethanesulfonate, bis(trifluoromethanesulfonyl)imide, bis(fluorosulfonyl)imide or hexafluorophosphate (Wang *et al.*, 2012).

2.11 Raman spectroscopy for the assessment of mechanical properties

2.11.1 Raman spectroscopy

The theoretical basis of Raman spectroscopy relies on the electron vibrational mode. In Raman spectroscopy, as an incident photon coming from a laser beam interacts with a molecule of a specimen, it induces an oscillating dipole moment by polarizing and vibrating the electron clouds within the molecule. This induced dipole moment can emit a photon that can be either elastic or inelastically scattered. If a photon polarizes the electron cloud and raises it from the ground energy state to a short lived ‘virtual’ energy state and then immediately returning to the ground state, simultaneously scattering a photon with the same energy (same frequency) as that of the incident photon, this elastic scattering is called Rayleigh scattering. However, in Raman scattering, the energy of the scattered photon is different from that of incident photon and, therefore, a different frequency. If the molecule rises to a virtual state from a ground state and then drops back to a higher energy state, the scattered photon has less energy than the incident photon, and therefore a lower frequency. This is called Stokes scattering. If a molecule starts with a vibrational state and after scattering a photon it drops back down to the ground state, which means it lost energy. The scattered photon has more energy and therefore higher frequency. This is called anti-Stokes scattering. The shifts in frequency in Stokes scattering and anti-Stokes scattering are called Stokes and anti-Stokes shifts, respectively. A typical energy-level diagram showing this process is shown in Figure 2.13. As Raman scattering is very sensitive to the in-plane crystalline size of carbon materials, it was used to investigate the structures of carbon fibre in this study.

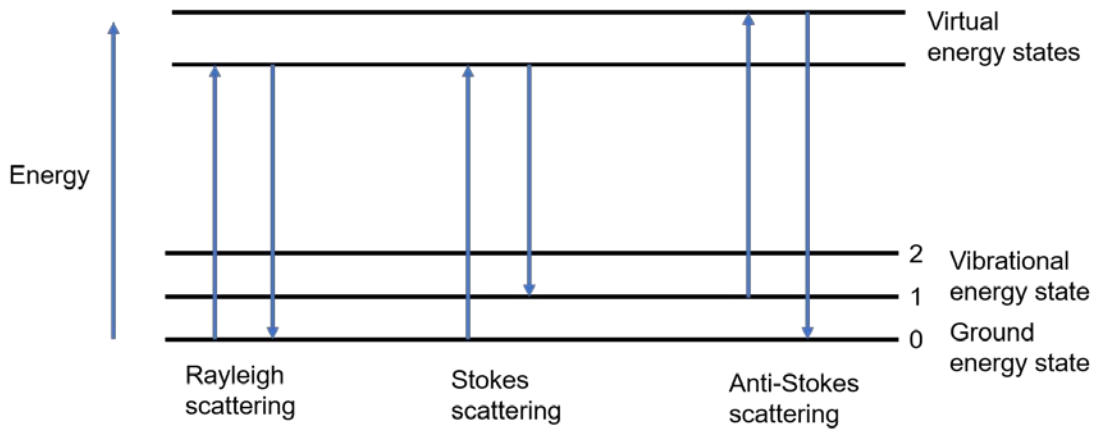

Figure 2.13 Energy-level diagram showing the different energy states.

Raman spectra are normally presented with wavenumbers (Δw) as an *x*-axis and intensities on the *y*-axis. The equation

$$\Delta w = \left(\frac{1}{\lambda_0} - \frac{1}{\lambda_1}\right) \times 10^7 \qquad 2.13$$

shows the relationship between wavenumber and wavelength, where Δw is the Raman shift reported in wavenumbers (cm^{-1}), λ_0 is the wavelength (nm) of the incident photon, and λ_1 is the wavelength (nm) of the Raman spectrum. For example, for a laser beam with a wavelength of 532 nm interacting with a carbon fibre specimen, scattering photons with a wavelength of 581 nm, a Raman shift of 1590 cm^{-1} (G band) can be detected in this Raman spectrum. The origin of Raman scattering can also be explained by an oscillating molecule. The polarizability (α) of the molecule is the ease with which the electron density distribution can be distorted by an electric field (Smith & Dent, 2005) according to the equation

$$P_{ind} = \alpha_0 E_0 \cos(2\pi v_{\mathrm{p}} t) + \frac{\alpha_0 E_0}{2} \cos(2\pi(v_{\mathrm{p}} - v_{\mathrm{vib}})t)$$

$$+ \frac{\alpha_0 E_0}{2} \cos(2\pi(v_{\mathrm{P}} + V_{\mathrm{vib}})t) \qquad 2.14$$

where v_{p} is the frequency of the incident photon, E_0 is the magnitude of the oscillating electric field of the photon, v_{vib} is the frequency of the molecule (Ball, 2001). A scattered photon oscillates at the same frequency as that of the oscillating dipole moment. Therefore, ν_{p}, $\nu_{\mathrm{p}} - \nu_{\mathrm{vib}}$ and $\nu_{\mathrm{p}} + \nu_{\mathrm{vib}}$ are the frequencies involved in the scattering of the photons, relating to Rayleigh scattering, Stokes scattering, and anti-Stokes scattering, respectively. Raman scattering will not occur if the polarizability does not change along the vibration.

2.11.2 In situ Raman spectroscopic method

Over the years, mechanical properties of carbon materials have been successfully evaluated by the observation of the shift of characteristic bands when the material is under strain (Papageorgiou *et al.*, 2017). The Raman shift arises from the change of vibrational frequencies of the normal modes when a strain is applied (Schadler *et al.*, 1998), during which the crystal phonons are modified; tensile strain leads to mode softening, and compression induces mode hardening (Mohiuddin, Lombardo, Nair, Bonetti, Savini, Jalil, Bonini, Basko, Galiotis, Marzari*, et al.*, 2009).

Good interfacial properties allow a great amount of applied stress to be transferred from matrix to high performance reinforcing materials, which helps to reduce stress concentrations and improves overall mechanical properties (Zhang *et al.*, 2012). The load transfer depends on the interfacial shear stress between

the fibre and the matrix (Schadler *et al.*, 1998). The Raman spectroscopic study has been used as an non-destructive method to evaluate the stress transfer for nanomaterials (Gouadec & Colomban, 2007). It is believed that higher stress transfer from the matrix to carbon fibres results in a larger Raman band shift (Xu *et al.*, 2012). This in situ Raman deformation technique was initially developed by Young and co-workers for the deformation of carbon fibres (Huang & Young, 1995). Since then, it has been applied to investigate the mechanical properties of other carbon materials such as CNTs (Cooper, Young, & Halsall, 2001; Prabhakaran *et al.*, 2007) and graphene (Ni *et al.*, 2008).

Mechanical properties such as stiffness and strength of carbon-based materials have been exploited by incorporating them into polymer nanocomposites. Raman spectroscopy has also been used for assessing the mechanical properties of carbon materials while they undergo deformation (tensile and compression). Shifts in the positions of Raman bands can be used as an indication of stress transfer from the matrix to carbon materials (Papageorgiou *et al.*, 2017). Young's modulus of fibres can then be related to the Raman band shifts using the equation (Eichhorn & Young, 2001)

$$E = \frac{\mathrm{d}\sigma}{\mathrm{d}(\Delta\nu)} \times \frac{\mathrm{d}(\Delta\nu)}{\mathrm{d}\varepsilon} = \frac{\mathrm{d}\sigma}{\mathrm{d}\varepsilon} \qquad (2.15)$$

where E is Young's modulus and $\mathrm{d}(\Delta\nu)/\mathrm{d}\varepsilon$ is the rate of Raman band shift with respect to strain. The stress sensitivity of the Raman band shift is expressed as $(\mathrm{d}(\Delta\nu)/\mathrm{d}\sigma)$, where $\Delta\nu$ is the value of Raman band shift and σ is the stress. The value of stress sensitivity of the Raman band shift varies for different materials, e.g. the value has been reported to be 4.7 cm^{-1}/GPa for cellulose (Sturcova, Davies, & Eichhorn, 2005) and 5 cm^{-1}/GPa for CNT (Cooper *et al.*, 2001). The

stress sensitivity of G band for carbon fibre and graphene is -5 ω_0^{-1} (cm^{-1} MPa^{-1}), where ω_0 is the G peak position at zero stress for both graphene and carbon fibre with annular morphology (Frank *et al.*, 2011). If the rate of the Raman band shift with strain ($d(\Delta\nu)/d\varepsilon$) is obtained by the Raman/bending test, the Young's modulus can be estimated by using equation 2.15.

The effect of the carbon fibre microstructure on the modulus of carbon fibres has been previously investigated. The rate of band shift was found to be proportional to the Young's modulus of the fibres, but different values were found for PAN and pitch-based fibres (Huang & Young, 1995). Lewandowska *et al.* (2015) characterised the graphitized cellulose fibres using the in situ Raman spectroscopic method, and a modulus of 77 GPa was obtained for carbon fibres processed at 2000 °C. This value of modulus was very closed to the one obtained via a standard tensile testing (70 GPa). Deng, Young, Kinloch, Zhu*, et al.* (2013) investigated the deformation of electrospun CNF1500 and CNF2200, and showed that the values of 2D Raman band shift rate with respect to strain were measured to be -3 and -5 cm^{-1}/%, respectively. The moduli were then estimated to be 60 GPa for CNF1500, and 100 GPa for CNF2200. The modulus of graphitized skin-core structured cellulose fibres was also estimated using the in situ Raman and deformation test (Kong *et al.*, 2012). Larger shifts were observed for the skin than the core, and therefore, a higher modulus of the skin was assumed compared to the core. The moduli of skin and core were estimated using this method to be 140 GPa and 40 GPa, respectively (Kong *et al.*, 2012). Very high values of Raman band shift rates per unit strain were obtained from single-walled carbon nanotubes (SWNTs) in poly(vinyl alcohol) (PVA) matrix-based electrospun nanocomposite fibres and films (Deng, Eichhorn, Kao, &

Young, 2011). The effective modulus of the SWNTs has been found to be in the range 530 - 700 GPa (Deng *et al.*, 2011).

2.12 References

Ahmed, F., Ayoub Arbab, A., Jatoi, A. W., Khatri, M., Memon, N., Khatri, Z., & Kim, I. S. (2017). Ultrasonic-assisted deacetylation of cellulose acetate nanofibers: A rapid method to produce cellulose nanofibers. *Ultrason Sonochem, 36*(Supplement C), 319-325. doi:10.1016/j.ultsonch.2016.12.013

Almuhamed, S., Khenoussi, N., Bonne, M., Schacher, L., Lebeau, B., Adolphe, D., & Brendle, J. (2014). Electrospinning of PAN nanofibers incorporating SBA-15-type ordered mesoporous silica particles. *European Polymer Journal, 54*, 71-78. doi:10.1016/j.eurpo1yrnj.2014.02.010

An, K. H., Kim, W. S., Park, Y. S., Moon, J. M., Bae, D. J., Lim, S. C., . . . Lee, Y. H. (2001). Electrochemical properties of high-power supercapacitors using single-walled carbon nanotube electrodes. *Advanced Functional Materials, 11*(5), 387-392. doi:10.1002/1616-3028(200110)11:5<387::Aid-Adfm387>3.0.Co;2-G

Aqel, A., Abou El-Nour, K. M. M., Ammar, R. A. A., & Al-Warthan, A. (2012). Carbon nanotubes, science and technology part (I) structure, synthesis and characterisation. *Arabian Journal of Chemistry, 5*(1), 1-23. doi:10.1016/j.arabjc.2010.08.022

Atalla, R. H., & Vanderhart, D. L. (1984). Native cellulose: a composite of two distinct crystalline forms. *Science, 223*(4633), 283-285. doi:10.1126/science.223.4633.283

Augustyn, V., Simon, P., & Dunn, B. (2014). Pseudocapacitive oxide materials for high-rate electrochemical energy storage. *Energy & Environmental Science, 7*(5), 1597-1614. doi:10.1039/c3ee44164d

Azizi Samir, M. A., Alloin, F., & Dufresne, A. (2005). Review of recent research into cellulosic whiskers, their properties and their application in nanocomposite field. *Biomacromolecules, 6*(2), 612-626. doi:10.1021/bm0493685

Babel, K., & Jurewicz, K. (2004). KOH activated carbon fabrics as supercapacitor material. *Journal of Physics and Chemistry of Solids, 65*(2-3), 275-280. doi:10.1016/j.jpcs.2003.08.023

Ball, D. W. (2001). Theory of Raman spectroscopy. *Spectroscopy, 16*(11), 32-+.

Barbieri, O., Hahn, M., Herzog, A., & Kotz, R. (2005). Capacitance limits of high surface area activated carbons for double layer capacitors. *Carbon, 43*(6), 1303-1310. doi:10.1016/j.carbon.2005.01.001

Barcena, J., Coleto, J., Zhang, S. C., Hilmas, G. E., & Fahrenholtz, W. G. (2010). Processing of Carbon Nanofiber Reinforced ZrB2 Matrix Composites for Aerospace Applications. *Advanced Engineering Materials, 12*(7), 623-626. doi:10.1002/adem.200900307

Barranco, V., Lillo-Rodenas, M. A., Linares-Solano, A., Oya, A., Pico, F., Ibanez, J., . . . Rojo, J. M. (2010). Amorphous Carbon Nanofibers and Their Activated Carbon Nanofibers as Supercapacitor Electrodes. *Journal of Physical Chemistry C, 114*(22), 10302-10307. doi:10.1021/jp1021278

Beachley, V., & Wen, X. (2009). Effect of electrospinning parameters on the nanofiber diameter and length. *Mater Sci Eng C Mater Biol Appl, 29*(3), 663-668. doi:10.1016/j.msec.2008.10.037

Becker, H. I. (1957). Low voltage electrolytic capacitor: Google Patents.

Bhardwaj, N., & Kundu, S. C. (2010). Electrospinning: a fascinating fiber fabrication technique. *Biotechnol Adv, 28*(3), 325-347. doi:10.1016/j.biotechadv.2010.01.004

Bodvik, R., Dedinaite, A., Karlson, L., Bergstrom, M., Baverback, P., Pedersen, J. S., . . . Claesson, P. M. (2010). Aggregation and network formation of aqueous methylcellulose and hydroxypropylmethylcellulose solutions. *Colloids and Surfaces a-Physicochemical and Engineering Aspects, 354*(1-3), 162-171. doi:10.1016/j.colsurfa.2009.09.040

Both, J. (2015). The Modern Era of Aluminum Electrolytic Capacitors. *Ieee Electrical Insulation Magazine, 31*(4), 24-34. doi:10.1109/Mei.2015.7126071

Brusso, B., & Chaparala, S. (2014). The Evolution of Capacitors [History]. *IEEE Industry Applications Magazine, 20*(6), 8-12. doi:10.1109/mias.2014.2342592

Callegari, G., Tyomkin, I., Kornev, K. G., Neimark, A. V., & Hsieh, Y. L. (2011). Absorption and transport properties of ultra-fine cellulose webs. *J Colloid Interface Sci, 353*(1), 290-293. doi:10.1016/j.jcis.2010.09.015

Cassell, A. M., Raymakers, J. A., Kong, J., & Dai, H. J. (1999). Large scale CVD synthesis of single-walled carbon nanotubes. *Journal of Physical Chemistry B, 103*(31), 6484-6492. doi:10.1021/jp990957s

Chapman, D. L. (1913). LI. A contribution to the theory of electrocapillarity. *The London, Edinburgh, and Dublin philosophical magazine and journal of science, 25*(148), 475-481.

Charles, P. (1896). United Kingdom Patent No. Her Majesty's Stationery Office.

Chen, S., Zhu, J., Wu, X., Han, Q., & Wang, X. (2010). Graphene oxide--MnO2 nanocomposites for supercapacitors. *ACS Nano, 4*(5), 2822-2830. doi:10.1021/nn901311t

Cheung, C. L., Kurtz, A., Park, H., & Lieber, C. M. (2002). Diameter-controlled synthesis of carbon nanotubes. *Journal of Physical Chemistry B, 106*(10), 2429-2433. doi:10.1021/jp0142278

Choi, H., & Yoon, H. (2015). Nanostructured Electrode Materials for Electrochemical Capacitor Applications. *Nanomaterials (Basel), 5*(2), 906-936. doi:10.3390/nano5020906

Conway, B. E. (2013). *Electrochemical Supercapacitors: Scientific Fundamentals and Technological Applications*: Springer US.

Cooper, C. A., Young, R. J., & Halsall, M. (2001). Investigation into the deformation of carbon nanotubes and their composites through the use of Raman spectroscopy. *Composites Part a-Applied Science and Manufacturing, 32*(3-4), 401-411. doi:10.1016/S1359-835x(00)00107-X

Costa, L. M. M., Bretas, R. E. S., & Gregorio, R. (2010). Effect of Solution Concentration on the Electrospray/Electrospinning Transition and on the Crystalline Phase of PVDF. *Materials Sciences and Applications, 01*(04), 247-252. doi:10.4236/msa.2010.14036

De Jong, K. P., & Geus, J. W. (2007). Carbon Nanofibers: Catalytic Synthesis and Applications. *Catalysis Reviews, 42*(4), 481-510. doi:10.1081/cr-100101954

Deitzel, J. M., Kleinmeyer, J., Harris, D., & Tan, N. C. B. (2001). The effect of processing variables on the morphology of electrospun nanofibers and textiles. *Polymer, 42*(1), 261-272. doi:10.1016/S0032-3861(00)00250-0

Deka, B. K., Hazarika, A., Kim, J., Park, Y. B., & Park, H. W. (2017). Recent development and challenges of multifunctional structural supercapacitors for automotive industries. *International Journal of Energy Research, 41*(10), 1397-1411. doi:10.1002/er.3707

Deng, L., Eichhorn, S. J., Kao, C. C., & Young, R. J. (2011). The effective Young's modulus of carbon nanotubes in composites. *ACS Appl Mater Interfaces, 3*(2), 433-440. doi:10.1021/am1010145

Deng, L., Young, R. J., Kinloch, I. A., Abdelkader, A. M., Holmes, S. M., De Haro-Del Rio, D. A., & Eichhorn, S. J. (2013). Supercapacitance from cellulose and carbon nanotube nanocomposite fibers. *ACS Appl Mater Interfaces, 5*(20), 9983-9990. doi:10.1021/am403622v

Deng, L. B., Young, R. J., Kinloch, I. A., Zhu, Y. Q., & Eichhorn, S. J. (2013). Carbon nanofibres produced from electrospun cellulose nanofibres. *Carbon, 58*, 66-75. doi:10.1016/j.carbon.2013.02.032

Deshpande, R. P. (2014). *Capacitors*: McGraw-Hill Education.

Dumanlı, A. G., & Windle, A. H. (2012). Carbon fibres from cellulosic precursors: a review. *Journal of Materials Science, 47*(10), 4236-4250. doi:10.1007/s10853-011-6081-8

Ebbesen, T. W., & Ajayan, P. M. (1992). Large-Scale Synthesis of Carbon Nanotubes. *Nature, 358*(6383), 220-222. doi:10.1038/358220a0

Eichhorn, S. J., Dufresne, A., Aranguren, M., Marcovich, N. E., Capadona, J. R., Rowan, S. J., . . . Peijs, T. (2010). Review: current international research into cellulose nanofibres and nanocomposites. *Journal of Materials Science, 45*(1), 1-33. doi:10.1007/s10853-009-3874-0

Eichhorn, S. J., & Young, R. J. (2001). The Young's modulus of a microcrystalline cellulose. *Cellulose, 8*(3), 197-207. doi:10.1023/A:1013181804540

Esconjauregui, S., Whelan, C. M., & Maex, K. (2009). The reasons why metals catalyze the nucleation and growth of carbon nanotubes and other carbon nanomorphologies. *Carbon, 47*(3), 659-669. doi:10.1016/j.carbon.2008.10.047

Faisal, M. S. S., Rahman, M. M., & Asmatulu, R. (2016). *Investigating effectiveness of activated carbons of natural sources on various supercapacitors.* Paper presented at the SPIE Smart Structures and Materials + Nondestructive Evaluation and Health Monitoring.

Frackowiak, E., Metenier, K., Bertagna, V., & Beguin, F. (2000). Supercapacitor electrodes from multiwalled carbon nanotubes. *Applied Physics Letters, 77*(15), 2421-2423. doi:10.1063/1.1290146

Frank, O., Tsoukleri, G., Riaz, I., Papagelis, K., Parthenios, J., Ferrari, A. C., . . . Galiotis, C. (2011). Development of a universal stress sensor for graphene and carbon fibres. *Nature Communications, 2*. doi:10.1038/ncomms1247

Galiński, M., Lewandowski, A., & Stępniak, I. (2006). Ionic liquids as electrolytes. *Electrochimica Acta, 51*(26), 5567-5580. doi:10.1016/j.electacta.2006.03.016

Gamby, J., Taberna, P. L., Simon, P., Fauvarque, J. F., & Chesneau, M. (2001). Studies and characterisations of various activated carbons used for carbon/carbon supercapacitors. *Journal of Power Sources, 101*(1), 109-116. doi:10.1016/S0378-7753(01)00707-8

Gao, Y., Pandey, G. P., Turner, J., Westgate, C. R., & Sammakia, B. (2012). Chemical vapor-deposited carbon nanofibers on carbon fabric for supercapacitor electrode applications. *Nanoscale Res Lett, 7*(1), 651. doi:10.1186/1556-276X-7-651

Ghaffarzadeh, K. (2016). *Graphene, 2D Materials and Carbon Nanotubes: Markets, Technologies and Opportunities 2016-2026; Granular Ten-year Market Forecasts, Data-driven and Quantitative Application Assessment, More Than 40 Interview Based Company Profiles, Revenue/investment/capacity by Player, Etc*: IDTechEx.

Gonzalez, A., Goikolea, E., Barrena, J. A., & Mysyk, R. (2016). Review on supercapacitors: Technologies and materials. *Renewable & Sustainable Energy Reviews, 58*, 1189-1206. doi:10.1016/j.rser.2015.12.249

Gouadec, G., & Colomban, P. (2007). Raman Spectroscopy of nanomaterials: How spectra relate to disorder, particle size and mechanical properties. *Progress in Crystal Growth and Characterization of Materials, 53*(1), 1-56. doi:10.1016/j.pcrysgrow.2007.01.001

Gouy, M. (1910). Sur la constitution de la charge électrique à la surface d'un électrolyte. *J. Phys. Theor. Appl., 9*(1), 457-468.

Guo, Q. H., Zhou, X. P., Li, X. Y., Chen, S. L., Seema, A., Greiner, A., & Hou, H. Q. (2009). Supercapacitors based on hybrid carbon nanofibers containing multiwalled carbon nanotubes. *Journal of Materials Chemistry, 19*(18), 2810-2816. doi:10.1039/b820170f

Han, S. O., Youk, J. H., Min, K. D., Kang, Y. O., & Park, W. H. (2008). Electrospinning of cellulose acetate nanofibers using a mixed solvent of acetic acid/water: Effects of solvent composition on the fiber diameter. *Materials Letters, 62*(4-5), 759-762. doi:10.1016/j.matlet.2007.06.059

Harris, B. (2011). The intractable cigarette 'filter problem'. *Tob Control, 20 Suppl 1*(Suppl 1), i10-16. doi:10.1136/tc.2010.040113

He, X. Z. (2017). Optimization of Deacetylation Process for Regenerated Cellulose Hollow Fiber Membranes. *International Journal of Polymer Science, 2017*, 8. doi:10.1155/2017/3125413

Helmholtz, H. v. (1853). Annalen der Physik. *Leipzig, 89*, 21.

Hiroshi, O., Daisuke, T., Kazuki, Y., Shohei, C., Akio, T., & Yoshikazu, H. (2008). Growth of Vertically Aligned Single-Walled Carbon Nanotubes on Alumina and Sapphire Substrates. *Japanese Journal of Applied Physics, 47*(4R), 1956. doi:10.1143/JJAP.47.1956

Hou, H. Q., & Reneker, D. H. (2004). Carbon nanotubes on carbon nanofibers: A novel structure based on electrospun polymer nanofibers. *Advanced Materials, 16*(1), 69-+. doi:10.1002/adma.200306205

Huang, X. S. (2009). Fabrication and Properties of Carbon Fibers. *Materials, 2*(4), 2369-2403. doi:10.3390/ma2042369

Huang, Y., & Young, R. J. (1995). Effect of Fiber Microstructure Upon the Modulus of Pan-and Pitch-Based Carbon-Fibers. *Carbon, 33*(2), 97-107. doi:10.1016/0008-6223(94)00109-D

Huang, Y. X., Liu, Y., Zhao, G. J., & Chen, J. Y. (2017). Sustainable activated carbon fiber from sawdust by reactivation for high-performance supercapacitors. *Journal of Materials Science, 52*(1), 478-488. doi:10.1007/s10853-016-0347-0

Huang, Z. M., Zhang, Y. Z., Kotaki, M., & Ramakrishna, S. (2003). A review on polymer nanofibers by electrospinning and their applications in nanocomposites. *Composites Science and Technology, 63*(15), 2223-2253. doi:10.1016/S0266-3538(03)00178-7

Hudak, N. S., Schlichting, A. D., & Eisenbeiser, K. (2017). Structural Supercapacitors with Enhanced Performance Using Carbon Nanotubes

and Polyaniline. *Journal of the Electrochemical Society, 164*(4), A691-A700. doi:10.1149/2.0721704jes

Huq, M. M., Hsieh, C. T., & Ho, C. Y. (2016). Preparation of carbon nanotube-activated carbon hybrid electrodes by electrophoretic deposition for supercapacitor applications. *Diamond and Related Materials, 62*(Supplement C), 58-64. doi:10.1016/j.diamond.2015.12.014

Islam, M. S., Deng, Y., Tong, L. Y., Faisal, S. N., Roy, A. K., Minett, A. I., & Gomes, V. G. (2016). Grafting carbon nanotubes directly onto carbon fibers for superior mechanical stability: Towards next generation aerospace composites and energy storage applications. *Carbon, 96*, 701-710. doi:10.1016/j.carbon.2015.10.002

Jaeger, R., Bergshoef, M. M., Batlle, C. M. I., Schönherr, H., & Julius Vancso, G. (1998). Electrospinning of ultra-thin polymer fibers. *Macromolecular Symposia, 127*(1), 141-150. doi:10.1002/masy.19981270119

Javaid, A., Ho, K. K. C., Bismarck, A., Steinke, J. H. G., Shaffer, M. S. P., & Greenhalgh, E. S. (2016). Carbon fibre-reinforced poly(ethylene glycol) diglycidylether based multifunctional structural supercapacitor composites for electrical energy storage applications. *Journal of Composite Materials, 50*(16), 2155-2163. doi:10.1177/0021998315602324

Jian, J., Linpo, L., Yani, L., Siyuan, L., Maowen, X., & Jianhui, Z. (2017). Uniform implantation of CNTs on total activated carbon surfaces: a smart engineering protocol for commercial supercapacitor applications. *Nanotechnology, 28*(14), 145402. doi:10.1088/1361-6528/aa5fad

Jiang, Q., Qu, M. Z., Zhou, G. M., Zhang, B. L., & Yu, Z. L. (2002). A study of activated carbon nanotubes as electrochemical super capacitors electrode

materials. *Materials Letters, 57*(4), 988-991. doi:10.1016/S0167-577x(02)00911-4

Jiang, X. (2014). CVD growth of carbon nanofibers. *Physica Status Solidi a-Applications and Materials Science, 211*(12), 2679-2687. doi:10.1002/pssa.201431631

Kamalakaran, R., Terrones, M., Seeger, T., Kohler-Redlich, P., Ruhle, M., Kim, Y. A., . . . Endo, M. (2000). Synthesis of thick and crystalline nanotube arrays by spray pyrolysis. *Applied Physics Letters, 77*(21), 3385-3387. doi:10.1063/1.1327611

Karimi, M., Solati, N., Amiri, M., Mirshekari, H., Mohamed, E., Taheri, M., . . . Hamblin, M. R. (2015). Carbon nanotubes part I: preparation of a novel and versatile drug-delivery vehicle. *Expert Opin Drug Deliv, 12*(7), 1071-1087. doi:10.1517/17425247.2015.1003806

Keithley, J. F., Instrumentation, I., & Society, M. (1999). *The Story of Electrical and Magnetic Measurements: From 500 BC to the 1940s*: Wiley.

Khanna, V., & Bakshi, B. R. (2009). Carbon Nanofiber Polymer Composites: Evaluation of Life Cycle Energy Use. *Environmental Science & Technology, 43*(6), 2078-2084. doi:10.1021/es802101x

Khatri, Z., Wei, K., Kim, B. S., & Kim, I. S. (2012). Effect of deacetylation on wicking behavior of co-electrospun cellulose acetate/polyvinyl alcohol nanofibers blend. *Carbohydrate Polymers, 87*(3), 2183-2188. doi:10.1016/j.carbpol.2011.10.046

Kim, C., & Yang, K. S. (2003). Electrochemical properties of carbon nanofiber web as an electrode for supercapacitor prepared by electrospinning. *Applied Physics Letters, 83*(6), 1216-1218. doi:10.1063/1.1599963

Kim, M. I., & Lee, Y. S. (2016). Deacetylation of cellulose acetate nanofibers by fluorination for carbon nanofibers. *Materials Letters, 181*(Supplement C), 236-239. doi:10.1016/j.matlet.2016.06.047

Kitiyanan, B., Alvarez, W. E., Harwell, J. H., & Resasco, D. E. (2000). Controlled production of single-wall carbon nanotubes by catalytic decomposition of CO on bimetallic Co–Mo catalysts. *Chemical Physics Letters, 317*(3-5), 497-503. doi:10.1016/s0009-2614(99)01379-2

Kolpak, F. J., Weih, M., & Blackwell, J. (1978). Mercerization of cellulose: 1. Determination of the structure of Mercerized cotton. *Polymer, 19*(2), 123-131. doi:10.1016/0032-3861(78)90027-7

Kong, K., Deng, L. B., Kinloch, I. A., Young, R. J., & Eichhorn, S. J. (2012). Production of carbon fibres from a pyrolysed and graphitised liquid crystalline cellulose fibre precursor. *Journal of Materials Science, 47*(14), 5402-5410. doi:10.1007/s10853-012-6426-y

Konwarh, R., Karak, N., & Misra, M. (2013). Electrospun cellulose acetate nanofibers: the present status and gamut of biotechnological applications. *Biotechnol Adv, 31*(4), 421-437. doi:10.1016/j.biotechadv.2013.01.002

Kotz, R., & Carlen, M. (2000). Principles and applications of electrochemical capacitors. *Electrochimica Acta, 45*(15-16), 2483-2498. doi:10.1016/S0013-4686(00)00354-6

Kumar, M., & Ando, Y. (2010). Chemical vapor deposition of carbon nanotubes: a review on growth mechanism and mass production. *J Nanosci Nanotechnol, 10*(6), 3739-3758. doi:10.1166/jnn.2010.2939

Kumar, M., Kakamu, K., Okazaki, T., & Ando, Y. (2004). Field emission from camphor–pyrolyzed carbon nanotubes. *Chemical Physics Letters, 385*(3-4), 161-165. doi:10.1016/j.cplett.2003.12.064

Kuzmenko, V., Saleem, A. M., Staaf, H., Haque, M., Bhaskar, A., Flygare, M., . . . Enoksson, P. (2016). Hierarchical cellulose-derived CNF/CNT composites for electrostatic energy storage. *Journal of Micromechanics and Microengineering, 26*(12), 124001. doi:10.1088/0960-1317/26/12/124001

Lai, C., Guo, Q., Wu, X. F., Reneker, D. H., & Hou, H. (2008). Growth of carbon nanostructures on carbonized electrospun nanofibers with palladium nanoparticles. *Nanotechnology, 19*(19), 195303. doi:10.1088/0957-4484/19/19/195303

Lee, C. J., Park, J., & Yu, J. A. (2002). Catalyst effect on carbon nanotubes synthesized by thermal chemical vapor deposition. *Chemical Physics Letters, 360*(3-4), 250-255. doi:10.1016/S0009-2614(02)00831-X

Lewandowska, A. E., Soutis, C., Savage, L., & Eichhorn, S. J. (2015). Carbon fibres with ordered graphitic-like aggregate structures from a regenerated cellulose fibre precursor. *Composites Science and Technology, 116*, 50-57. doi:10.1016/j.compscitech.2015.05.009

Li, D., & Xia, Y. (2004). Electrospinning of Nanofibers: Reinventing the Wheel? *Advanced Materials, 16*(14), 1151-1170. doi:10.1002/adma.200400719

Li, S., Lyons-Hart, J., Banyasz, J., & Shafer, K. (2001). Real-time evolved gas analysis by FTIR method: an experimental study of cellulose pyrolysis. *Fuel, 80*(12), 1809-1817. doi:10.1016/S0016-2361(01)00064-3

Li, W. Z., Xie, S. S., Qian, L. X., Chang, B. H., Zou, B. S., Zhou, W. Y., . . . Wang, G. (1996). Large-Scale Synthesis of Aligned Carbon Nanotubes. *Science, 274*(5293), 1701-1703. doi:10.1126/science.274.5293.1701

Li, Y., & Chen, C. (2017). Polyaniline/carbon nanotubes-decorated activated carbon fiber felt as high-performance, free-standing and flexible

supercapacitor electrodes. *Journal of Materials Science, 52*(20), 12348-12357. doi:10.1007/s10853-017-1291-3

Liu, C., Li, F., Ma, L. P., & Cheng, H. M. (2010). Advanced materials for energy storage. *Advanced Materials, 22*(8), E28-62. doi:10.1002/adma.200903328

Liu, H., & Tang, C. (2006). Electrospinning of Cellulose Acetate in Solvent Mixture N,N-Dimethylacetamide (DMAc)/Acetone. *Polymer Journal, 39*(1), 65-72. doi:10.1295/polymj.PJ2006117

Liu, H. Q., & Hsieh, Y. L. (2002). Ultrafine fibrous cellulose membranes from electrospinning of cellulose acetate. *Journal of Polymer Science Part B-Polymer Physics, 40*(18), 2119-2129. doi:10.1002/polb.10261

Lozano-Castello, D., Calo, J. M., Cazorla-Amoros, D., & Linares-Solano, A. (2007). Carbon activation with KOH as explored by temperature programmed techniques, and the effects of hydrogen. *Carbon, 45*(13), 2529-2536. doi:10.1016/j.carbon.2007.08.021

Lu, P., & Hsieh, Y. L. (2010). Multiwalled carbon nanotube (MWCNT) reinforced cellulose fibers by electrospinning. *ACS Appl Mater Interfaces, 2*(8), 2413-2420. doi:10.1021/am1004128

Makhija, S. N., & Vavia, P. R. (2003). Controlled porosity osmotic pump-based controlled release systems of pseudoephedrine - I. Cellulose acetate as a semipermeable membrane. *Journal of Controlled Release, 89*(1), 5-18. doi:10.1016/S0168-3659(02)00482-0

Maruyama, S., Kojima, R., Miyauchi, Y., Chiashi, S., & Kohno, M. (2002). Low-temperature synthesis of high-purity single-walled carbon nanotubes from alcohol. *Chemical Physics Letters, 360*(3-4), 229-234. doi:10.1016/S0009-2614(02)00838-2

Medronho, B., Romano, A., Miguel, M. G., Stigsson, L., & Lindman, B. (2012). Rationalizing cellulose (in)solubility: reviewing basic physicochemical aspects and role of hydrophobic interactions. *Cellulose, 19*(3), 581-587. doi:10.1007/s10570-011-9644-6

Meechaisue, C., Dubin, R., Supaphol, P., Hoven, V. P., & Kohn, J. (2006). Electrospun mat of tyrosine-derived polycarbonate fibers for potential use as tissue scaffolding material. *Journal of Biomaterials Science-Polymer Edition, 17*(9), 1039-1056. doi:10.1163/156856206778365988

Mohiuddin, T. M. G., Lombardo, A., Nair, R. R., Bonetti, A., Savini, G., Jalil, R., . . . Ferrari, A. C. (2009). Uniaxial strain in graphene by Raman spectroscopy:Gpeak splitting, Grüneisen parameters, and sample orientation. *Physical Review B, 79*(20), 205433. doi:10.1103/PhysRevB.79.205433

Morgan, P. (2005). *Carbon Fibers and Their Composites*: CRC Press.

Mukul, K., & Yoshinori, A. (2007). Carbon Nanotubes from Camphor: An Environment-Friendly Nanotechnology. *Journal of Physics: Conference Series, 61*(1), 643. doi:10.1088/1742-6596/61/1/129

Murakami, T., Sako, T., Harima, H., Kisoda, K., Mitikami, K., & Isshiki, T. (2004). Raman study of SWNTs grown by CCVD method on SiC. *Thin Solid Films, 464*(Supplement C), 319-322. doi:10.1016/j.tsf.2004.06.037

Nanot, S., Haroz, E. H., Kim, J. H., Hauge, R. H., & Kono, J. (2012). Optoelectronic properties of single-wall carbon nanotubes. *Advanced Materials, 24*(36), 4977-4994. doi:10.1002/adma.201201751

Ni, Z. H., Yu, T., Lu, Y. H., Wang, Y. Y., Feng, Y. P., & Shen, Z. X. (2008). Uniaxial strain on graphene: Raman spectroscopy study and band-gap opening. *ACS Nano, 2*(11), 2301-2305. doi:10.1021/nn800459e

Niu, C. M., Sichel, E. K., Hoch, R., Moy, D., & Tennent, H. (1997). High power electrochemical capacitors based on carbon nanotube electrodes. *Applied Physics Letters, 70*(11), 1480-1482. doi:10.1063/1.118568

Oberdorster, G., Castranova, V., Asgharian, B., & Sayre, P. (2015). Inhalation Exposure to Carbon Nanotubes (CNT) and Carbon Nanofibers (CNF): Methodology and Dosimetry. *J Toxicol Environ Health B Crit Rev, 18*(3-4), 121-212. doi:10.1080/10937404.2015.1051611

Pandolfo, A. G., & Hollenkamp, A. F. (2006). Carbon properties and their role in supercapacitors. *Journal of Power Sources, 157*(1), 11-27. doi:10.1016/j.jpowsour.2006.02.065

Papageorgiou, D. G., Kinloch, I. A., & Young, R. J. (2017). Mechanical properties of graphene and graphene-based nanocomposites. *Progress in Materials Science, 90*, 75-127. doi:10.1016/j.pmatsci.2017.07.004

Prabhakaran, K., Stephen, J. E., & Robert, J. Y. (2007). Deformation of isolated single-wall carbon nanotubes in electrospun polymer nanofibres. *Nanotechnology, 18*(23), 235707. doi:10.1088/0957-4484/18/23/235707

Puretzky, A. A., Schittenhelm, H., Fan, X. D., Lance, M. J., Allard, L. F., & Geohegan, D. B. (2002). Investigations of single-wall carbon nanotube growth by time-restricted laser vaporization. *Physical Review B, 65*(24), 245425. doi:10.1103/PhysRevB.65.245425

Qian, H., Diao, H., Shirshova, N., Greenhalgh, E. S., Steinke, J. G., Shaffer, M. S., & Bismarck, A. (2013). Activation of structural carbon fibres for potential applications in multifunctional structural supercapacitors. *J Colloid Interface Sci, 395*, 241-248. doi:10.1016/j.jcis.2012.12.015

Qian, H., Kucernak, A. R., Greenhalgh, E. S., Bismarck, A., & Shaffer, M. S. (2013). Multifunctional structural supercapacitor composites based on

carbon aerogel modified high performance carbon fiber fabric. *ACS Appl Mater Interfaces, 5*(13), 6113-6122. doi:10.1021/am400947j

Ramakrishna, S., Fujihara, K., Teo, W. E., Yong, T., Ma, Z. W., & Ramaseshan, R. (2006). Electrospun nanofibers: solving global issues. *Materials Today, 9*(3), 40-50. doi:10.1016/S1369-7021(06)71389-X

Raymundo-Pinero, E., Azais, P., Cacciaguerra, T., Cazorla-Amoros, D., Linares-Solano, A., & Beguin, F. (2005). KOH and NaOH activation mechanisms of multiwalled carbon nanotubes with different structural organisation. *Carbon, 43*(4), 786-795. doi:10.1016/j.carbon.2004.11.005

Rightmire, R. A. (1966). Electrical energy storage apparatus: Google Patents.

Rodriguez, K., Gatenholm, P., & Renneckar, S. (2012). Electrospinning cellulosic nanofibers for biomedical applications: structure and in vitro biocompatibility. *Cellulose, 19*(5), 1583-1598. doi:10.1007/s10570-012-9734-0

Salanne, M., Rotenberg, B., Naoi, K., Kaneko, K., Taberna, P. L., Grey, C. P., . . . Simon, P. (2016). Efficient storage mechanisms for building better supercapacitors. *Nature Energy, 1*, 16070. doi:10.1038/Nenergy.2016.70

Samsur, R., Rangari, V. K., Jeelani, S., Zhang, L., & Cheng, Z. Y. (2013). Fabrication of carbon nanotubes grown woven carbon fiber/epoxy composites and their electrical and mechanical properties. *Journal of Applied Physics, 113*(21), 214903. doi:10.1063/1.4808105

Schadler, L. S., Giannaris, S. C., & Ajayan, P. M. (1998). Load transfer in carbon nanotube epoxy composites. *Applied Physics Letters, 73*(26), 3842-3844. doi:10.1063/1.122911

Schindall, J. (2007). The charge of the ultracapacitors. *IEEE Spectrum, 44*(11), 42-46.

Serp, P., & Machado, B. (2015). *Nanostructured Carbon Materials for Catalysis*: Royal Society of Chemistry.

Shazed, M. A., Suraya, A. R., Rahmanian, S., & Salleh, M. A. M. (2014). Effect of fibre coating and geometry on the tensile properties of hybrid carbon nanotube coated carbon fibre reinforced composite. *Materials & Design, 54*, 660-669. doi:10.1016/j.matdes.2013.08.063

Simon, P., & Gogotsi, Y. (2008). Materials for electrochemical capacitors. *Nat Mater, 7*(11), 845-854. doi:10.1038/nmat2297

Siqueira, G., Bras, J., & Dufresne, A. (2010). Cellulosic Bionanocomposites: A Review of Preparation, Properties and Applications. *Polymers, 2*(4), 728-765. doi:10.3390/polym2040728

Sjostrom, E. (2013). *Wood chemistry: fundamentals and applications*: Elsevier.

Smith, E., & Dent, G. (2005). The Theory of Raman Spectroscopy *Modern Raman Spectroscopy – A Practical Approach* (pp. 71-92): John Wiley & Sons, Ltd.

Sodtipinta, J., Ieosakulrat, C., Poonyayant, N., Kidkhunthod, P., Chanlek, N., Amornsakchai, T., & Pakawatpanurut, P. (2017). Interconnected open-channel carbon nanosheets derived from pineapple leaf fiber as a sustainable active material for supercapacitors. *Industrial Crops and Products, 104*, 13-20. doi:10.1016/j.indcrop.2017.04.015

Stern, O. (1924). Zur theorie der elektrolytischen doppelschicht. *Berichte der Bunsengesellschaft für physikalische Chemie, 30*(21-22), 508-516.

Sturcova, A., Davies, G. R., & Eichhorn, S. J. (2005). Elastic modulus and stress-transfer properties of tunicate cellulose whiskers. *Biomacromolecules, 6*(2), 1055-1061. doi:10.1021/bm049291k

Suss, M. E., Porada, S., Sun, X., Biesheuvel, P. M., Yoon, J., & Presser, V. (2015). Water desalination via capacitive deionization: what is it and what can we

expect from it? *Energy & Environmental Science, 8*(8), 2296-2319. doi:10.1039/c5ee00519a

Taberna, P. L., Chevallier, G., Simon, P., Plee, D., & Aubert, T. (2006). Activated carbon-carbon nanotube composite porous film for supercapacitor applications. *Materials Research Bulletin, 41*(3), 478-484. doi:10.1016/j.materresbull.2005.09.029

Takagi, D., Hibino, H., Suzuki, S., Kobayashi, Y., & Homma, Y. (2007). Carbon nanotube growth from semiconductor nanoparticles. *Nano Lett, 7*(8), 2272-2275. doi:10.1021/nl0708011

Takagi, D., Kobayashi, Y., & Homma, Y. (2009). Carbon nanotube growth from diamond. *J Am Chem Soc, 131*(20), 6922-6923. doi:10.1021/ja901295j

Tang, M. M., & Bacon, R. (1964). Carbonization of cellulose fibers—I. Low temperature pyrolysis. *Carbon, 2*(3), 211-220. doi:10.1016/0008-6223(64)90035-1

Tarus, B., Fadel, N., Al-Oufy, A., & El-Messiry, M. (2016). Effect of polymer concentration on the morphology and mechanical characteristics of electrospun cellulose acetate and poly (vinyl chloride) nanofiber mats. *Alexandria Engineering Journal, 55*(3), 2975-2984. doi:10.1016/j.aej.2016.04.025

Taylor, G. (1969). Electrically Driven Jets. *Proceedings of the Royal Society of London Series a-Mathematical and Physical Sciences, 313*(1515), 453-&. doi:10.1098/rspa.1969.0205

Teng, H. S., & Yeh, T. S. (1998). Preparation of activated carbons from bituminous coals with zinc chloride activation. *Industrial & Engineering Chemistry Research, 37*(1), 58-65. doi:10.1021/ie970534h

Thostenson, E. T., Li, W. Z., Wang, D. Z., Ren, Z. F., & Chou, T. W. (2002). Carbon nanotube/carbon fiber hybrid multiscale composites. *Journal of Applied Physics, 91*(9), 6034-6037. doi:10.1063/1.1466880

Thostenson, E. T., Ren, Z. F., & Chou, T. W. (2001). Advances in the science and technology of carbon nanotubes and their composites: a review. *Composites Science and Technology, 61*(13), 1899-1912. doi:10.1016/S0266-3538(01)00094-X

Tian, Y., Wu, M., Liu, R. G., Li, Y. X., Wang, D. Q., Tan, J. J., . . . Huang, Y. (2011). Electrospun membrane of cellulose acetate for heavy metal ion adsorption in water treatment. *Carbohydrate Polymers, 83*(2), 743-748. doi:10.1016/j.carbpol.2010.08.054

Trasatti, S., & Buzzanca, G. (1971). Ruthenium dioxide: a new interesting electrode material. Solid state structure and electrochemical behaviour. *Journal of Electroanalytical Chemistry and Interfacial Electrochemistry, 29*(2), A1-A5.

Tungprapa, S., Puangparn, T., Weerasombut, M., Jangchud, I., Fakum, P., Semongkhol, S., . . . Supaphol, P. (2007). Electrospun cellulose acetate fibers: effect of solvent system on morphology and fiber diameter. *Cellulose, 14*(6), 563-575. doi:10.1007/s10570-007-9113-4

Wang, C. G., Shao, X. H., & Xue, R. S. (2015). The Formation of Carbon Nanostructures via Catalytic Pyrolysis of Naphthalene under Its Autogenic Pressure. *Journal of Nanomaterials, 2015*, 5. doi:10.1155/2015/752647

Wang, C. L., Feng, Y. J., Sun, X. C., Sun, H. B., Peng, T., Lu, Y., . . . Yu, B. H. (2017). Fabrication and activation of carbon nanotube foam and its application in energy storage. *Electrochimica Acta, 236*(Supplement C), 333-340. doi:10.1016/j.electacta.2017.03.173

Wang, G., Zhang, L., & Zhang, J. (2012). A review of electrode materials for electrochemical supercapacitors. *Chem Soc Rev, 41*(2), 797-828. doi:10.1039/c1cs15060j

Wang, J. C., & Kaskel, S. (2012). KOH activation of carbon-based materials for energy storage. *Journal of Materials Chemistry, 22*(45), 23710-23725. doi:10.1039/c2jm34066f

Wei, C., Yu, J., Yang, X., & Zhang, G. (2017). Activated Carbon Fibers with Hierarchical Nanostructure Derived from Waste Cotton Gloves as High-Performance Electrodes for Supercapacitors. *Nanoscale Res Lett, 12*(1), 379. doi:10.1186/s11671-017-2151-4

Xia, X. H., Tu, J. P., Mai, Y. J., Wang, X. L., Gu, C. D., & Zhao, X. B. (2011). Self-supported hydrothermal synthesized hollow Co3O4 nanowire arrays with high supercapacitor capacitance. *Journal of Materials Chemistry, 21*(25), 9319-9325. doi:10.1039/c1jm10946d

Xu, B., Wu, F., Chen, R. J., Cao, G. P., Chen, S., & Yang, Y. S. (2010). Mesoporous activated carbon fiber as electrode material for high-performance electrochemical double layer capacitors with ionic liquid electrolyte. *Journal of Power Sources, 195*(7), 2118-2124. doi:10.1016/j.jpowsour.2009.09.077

Xu, G. H., Zheng, C., Zhang, Q., Huang, J. Q., Zhao, M. Q., Nie, J. Q., . . . Wei, F. (2011). Binder-free activated carbon/carbon nanotube paper electrodes for use in supercapacitors. *Nano Research, 4*(9), 870-881. doi:10.1007/s12274-011-0143-8

Xu, J. M., & Zhang, D. (2017). Multifunctional structural supercapacitor based on graphene and geopolymer. *Electrochimica Acta, 224*, 105-112. doi:10.1016/j.electacta.2016.12.045

Xu, P., Loomis, J., Bradshaw, R. D., & Panchapakesan, B. (2012). Load transfer and mechanical properties of chemically reduced graphene reinforcements in polymer composites. *Nanotechnology, 23*(50), 505713. doi:10.1088/0957-4484/23/50/505713

Yamashita, S., Saito, Y., & Choi, J. H. (2013). *Carbon Nanotubes and Graphene for Photonic Applications*: Elsevier Science.

Yanagi, K., Udoguchi, H., Sagitani, S., Oshima, Y., Takenobu, T., Kataura, H., . . . Maniwa, Y. (2010). Transport mechanisms in metallic and semiconducting single-wall carbon nanotube networks. *ACS Nano, 4*(7), 4027-4032. doi:10.1021/nn101177n

Yin, L. H., Chen, Y., Li, D., Zhao, X. Q., Hou, B., & Cao, B. K. (2016). 3-Dimensional hierarchical porous activated carbon derived from coconut fibers with high-rate performance for symmetric supercapacitors. *Materials & Design, 111*, 44-50. doi:10.1016/j.matdes.2016.08.070

Yoon, S. H., Lim, S., Song, Y., Ota, Y., Qiao, W. M., Tanaka, A., & Mochida, I. (2004). KOH activation of carbon nanofibers. *Carbon, 42*(8-9), 1723-1729. doi:10.1016/j.carbon.2004.03.006

Yun, Y. S., Park, M. H., Hong, S. J., Lee, M. E., Park, Y. W., & Jin, H. J. (2015). Hierarchically porous carbon nanosheets from waste coffee grounds for supercapacitors. *ACS Appl Mater Interfaces, 7*(6), 3684-3690. doi:10.1021/am5081919

Zhang, B. A., Kang, F. Y., Tarascon, J. M., & Kim, J. K. (2016). Recent advances in electrospun carbon nanofibers and their application in electrochemical energy storage. *Progress in Materials Science, 76*, 319-380. doi:10.1016/j.pmatsci.2015.08.002

Zhang, J. W., Dong, L. B., Xu, C. J., Hao, J. W., Kang, F. Y., & Li, J. (2017). Comprehensive approaches to three-dimensional flexible supercapacitor electrodes based on MnO2/carbon nanotube/activated carbon fiber felt. *Journal of Materials Science, 52*(10), 5788-5798. doi:10.1007/s10853-017-0813-3

Zhang, L. L., & Zhao, X. S. (2009). Carbon-based materials as supercapacitor electrodes. *Chem Soc Rev, 38*(9), 2520-2531. doi:10.1039/b813846j

Zhang, X., Fan, X., Yan, C., Li, H., Zhu, Y., Li, X., & Yu, L. (2012). Interfacial microstructure and properties of carbon fiber composites modified with graphene oxide. *ACS Appl Mater Interfaces, 4*(3), 1543-1552. doi:10.1021/am201757v

Zheng, C., Qian, W. Z., & Wei, F. (2012). Integrating carbon nanotube into activated carbon matrix for improving the performance of supercapacitor. *Materials Science and Engineering B-Advanced Functional Solid-State Materials, 177*(13), 1138-1143. doi:10.1016/j.mseb.2012.05.024

Zhou, Z. P., Wu, X. F., & Fong, H. (2012). Electrospun carbon nanofibers surface-grafted with vapor-grown carbon nanotubes as hierarchical electrodes for supercapacitors. *Applied Physics Letters, 100*(2), 023115. doi:10.1063/1.3676193

Chapter 3 Growth of Carbon Nanotubes on Electrospun Cellulose Fibres for High Performance Supercapacitors

3.1 Introduction

As demand continuously increases in numerous industries such as portable electronics and new 'green' vehicles, energy storage devices such as supercapacitors should be further developed to provide increased performance. These improvements will be better understood by investigating electrode materials at the nanoscale, where a large surface area provides an increased charge mobility and a network which can interact well with the dielectric. Supercapacitors, also known as electrochemical double layer capacitors (EDLC), store energy by accumulation of the electrostatic charges at the electrode interfaces (Wang & Kaskel, 2012). They stand out among the energy storage devices such as lithium ion batteries and fuel cells owing to their high power density, fast charge/discharge mobility, and good life cycle stability (Yu *et al.*, 2015). The high performance of EDLC benefit from the extremely small separation (molecular scale) of charges generated at the interface between the electrode and electrolyte. Electrode materials for these devices typically aim to maximise surface area in order to store more charge than traditional parallel-plate capacitors (Gonzalez *et al.*, 2016). Carbon nanofibres are particularly promising for the fabrication of electrodes owing to their relatively high surface area, pore size distribution, high electrical conductivity, good mechanical properties, and excellent cyclic stability (Salanne *et al.*, 2016).

Cellulose nanofibres have a huge potential for the production of carbon fibre-based electrodes to complement commercial oil-based polyacrylonitrile (PAN) precursors. This potential arises because they are inexpensive, renewable, highly crystalline and abundant in nature (Frank *et al.*, 2014). When performing thermal treatment of cellulose fibres, at elevated temperatures above 400 °C, the carbonaceous structure is developed from the cellulose precursor by the process involving physical removal of water, dehydration, scission of glycosidic linkages, and aromatization (Dumanlı & Windle, 2012).

Electrospinning is a simple and continuous approach to generate nanofibres by applying electrostatic forces to a polymer solution (Zhang & Yu, 2014). Electrospinning is capable of producing fibres with large surface to volume ratios (Sun *et al.*, 2014). Although the application of electrospun fibres has largely enhanced the electrochemical properties of supercapacitors, a further approach to hybridise the surface with the presence of other nanomaterials may realise the full potential of the storage ability of the ions in the electrolyte (Zhang *et al.*, 2016).

Carbon nanotubes (CNTs), first discovered by Iijima (1991), have been intensively investigated as additives for the production of supercapacitors in recent years (Miao *et al.*, 2016; Wang, Song*, et al.*, 2015; Yu *et al.*, 2016; Zheng *et al.*, 2015). As the diameters of CNTs are much smaller than typical electrospun carbon nanofibres (CNFs), their incorporation with CNFs can achieve a significant increase in the surface area of the electrodes, subsequently increasing their electrochemical performance. Deng *et al.* have reported that by adding 6 wt.% CNTs into an electrospun cellulose acetate solution, the subsequently activated CNFs led to an increase of 38% of the specific electrochemical capacitance (Deng, Young, Kinloch, Abdelkader*, et al.*, 2013). Deng *et al.* used an approach

whereby CNTs were added to the electrospinning solution (Deng, Young, Kinloch, Abdelkader*, et al.*, 2013), whereas the in situ production of nanotubes on the surface of the spun fibres was proposed. The concentration of CNTs within the fibres in Deng's work was limited in this case by the viscosity of the electrospun solution such that it hindered any further improvement of capacitive performance (Deng, Young, Kinloch, Abdelkader*, et al.*, 2013). In the present work further increase in the specific capacitance was demonstrated, but also a method to form hybrid structured fibres for incorporation into structural capacitors and hierarchical composites (Qian, Diao*, et al.*, 2013; Qian, Greenhalgh, Shaffer, & Bismarck, 2010).

Chemical Vapour Deposition (CVD) is an excellent method to grow CNTs on a CNF substrate. In general, it is a fast and easy method in comparison to other approaches for the incorporation of CNTs on CNFs, e.g. dispersion of CNTs in the electrospun polymeric solution (Deng, Young, Kinloch, Abdelkader*, et al.*, 2013) or physically grafting CNTs onto the surface of CNFs (Islam *et al.*, 2016). CVD processes that have been used to grow CNTs on CNFs include a floating catalyst approach (Shazed *et al.*, 2014), grafting the catalyst by simply dipping CNFs into the solution containing the catalyst (Samsur *et al.*, 2013), and encapsulating the catalyst nanoparticles into the CNFs by electrospinning (Hou & Reneker, 2004; Lai *et al.*, 2008). Among these methods, the floating catalyst approach is considered to be the most convenient processing route to make CNF/CNTs. In the present Chapter, CNF/CNTs composites were made by producing in situ grown CNTs on the top surface of electrospun cellulose derived activated carbon nanofibres. The resulting hierarchical composite fibres showed better electrochemical performance over the plain CNFs. The approach

represents a new way of making capacitive electrodes, and offers a route to transform a sustainable material (cellulose) into energy storage devices that could have wide-ranging applications.

3.2 Experimental methods

3.2.1 Materials preparation

Cellulose acetate (CA, average M_n = 100,000 g mol^{-1}) was supplied by Fisher-Scientific (Loughborough, UK). Acetone, N,N-dimethylacetamide (DMAc), sodium hydroxide (NaOH), and potassium hydroxide (KOH) were purchased directly from Sigma-Aldrich (Dorset, UK). The polymeric solution used for electrospinning was made by dissolving 20 wt.% CA powder in a mixed solution of acetone and DMAc (2:1 w/w). The solution was stirred using a magnetic stirrer overnight at room temperature.

3.2.2 Electrospinning and deacetylation of fibres

Electrospinning was carried out using the prepared CA solution. The spinning conditions were a voltage of 14 kV, a flow rate of 1 mL h^{-1} and a needle tip-to-collector distance of 14 cm. The electrospinning process was continued for 3 hours and the electrospun CA nanofibres were deposited onto an aluminium foil collector to form a fibrous mat. These fibrous mats were then deacetylated in a 0.05 M NaOH aqueous solution for 48 h to allow regeneration into pure cellulose fibres, and were then fully rinsed with deionized water until neutral, and finally air dried.

3.2.3 Pyrolysis of regenerated cellulose and Chemical Vapor Deposition (CVD)

Stabilization and carbonization were undertaken in a high temperature tube furnace (Elite TSH16 furnace). Stabilization was firstly carried out for regenerated cellulose fibres by ramping the furnace from room temperature to 240 °C at a heating rate of 5 °C min^{-1} in air, followed by dwelling for 60 minutes. The stabilized fibres were then carbonized by ramping the temperature from 240 °C to 900 °C at a ramping rate of 10 °C min^{-1}, followed by dwelling for 30 minutes in an argon atmosphere. The carbonized fibres were denoted as CF900.

CF900 fibres were pre-located in the hot zone of the quartz tube in a CVD furnace, as shown in Figure 3.1a. The quartz tube had an inner diameter of 26 mm. The furnace was then heated to the required temperature of 800 °C. A mixed solution of 0.01 g ml^{-1} of ferrocene in styrene was fed into the quartz tube via a pump-controlled syringe at a flow rate of 0.8 cm^3 h^{-1}. The styrene acts as a carbon source and ferrocene as a catalyst to promote the CNT growth. The temperature versus distance profile from the syringe end to the centre of the hot reaction zone is shown in Figure 3.1b. The syringe end located inside of the quartz tube was maintained at 200 °C, which is higher than the ferrocene sublimation temperature (140 °C) and the styrene boiling point (145 °C) to ensure a ferrocene/styrene vapor was being produced. The mixed vapor was fed with a mixture of flowing argon-hydrogen gas of ratio (v:v = 1:1) at a flow rate of 200 cm^3 min^{-1} into the reaction zone of the heated quartz tube. The reaction was carried out for 25 minutes. The resulting composite structure, produced by the combination of carbonized electrospun cellulose fibres (CF900) and CNTs is subsequently denoted as CF900/CNTs.

(a)

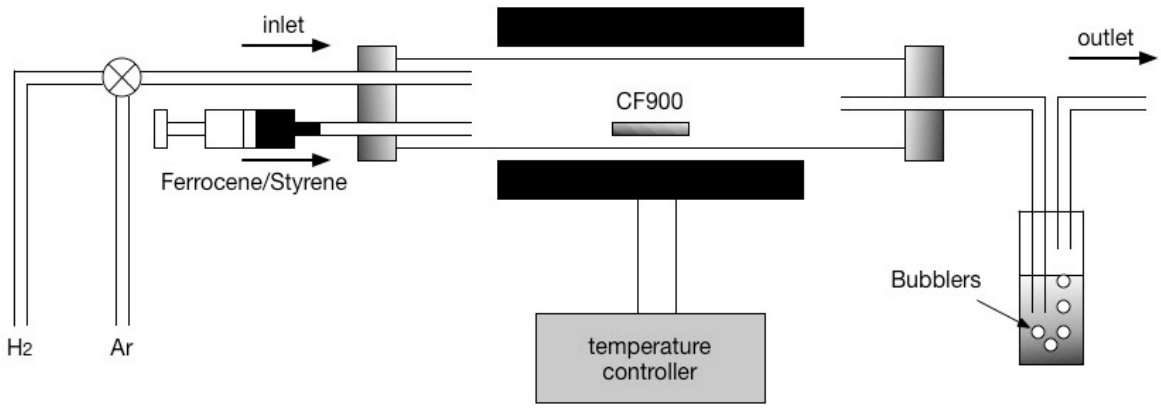

(b)

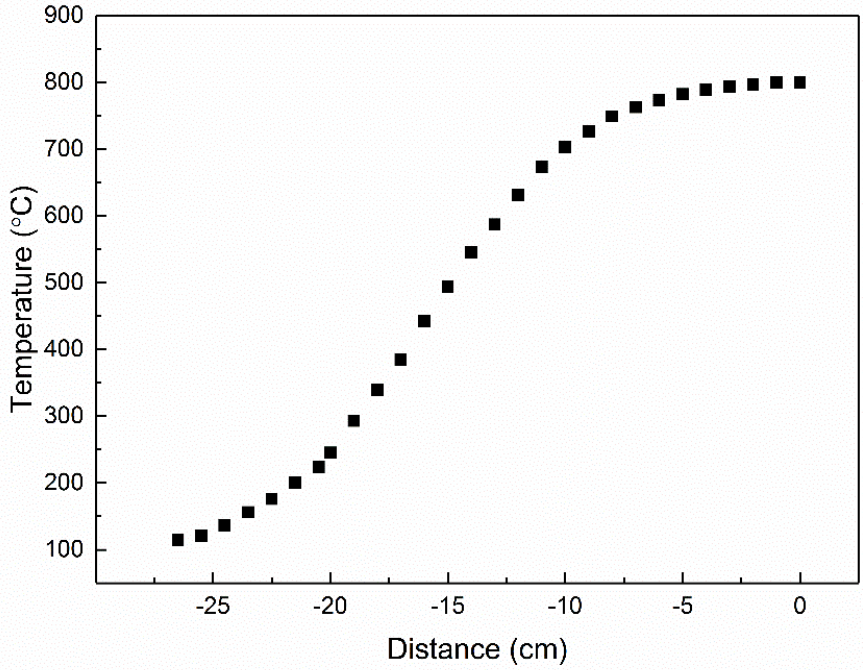

Figure 3.1 (a) A schematic of the CVD procedure for the CNT growth on the CNF mat. (b) The temperature versus distance profile from the syringe end to the centre of the hot reaction zone. The length of the reaction zone is 4 cm in total.

3.2.4 Activation of carbon fibres

For KOH activation of the electrode materials, 0.005 g mL^{-1} KOH aqueous solution was deposited on both sides of the CF900 and CF900/CNTs fibre mats. The mats were then dried at 60 °C to remove the water. KOH therefore remained on the surface of the fibres. The process of deposition of KOH solution and drying were repeated until the ratio of KOH and CF900 or CF900/CNTs was 1:2 (g/g). Activation was then performed in a tubular furnace by heating to 700 °C from room temperature at a heating rate of 2 °C min^{-1} in an Ar atmosphere, followed by a dwell time of 45 minutes. The activated electrode materials were then dipped into a 4.8 M aqueous nitric acid solution to remove as much of the remaining catalyst as possible and other impurities. Then these samples were rinsed and dried.

3.3 Characterisation of fibres

A scanning electron microscope (SEM) (HITACHI S3200N SEM-EDS) with a voltage of 10 kV was used to observe the morphologies of the electrospun CA and cellulose fibres. The SEM with a voltage of 20 kV was utilized to observe the morphologies of the carbon fibres and the CNTs. The CF900/CNTs fibre mats were sonicated in water for 15 minutes and deposited onto transmission electron microscopy (TEM) grids to examine the nanostructures and the morphology of CNTs with CNFs. Raman spectroscopy was utilized to characterise the electrospun CA and cellulose fibres, and the carbonized CNFs and CVD grown samples. Spectra were obtained using a 532 nm laser coupled to a Renishaw RM1000 spectrometer. A Leica CCD detector was used to record the spectral output. The laser spot size was ~1-2 μm, and the power was ~1 mW when the laser was focused on the sample using a 50× objective microscope lens. Fourier

transform infrared spectroscopy (FTIR) was used together with Raman spectroscopy to verify the deacetylation of the electrospun CA fibres by comparing the differences in spectra obtained before and after deacetylation. The FTIR was also used to estimate of the crystallinity of regenerated cellulose fibres. The specific surface area was calculated by Brunauer-Emmett-Teller (BET) method. The micropore volume (V_{micro}) and micropore area (S_{micro}) were obtained by using the t-plot method, while the mesopore volume (V_{meso}) and mesopore area (S_{meso}) were estimated by the Barrett-Joyner-Halenda (BJH) method. The total pore volume (V_{tot}) was measured by the nitrogen adsorption volume at the highest relative pressure. Pore size distribution was determined by the Non-local Density Functional Theory (NLDFT). Thermogravimetric analysis (TGA) was used to characterise the regenerated cellulose fibres during stabilization and carbonization. The TGA was also performed by heating activated CF900/CNTs at a heating rate of 10 °C min^{-1} from room temperature to 700 °C in the air. The TGA was used to estimate the remaining Fe catalysts in the activated CF900/CNTs samples.

A symmetric 'coin cell' supercapacitor was fabricated by assembling two pieces of activated CNF electrodes with GF/A Whatman filter paper as a separator, and a 6 mol L^{-1} aqueous KOH as the electrolyte. The areal mass for each electrode of CF900 and CF900/CNTs were 0.8 mg cm^{-2} and 1.1 mg cm^{-2}, respectively. A cyclic voltammetry (CV) test was performed on a CHI600C electrochemical workstation (CEW) at a scan rate 10 mV s^{-1} for both CF900 and CF900/CNTs electrodes. To test the rate performance of the composite capacitor (CF900/CNTs), a voltage range between 0 and 0.8 V was used for the CV measurements at four different scan rates (10, 50, 100 and 200 mV s^{-1}), and

galvanostatic charge/discharge (GCD) tests were performed at three different current densities (0.25, 1, and 5 A g^{-1}). Electrochemical impedance spectra (EIS) were obtained at a constant perturbation amplitude of 5 mV at frequencies ranging from 0.01 Hz to 100 kHz. Electrochemical stability tests for both CF900 and CF900/CNTs were also performed by chronopotentiometry on the CEW for 1000 cycles at a current density of 1 A g^{-1}. Values of specific capacitance C_{SP} for 2-electrode supercapacitors were calculated from the GCD curves using the equation

$$C_{\mathrm{sp}} = I/\left(m(\mathrm{d}V/\,\mathrm{d}t)\right) \qquad (3.1)$$

where d*V* is the voltage difference, d*t* is the discharge duration, *I* is the current and *m* is the total mass of the two electrodes.

3.4 Results and discussion

3.4.1 Morphology of electrospun cellulose acetate fibres and cellulose fibres

Electrospinning of CA solutions was performed at a fixed electric field strength of 14 kV/14 cm. The Taylor cone was stable throughout the process of electrospinning to produce bead-free CA fibres. Electrospun fibres were collected from a stationary collector and were found to be randomly orientated. Figures 3.2a and 3.2b show the SEM images of the CA fibres and regenerated cellulose fibres, respectively.

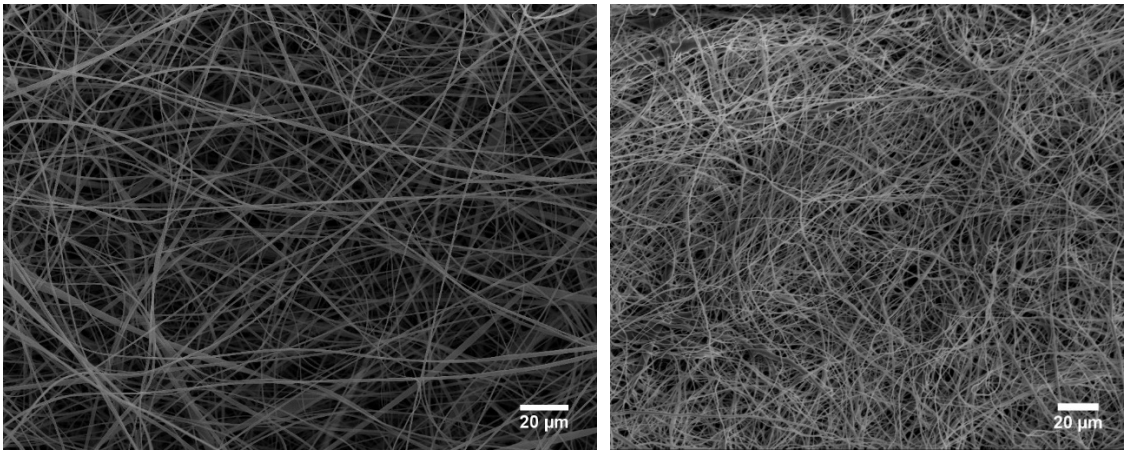

(a) (b)

Figure 3.2 Typical SEM images of (a) CA fibres and (b) regenerated cellulose fibres.

The diameters of both fibres were determined using ImageJ software. Histograms of the diameter distributions for CA and regenerated cellulose fibres are shown in Figures 3.3a and 3.3b, respectively. Table 3.1 summarises the values of the average diameters, minimum diameters, and maximum diameters for both CA and regenerated cellulose fibres. Smooth and circular CA fibres with diameters varying from 325 to 1629 nm were obtained, while the diameters of regenerated cellulose nanofibres varied from 106 to 1504 nm after deacetylation. The average diameter of the CA fibres was found to be 875 ± 286 nm. After deacetylation and drying, the average diameter of fibres decreased to 621 ± 256 nm; during the regeneration the weight loss was about 44%. The weight loss of CA fibres is because of the replacement of the acetyl group with hydroxyl group in the molecular chain (He, 2017).

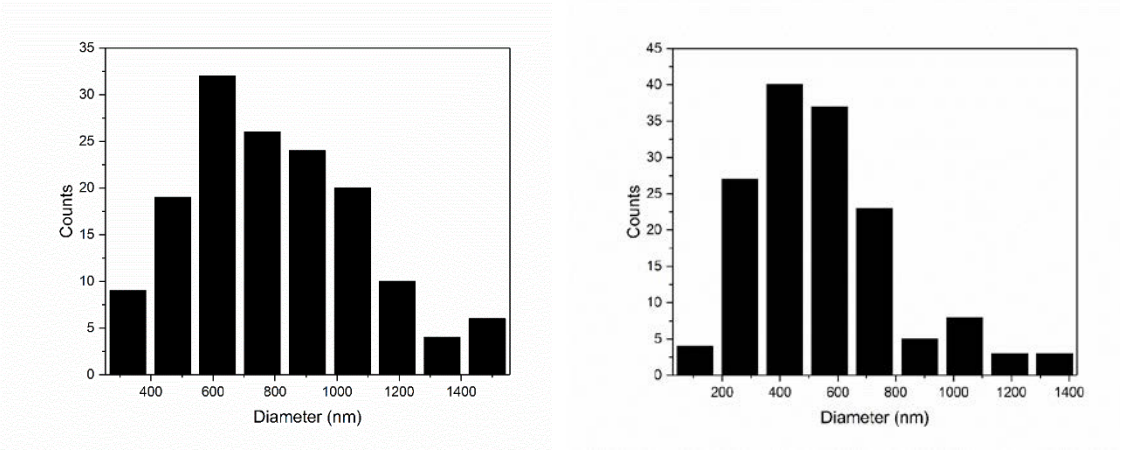

(a) (b)

Figure 3.3 Diameter distribution of (a) the CA fibres and (b) the regenerated cellulose fibres.

Table 3.1 Diameters of CA fibres and regenerated cellulose fibres.

Sample	Average diameter (nm)	Min diameter (nm)	Max diameter (nm)
CA	875 ± 286	325	1629
Regenerated Cellulose	621 ± 256	106	1504

3.4.2 Deacetylation characterisation by Raman spectroscopy

Raman spectra within a wavenumber range from 800 to 1500 cm^{-1} for the CA and regenerated cellulose fibres are shown in Figure 3.4. After deacetylation, an intense peak appeared at ~1095 cm^{-1}, which is attributed to the C-O ring and glycosidic linkage stretching modes, indicating the presence of cellulose (Deng, Young, Kinloch, Zhu*, et al.*, 2013). However, this peak is absent in the spectra for

the original CA fibres, suggesting deacetylation has occurred. Additionally, three peaks located at ~898 cm^{-1}, ~1262 cm^{-1} and ~1462 cm^{-1} are attributed to the cellulose II crystal lattice (Kavkler & Demsar, 2011; Wiley & Atalla, 1987). A much broader and significant peak also appears at ~1374 cm^{-1} due to the $\delta(CH_2)$ mode (Kavkler & Demsar, 2011).

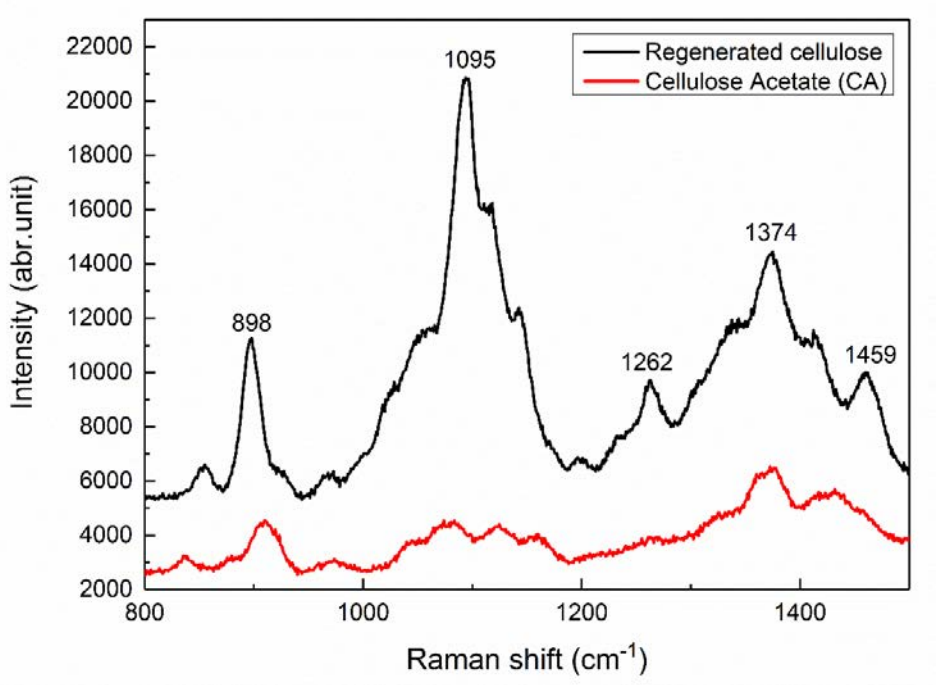

Figure 3.4 Raman spectra of the cellulose acetate (CA) and regenerated cellulose fibres.

3.4.3 Deacetylation characterisation by FTIR

FTIR spectra were obtained for both CA and regenerated cellulose fibres within a wavenumber range between 500 and 4000 cm^{-1}, as shown in Figure 3.5.

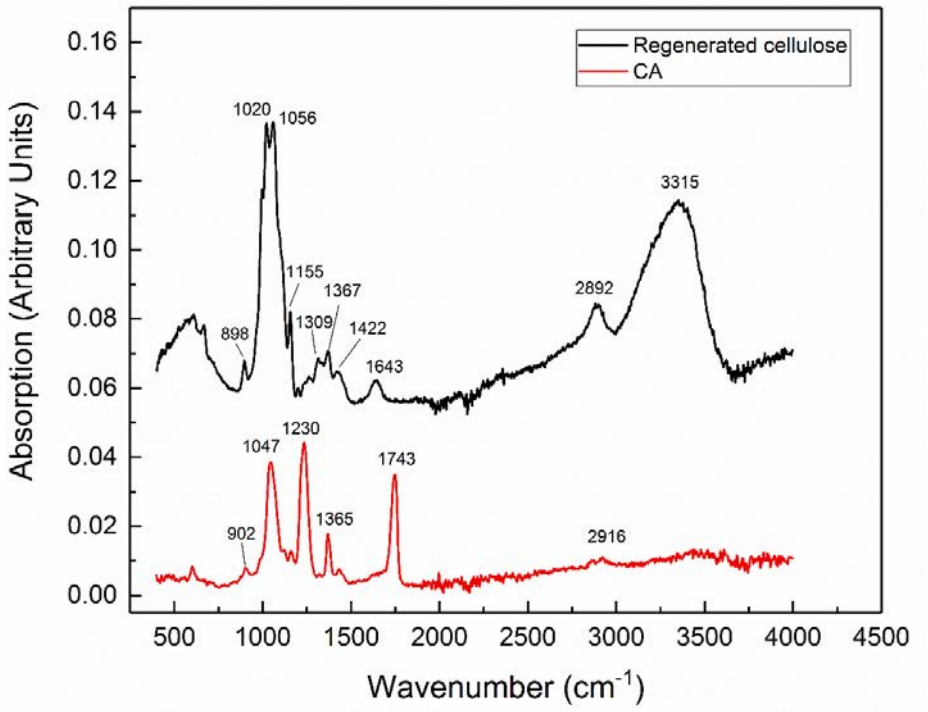

Figure 3.5 Typical FTIR spectra for cellulose acetate fibres (CA; red) and regenerated cellulose fibres (black).

Table 3.2 shows the most significant absorbance bands assigned for regenerated cellulose fibres (Carrillo, Colom, Sunol, & Saurina, 2004). Estimation of the crystallinity of regenerated cellulose fibres using FTIR spectroscopy has been previously proposed. The technique is based on the measurement of the intensity ratios of IR bands 1420/893 cm^{-1} (Nelson & O'Connor, 1964b) and the bands 1375/2902 cm^{-1} (Nelson & O'Connor, 1964a). In crystalline cellulose Ⅱ dominated samples, the ratio of bands 1420/893 cm^{-1} is referred to as the lateral order index (*LOI*) which represents the crystalline fraction perpendicular to the chain direction. The *LOI* increases as the crystallinity decreases. The ratio 1375/2902 cm^{-1} is referred to as the total crystalline index (*TCI*), which is proportional to the crystallinity degree of the cellulose samples. *TCI* increases with an increase in the crystallinity. The *LOI* and *TCI* for regenerated electrospun cellulose fibres are

calculated to be 0.80 and 0.77, respectively. The *TCI* of regenerated cellulose fibre has similar value but a larger *LOI* compared to previously published work on lyocell (Carrillo *et al.*, 2004). This indicated a relatively lower crystallinity degree of the regenerated electrospun cellulose samples compared to lyocell fibres. However, the regenerated cellulose fibres have a relatively higher crystallinity degree than previously reported values for cellulose fibres directly produced by electrospinning cellulose and 1-ethyl-3-methylimidazolium acetate (Freire *et al.*, 2011). The *TCI* and *LOI* values are thought to be related to the method for producing the samples (Carrillo *et al.*, 2004).

Table 3.2 Characteristic frequencies from the infrared spectra in regenerated cellulose fibres (Carrillo *et al.*, 2004).

Frequency (cm^{-1})	Assignment
3315	OH stretching
2892	CH stretching
1643	OH groups of absorbed water
1422	CH_2 symmetric bending
1367	CH bending
1309	CH_2 wagging
1155	C-O-C asymmetric stretching
1056	C-O stretching
1020	stretching C-O
898	Group C_1 frequency

For the FTIR of CA fibres, a clear acetyl carbonyl adsorption was observed at ~1743 cm^{-1} in the FTIR spectrum, verifying the formation of CA, and the ~1230 cm^{-1} band assigned to the stretching of the C-O within the acetyl group. The other obvious peaks are located at ~1356 cm^{-1} (CH bending) and ~1047 cm^{-1} (C-O stretching), which were also observed for the regenerated cellulose fibres. The band located at ~898 cm^{-1} shifts to ~902 cm^{-1} after deacetylation, which is assigned to β glucosidic linkages between the sugar units (Barud *et al.*, 2008). A weak band located at ~2916 cm^{-1} represents the CH stretching absorption.

3.4.4 TGA characterisation of cellulose acetate (CA) and regenerated cellulose fibres

Figure 3.6 shows the TGA for the stabilization process of regenerated cellulose fibres. The stabilization was performed at 240 °C for 1 hour at a ramping rate of 5 °C min^{-1} from room temperature in air. The TG diagram shows that there was a relative fast weight loss of 10% starting from the room temperature to 70 °C, followed by a further smooth weight loss of 6% with an increase in the temperature to 100 °C. Subsequently, an plateau was observed within a temperature range between 100 to 150 °C. The regenerated cellulose is a material that can absorb moisture from the air at room temperature, the percentage of which is normally 6 to 10 wt.% (Tang & Bacon, 1964). The weight loss of regenerated cellulose fibres at the first stage of degradation from the room temperature to around 150 °C can be explained by physical removal of water. A small weight loss of 1% was noted from 150 to 240 °C, which is associated with the very early stage of the dehydration. During dehydration, the elimination of the hydroxyl groups results in the formation of conjugated double bonds. In addition, a board exothermic peak from 50 to 200 °C in differential scanning calorimeter

(DSC) diagram is thought to be related to the removal of water physically and chemically, in agreement with the TGA data. When dwelling at a temperature of 240 °C for 1 hour, the weight of the regenerated cellulose fibres dropped from 85% to 77%, leading to the final yield of the stabilized cellulose fibres.

When heating from 150 °C to 240 °C and then during the dwelling time of 1 hour in the air, dehydration is thought to take place (Tang & Bacon, 1964). It is worthy to note that the intramolecular dehydration is preferred to form the C=C and C=O bonds for the cellulose precursors (Huang, 2009). Thermal session takes place by disconnection of the 1,4 glycosidic bonds along the cellulose molecule chain, resulting in the formation of the levoglucosan complex. Due to the unstable and reactive properties of the levoglucosan, it tends to form tar at 550 °C along with other organic compounds such as furfural and methylfurfural (Dobele, Rossinskaja, Telysheva, Meier, & Faix, 1999). The majority of the weight loss of the cellulose is caused by the decomposition of levoglucosan during carbonization, which is an undesirable reaction. Thus, minimizing the formation of the levoglucosan complex is of importance for increasing the carbon yield. By prolonging the time of the early stages (temperature of 240 °C) of the depolymerization (240 - 400°C), the formation of the cellulose rings will increase, resulting in a lowering the formation of the unwanted levoglucosan and hence increasing the carbon yield of the final carbon fibres.

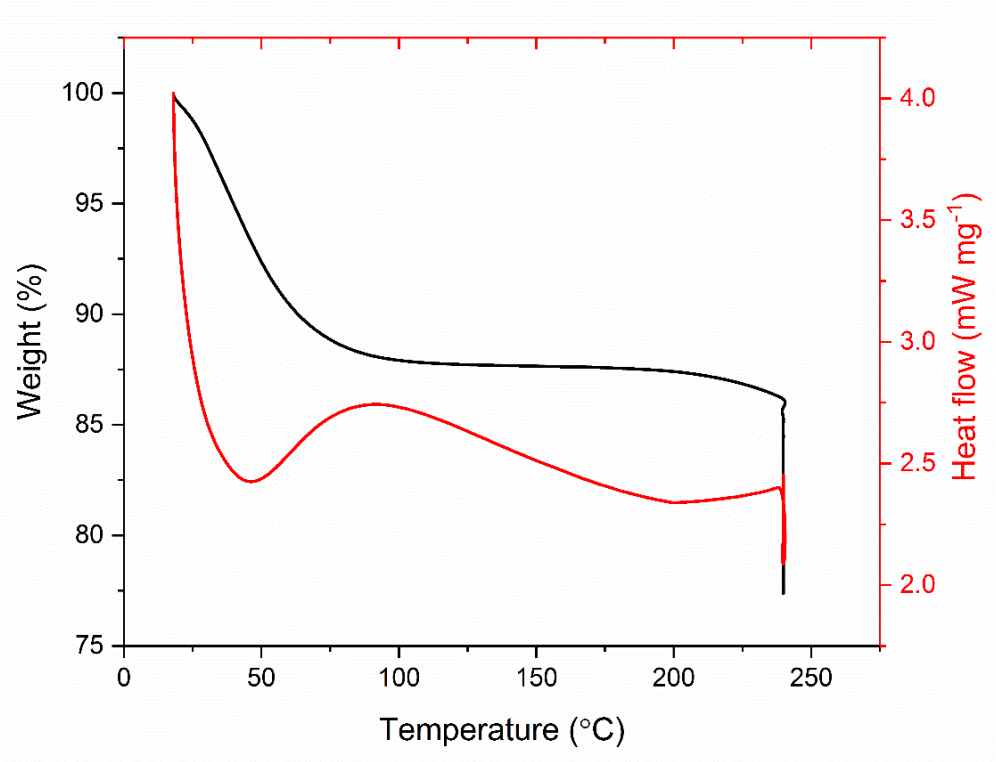

Figure 3.6 Typical TGA data showing weight loss versus temperature for the stabilization process of regenerated cellulose fibres.

Figure 3.7 shows the TG curves during the pyrolysis process for the regenerated cellulose fibres and stabilized cellulose fibres in the temperature range 25 - 900 °C in an argon atmosphere, and a final dwell time of 30 minutes. Similar TGA curves have been reported for bacterial cellulose (Perotti, Barud, Ribeiro, & Constantino, 2014). The degradation of regenerated cellulose is thought to consist of four stages. The decrease of weight during 25 - 150 °C is due to the physical desorption of water. It can be seen there was a rapid weight loss between 240 and 400 °C with 29% of weight remaining, which is due to the thermal scission of glycosidic linkage and ether bonds. At this stage, the levoglucosan complex is also formed by thermal cleavage starting from 240 °C. The starting temperature for the degradation of native and regenerated cellulose depends on different cellulose materials. The commencement of degradation for

Rayon is 240 °C (Tang & Bacon, 1964), and the degradation of Rayon is also reported to start between 250 and 400 °C (Plaisantin *et al.*, 2001). Lyocell fibre degrades from 298 °C (Carrillo, Defays, Colom, Sunol, & Lopez-Mesas, 2009). A recent study of the degradation of electrospun cellulose fibres gave 240 °C as the starting point by evaluation of TGA (Deng, Young, Kinloch, Zhu*, et al.*, 2013). During the next stage, from 370 to 550 °C, there was a slow weight loss of 19%, which is thought to be partly attributed to the decomposition of levoglucosan. The weight of the regenerated cellulose fibres does not change at the temperature between 550 to 900 °C. It keeps the same carbon yield of 10% after 30 mins dwelling time. This indicates that a more ordered and stable form of carbonaceous structure has been formed.

As a comparison, the thermal properties of the stabilized cellulose precursors were evaluated from the TGA curves in an argon atmosphere. There are only 3 stages that were observed. The first stage started from room temperature to 150 °C. The weight change of the original stabilized cellulose fibres was smaller than that of regenerated cellulose fibres. This is thought to be due to the moisture absorption for stabilized carbon being less than regenerated cellulose fibres. It can also be seen that the temperature where the weight started to have significantly reduce shifted to a higher value - from 240 to 330 °C. This is an indication that part of the hydroxyl groups were eliminated by dehydration during stabilization, allowing the degradation process directly to move to depolymerization at a higher temperature (> 240°C). After a sharp decrease in the weight of the stabilized cellulose fibres, it then remained at around 39% – within the temperature range 550 to 900 °C, also showing a significant improvement of the carbon yield. Also, the weight loss rate of the stabilized

cellulose fibres between 240 and 550 °C was smaller than that of regenerated fibres. The carbon yield for stabilized cellulose is higher in comparison to the pure regenerated cellulose fibres; increases from 10% to 39%, which is approaching the theoretical yield of 44% (Dumanlı & Windle, 2012).

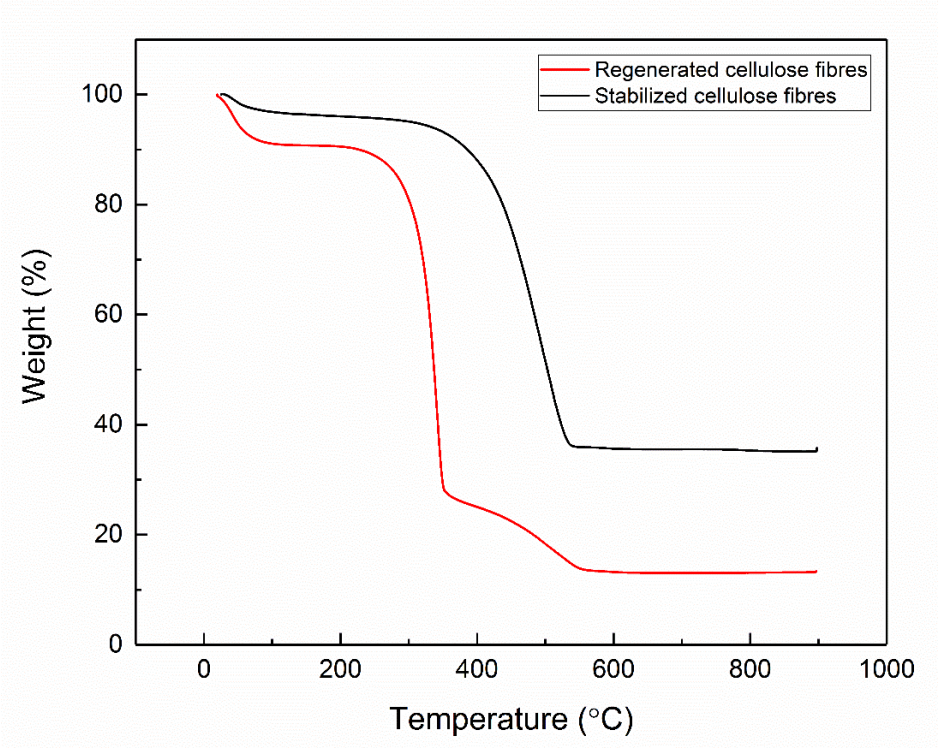

Figure 3.7 Typical TGA curves showing weight loss versus temperature for regenerated cellulose fibres and stabilized cellulose fibres in an argon atmosphere during carbonization.

Figure 3.8 shows DSC data for the stabilized cellulose fibres and regenerated cellulose fibres performed in argon atmosphere. A sharp exothermic peak between 240 and 370 °C can be seen for the regenerated cellulose, which is related to the thermal scission of glycosidic linkage and ether bonds, and aromatization (Huang, 2009), which generate heat. However, this peak in stabilized cellulose fibres moves to a temperature range between 400 to 600 °C,

which is in agreement with the TGA analysis. Less heat is generated for stabilized cellulose fibres when dwelling at 900 °C due to the limited reaction of levoglucosan.

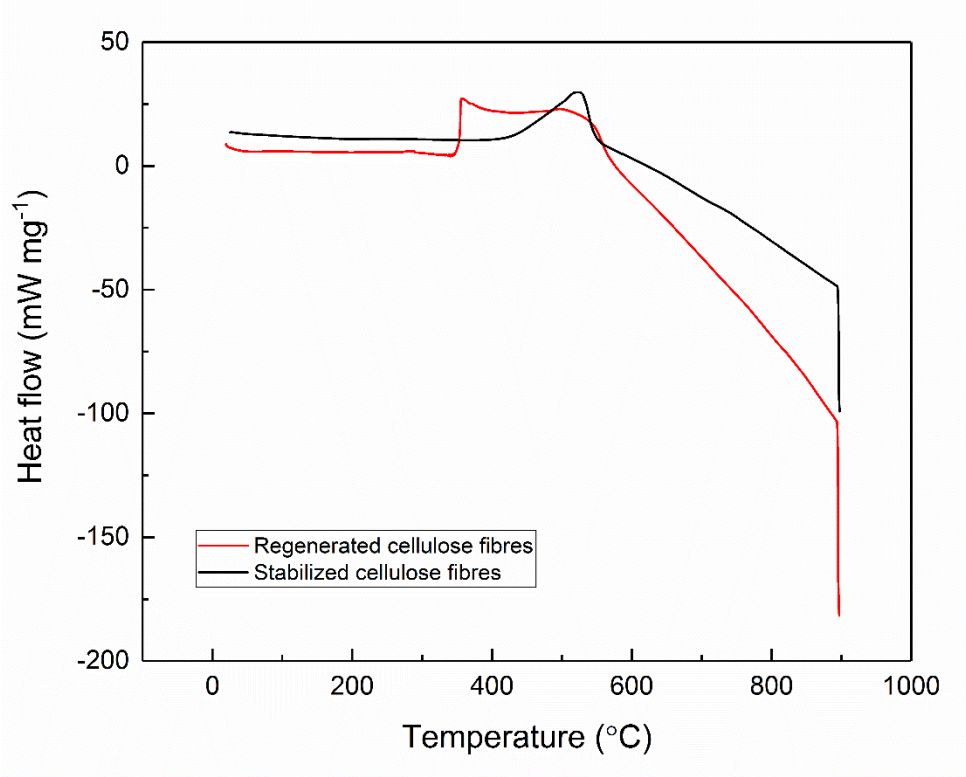

Figure 3.8 Typical Differential Scanning Calorimetry (DSC) data for the stabilized cellulose fibres (black) and regenerated cellulose fibres (red) during carbonization.

3.4.5 Investigation of influence of CVD temperature for growth of CNTs

The effect of CVD temperature was investigated by comparing two operating temperatures; namely at 800 and 900 °C. When performing CVD at 800 °C, CNTs were obtained without the appearance of other carbon impurities, e.g. amorphous carbon. A thick CNT layer was formed on the surface of the CNFs (Figure 3.9a). Many long CNTs were observed to be entangled at the circumferential surfaces of CNFs. TEM images of CNTs were also obtained and shown in Figure 3.9b.

In contrast, the amorphous carbon and clusters thereof are clearly observed when using a CVD temperature of 900 °C (Figure 3.9c). The amorphous carbons are larger than the CNTs in diameter. In the CVD process, the ferrocene catalyst first decomposes into Fe nanoparticles at 900 °C facilitated by H_2 (Bhattacharjee, Rooj, Roy, & Roy, 2014). Styrene, as a carbon source, decomposes into carbon atoms, followed by diffusion into the Fe nanoparticles. However, it is difficult for diffused carbon atoms to precipitate CNTs on the large catalyst particles and therefore they form iron carbide (Fe_3C) along with amorphous carbon, or 'carbon balls' instead (Zhu, Su, Lehoczky, Muntele, & Ila, 2003). The amorphous carbon then coats the Fe nanoparticles causing so-called catalyst 'poisoning'; this effect can be clearly seen in Figure 3.9d. This effect results in catalyst deactivation impeding the growth of CNTs. Other studies have also shown that amorphous carbon appears at temperatures above a window of 800 to 825 °C (Andrews, Jacques, Qian, & Rantell, 2002). Also, the relationship between growth temperature and the density of CNTs on carbon fibre surfaces has been previously investigated (Zhang, Liu, Sager, Dai, & Baur, 2009). This previous work suggests that a very low number of CNTs form at 700 °C due to the low solubility of carbon in the iron catalyst at temperatures lower than the carbon-iron eutectic temperature of 723 °C (Zhang *et al.*, 2009). The density of CNTs experienced a substantial increase at 750 °C and reached its highest level at 800 °C. Thus, the most suitable temperature window was found to be 750 - 825 °C for the growth of pure CNTs in a floating catalyst CVD process.

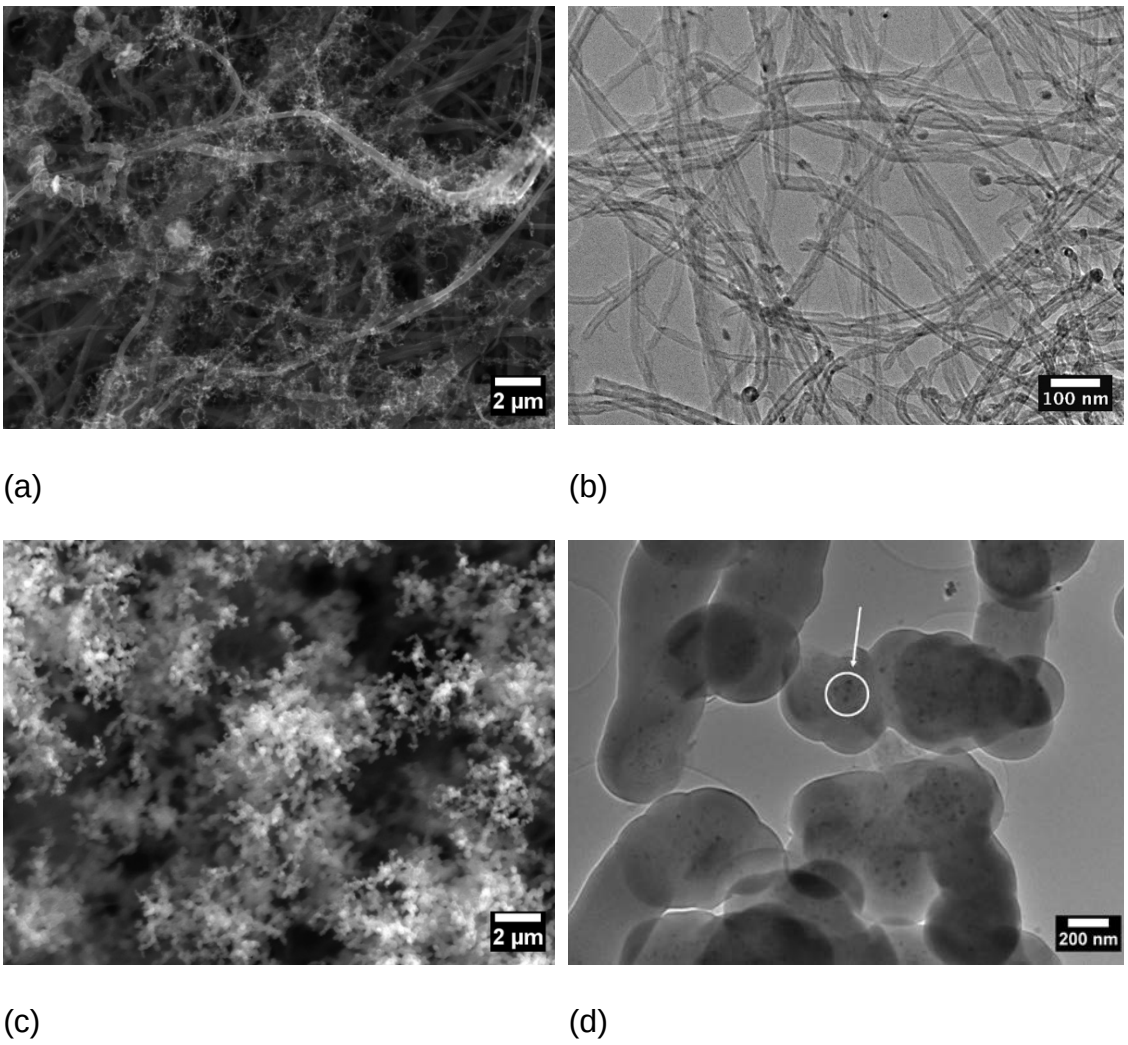

Figure 3.9 (a) A typical SEM image of CNTs grown on the surface of CNFs at a CVD temperature of 800 °C; (b) A typical TEM image of CNTs grown at a CVD temperature of 800 °C; (c) A typical SEM image of the mixture of amorphous carbon and CNTs grown at a CVD temperature of 900 °C; (d) A typical TEM image of amorphous carbon with the Fe nanoparticles (white arrow) at a CVD temperature of 900 °C.

3.4.6 Morphology of CNF and CNF/CNTs by SEM and TEM

The morphology of CNFs is shown in Figure 3.10a along with the diameter distribution in Figure 3.10b. The values of average diameters, minimum diameters, and maximum diameters are shown in Table 3.3. The average CNF

diameter was found to be 259 ± 83 nm, which is less than half that of the regenerated cellulose fibres.

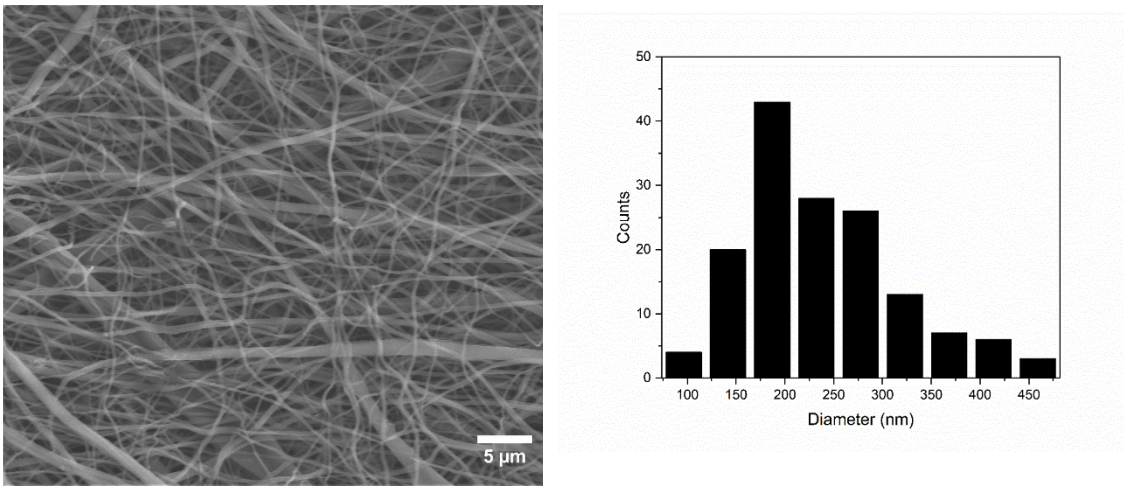

(a) (b)

Figure 3.10 (a) Typical SEM image of CNFs; (b) Diameter distribution diagram.

Table 3.3 Diameters of CNFs including average diameters, minimum diameters, and maximum diameters. Errors (±) are standard deviations from the mean.

Sample	Average	Max	Min
CF900	259 ± 83	505	96

Unlike the so-called two-step CVD method which is to grow CNT on a pre-deposited catalytic layer, the floating catalyst CVD growth mechanism is relatively complicated because decomposition of catalytic nanoparticles and nucleation of CNTs almost occurs at the same time throughout the reaction period. It is accepted that the diameter of CNTs is highly dependent on the size of the catalytic nanoparticles (Cheung *et al.*, 2002). In a two-step CVD process, the diameter of the pre-deposited catalysts and CNTs are controllable. However, the

in situ size control of CNTs becomes much more difficult as the catalyst nanoparticles are dispersed unevenly in the reaction zone (Kunadian, Andrews, Qian, & Menguc, 2009), resulting in different diameters and morphologies of the grown CNTs. In the present study, several types of MWCNTs with different morphologies were identified in the TEM images, corresponding to different mechanisms of growth for each type of CNT.

Type 1 and 2 CNTs were found to have similar morphologies whereby catalytic nanoparticles are located on the tip of the tube end, as seen in Figures 3.11a and 3.11b. This observation revealed that the growth mechanism of the CNTs is likely to have followed a “tip-growth model”, which only takes place when the catalyst is weakly attached to the substrate with an acute contact angle (Kunadian *et al.*, 2009). It is noted that if the CNTs grow with a “root-growth model”, the tip of the CNT should be clear and empty (Tessonnier & Su, 2011). In a type 1 CNT, the catalyst is in a “pear shape” with a larger diameter than the inner wall of the CNT. Specifically, the larger side of the ‘pear-like’ nanoparticle attaches the graphic cap while its smaller side faces the hollow core of the tube. The catalytic nanoparticle in type 1 CNT is covered by a closed cap to form an encapsulated space. In contrast to the type 1 CNT, the edge plane of a type 2 CNT attaches and inserts into the nanoparticle rather than growing via the surface of the nanoparticle.

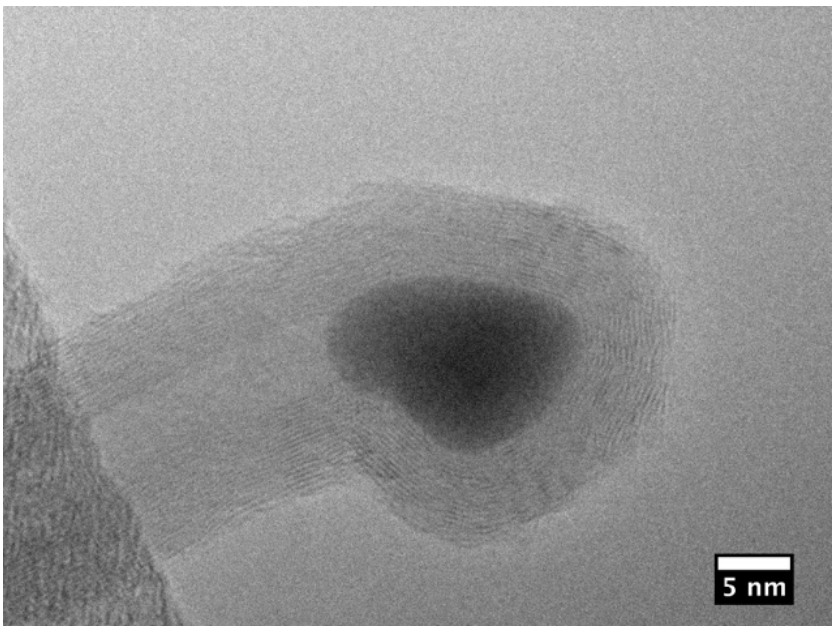

(a)

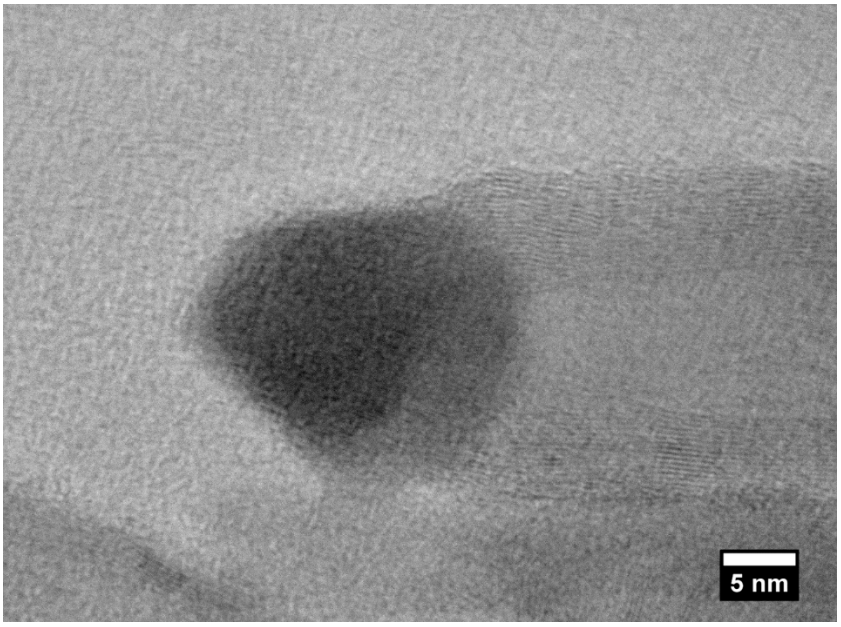

(b)

Figure 3.11 Typical Transmission Electron Microscopy imges of (a) a Type 1 CNT with a closed end covered by graphitic layers and (b) a Type 2 CNT with an open end.

These two types of CNT/catalyst morphology indicate they have different mechanisms for their growth. It can be observed that there is a region of

dislocated graphitic layers in the type 1 CNT. This is thought to be due to the fact that less energy is required to precipitate graphitic layers with a small curvature than the large one (Tibbetts, 1984), and therefore the non-uniform shape of the catalytic nanoparticle leads to a preferable growth direction. Thus, the CNT walls grow via a route surrounding the outline of the nanoparticle. They grow from an initially small curvature, eventually reaching the CNTs' walls on the other side. It is reasonable to make this assumption as the formation of the graphitic cap is dependent upon the shape of the catalytic nanoparticles during the growing CNTs via vapour-liquid-solid (VLS) mode (Kukovitsky, L'vov, Sainov, Shustov, & Chernozatonskii, 2002). In addition, the catalytic nanoparticle is more symmetric in type 2 CNTs. Also, the multi-walls have no obvious trend to further nucleate to form a closed cap because the catalyst has already been anchored to the graphited layers. This negates the assumption that type 2 is formed midway through the formation of type 1. Thus, whether the catalytic nanoparticles are encapsulated by the graphitic cap or leave an open end depends on the shape of the catalytic nanoparticles during the process of growing CNTs.

Type 3 CNTs shows that the catalyst is obviously elongated at the tip of the CNT, shown in Figure 3.12. It is assumed that the direction of movement of the catalyst is opposite to the tip of the CNTs. This nanoparticle is in a liquid-like shape (filled in the tip end of the CNT), giving the evidence that the catalyst was in a liquid phase during the growth of CNT. This type of CNT has been previously observed and investigated (Kukovitsky *et al.*, 2002). The authors of this work claim the mechanism of growth of this type of CNTs is based on the VLS mode as it is difficult to explain how to form this type of CNT if the catalyst is in a solid phase (Kukovitsky *et al.*, 2002). It is worth noting that in the VLS mode, the carbon

source first decomposes into carbon atoms, followed by a bulk diffusion into the catalytic nanoparticles. The graphitic layers precipitate once the carbon becomes supersaturated. The driving force for the carbon atoms' diffusion can be explained by the temperature gradient or concentration gradient or a combination of both (Dupuis, 2005). In the case of the VLS mode, only the equilibrium shape (influenced by surface tension and capillary forces) of the liquid nanoparticles can determine the diameter of CNTs rather than the particle size that is present in the vapor-solid-solid (VSS) mechanism. Although this model is well accepted by researchers, the critical question is how the Fe could be in a liquid phase at a CVD temperature of 800 °C, which is clearly much lower than its melting point of 1147 °C. However, the melting point of nanoparticles are known to decrease significantly when the particle size is below 10 nm (Moisala, Nasibulin, & Kauppinen, 2003). The relationship between the particle size and the melting point is shown in Figure 3.13 (Moisala *et al.*, 2003). However, in the present study the diameter of most of the nanoparticles was slightly larger than 10 nm, and so it is thought that the melting point would be higher than 800° C. Also, the particle size is not identical for all catalysts. Therefore, this theory is not sufficient to confirm if the catalytic nanoparticle is in the liquid phase. But the previous studies do give an indication that the CNTs growth may follow a new mechanism because the existence of hydrogen also contributes to a change in the melting point of Fe by building up a ternary phase diagram (Hou & Reneker, 2004).

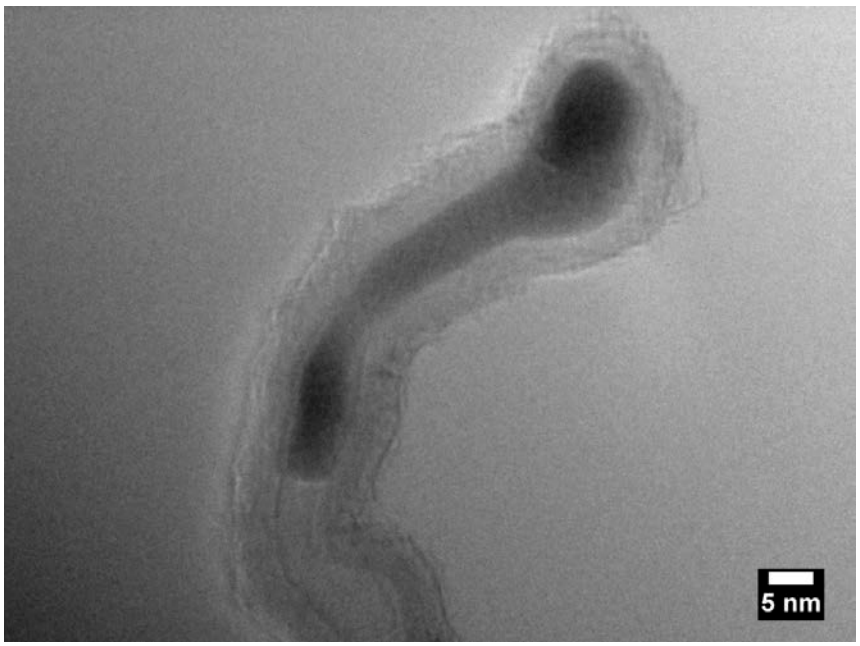

Figure 3.12 Typical TEM micrograph of a Type 3 CNT with an elongated catalytic nanoparticle at its tip.

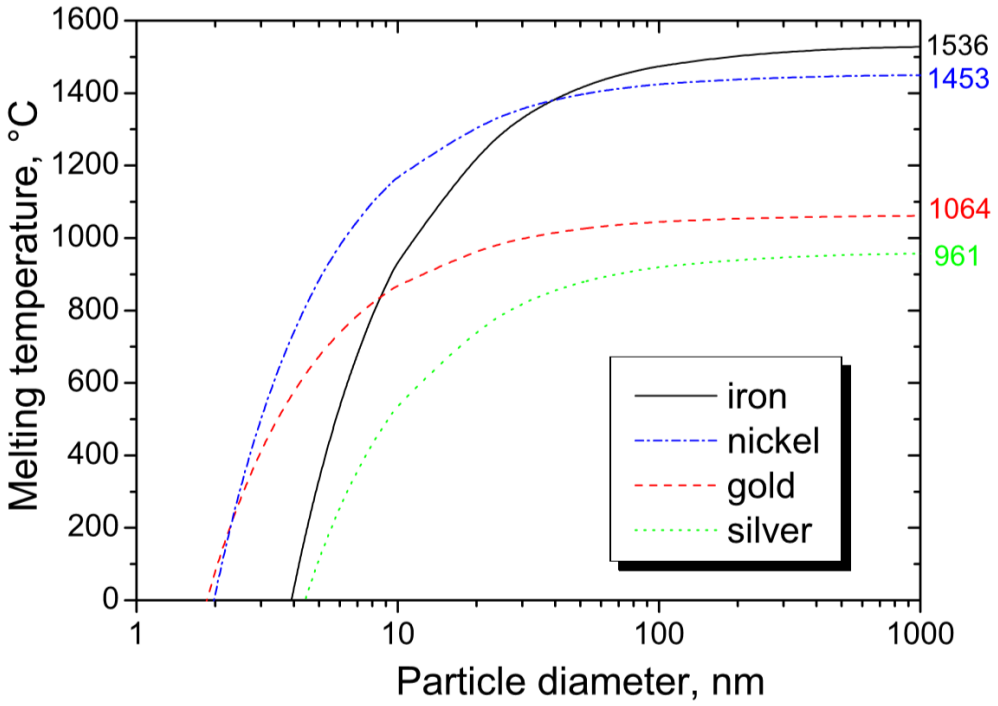

Figure 3.13 Melting temperature of iron, nickel, gold and silver particles as a function of their diameter. Taken from (Moisala *et al.*, 2003).

A Type 4 CNT is shown in Figure 3.14, where a catalyst on the tip is adjacent to another catalytic nanoparticle. As the catalyst and carbon source mixed solution enters the reaction zone, both the compounds decompose to free metallic nanoparticles and carbon atoms (Deck & Vecchio, 2005). The carbon atoms then directly diffuse into the metallic nanoparticles in the free space of the reaction zone prior to depositing on the carbon fibre substrate. Once the carbon reaches saturation, the formation of graphitic layers can rapidly initiate. If the open-ended side of these CNTs reaches the closed cap of already grown CNT, it will initiate a so-called secondary growth (Kunadian *et al.*, 2009). If the wettability of the metal catalyst is low enough, it will allow detachment from the CNT cap (Weissker, Hampel, Leonhardt, & Buchner, 2010). Further growth of CNTs will lead to this form. This phenomenon takes place especially for floating catalytic CVD.

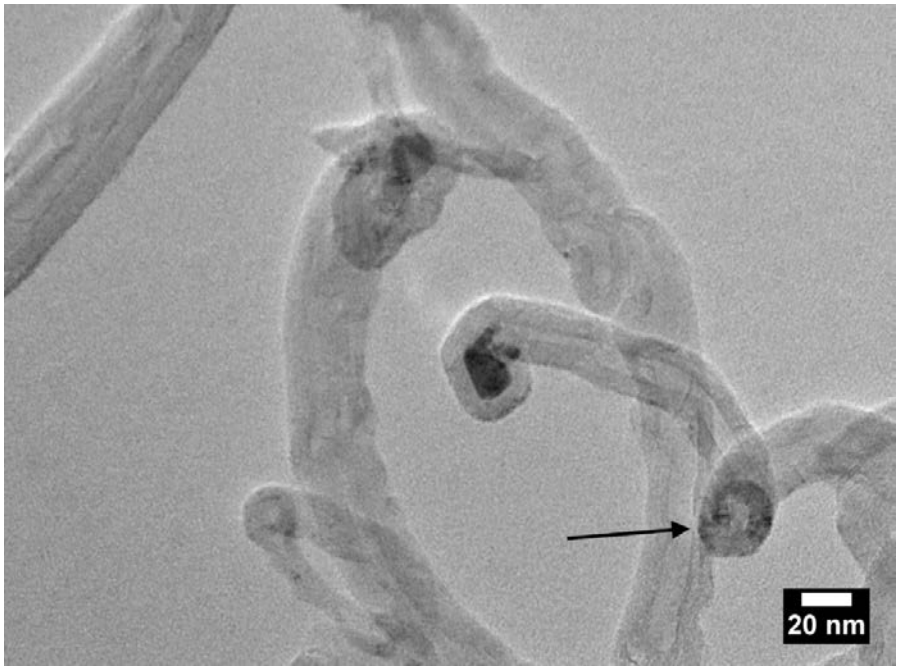

Figure 3.14 A typical image of a type 5 CNT showing one CNT grown from the tip of the other CNT (black arrow).

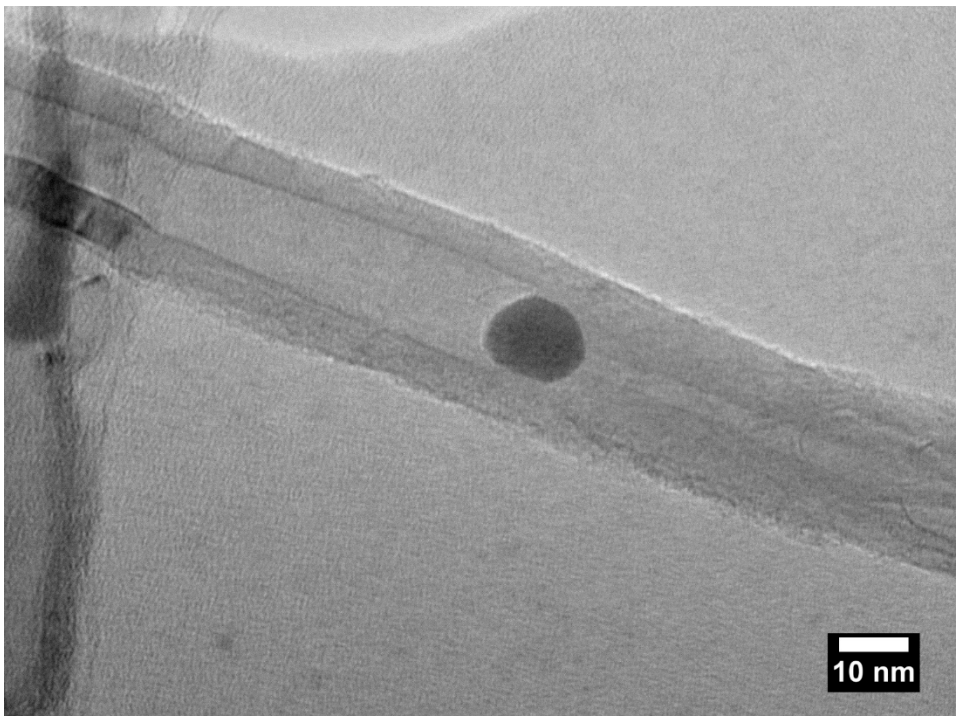

Figure 3.15 A typical TEM image of a Type 5 CNT showing one CNT grown inside of another, with a catalyst nanoparticle embedded in the centre of the growth region.

A type 5 CNT is shown in Figure 3.15, where a round catalyst is encapsulated in the middle of a MWCNT with several graphitized layers attached to it. The growth mechanism proposed for this type of CNTs where a smaller catalyst has been deposited on the larger one at the CNT's tip end. In the tip growth mechanism of CNTs, the catalytic nanoparticle is raised up through the growing structure (Deck & Vecchio, 2005; Zhang *et al.*, 2002). The friction between the catalyst particles and the nanotube walls can hinder the movement of the catalytic nanoparticle (Deck & Vecchio, 2005). A smaller particle travels a larger distance until it grew large enough for friction to stop its movement (Deck & Vecchio, 2005). This results in the presence of catalytic nanoparticles in the middle of CNTs. Similar morphologies of CNTs were observed in a previous study (Rodriguez-Manzo *et*

al., 2007). In this previous study. an in situ TEM was used to image a single walled CNT growing towards the direction where the graphitic layers filled in the hollow core while the carbon atoms were fed towards the other direction within the hollow core (Rodriguez-Manzo *et al.*, 2007). However, they did not mention why the catalytic nanoparticle is possibly in the middle of the CNT.

Different types of CNT growth have shown that there is not only one mechanism taking place during the floating catalytic CVD. Difficulties in estimating the CNT growth mode are the in situ monitoring of the phase change of the catalyst particle during the nanotube growth under typical CVD conditions. Observations by TEM are normally made after the CNTs growth, which can give only limited information on the particle behaviour during the process itself. Moreover, the catalyst particles can undergo reshaping and phase transformations during cooling when the synthesis is arrested (Moshkalev & Verissimo, 2007).

3.4.7 Raman spectroscopy of CNFs and CNF/CNTs

Raman spectra of the CF900 and CF900/CNTs samples are presented in Figure 3.16. These Raman spectra were fitted using a 2-peak Lorentzian curve to determine their intensity ratio (I_D/I_G) of the D and G bands was obtained. In a phonon dispersion mode, the G band is attributed to the doubly degenerate in-plane transverse (iTO) mode and the longitudinal (LO) phonon mode with E_{2g} symmetry at the Γ point inside the first Brillouin zone (BZ) (Pimenta *et al.*, 2007). The G band in the Raman spectrum is found to be located at ~1590 cm^{-1} for sp^2 carbon hexagonal in-plane bond-stretching motions. The D band is assigned to a non-degenerate phonon coming from the iTO branch at the K-point with A_{1g} symmetry (Pimenta *et al.*, 2007). The D band is located at ~1350 cm^{-1} and results from the vibrations of carbon atoms that are located at the graphite sheet edge

and relates to defects in sp^2 carbon structures, including edge dislocations, vacancies, and crystal edges (Pimenta *et al.*, 2007). The 2D band is attributed to 2 phonons near the K-point (Ferrari *et al.*, 2006; Lehman, Terrones, Mansfield, Hurst, & Meunier, 2011), located at ~2700 cm^{-1} which is caused by an overtone of the D band and is observed in Raman spectra for multi-walled CNTs (Bokobza & Zhang, 2012).

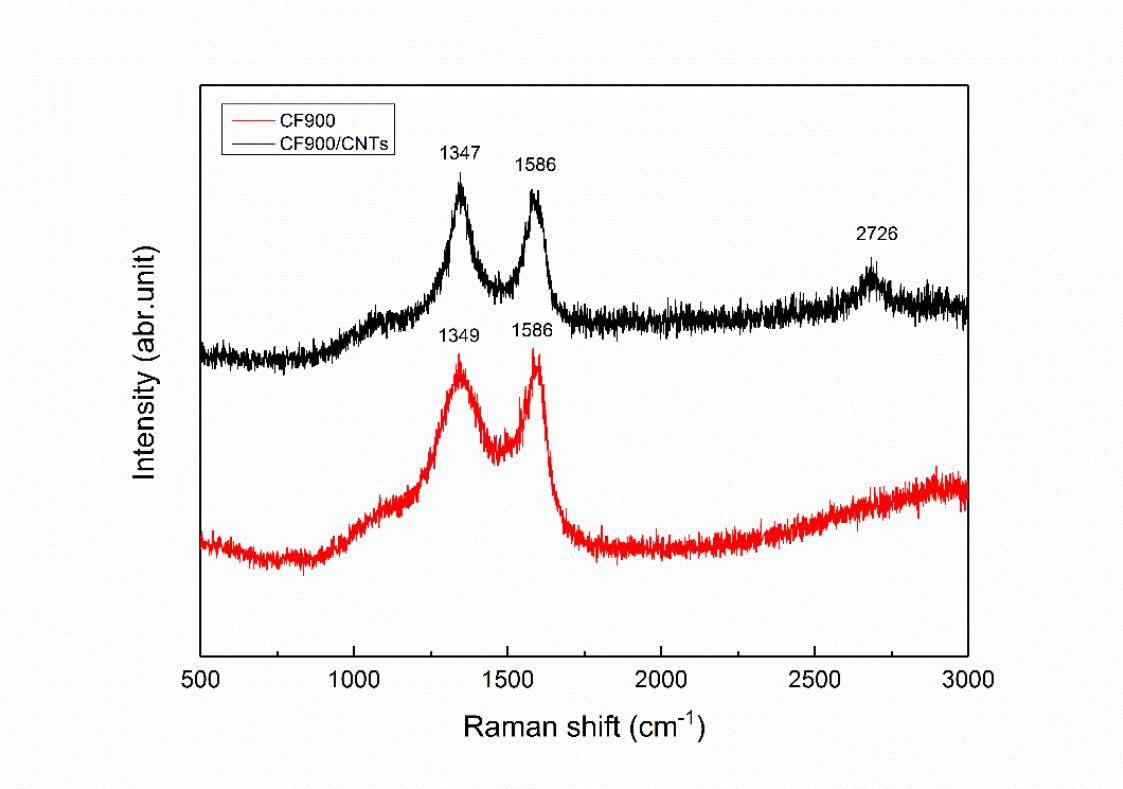

Figure 3.16 Typical Raman spectra of CF900 and CF900/CNTs samples.

The intensity ratio I_D/I_G for the D and G bands is widely used to characterise the disorder and the degree of crystallinity in graphitic materials. The evolution of disorder is typically quantified using the Tuinstra–Koenig (TK) equation (Tuinstra & Koenig, 1970) described by the equation

$$I_D/I_G = C(\lambda)/L_a \qquad (3.2)$$

The value of C (λ) has been reported to be 4.4 nm for a laser wavelength λ = 514 nm (Ferrari & Robertson, 2000); this constant depends on the excitation laser wavelength used (Cançado *et al.*, 2006). L_a represents the in-plane crystalline size in graphitic materials.

Ferrari and Robertson have however found that the TK equation is invalid when L_a is smaller than 2 nm (Ferrari & Robertson, 2000), and they proposed a new modified equation:

$$I_D/I_G = C'(\lambda)\, L_a^2 \qquad (3.3)$$

C (λ)' was estimated to be 0.0055 for a laser wavelength λ = 514 nm when combining equations 3.2 and 3.3. From previous work graphitization is not achieved below a temperature of ~1600 °C (Kong *et al.*, 2012), therefore , for the present fibres, the crystallite size is not expected to evolve and be as large as for a fully graphitized structure (L_a > 2 nm). In this case L_a can be then calculated by using Equation 3.3, for which the in-plane crystalline size L_a < 2 nm. However, in the present work, the Raman spectra were obtained using a 532 nm (2.33 eV) laser rather than a 514 nm wavelength source. From previous work by Matthews *et al.* (Matthews, Pimenta, Dresselhaus, Dresselhaus, & Endo, 1999), for wavelengths in the range 400 - 700 nm the variable scaling coefficient C (λ) in the linear regime is estimated from the equation

$$C(\lambda) \approx C_0 + \lambda C_1 \qquad (3.4)$$

C_0 and C_1 are estimated to be -126 Å and 0.033, respectively (Matthews *et al.*, 1999). Thus, the value of C (λ = 532 nm) is found to be 49.5 Å. The relationship between I_D/I_G and L_a is then:

$$I_{\mathrm{D}}/I_{\mathrm{G}} = 49.5\,\text{Å}/L_{\mathrm{a}} \qquad (3.5)$$

When combining Equations 3.5 and 3.3 ($I_{\mathrm{D}}/I_{\mathrm{G}} = C'(\lambda)\, L_a^2$), the constant C' (λ = 532 nm) is found to be 0.0062 and the relationship between I_D/I_G and L_a therefore obtained for L_a < 2 nm is

$$I_{\mathrm{D}}/I_{\mathrm{G}} = 0.0062\, L_a^2 \qquad (3.6)$$

The I_D/I_G ratio does not appear to change (from 1.01 ± 0.05 to 1.04 ± 0.06, Table 3.4)) when growing CNTs on CNFs. This suggests that there is little change in the crystallinity of CF900/CNTs in comparison to CF900. In theory, a carbon fibre with a higher crystalline planar size L_a exhibits an improved graphitization degree and increased grain size, which results in stronger sp^2 carbon bonds and in turn improves the mechanical properties and electrical resistivity (Pimenta *et al.*, 2007).

Table 3.4 Intensity ratios (I_D/I_G), and FWHM of Raman D and G band for CF900 and CF900/CNTs.

		FWHM (cm^{-1})	
Sample	I_D/I_G	D-band	G-band
CF900	1.01 ± 0.05	160.0 ± 5.1	75.7 ± 3.3
CF900/CNTs	1.04 ± 0.06	92.4 ± 3.6	78.1 ± 3.4

A low intensity 2D band appears at ~2726 cm^{-1}, which is thought to arise from the presence of CNTs decorating the surface of the carbon fibres (see Figure 3.15). Further evidence for this is obtained by the absence of this band for pure CF900.

The Full width at half maximum (FWHM) of a Raman peak is another indicator of crystallinity in carbonaceous materials. The FWHM of the D band in CF900 sharply decreases from 160.0 ± 5.1 to 92.4 ± 3.6 cm^{-1} after growth of the CNTs (see Table 3.4). According to Ferrari (2007), a narrowing peak width reflects lower disorder, which indicates that the growth of CNTs leads to a higher crystalline structure of the CNF/CNTs composite fibres. This provides some evidence of an increasing overall crystallinity of the sample, but it is not conclusive given the lack of an increase in the I_D/I_G ratio. It could be that there is an averaging effect of the laser, whereby a broad distribution of material contributing to the intensities results in a smaller than expected change in this ratio.

3.4.8 Morphology of activated CNFs and CNF/CNTs by SEM and TEM

SEM images of the activated CF900 and activated CF900/CNTs are presented in Figure 3.17a and b. It can be seen the CNT clusters become more condensed on the surface of activated CF900/CNTs when compared to the original CF900/CNTs. Figure 3.17c also shows the TEM image of entangled CNTs on the surface of activated CF900. The KOH solution that was used during activation causes the CNTs “stick to” the surface of CF900. The diameter distribution of activated CF900 is shown in Figure 3.17d; the average diameter does not have significate change after activation, from 259 ± 83 nm to 258 ± 96 nm for CF900 and activated CF900 respectively (Table 3.5). This is because the pores generated by KOH activation are too small to influence the diameter of the fibres. Figure 3.17e shows that the surface of CF900/CNTs is etched by the KOH during activation, resulting in the production of pores with different sizes and shapes. These pores can lead to a high surface area, which is useful for storing charges in supercapacitors.

The KOH activation is a complex process that contains several consecutive reactions. It is mostly accepted that the followed reactions take place (Wang & Kaskel, 2012)

$$6KOH + 2C \rightarrow 2K + 3H_2 + 2K_2CO_3 \quad (3.7)$$

$$K_2CO_3 \rightarrow K_2O + CO_2 \quad (3.8)$$

$$CO_2 + C \rightarrow 2CO \quad (3.9)$$

$$K_2CO_3 + 2C \rightarrow 2K + 3CO \quad (3.10)$$

$$C + K_2O \rightarrow 2K + CO \quad (3.11)$$

Table 3.5 Mean, maximum and minimum values of the Diameters of the activated CF900.

	Mean	Max	Min
Activated CF900	258 ± 96	525	61

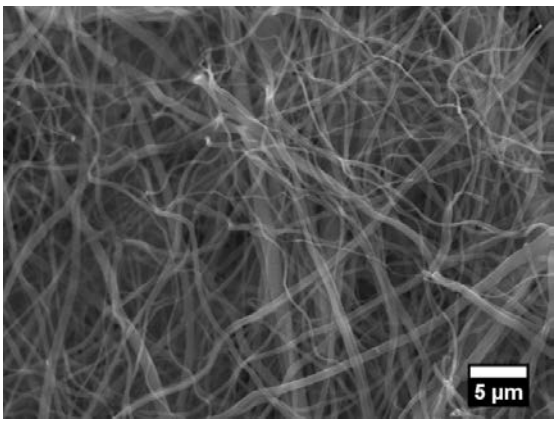

(a)

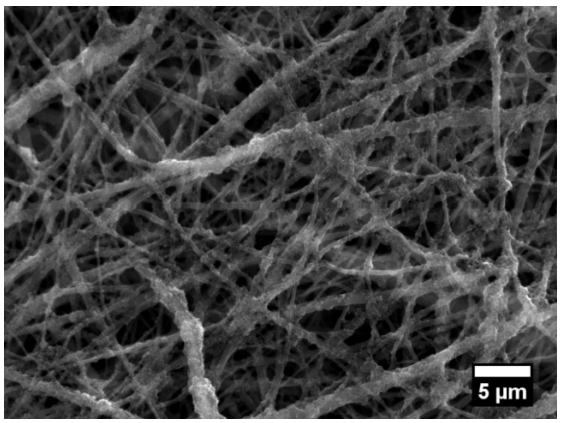

(b)

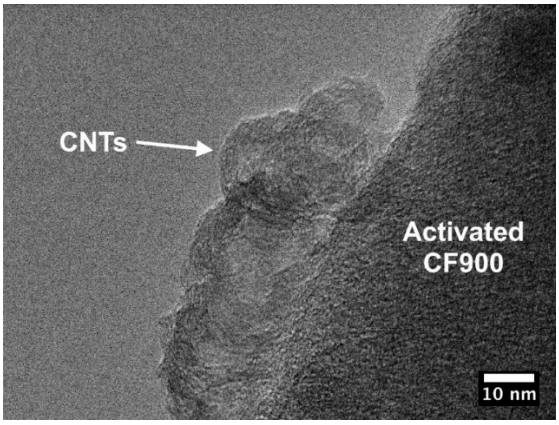

(c)

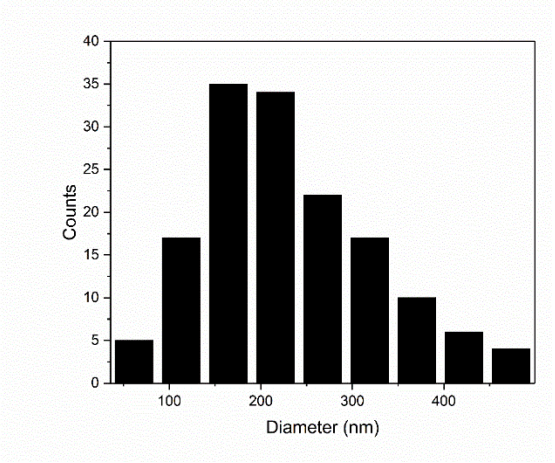

(d)

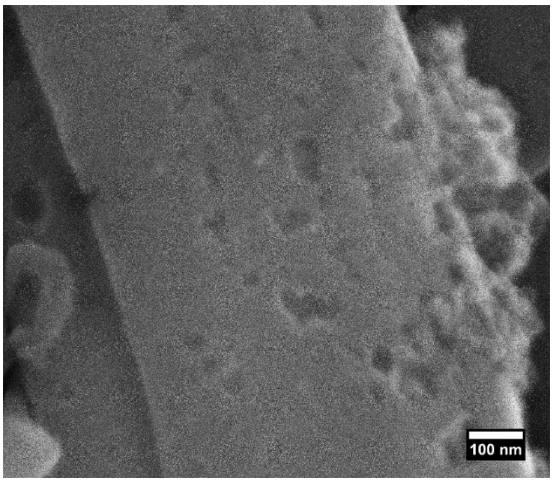

(e)

Figure 3.17 (a) A typical SEM image of activated CF900; (b) A typical SEM image of CF900/CNTs; (c) A typical TEM image of activated CF900 with entangled CNTs on the surface; (d) Diameter distribution of activated CF900; (e) A typical enlarged SEM image of CF900/CNTs with pores.

3.4.9 Surface area of activated CNFs and CNF/CNTs

The N_2 adsorption/desorption isotherms of CF900 and CF900/CNTs are shown in Figure 3.18a. Both of the isotherms are Type H4 in accordance with IUPAC isotherms classification (Thommes *et al.*, 2015). The isotherms experience a sharp increase at very low relative pressures, which indicates that both of the materials are dominated by micropores. This includes primary and secondary micropore filling, which can be classified in accordance with the pore sizes. Primary micropore filling occurs when the relative pressures (P/P^0) (P is the equilibrium pressure and the P^0 is the saturation pressure) are lower than 0.01, at which micropores with widths up to 0.7 - 0.8 nm are filled by nitrogen at 77K. At higher P/P^0 ratios up to 0.2 - 0.3 for nitrogen adsorption at 77K, wider secondary micropores (width up to 2 nm) filling takes place (Carrott, Roberts, & Sing, 1987). The slight hysteresis loops of both isotherms appear at a value of P/P^0 of 0.4 - 0.5, suggesting the materials are micro-mesoporous. Also, the H4 type isotherm is associated with the narrow slit-like pores (Sych *et al.*, 2012). As soon as the filling of the micropores is completed, the mesopore filling starts at a P/P^0 value of over 0.3. During the mesopore filling, the pore walls are covered by monolayer molecules and consequently multilayer adsorption takes place. At higher P/P^0 values, capillary condensation commences once the multilayer adsorption completes. This process is a transition from a gas to a liquid phase by condensation as the pressure continuously increases to the saturation pressure (Thommes *et al.*, 2015). The formation of the hysteresis loop is closely related to the capillary condensation. The hysteresis loop appears when the vapour pressure during filling is larger than that during emptying, due to the delay of the formation of the meniscus during adsorption (Foster, 1932). The N_2 adsorption

plateaus when P/P^0 > 0.5, showing the materials have a very small number of large mesopores and macropores (Ma, Zhang, Zhu, Yu, & Liu, 2014).

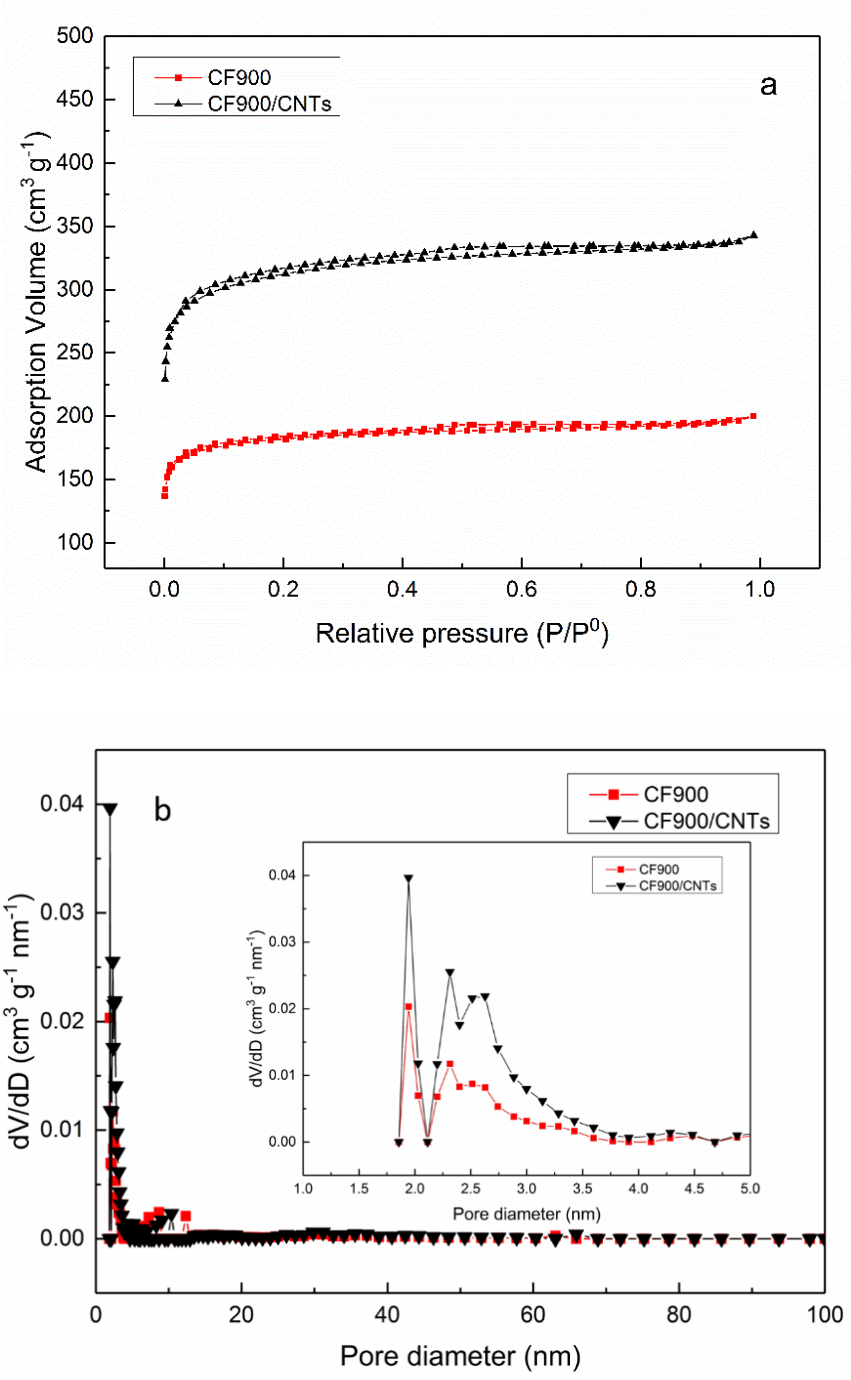

Figure 3.18 Typical (a) isotherms of CF900 and CF900/CNTs and (b) pore size distribution of CF900 and CF900/CNTs.

As shown in Table 3.6, the CF900/CNTs sample exhibits a higher S_{BET} (1211 m^2 g^{-1}) and a total pore volume V_{tot} (0.53 m^3 g^{-1}) than CF900 with S_{BET} (712 m^2 g^{-1}) and V_{tot} (0.31 m^3 g^{-1}); this is considered to be attributed to the large surface area of CVD-grown CNTs. The value of S_{micro}/S_{BET} of both materials is greater than 80%, demonstrating that the specific surface area is mostly due to the presence of micropores. Both the V_{micro} and V_{meso} values are higher for the CF900/CNTs material compared to CF900. Moreover, the pore size distribution curves (Figure 3.18b) reveal that the pore size of both materials exhibit a range of sizes between 2 - 4 nm.

Table 3.6 Pore properties of CF900 and CF900/CNTs.

	S_{BET} (m^2 g^{-1})	S_{micro} (m^2 g^{-1})	S_{meso} (m^2 g^{-1})	V_{tot} (m^3 g^{-1})	V_{micro} (m^3 g^{-1})	V_{meso} (m^3 g^{-1})
CF900	712	611	63	0.31	0.24	0.05
CF900/CNTs	1211	1001	131	0.53	0.39	0.10

3.4.10 TGA analysis of the activated CNF/CNTs samples

As can be seen from Figure 3.19, a steady weight loss takes place from the room temperature to 350 °C, which is attributed to removal of moisture. A sharp weight loss is observed from 350 °C to 550 °C due to the degradation of CNFs and CNTs. The residue product comprising 14.6 wt.% is considered to be Fe_2O_3 after CNF/CNTs are completely burnt-off. The Fe nanoparticles in activated CNF/CNTs then can be calculated to be 10.2 wt.% (2.4 mol %).

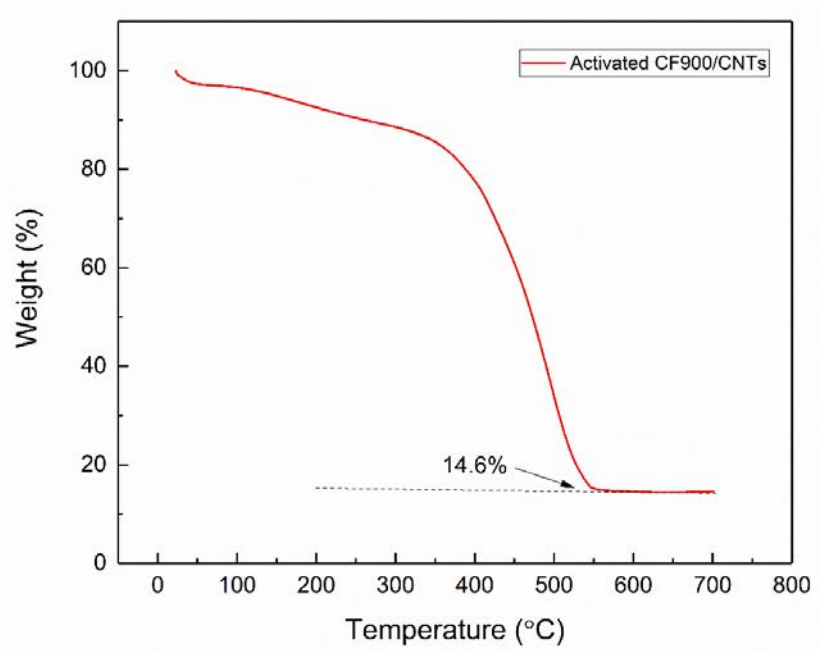

Figure 3.19 TGA for CF900/CNTs obtained at temperature heating from room temperature to 700 °C.

3.4.11 Capacitance of the CNF/CNTs samples

Hierarchical CNF/CNTs composites, with good mechanical stability and electrical conductivity when connecting to the current collector, have been directly utilized as a supercapacitor electrode without any binder. Such a simplified route to fabricate a supercapacitor device has the advantage of improving capacitive performance by removing the poorly conducting binder and reducing the weight to volume ratio of the electrodes.

The CV curves obtained for the CF900 and CF900/CNTs electrodes at a scan rate of 10 mV s^{-1} exhibit a rectangular shape (Figure 3.20a), showing a typical behaviour seen previously for EDLC without obvious Faradaic reactions. The CF900/CNTs electrode has a larger CV bound area, and in turn a higher value of capacitance in comparison to the pristine CF900 electrode. The presence of CNTs on fibre surface results in a ~15% increase in the capacitance compared

with the pristine fibres. This finding arises because the CNTs increase both the surface area and electrical conductivity of the electrode, giving rise to enlarged electrochemical active sites with enhanced electron transport characteristics. It also important to mention the role of Fe catalysts in the growth of CNTs. The catalytic Fe nanoparticles diffuse into the electrospun carbon fibre substrate to form FeC_3 before the commencement of the nucleation of CNTs. Previous investigations have also observed inhomogeneous and very low-density CNTs growth on carbon fibre mats via CVD at 800 °C (Sonoyama *et al.*, 2006). It has been suggested that it is more difficult to grow CNTs on carbon fibre substrates than on quartz. The proposed reason is that the catalytic nanoparticles readily react with carbon fibre matrices to form mixed sp^2-sp^3 carbons which result in a decreased number of catalytic nanoparticles remaining on the carbon fibre surface. In addition, a low yield of CNTs may also arise from the relatively small diameter of the electrospun carbon fibres. This potentially makes it difficult to provide large loading sites for catalytic nanoparticles on a single carbon fibre surface. However, to improve this situation, an introduction of reductive gas to keep the Fe nanoparticles from reacting with the carbon matrix or an application of a barrier coating on the carbon fibre surface can be used (Steiner, Li, & Wardle, 2013). Therefore, an increased CNT growth could be optimised through this process but this is left as a future work objective.

In general, all the CV curves of CF900/CNTs obtained at different scan rates retain their rectangular shapes without obvious peaks (shown in Figure 3.20b). This indicates a good capacitive behaviour at a high scan rate. In addition, the slope of V/I yields the equivalent series resistance (R_s) (Guo *et al.*, 2009). As the scan rate increases to 200 mV s^{-1}, the CV curves do not change shape, in which

the slope of V/I undergoes a small change. This indicates the devices have a small R_S.

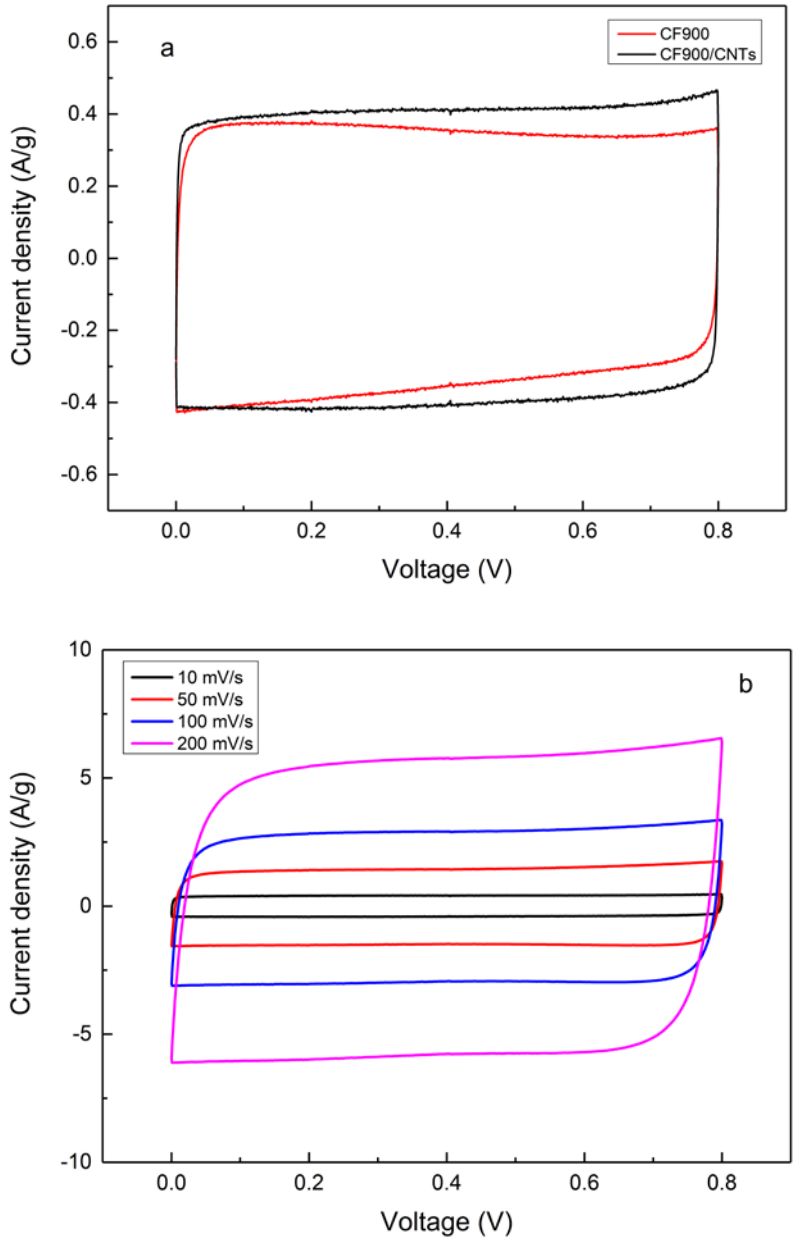

Figure 3.20 (a) CV curves of CF900 and CF900/CNTs at a scan rate of 10 mV s^{-1}; (b) CV curves of CF900/CNTs obtained at a scan rate ranging from 10 to 200 mV s^{-1}. CV curves were obtained from 2-electrode configurated 'coin cell' supercapacitors with 6 mol L^{-1} aqueous KOH as the electrolyte.

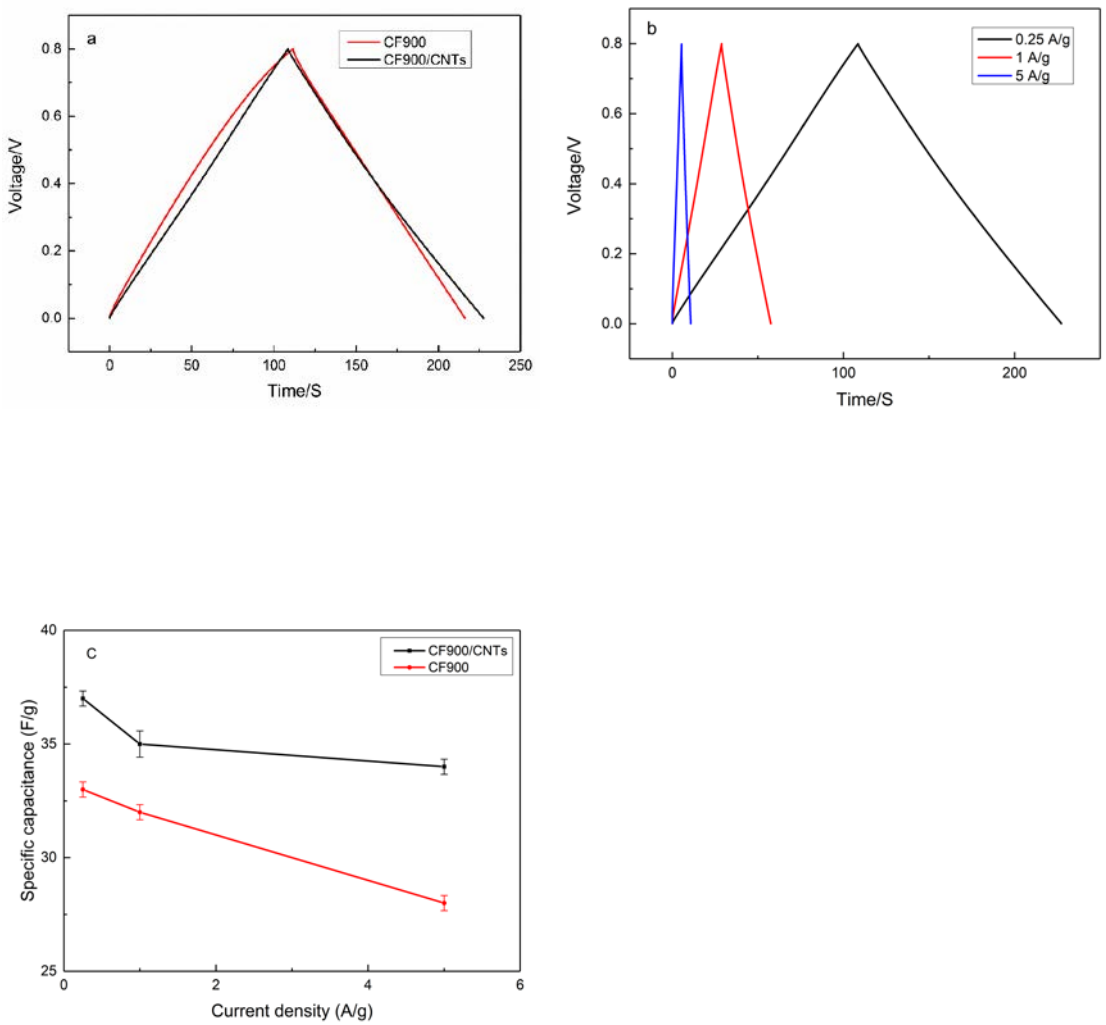

Figure 3.21 (a) Charge/discharge curves obtained at a current density of 0.25 A g^{-1} for CF900, and CF900/CNTs electrodes; (b) Charge/discharge curves obtained at current densities ranging from 0.25 to 5 A g^{-1} for CF900/CNTs electrodes; (c) Specific capacitances of the CF900 and CF900/CNTs electrodes as a function of the current density; error bars represent standard errors of three repetitions. Charge/discharge curves were obtained from 2-electrode configurated 'coin cell' supercapacitors with 6 mol L^{-1} aqueous KOH as the electrolyte.

The comparison of GCD for the CF900, CF900/CNTs electrodes is presented in Figure 3.21a. At a low current density of 0.25 A g^{-1}, the performance of the

electrodes is of the order of CF900/CNTs > CF900, which is consistent with their CV behaviour at a low scan rate. Specifically, the GCD curves at a current density of 0.25 A g^{-1} give capacitances of 37 and 33 F g^{-1} for CF900/CNTs and CF900, respectively. The capacitance increases by 15% from CF900 to CF900/CNTs due to the CNTs on the fibres' surface. Taken as value normalised to the surface area, values of 25 mF cm^{-2} and 43 mF cm^{-2} for the CF900 to CF900/CNTs samples are respectively obtained. The areal specific capacitances of the electrode materials are competitive with the other carbon-based electrodes, e.g. coaxial carbon fibre (Le *et al.*, 2013), ZnO activated carbon textile (Lam *et al.*, 2016), carbon nanosheets coated carbon fibre (Zhao *et al.*, 2009), and even carbon Nanoparticles/MnO_2 Nanorods for pseudocapacitors (Yuan *et al.*, 2012). In addition to CF900, the CNTs that have grown on the surface of CF900 are also activated by KOH. The specific capacitance of the activated pure MWCNTs could experience a 5-fold increase in comparison to the original MWCNTs. This development of high capacitive performance results from the generation of micropores on CNTs' graphitic walls (Frackowiak *et al.*, 2002). The microporous structure of CNTs with large reactive sites and their highly conductive properties are attributed to the adsorption of a large number of ions on to the electrodes, leading to a higher capacitance in CF900/CNTs. The specific capacitance obtained for CF900/CNTs is competitive with previous work with cellulose precursors, in which they produced electrode materials by directly electrospinning a mixed solution of 6 wt.% CNTs with a cellulose precursor (Deng, Young, Kinloch, Abdelkader*, et al.*, 2013). The increase in capacitance was attributed to the presence of CNTs protruding from the fibre surface (Deng, Young, Kinloch, Abdelkader*, et al.*, 2013). The presence of such CNTs protruding from the surface was however serendipitous. Here the same result by an alternative route is

obtained. The availability of the CNTs at the surface could allow for the coupling of these devices to a solid matrix dielectric, obtaining a structural capacitor, the subject of which has been recently reviewed (Qian *et al.*, 2010).

The GCD curves for CF900/CNTs (Figure 3.21b) at different current densities show an almost symmetrical triangular shape with small voltage drops at the initial point of the discharge curve (0.032 V at a current density of 5 A g^{-1}), indicating a low R_s of the device. This triangular shape is retained at a higher current density of 5 A g^{-1}, showing an excellent capacitive behaviour of the electrode.

As can be seen from Figure 3.21c, as the current density increases from 0.25 to 5 A g^{-1}, the capacitance of both materials decreases. In general, a low scan rate (0.25 A g^{-1}) results in a slow mobility of the electrolyte ions, allowing them to have enough time to diffuse into the available reactive sites of the electrodes. However, at higher scan rates (5 A g^{-1}), the electrolyte ions can only approach the surface of the electrode rather than access into the porous structure, therefore negatively influencing of capacitive behaviour (Fatnassi & Es-Souni, 2015). In addition, the capacitances of CF900/CNTs at all the current densities are higher than those of CF900 counterpart, which confirms that the growth of CNTs improves the capacitive performance. It is also noted that a greater increase in capacitance by virtue of the growth of CNTs is observed at a high current density of 5 A g^{-1}. Specifically, although the capacitance of CF900/CNTs increased by 15% at a current density of 0.25 A g^{-1} in comparison to CF900, a 22% improvement is noted at a current density of 5 A g^{-1}. When increasing to a higher current density of 5 A g^{-1}, the specific capacitance retains 84% and 90% of its initial value for the CF900 and CF900/CNTs samples respectively. The improvement of rate capability from

CF900 to CF900/CNTs suggests the growth of CNTs enhances the electrical conductivity performance to accelerate the electron transfer.

The EIS profiles exhibit behaviour of a supercapacitor with a porous carbon fibre electrode (Figure 3.22). The equivalent circuit model is presented in the inset, which includes equivalent series resistance (R_s), charge transfer resistance (R_{ct}), Warburg resistance (Z_w), double layer capacitance (C). Table 3.7 shows the resistance parameters of both electrodes. In the Nyquist plot, the R_s of a system is defined as the initial intercept of the semicircle with the Z'-axis in the high frequency region. In accordance to EIS, the CF900, CF900/CNTs samples have small R_s values (1.388 ± 0.018 and 0.534 ± 0.008 $\Omega \cdot cm^2$, respectively). This shows the growth of CNTs results in a decrease of R_s, which increases the electron transport properties of the electrodes. The R_{ct} at the electrolyte/electrode interfaces can be expressed as the intercept of the semicircle in the mid-to-high frequency region. The charge transfer resistance is resulted from the movement of charges close to the Helmholtz plane (Hung, Masarapu, Ko, & Wei, 2009). It is noted that R_{ct} is lower for the CF900/CNTs (2.592 ± 0.020 $\Omega \cdot cm^2$) electrode in comparison to the CF900 electrode (2.694 ± 0.028 $\Omega \cdot cm^2$); the growth of CNTs on CF900 lowers the R_{ct}. At a 45° region in the Nyquist plot, known as the Warburg region; the slope of this portion of the curve is called the Z_w and is a result of the frequency dependence of ion diffusion/transport in the electrolyte (Le *et al.*, 2013). Normally the vertical line represents the formation of an ideal capacitors. However, from the Nyquist plot the supercapacitors in present project is controlled by both kinetic and diffusion processes. The reason may arise from the existence of iron nanoparticles which can influence the diffusion process. The Warburg resistance of CF900/CNTs (9.186 ± 0.446 $\Omega \cdot cm^2$) is higher than that of

CF900 (7.550 ± 0.310 Ω·cm^2). This is indicative of a shorter ion diffusion path for CF900/CNTs, resulting in a faster mobility of ions compared to CF900 (Zhang, Zhang*, et al.*, 2011). A more comprehensive analysis of all relevant impedance parameters, including resistance of electrolyte, R_{ct} and Warburg impedance, can be done using an equivalent circuit.

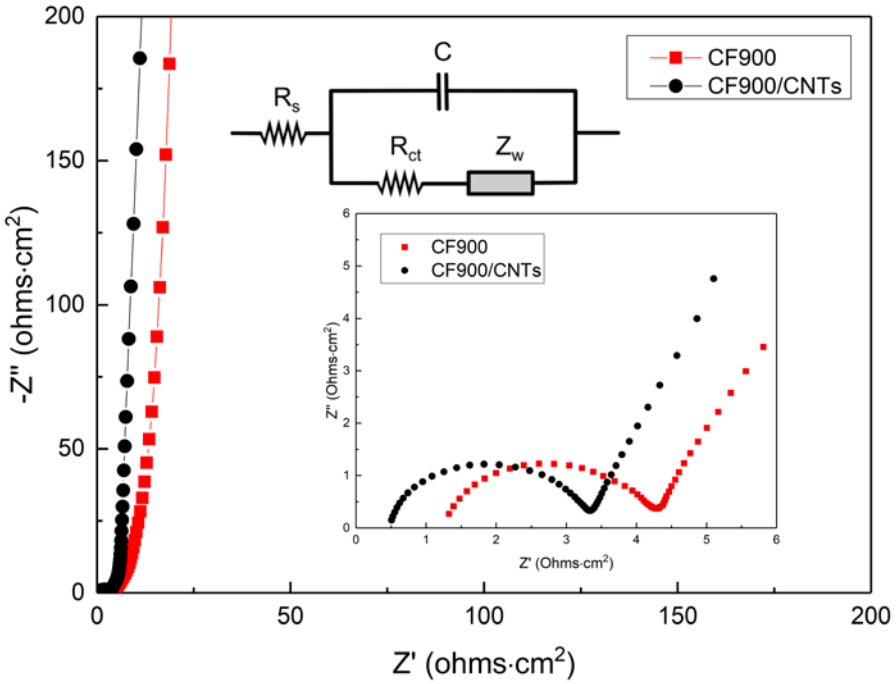

Figure 3.22 EIS curves for the CF900 and CF900/CNTs samples. EIS curves were obtained from 2-electrode configurated 'coin cell' supercapacitors with 6 mol L^{-1} aqueous KOH as the electrolyte.

Table 3.7 Impedance parameters for CF900 and CF900/CNTs.

Electrodes	R_s/Ω·cm^2	R_t/Ω·cm^2	Z_W/Ω·cm^2
CF900	1.388 ± 0.018	2.694 ± 0.028	9.186 ± 0.446
CF900/CNTs	0.534 ± 0.008	2.592 ± 0.020	7.550 ± 0.310

Repetitive charge/discharge tests for the CF900 and CF900/CNTs-based devices were performed at a current density of 1 A g^{-1} for 1000 cycles to assess their cyclic performance (Figure 3.23). Both of the CF900 and CF900/CNTs samples retain 90% of the capacitance of their initial values after 1000 cycles, which shows the excellent stability and lifetime of both devices.

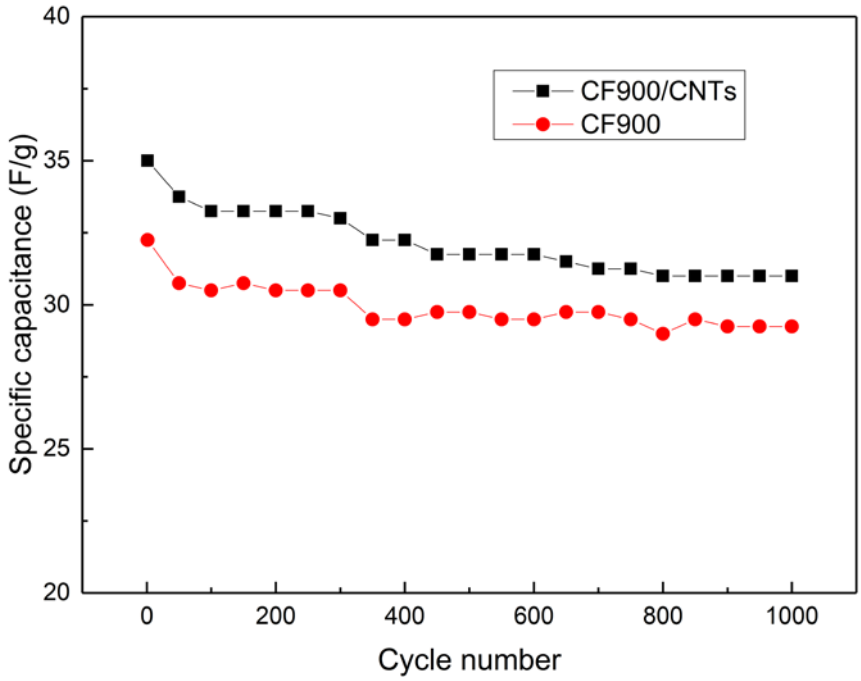

Figure 3.23 Cycling performance of the electrodes over 1000 cycles at a constant current density of 1 A g^{-1} for CF900 and CF900/CNTs.

3.5 Conclusions

Hierarchical cellulose-based CNF/CNTs composite fibres were produced by growing CNTs on the surface of electrospun CNFs using a floating catalyst CVD process. A CVD temperature of 800 °C has been shown to be optimal to grow pure CNTs without the formation of amorphous carbons. Mechanisms of growing CNTs on CNFs were revealed by observing different morphologies of CNTs. The specific capacitance for samples with grown CNTs on the surface achieved a

value 37 F g^{-1} (43 mF cm^{-2}) at a current density 0.25 A g^{-1}, an increase of 15% compared to the neat CNF counterpart. The growth of CNTs improves the electrochemical performance by lowering the R_s, R_{ct}, and Z_w of the electrodes. The hierarchical CNF/CNTs composite can retain ~90% of its initial capacitance after being cycled 1000 times at 1 A g^{-1}. This is thought to be due to the fact that the growth of CNTs enlarges the reactive sites through enhanced surface area and porosity. Accordingly, the BET specific surface area increases from 712 m^2 g^{-1} to 1211 m^2 g^{-1}, while the pore volume increases from 0.31 to 0.53 m^3 g^{-1} after the growth of CNTs. In a Raman spectroscopic analysis, the FWHM of the D band in CF900 sharply decreases from 160 to 92 cm^{-1} after growth of the CNTs. This indicates that the growth of CNTs on the CNFs also leads to a higher degree of overall crystallinity to improve the conductivity of CNFs.

3.6 References

Andrews, R., Jacques, D., Qian, D., & Rantell, T. (2002). Multiwall carbon nanotubes: synthesis and application. *Acc Chem Res, 35*(12), 1008-1017. doi:10.1021/ar010151m

Barud, H. S., de Araujo, A. M., Santos, D. B., de Assuncao, R. M. N., Meireles, C. S., Cerqueira, D. A., . . . Ribeiro, S. J. L. (2008). Thermal behavior of cellulose acetate produced from homogeneous acetylation of bacterial cellulose. *Thermochimica Acta, 471*(1-2), 61-69. doi:10.1016/j.tca.2008.02.009

Bhattacharjee, A., Rooj, A., Roy, D., & Roy, M. (2014). Thermal Decomposition Study of Ferrocene [(C5H5)2Fe]. *Journal of Experimental Physics, 2014*, 1-8. doi:10.1155/2014/513268

Bokobza, L., & Zhang, J. (2012). Raman spectroscopic characterization of multiwall carbon nanotubes and of composites. *Express Polymer Letters, 6*(7), 601-608. doi:10.3144/expresspolymlett.2012.63

Cançado, L. G., Takai, K., Enoki, T., Endo, M., Kim, Y. A., Mizusaki, H., . . . Pimenta, M. A. (2006). General equation for the determination of the crystallite size La of nanographite by Raman spectroscopy. *Applied Physics Letters, 88*(16), 163106. doi:10.1063/1.2196057

Carrillo, A., Colom, X., Sunol, J. J., & Saurina, J. (2004). Structural FTIR analysis and thermal characterisation of lyocell and viscose-type fibres. *European Polymer Journal, 40*(9), 2229-2234. doi:10.1016/j.eurpolmj.2004.05.003

Carrillo, F., Defays, B., Colom, X., Sunol, J. J., & Lopez-Mesas, M. (2009). Thermal degradation of lyocell/poly-N-isopropylacrylamide graft copolymers gels. *Journal of Thermal Analysis and Calorimetry, 97*(3), 945-948. doi:10.1007/s10973-009-0090-8

Carrott, P., Roberts, R., & Sing, K. (1987). Adsorption of nitrogen by porous and non-porous carbons. *Carbon, 25*(1), 59-68.

Cheung, C. L., Kurtz, A., Park, H., & Lieber, C. M. (2002). Diameter-controlled synthesis of carbon nanotubes. *Journal of Physical Chemistry B, 106*(10), 2429-2433. doi:10.1021/jp0142278

Deck, C. P., & Vecchio, K. (2005). Growth mechanism of vapor phase CVD-grown multi-walled carbon nanotubes. *Carbon, 43*(12), 2608-2617. doi:10.1016/j.carbon.2005.05.012

Deng, L., Young, R. J., Kinloch, I. A., Abdelkader, A. M., Holmes, S. M., De Haro-Del Rio, D. A., & Eichhorn, S. J. (2013). Supercapacitance from cellulose and carbon nanotube nanocomposite fibers. *ACS Appl Mater Interfaces, 5*(20), 9983-9990. doi:10.1021/am403622v

Deng, L. B., Young, R. J., Kinloch, I. A., Zhu, Y. Q., & Eichhorn, S. J. (2013). Carbon nanofibres produced from electrospun cellulose nanofibres. *Carbon, 58*, 66-75. doi:10.1016/j.carbon.2013.02.032

Dobele, G., Rossinskaja, G., Telysheva, G., Meier, D., & Faix, O. (1999). Cellulose dehydration and depolymerization reactions during pyrolysis in the presence of phosphoric acid. *Journal of Analytical and Applied Pyrolysis, 49*(1-2), 307-317. doi:10.1016/S0165-2370(98)00126-0

Dumanlı, A. G., & Windle, A. H. (2012). Carbon fibres from cellulosic precursors: a review. *Journal of Materials Science, 47*(10), 4236-4250. doi:10.1007/s10853-011-6081-8

Dupuis, A. C. (2005). The catalyst in the CCVD of carbon nanotubes - a review. *Progress in Materials Science, 50*(8), 929-961. doi:10.1016/j.pmatsci.2005.04.003

Fatnassi, M., & Es-Souni, M. (2015). Nanoscale phase separation in laponite-polypyrrole nanocomposites. Application to electrodes for energy storage. *Rsc Advances, 5*(28), 21550-21557. doi:10.1039/c4ra16540c

Ferrari, A. C. (2007). Raman spectroscopy of graphene and graphite: Disorder, electron-phonon coupling, doping and nonadiabatic effects. *Solid State Communications, 143*(1-2), 47-57. doi:10.1016/j.ssc.2007.03.052

Ferrari, A. C., Meyer, J. C., Scardaci, V., Casiraghi, C., Lazzeri, M., Mauri, F., . . . Geim, A. K. (2006). Raman spectrum of graphene and graphene layers. *Phys Rev Lett, 97*(18), 187401. doi:10.1103/PhysRevLett.97.187401

Ferrari, A. C., & Robertson, J. (2000). Interpretation of Raman spectra of disordered and amorphous carbon. *Physical Review B, 61*(20), 14095-14107. doi:10.1103/PhysRevB.61.14095

Foster, A. G. (1932). The sorption of condensible vapours by porous solids. Part I. The applicability of the capillary theory. *Transactions of the Faraday Society, 28*, 0645-0656. doi:10.1039/tf9322800645

Frackowiak, E., Delpeux, S., Jurewicz, K., Szostak, K., Cazorla-Amoros, D., & Beguin, F. (2002). Enhanced capacitance of carbon nanotubes through chemical activation. *Chemical Physics Letters, 361*(1-2), 35-41. doi:10.1016/S0009-2614(02)00684-X

Frank, E., Steudle, L. M., Ingildeev, D., Sporl, J. M., & Buchmeiser, M. R. (2014). Carbon fibers: precursor systems, processing, structure, and properties. *Angew Chem Int Ed Engl, 53*(21), 5262-5298. doi:10.1002/anie.201306129

Freire, M. G., Teles, A. R. R., Ferreira, R. A. S., Carlos, L. D., Lopes-da-Silva, J. A., & Coutinho, J. A. P. (2011). Electrospun nanosized cellulose fibers using ionic liquids at room temperature. *Green Chemistry, 13*(11), 3173-3180. doi:10.1039/c1gc15930e

Gonzalez, A., Goikolea, E., Barrena, J. A., & Mysyk, R. (2016). Review on supercapacitors: Technologies and materials. *Renewable & Sustainable Energy Reviews, 58*, 1189-1206. doi:10.1016/j.rser.2015.12.249

Guo, Q. H., Zhou, X. P., Li, X. Y., Chen, S. L., Seema, A., Greiner, A., & Hou, H. Q. (2009). Supercapacitors based on hybrid carbon nanofibers containing multiwalled carbon nanotubes. *Journal of Materials Chemistry, 19*(18), 2810-2816. doi:10.1039/b820170f

He, X. Z. (2017). Optimization of Deacetylation Process for Regenerated Cellulose Hollow Fiber Membranes. *International Journal of Polymer Science, 2017*, 8. doi:10.1155/2017/3125413

Hou, H. Q., & Reneker, D. H. (2004). Carbon nanotubes on carbon nanofibers: A novel structure based on electrospun polymer nanofibers. *Advanced Materials, 16*(1), 69-+. doi:10.1002/adma.200306205

Huang, X. S. (2009). Fabrication and Properties of Carbon Fibers. *Materials, 2*(4), 2369-2403. doi:10.3390/ma2042369

Hung, K. S., Masarapu, C., Ko, T. H., & Wei, B. Q. (2009). Wide-temperature range operation supercapacitors from nanostructured activated carbon fabric. *Journal of Power Sources, 193*(2), 944-949. doi:10.1016/j.jpowsour.2009.01.083

Iijima, S. (1991). Helical Microtubules of Graphitic Carbon. *Nature, 354*(6348), 56-58. doi:10.1038/354056a0

Islam, M. S., Deng, Y., Tong, L. Y., Faisal, S. N., Roy, A. K., Minett, A. I., & Gomes, V. G. (2016). Grafting carbon nanotubes directly onto carbon fibers for superior mechanical stability: Towards next generation aerospace composites and energy storage applications. *Carbon, 96*, 701-710. doi:10.1016/j.carbon.2015.10.002

Kavkler, K., & Demsar, A. (2011). Examination of cellulose textile fibres in historical objects by micro-Raman spectroscopy. *Spectrochim Acta A Mol Biomol Spectrosc, 78*(2), 740-746. doi:10.1016/j.saa.2010.12.006

Kong, K., Deng, L. B., Kinloch, I. A., Young, R. J., & Eichhorn, S. J. (2012). Production of carbon fibres from a pyrolysed and graphitised liquid crystalline cellulose fibre precursor. *Journal of Materials Science, 47*(14), 5402-5410. doi:10.1007/s10853-012-6426-y

Kukovitsky, E. F., L'vov, S. G., Sainov, N. A., Shustov, V. A., & Chernozatonskii, L. A. (2002). Correlation between metal catalyst particle size and carbon

nanotube growth. *Chemical Physics Letters, 355*(5-6), 497-503. doi:10.1016/S0009-2614(02)00283-X

Kunadian, I., Andrews, R., Qian, D. L., & Menguc, M. P. (2009). Growth kinetics of MWCNTs synthesized by a continuous-feed CVD method. *Carbon, 47*(2), 384-395. doi:10.1016/j.carbon.2008.10.022

Lai, C., Guo, Q., Wu, X. F., Reneker, D. H., & Hou, H. (2008). Growth of carbon nanostructures on carbonized electrospun nanofibers with palladium nanoparticles. *Nanotechnology, 19*(19), 195303. doi:10.1088/0957-4484/19/19/195303

Lam, D. V., Jo, K., Kim, C. H., Kim, J. H., Lee, H. J., & Lee, S. M. (2016). Activated Carbon Textile via Chemistry of Metal Extraction for Supercapacitors. *ACS Nano, 10*(12), 11351-11359. doi:10.1021/acsnano.6b06608

Le, V. T., Kim, H., Ghosh, A., Kim, J., Chang, J., Vu, Q. A., . . . Lee, Y. H. (2013). Coaxial fiber supercapacitor using all-carbon material electrodes. *ACS Nano, 7*(7), 5940-5947. doi:10.1021/nn4016345

Lehman, J. H., Terrones, M., Mansfield, E., Hurst, K. E., & Meunier, V. (2011). Evaluating the characteristics of multiwall carbon nanotubes. *Carbon, 49*(8), 2581-2602. doi:10.1016/j.carbon.2011.03.028

Ma, X., Zhang, F., Zhu, J., Yu, L., & Liu, X. (2014). Preparation of highly developed mesoporous activated carbon fiber from liquefied wood using wood charcoal as additive and its adsorption of methylene blue from solution. *Bioresour Technol, 164*, 1-6. doi:10.1016/j.biortech.2014.04.050

Matthews, M. J., Pimenta, M. A., Dresselhaus, G., Dresselhaus, M. S., & Endo, M. (1999). Origin of dispersive effects of the Raman D band in carbon materials. *Physical Review B, 59*(10), R6585-R6588. doi:10.1103/PhysRevB.59.R6585

Miao, F. J., Shao, C. L., Li, X. H., Wang, K. X., Lu, N., & Liu, Y. C. (2016). Electrospun Carbon Nanofibers/Carbon Nanotubes/Polyaniline Ternary Composites with Enhanced Electrochemical Performance for Flexible Solid-State Supercapacitors. *Acs Sustainable Chemistry & Engineering, 4*(3), 1689-1696. doi:10.1021/acssuschemeng.5b01631

Moisala, A., Nasibulin, A. G., & Kauppinen, E. I. (2003). The role of metal nanoparticles in the catalytic production of single-walled carbon nanotubes—a review. *Journal of Physics: condensed matter, 15*(42), S3011.

Moshkalev, S. A., & Verissimo, C. (2007). Nucleation and growth of carbon nanotubes in catalytic chemical vapor deposition. *Journal of Applied Physics, 102*(4), 044303. doi:10.1063/1.2769354

Nelson, M. L., & O'Connor, R. T. (1964a). Relation of certain infrared bands to cellulose crystallinity and crystal lattice type. Part II. A new infrared ratio for estimation of crystallinity in celluloses I and II. *Journal of Applied Polymer Science, 8*(3), 1325-1341. doi:10.1002/app.1964.070080323

Nelson, M. L., & O'Connor, R. T. (1964b). Relation of certain infrared bands to cellulose crystallinity and crystal latticed type. Part I. Spectra of lattice types I, II, III and of amorphous cellulose. *Journal of Applied Polymer Science, 8*(3), 1311-1324. doi:10.1002/app.1964.070080322

Perotti, G. F., Barud, H. S., Ribeiro, S. J. L., & Constantino, V. R. L. (2014). Bacterial Cellulose as a Template for Preparation of Hydrotalcite-Like Compounds. *Journal of the Brazilian Chemical Society, 25*(9), 1647-1655. doi:10.5935/0103-5053.20140153

Pimenta, M. A., Dresselhaus, G., Dresselhaus, M. S., Cancado, L. G., Jorio, A., & Saito, R. (2007). Studying disorder in graphite-based systems by Raman

spectroscopy. *Phys Chem Chem Phys, 9*(11), 1276-1291. doi:10.1039/b613962k

Plaisantin, H., Pailler, R., Guette, A., Daude, G., Petraud, M., Barbe, B., . . . Olry, P. (2001). Conversion of cellulosic fibres into carbon fibres: a study of the mechanical properties and correlation with chemical structure. *Composites Science and Technology, 61*(14), 2063-2068. doi:10.1016/S0266-3538(01)00107-5

Qian, H., Diao, H., Shirshova, N., Greenhalgh, E. S., Steinke, J. G., Shaffer, M. S., & Bismarck, A. (2013). Activation of structural carbon fibres for potential applications in multifunctional structural supercapacitors. *J Colloid Interface Sci, 395*, 241-248. doi:10.1016/j.jcis.2012.12.015

Qian, H., Greenhalgh, E. S., Shaffer, M. S. P., & Bismarck, A. (2010). Carbon nanotube-based hierarchical composites: a review. *Journal of Materials Chemistry, 20*(23), 4751-4762. doi:10.1039/c000041h

Rodriguez-Manzo, J. A., Terrones, M., Terrones, H., Kroto, H. W., Sun, L., & Banhart, F. (2007). In situ nucleation of carbon nanotubes by the injection of carbon atoms into metal particles. *Nat Nanotechnol, 2*(5), 307-311. doi:10.1038/nnano.2007.107

Salanne, M., Rotenberg, B., Naoi, K., Kaneko, K., Taberna, P. L., Grey, C. P., . . . Simon, P. (2016). Efficient storage mechanisms for building better supercapacitors. *Nature Energy, 1*, 16070. doi:10.1038/Nenergy.2016.70

Samsur, R., Rangari, V. K., Jeelani, S., Zhang, L., & Cheng, Z. Y. (2013). Fabrication of carbon nanotubes grown woven carbon fiber/epoxy composites and their electrical and mechanical properties. *Journal of Applied Physics, 113*(21), 214903. doi:10.1063/1.4808105

Shazed, M. A., Suraya, A. R., Rahmanian, S., & Salleh, M. A. M. (2014). Effect of fibre coating and geometry on the tensile properties of hybrid carbon nanotube coated carbon fibre reinforced composite. *Materials & Design, 54*, 660-669. doi:10.1016/j.matdes.2013.08.063

Sonoyama, N., Ohshita, M., Nijubu, A., Nishikawa, H., Yanase, H., Hayashi, J., & Chiba, T. (2006). Synthesis of carbon nanotubes on carbon fibers by means of two-step thermochemical vapor deposition. *Carbon, 44*(9), 1754-1761. doi:10.1016/j.carbon.2005.12.039

Steiner, S. A., 3rd, Li, R., & Wardle, B. L. (2013). Circumventing the mechanochemical origins of strength loss in the synthesis of hierarchical carbon fibers. *ACS Appl Mater Interfaces, 5*(11), 4892-4903. doi:10.1021/am4006385

Sun, B., Long, Y. Z., Zhang, H. D., Li, M. M., Duvail, J. L., Jiang, X. Y., & Yin, H. L. (2014). Advances in three-dimensional nanofibrous macrostructures via electrospinning. *Progress in Polymer Science, 39*(5), 862-890. doi:10.1016/j.progpolymsci.2013.06.002

Sych, N. V., Trofymenko, S. I., Poddubnaya, O. I., Tsyba, M. M., Sapsay, V. I., Klymchuk, D. O., & Puziy, A. M. (2012). Porous structure and surface chemistry of phosphoric acid activated carbon from corncob. *Applied Surface Science, 261*, 75-82. doi:10.1016/j.apsusc.2012.07.084

Tang, M. M., & Bacon, R. (1964). Carbonization of cellulose fibers—I. Low temperature pyrolysis. *Carbon, 2*(3), 211-220. doi:10.1016/0008-6223(64)90035-1

Tessonnier, J. P., & Su, D. S. (2011). Recent progress on the growth mechanism of carbon nanotubes: a review. *ChemSusChem, 4*(7), 824-847. doi:10.1002/cssc.201100175

Thommes, M., Kaneko, K., Neimark, A. V., Olivier, J. P., Rodriguez-Reinoso, F., Rouquerol, J., & Sing, K. S. W. (2015). Physisorption of gases, with special reference to the evaluation of surface area and pore size distribution (IUPAC Technical Report). *Pure and Applied Chemistry, 87*(9-10), 1051-1069. doi:10.1515/pac-2014-1117

Tibbetts, G. G. (1984). Why Are Carbon Filaments Tubular. *Journal of Crystal Growth, 66*(3), 632-638. doi:10.1016/0022-0248(84)90163-5

Tuinstra, F., & Koenig, J. L. (1970). Raman Spectrum of Graphite. *The Journal of Chemical Physics, 53*(3), 1126-1130. doi:10.1063/1.1674108

Wang, J. C., & Kaskel, S. (2012). KOH activation of carbon-based materials for energy storage. *Journal of Materials Chemistry, 22*(45), 23710-23725. doi:10.1039/c2jm34066f

Wang, T., Song, D. F., Zhao, H., Chen, J. Y., Zhao, C. H., Chen, L. L., . . . Xie, E. Q. (2015). Facilitated transport channels in carbon nanotube/carbon nanofiber hierarchical composites decorated with manganese dioxide for flexible supercapacitors. *Journal of Power Sources, 274*, 709-717. doi:10.1016/j.jpowsour.2014.10.102

Weissker, U., Hampel, S., Leonhardt, A., & Buchner, B. (2010). Carbon Nanotubes Filled with Ferromagnetic Materials. *Materials (Basel), 3*(8), 4387-4427. doi:10.3390/ma3084387

Wiley, J. H., & Atalla, R. H. (1987). Band Assignments in the Raman-Spectra of Celluloses. *Carbohydrate Research, 160*, 113-129. doi:10.1016/0008-6215(87)80306-3

Yu, J., Lu, W., Pei, S., Gong, K., Wang, L., Meng, L., . . . Chou, T. W. (2016). Omnidirectionally Stretchable High-Performance Supercapacitor Based

on Isotropic Buckled Carbon Nanotube Films. *ACS Nano, 10*(5), 5204-5211. doi:10.1021/acsnano.6b00752

Yu, Z. N., Tetard, L., Zhai, L., & Thomas, J. (2015). Supercapacitor electrode materials: nanostructures from 0 to 3 dimensions. *Energy & Environmental Science, 8*(3), 702-730. doi:10.1039/c4ee03229b

Yuan, L., Lu, X. H., Xiao, X., Zhai, T., Dai, J., Zhang, F., . . . Wang, Z. L. (2012). Flexible solid-state supercapacitors based on carbon nanoparticles/MnO2 nanorods hybrid structure. *ACS Nano, 6*(1), 656-661. doi:10.1021/nn2041279

Zhang, B. A., Kang, F. Y., Tarascon, J. M., & Kim, J. K. (2016). Recent advances in electrospun carbon nanofibers and their application in electrochemical energy storage. *Progress in Materials Science, 76*, 319-380. doi:10.1016/j.pmatsci.2015.08.002

Zhang, C. L., & Yu, S. H. (2014). Nanoparticles meet electrospinning: recent advances and future prospects. *Chem Soc Rev, 43*(13), 4423-4448. doi:10.1039/c3cs60426h

Zhang, D. C., Zhang, X., Chen, Y., Yu, P., Wang, C. H., & Ma, Y. W. (2011). Enhanced capacitance and rate capability of graphene/polypyrrole composite as electrode material for supercapacitors. *Journal of Power Sources, 196*(14), 5990-5996. doi:10.1016/j.jpowsour.2011.02.090

Zhang, Q. H., Liu, J. W., Sager, R., Dai, L. M., & Baur, J. (2009). Hierarchical composites of carbon nanotubes on carbon fiber: influence of growth condition on fiber tensile properties. *Composites Science and Technology, 69*(5), 594-601. doi:10.1016/j.compscitech.2008.12.002

Zhang, X. F., Cao, A. Y., Wei, B. Q., Li, Y. H., Wei, J. Q., Xu, C. L., & Wu, D. H. (2002). Rapid growth of well-aligned carbon nanotube arrays. *Chemical Physics Letters, 362*(3-4), 285-290. doi:10.1016/S0009-2614(02)01025-4

Zhao, X., Tian, H., Zhu, M. Y., Tian, K., Wang, J. J., Kang, F. Y., & Outlaw, R. A. (2009). Carbon nanosheets as the electrode material in supercapacitors. *Journal of Power Sources, 194*(2), 1208-1212. doi:10.1016/j.jpowsour.2009.06.004

Zheng, Q., Cai, Z., Ma, Z., & Gong, S. (2015). Cellulose nanofibril/reduced graphene oxide/carbon nanotube hybrid aerogels for highly flexible and all-solid-state supercapacitors. *ACS Appl Mater Interfaces, 7*(5), 3263-3271. doi:10.1021/am507999s

Zhu, S., Su, C. H., Lehoczky, S. L., Muntele, I., & Ila, D. (2003). Carbon nanotube growth on carbon fibers. *Diamond and Related Materials, 12*(10-11), 1825-1828. doi:10.1016/S0925-9635(03)00205-X

Chapter 4 Carbonized Electrospun Cellulose Composite Nanofibres Containing Silicon Carbide Nanoparticles

4.1 Introduction

Carbon fibres are useful for reinforcing composite materials because they have high specific modulus and high specific strength (Chand, 2000). The mechanical properties of carbon fibre composites could benefit from forming a more complexed structure (Xu, Zhou, Hong, Han, & Zhang, 2016). To achieve this in the past, ceramic nanoparticles have been added into carbon fibre composites to achieve an improvement in the mechanical properties (Kaybal, Ulus, Demir, Sahin, & Avci, 2018).

Silicon carbide (SiC), a widely used ceramic material, exhibits excellent properties such as high abrasive resistance, low thermal expansion, superior chemical compatibility, good thermal conductivity, high strength, modulus and low density (Patnaik, Satapathy, Mahapatra, & Dash, 2008). Because of these outstanding properties, SiC nanoparticles have the potential to act as a reinforcing material for carbon fibre composites (Mehmet, Mohamad, & Ahmet, 2018). Several methods have been demonstrated for the fabrication of carbon fibre/SiC composites; e.g. by coating SiC on the fibre's surface (Xie, Mirza, Mobus, & Zhang, 2012), and conventional chemical vapor infiltration methods (Petroski et al., 2018). The production of carbon fibre/SiC composites however has issues with weak interactions between the carbon fibre and the SiC nanoparticles and agglomeration of the latter (Wang, Chen, & Yu, 2016; Xie et al., 2018). To address these issues, one effective strategy is to in situ synthesize the carbon fibre/SiC composites. During this process, the formation of strong

interactions between the carbon fibre and SiC nanoparticles prevents the nanoparticles from agglomerating and/or detaching from the surface (Xie et al., 2018). Electrospinning is one of the best approaches to achieve the in situ synthesis of carbon fibre/nanoparticle composites (Xu, Zhang, & Kim, 2014). Specifically, carbon fibre/SiC composites can be produced by using an electrospun solution that contains both SiC nanoparticles and a carbon fibre precursor. Furthermore, the growth of carbon nanotubes (CNTs) on the surface of carbon fibre/SiC composites by a chemical vapour deposition (CVD) is thought to enhance their mechanical properties. Improved mechanical properties have been previously demonstrated by growing CNTs on carbon fibre substrates (Sharma & Lakkad, 2011).

Herein the production of electrospun carbon nanofibres (CNFs) with incorporated SiC nanoparticles was described. CNTs were subsequently grown on the surface of the CNF/SiC nanofibres by the CVD technique. The elastic modulus of the CNF/SiC/CNTs composite nanofibres was estimated using an in situ Raman spectroscopic method. This approach demonstrates that medium modulus (~200 GPa) carbon nanofibres can be produced, which could find applications in composite materials.

4.2 Experimental methods

4.2.1 Materials

Cellulose acetate (CA, average M_n = 100,000 g mol^{-1}) was dissolved in a mixed solution of acetone and N,N-dimethylacetamide (DMAc) (2:1 w/w). Following this, SiC nanoparticles with a particle size < 100 nm (Sigma-Aldrich, Dorset, UK) were added to the mixed solution of CA/DMAc/acetone. The concentrations of CA and

SiC were 20 and 0.4 wt.%, respectively. The CA/DMAc/acetone/SiC solution was stirred using a magnetic stirrer overnight at room temperature.

4.2.2 Electrospinning of composite nanofibres

Electrospinning was carried out using the mixed CA/DMAc/acetone/SiC suspension. The electrospinning set-up consisted of a syringe connected to a pump (Harvard apparatus, Holliston, USA), a voltage supplier (Electrospinz, Blenheim, New Zealand), an Al foil collector (Fisher-Scientific, Loughborough, UK), and a platform (Electrospinz, Blenheim, New Zealand). Optimal spinning conditions were found; namely a voltage of 20 kV, a flow rate of 1 mL h^{-1} and a needle tip-to-collector distance of ~13 cm. Electrospun CA/SiC fibres were spun onto an Al foil collector over a period of 3 h. The CA/SiC fibrous mats were then deacetylated in a 0.05 M NaOH/ethanol solution for 48 h to allow them to regenerate into cellulose/SiC fibres. The fibrous mats were then rinsed with water until neutral and then dried in air.

4.2.3 Carbonization of the cellulose fibres

Regenerated cellulose/SiC fibres were firstly stabilized by heating to 240 °C from room temperature in air at a rate of 5 °C min^{-1}, followed by keeping at a stable maximum temperature for 60 min. These stabilized fibres were then carbonized by heating to 900 °C in an Ar atmosphere at a heating rate of 10 °C min^{-1}, followed by keeping at the final maximum temperature (900 °C) for 30 min. The carbonized regenerated cellulose fibres containing SiC are denoted as CNF/SiC.

4.2.4 CVD production of CNTs

The CNF/SiC sample was pre-located in the hot zone of a CVD furnace. This furnace was then heated to 800 °C at a heating rate of 10 °C min^{-1}. A mixture of ferrocene/styrene (0.01 g ml^{-1}) was fed into the CVD furnace at a flow rate of 1.3 cm^3 h^{-1} for 25 min. The CNF/SiC fibres after CVD treatment are denoted as CNF/SiC/CNTs.

4.3 Characterisation of samples using Electron Microscopy and Electron Diffraction

A Scanning Electron Microscope (SEM) (HITACHI S3200N SEM-EDS) with a voltage of 20 kV was utilized to observe the morphologies of the CA/SiC, regenerated cellulose/SiC, CNF/SiC, and CNF/SiC/CNTs fibre samples. A Transmission Electron Microscope (TEM) (JEOL 2100) was used to examine the nanostructures and the morphologies of the CA/SiC and CNF/SiC fibres. To prepare the TEM samples, the CA/SiC fibres were directly collected onto a copper grid during electrospinning, while the CNF/SiC fibres were sonicated in ethanol for 15 min and deposited onto the grids. Selective Area Electron Diffraction (SAED) within the TEM was used to identify the polytypes of the SiC nanoparticles.

4.4 Characterisation of the composite nanofibres using Raman spectroscopy

A Renishaw RM1000 Raman spectrometer with a laser of wavelength of 532 nm was utilized to record spectra from the SiC nanoparticles, CA, CA/SiC, regenerated cellulose, regenerated cellulose/SiC, CNF/SiC, and CNF/SiC/CNTs

fibres. It was also used to record the spectra for the in situ Raman spectroscopy/bending experiments on the CNFs, CNF/SiC, and CNF/SiC/CNTs samples. A Leica CCD detector was used to record the spectral output. The laser spot size was ~1 - 2 μm, and the power was ~1 mW when the laser was focused on the sample using a 50× objective microscope lens. For each measurement an exposure time of 30 s was used.

For in situ Raman spectroscopy studies, a 5 mm × 5 mm square sample of the CNFs, CNF/SiC, or CNF/SiC/CNT fibre mats was placed centrally on a 70 mm × 22 mm × 1.5 mm poly(methyl methacrylate) (PMMA) beam. Two drops (0.25 mL) of a 0.1 g ml^{-1} PMMA/acetone mixed solution were deposited on the top of these samples and dried at room temperature for 1 h. A strain gauge (type CEA-06-240UZ-120, Vishay Micro-Measurements) was attached to the surface of the PMMA beam using cyanoacrylate adhesive. Two wires were soldered to each copper tab of the strain gauge, which was connected to a transducer. A four-point bending rig was used to deform the samples in tension. Raman spectra were recorded in 0.05% strain increments up to 0.6% strain.

4.5 Results and discussion

4.5.1 SEM characterisation of composite nanofibres

Typical SEM images for the CA/SiC fibres and regenerated cellulose/SiC fibres are shown in Figures 4.1a and 4.1b. The regenerated cellulose/SiC fibres are not as straight as the CA/SiC fibres, possibly as a result of the regeneration process.

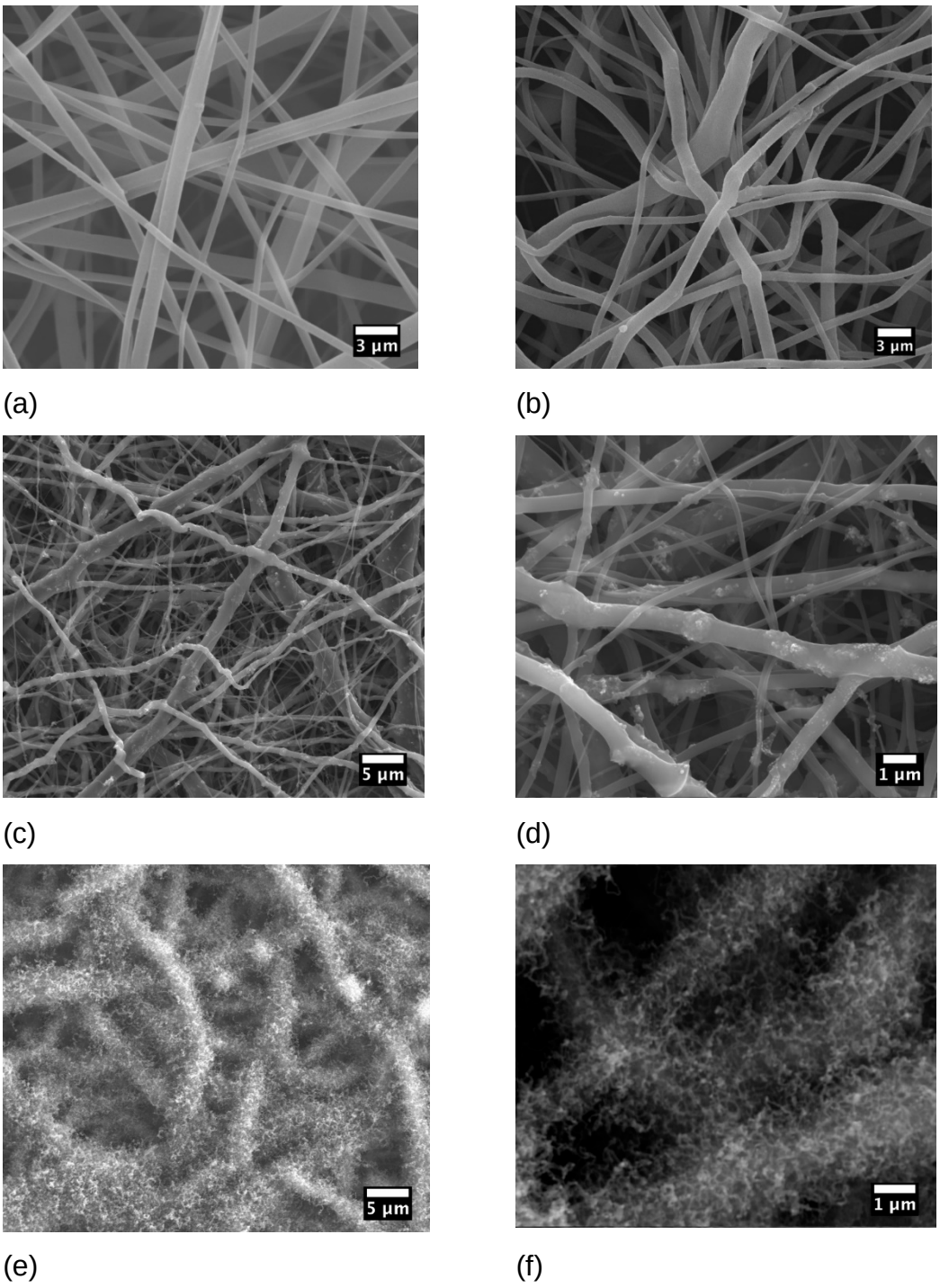

Figure 4.1 Typical SEM images of (a) CA fibre/SiC, (b) regenerated cellulose fibre/SiC and (c) CNF/SiC; (d) an enlarged image of CNF/SiC; (e) CNF/SiC/CNTs fibres and (f) an enlarged image of the CNF/SiC/CNTs fibres.

SEM images were also obtained for the CNF/SiC fibres; typical examples are shown in Figures 4.1c and 4.1d. Some clusters of SiC nanoparticles are clearly

present on the surfaces of the CNF fibres. These clusters are thought to form because the SiC nanoparticles protrude from the surface of the CNFs when the diameter of the regenerated cellulose fibres reduces due to shrinkage during the carbonization process. Typical SEM images of CNF/SiC/CNTs fibres are shown in Figures 4.1e and 4.1f, showing that the CNTs completely cover the surface of the fibres.

4.5.2 TEM characterisation of composite nanofibres

Typical TEM images of the composite nanofibres are shown in Figure 4.2. Figures 4.2a and 4.2b show that there are more SiC nanoparticle clusters present on the surface of the CNF samples compared to the CA fibres. In Figure 4.2c, the lines presented in the inset are closely related to planes of atoms in the crystalline lattice of SiC. The d-spacing of the marked planes is estimated from these lines to be ~0.25 nm; this value corresponds to the d-spacing of the (111) planes (Ye et al., 2017). Crystal defects such as stacking faults can be seen (black lines within the marked dashed rectangle in Figure 4.2c); in some particles many stacking faults are observed (Figure 4.2d). The presence of stacking faults for the 3C-SiC polytype has been reported in a previous study (Zhang et al., 2007). SAED was carried out using the TEM electron beam to confirm the polytypes of the SiC nanoparticles. Diffraction patterns were obtained by focusing on a single SiC particle in Figure 4.2c. Miller indices of the spots, observed in the diffraction patterns from SAED of the SiC particles, are found to be (111), (220) and (222); these correspond to d-spacings of 0.25, 0.15 and 0.12 nm, respectively as shown in Figure 4.2e. These three planes correspond to the planes of the 3C-SiC polytype (Liu, Hou, He, & Yang, 2017).

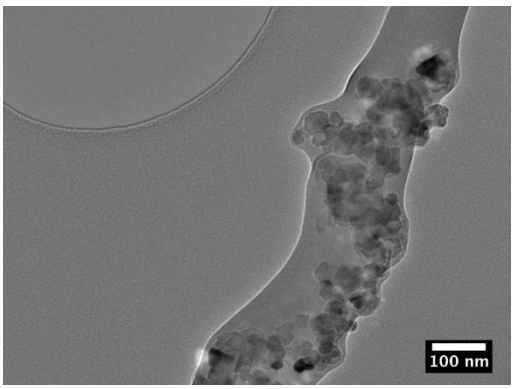

(a)

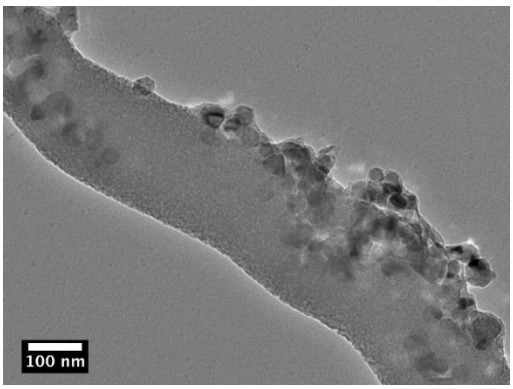

(b)

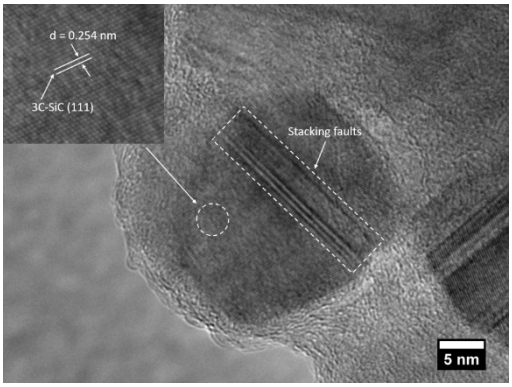

(c)

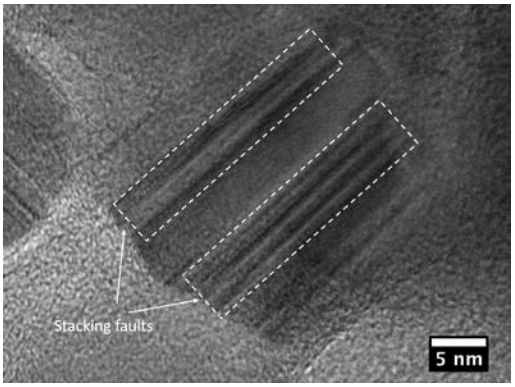

(d)

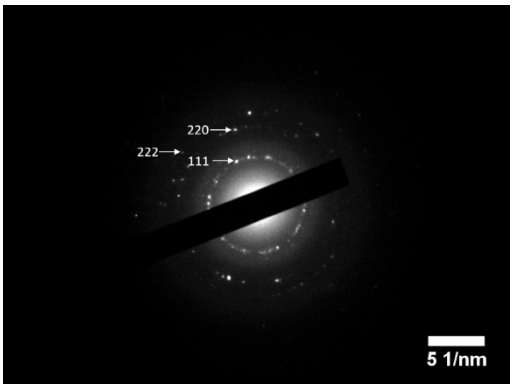

(e)

Figure 4.2 A typical TEM image of (a) CA with SiC nanoparticles and (b) CNF/SiC; (c) A typical SiC nanoparticle encapsulated in the CA with a 0.25 nm d-spacing of the 3C-SiC (111) planes (inset) – stacking faults also indicated; (d) A typical SiC nanoparticle with stacking faults (labeled with dashed rectangles); (e) An indexed SAED pattern for the SiC nanoparticle in (c).

4.5.3 Raman spectroscopic characterisation of SiC composites

Typical Raman spectra for SiC nanoparticles, CA, CA/SiC, regenerated cellulose and regenerated cellulose/SiC composite nanofibres are shown in Figure 4.3a. The Raman bands located at ~ 656 and 1739 cm^{-1} are observed for CA and CA/SiC but are absent for the regenerated cellulose and regenerated cellulose/SiC samples. Specifically, the band located at ~ 656 cm^{-1} corresponds to stretching mode vibrations of C=O bonds emanating from ester groups (Zhang, Feldner, & Fischer, 2011). The other band located at ~ 1739 cm^{-1} corresponds to the vibration of the carbonyl bonds (C=O) present in the acetyl groups (Sanchez-Marquez *et al.*, 2015). In addition, the band located at ~ 796 cm^{-1} for the SiC, CA/SiC and regenerated cellulose/SiC samples corresponds to the zone center transverse optical phonon (TO) mode for the 3C-SiC polytype (β-SiC) (Ward, Young, & Shatwell, 2004). In addition, an intense peak is located at ~1095 cm^{-1} in the regenerated cellulose and regenerated cellulose/SiC samples, which is attributed to the C-O ring and glycosidic linkage stretching modes, indicating the presence of cellulose (Deng, Young, Kinloch, Zhu*, et al.*, 2013). Samples that contain SiC exhibit bands located at ~1352 cm^{-1} and ~1600 cm^{-1}, which are respectively assigned to D and G bands of the graphite layers of carbon deposits, in agreement with the findings of other studies (Gadzira, Gnesin, Mykhaylyk, & Andreyev, 1998; Parida, Choi, Lim, Kim, & Kim, 2013). These bands may arise due to the production of carbon deposits in the SiC particles during manufacturing.

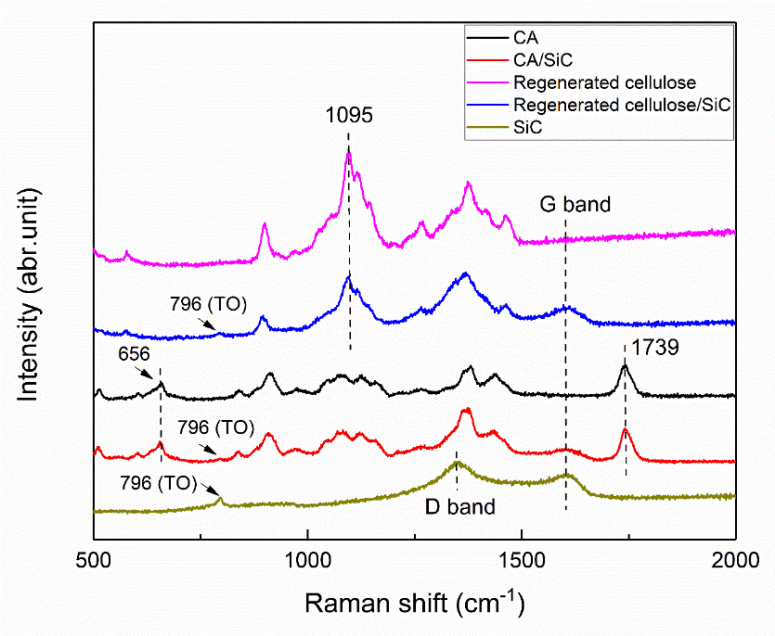

(a)

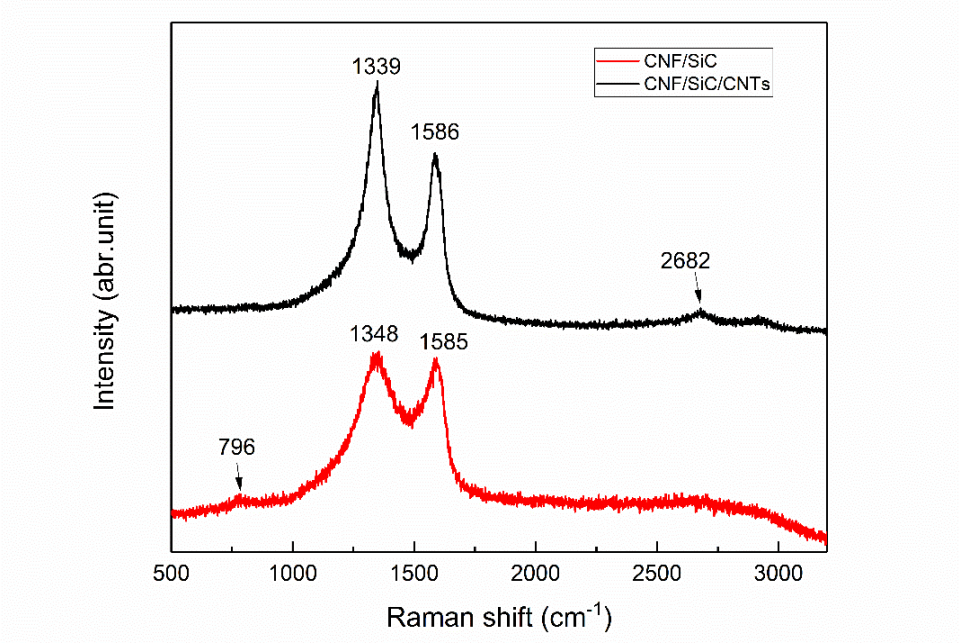

(b)

Figure 4.3 Typical Raman spectra of (a) SiC nanoparticles, CA, CA/SiC, regenerated cellulose, and regenerated cellulose/SiC fibres and (b) CNF/SiC, and CNF/SiC/CNTs nanofibres indicating the presence of bands located at ~796, 1339, 1348, 1585, 1586 and 2682 cm^{-1}.

Typical Raman spectra for the carbon CNF/SiC and CNF/SiC/CNTs samples are shown in Figure 4.3b. Both exhibit characteristic Raman bands located at ~1350 cm^{-1} (D band) and ~1590 cm^{-1} (G band). The Raman band observed at ~796 cm^{-1} for the CNF/SiC sample corresponds to the TO mode in the 3C-SiC polytype. This band is however absent after the growth of CNTs, which is thought to be due to the full coverage of CNTs on the CNF/SiC surface, which hinders the interaction between the spectrometer laser and the SiC. There is a low intensity Raman band located at ~2682 cm^{-1} that is observed for the CNF/SiC/CNTs sample. This band is called 2D band, which is caused by an overtone of the D band and is normally present in Raman spectra from multi-walled CNTs (Bokobza & Zhang, 2012).

The intensity ratio for the D and G bands (I_D/I_G) has been used to quantify disorder in carbon materials (Dresselhaus, Jorio, Souza Filho, & Saito, 2010). The magnitude of the I_D/I_G ratio is thought to be representative of a lateral crystal size L_a < 2 nm for the CNF/SiC samples (Kong *et al.*, 2012). The relationship between the I_D/I_G ratio and L_a, therefore, obtained for L_a < 2 nm is (Ferrari & Robertson, 2000; Li *et al.*, 2017; Matthews *et al.*, 1999)

$$\mathrm{I_D/I_G} = 0.0062\, L_\mathrm{a}^2 \qquad (4.1)$$

For a crystallite size larger than 2 nm, with a Raman laser wavelength λ = 532 nm, the evolution of disorder is typically quantified using the Tuinstra–Koenig relationship (Tuinstra & Koenig, 1970), described by the equation

$$\mathrm{I_D/I_G} = 49.5\,\text{Å}/L_\mathrm{a} \qquad (4.2)$$

The intensity ratio for the D and G bands (I_D/I_G) increases after the growth of CNTs; from 1.19 ± 0.02 to 1.31 ± 0.02 (Table 1), indicating a larger value of L_a for this sample. In theory, a carbon fibre with a larger L_a indicates an increase in the degree of graphitization, and an increased grain size, which results in stronger sp^2 carbon bonds and in turn improved mechanical properties and electrical resistivity (Pimenta et al., 2007).

The full width at half maximum (FWHM) of the D and G bands is another indicator of crystallinity in carbonaceous materials. The FWHM of both D and G bands tends to decrease after the growth of CNTs (Table 4.1). The FWHM of the D and G bands in CNF/SiC sharply decreases from 250.8 ± 3.0 to 149.1 ± 1.3 cm^{-1} and 99.4 ± 2.0 to 69.3 ± 1.1 cm^{-1}, respectively. This decrease is thought to occur because of the presence of the well-ordered carbon structure of the CNTs (Ferrari, 2007).

Table 4.1 I_D/I_G and FWHM of D and G bands for CNF/SiC and CNF/SiC/CNTs.

		FWHM (cm^{-1})	
Sample	I_D/I_G	D-band	G-band
CNF/SiC	1.19 ± 0.02	250.8 ± 3.0	99.4 ± 2.0
CNF/SiC/CNTs	1.31 ± 0.02	149.1 ± 1.3	69.3 ± 1.1

Shifts in the position of the G band upon tensile deformation have been previously used to investigate the stress-transfer behaviour between resins and carbon fibres (Frank *et al.*, 2011). In this study, however, no obvious G band shifts were observed for CNFs, CNF/SiC, and CNF/SiC/CNTs (Figure 4.4a-c). This lack of a clear shift is possibly because the ordered carbon structures for CNFs and

CNF/SiC are not well developed below a carbonization temperature of 900 °C. In addition, for the samples with CNTs grown on the surface, the G band is not sensitive to strain. This is surprising since the CNTs are highly crystalline, but some averaging between the poorly formed carbon fibres and these structures might occur. The position of the 2D Raman band is however thought to be extremely sensitive to tensile deformation (Mohiuddin, Lombardo, Nair, Bonetti, Savini, Jalil, Bonini, Basko, Galiotis, & Marzari, 2009); this band is then used to study the stress transfer properties between the resin and CNF/SiC/CNTs. Figure 4.5 shows that tensile deformation of these samples causes an apparent downshift in the position of the 2D band in the range from 0 to 0.6% strain; the 2D band shift has an approximately linear relationship with the level of applied deformation. Using the slope of a linear regression of the data, the strain dependence of the Raman band shift, $(d(\Delta\nu)/d\varepsilon)$, for the 2D band, is found to be -10.4 cm^{-1} $\%^{-1}$. The Young's modulus of the fibres can be related, in the elastic limit, to the Raman band shifts with respect to both stress and strain using the equation 2.15. The value of stress sensitivity of the Raman 2D band shift has been reported to be -5 cm^{-1}/GPa for CNT (Cooper *et al.*, 2001). Using equation 2.15, and this value of stress sensitivity, we estimate an elastic modulus (E) of 208 ± 26 GPa for the CNF/SiC/CNTs sample. This value is comparable to commercial T650 and IM-7 CFs (200 GPa; (Zhang *et al.*, 2009)), indicating that the CNF/SiC/CNTs composite fibres have high stiffnesses. The modulus of the CNF/SiC/CNTs fibres is also higher than that for the plain CNFs produced at 1500 °C (60 GPa) and 2200 °C (100 GPa), that were obtained using similar methodology (Deng, Young, Kinloch, Zhu*, et al.*, 2013). The modulus of the composite CNF/SiC/CNTs nanofibres is however much lower than pure individual

multi-walled CNTs (1.7 – 2.4 TPa) (Lourie & Wagner, 1998), which may arise from the presence of the less crystalline CNF fibres.

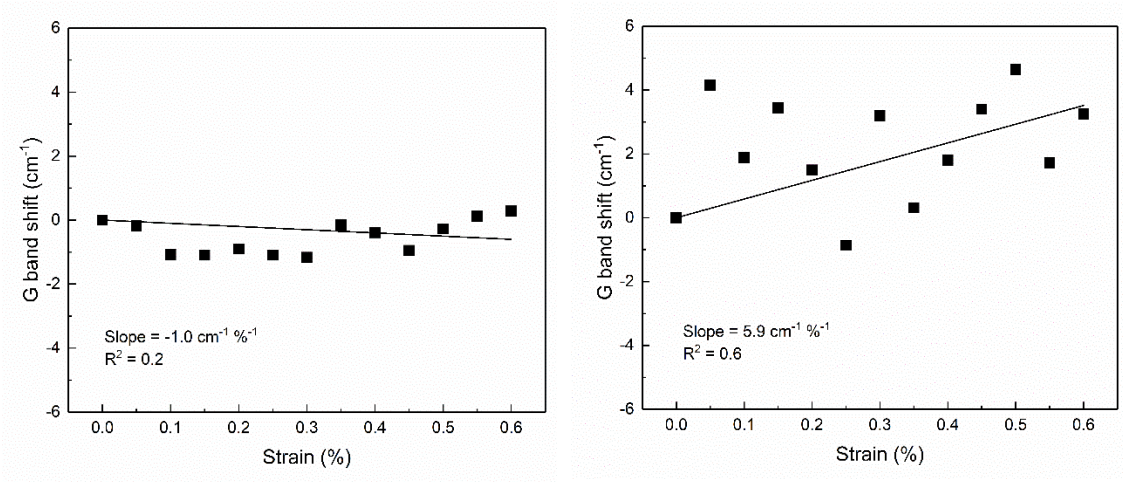

(a) (b)

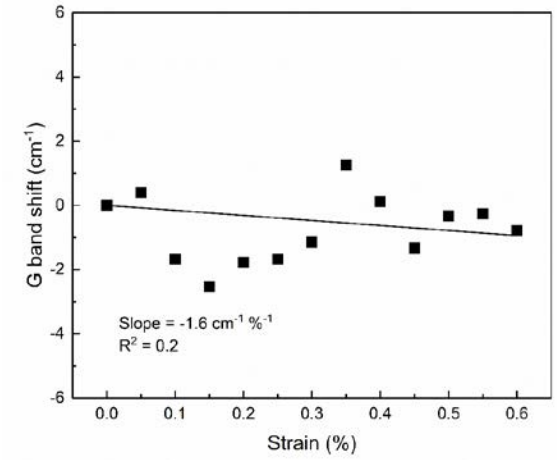

(c)

Figure 4.4 Typical plots of Raman G band shift versus strain for (a) CNFs, (b) CNF/SiC, and (c) CNF/SiC/CNTs samples, with linear regressions to the data (black line).

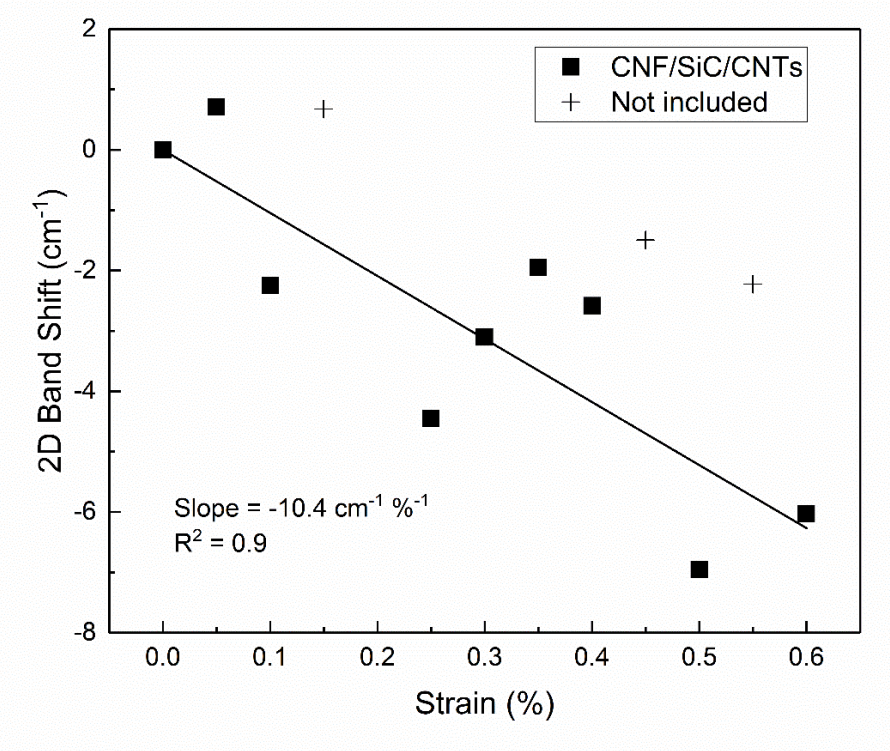

Figure 4.5 Typical Raman shift of the 2D band with tensile deformation applied to the CNF/SiC/CNTs sample in 4-point bending. Solid line is a linear regression to the data. Data labelled + are not included in the fit.

It is thought that some load sharing might occur between these two components of the fibres. It is noted that no TO bands from the SiC nanoparticles are observed from the samples prepared for the Raman spectroscopic study. This is either because the CNTs have fully covered the CNF/SiC surface, or that bands from the SiC overlap with those from PMMA. Therefore, load sharing between the SiC nanoparticles and the carbon nanofibres cannot be estimated using this approach. Nevertheless, using the electrospinning method to synthesise the CNF/SiC/CNTs composite fibres paves the way to produce high-performance SiC reinforced carbon fibre composite.

4.6 Conclusions

CNF/SiC and CNF/SiC/CNTs composite fibres were fabricated from a cellulose precursor by electrospinning, and for the latter samples using a CVD technique. The polytype of the SiC nanoparticles in CA fibres was determined to be 3C-SiC by SAED using TEM. Raman spectroscopy shows that the CNF/SiC/CNTs samples have a higher crystallinity than the CNF/SiC samples when comparing the I_D/I_G ratios, and the FWHM of the D and G bands. An in situ Raman spectroscopic study was used to determine the elastic modulus of the CNF/SiC/CNTs composite nanofibres. The 2D band exhibited a linear downshift with the application of tensile deformation. The elastic modulus of the CNF/SiC/CNTs was estimated to be 208 ± 26 GPa. The unique structure of these composite nanofibres, combined with their high stiffness, could enable them to be used to reinforce composite materials. Furthermore, the in situ Raman deformation test has the potential to be used as a calibration for non-contact inspection of C/SiC-based structures (e.g. brake pads) by converting the Raman shifts into stress.

4.7 References

Bokobza, L., & Zhang, J. (2012). Raman spectroscopic characterization of multiwall carbon nanotubes and of composites. *Express Polymer Letters, 6*(7), 601-608. doi:10.3144/expresspolymlett.2012.63

Chand, S. (2000). Review Carbon fibers for composites. *Journal of Materials Science, 35*(6), 1303-1313. doi:10.1023/a:1004780301489

Cooper, C. A., Young, R. J., & Halsall, M. (2001). Investigation into the deformation of carbon nanotubes and their composites through the use of

Raman spectroscopy. *Composites Part a-Applied Science and Manufacturing, 32*(3-4), 401-411. doi:10.1016/S1359-835x(00)00107-X

Deng, L. B., Young, R. J., Kinloch, I. A., Zhu, Y. Q., & Eichhorn, S. J. (2013). Carbon nanofibres produced from electrospun cellulose nanofibres. *Carbon, 58*, 66-75. doi:10.1016/j.carbon.2013.02.032

Dresselhaus, M. S., Jorio, A., Souza Filho, A. G., & Saito, R. (2010). Defect characterization in graphene and carbon nanotubes using Raman spectroscopy. *Philos Trans A Math Phys Eng Sci, 368*(1932), 5355-5377. doi:10.1098/rsta.2010.0213

Ferrari, A. C. (2007). Raman spectroscopy of graphene and graphite: Disorder, electron-phonon coupling, doping and nonadiabatic effects. *Solid State Communications, 143*(1-2), 47-57. doi:10.1016/j.ssc.2007.03.052

Ferrari, A. C., & Robertson, J. (2000). Interpretation of Raman spectra of disordered and amorphous carbon. *Physical Review B, 61*(20), 14095-14107. doi:10.1103/PhysRevB.61.14095

Frank, O., Tsoukleri, G., Riaz, I., Papagelis, K., Parthenios, J., Ferrari, A. C., . . . Galiotis, C. (2011). Development of a universal stress sensor for graphene and carbon fibres. *Nature Communications, 2*. doi:10.1038/ncomms1247

Gadzira, M., Gnesin, G., Mykhaylyk, O., & Andreyev, O. (1998). Synthesis and structural peculiarities of nonstoichiometric β-SiC. *Diamond and Related Materials, 7*(10), 1466-1470. doi:10.1016/s0925-9635(98)00201-5

Kaybal, H. B., Ulus, H., Demir, O., Sahin, O. S., & Avci, A. (2018). Effects of alumina nanoparticles on dynamic impact responses of carbon fiber reinforced epoxy matrix nanocomposites. *Engineering Science and Technology-an International Journal-Jestech, 21*(3), 399-407. doi:10.1016/j.jestch.2018.03.011

Kong, K., Deng, L. B., Kinloch, I. A., Young, R. J., & Eichhorn, S. J. (2012). Production of carbon fibres from a pyrolysed and graphitised liquid crystalline cellulose fibre precursor. *Journal of Materials Science, 47*(14), 5402-5410. doi:10.1007/s10853-012-6426-y

Li, Q., Deng, L. B., Kim, J. K., Zhu, Y. Q. Q., Holmes, S. M., Perez-Page, M., & Eichhorn, S. J. (2017). Growth of Carbon Nanotubes on Electrospun Cellulose Fibers for High Performance Supercapacitors. *Journal of the Electrochemical Society, 164*(13), A3220-A3228. doi:10.1149/2.1181713jes

Liu, Y., Hou, H., He, X., & Yang, W. (2017). Mesporous 3C-SiC Hollow Fibers. *Sci Rep, 7*(1), 1893. doi:10.1038/s41598-017-02147-8

Lourie, O., & Wagner, H. D. (1998). Evaluation of Young's modulus of carbon nanotubes by micro-Raman spectroscopy. *Journal of Materials Research, 13*(9), 2418-2422. doi:10.1557/Jmr.1998.0336

Matthews, M. J., Pimenta, M. A., Dresselhaus, G., Dresselhaus, M. S., & Endo, M. (1999). Origin of dispersive effects of the Raman D band in carbon materials. *Physical Review B, 59*(10), R6585-R6588. doi:10.1103/PhysRevB.59.R6585

Mehmet, B., Mohamad, A., & Ahmet, E. (2018). A comparative study on the tensile and impact properties of Kevlar, carbon, and S-glass/epoxy composites reinforced with SiC particles. *Materials Research Express, 5*(2), 025301. doi:10.1088/2053-1591/aaa991

Mohiuddin, T., Lombardo, A., Nair, R., Bonetti, A., Savini, G., Jalil, R., . . . Marzari, N. (2009). Uniaxial strain in graphene by Raman spectroscopy: G peak splitting, Grüneisen parameters, and sample orientation. *Physical review B, 79*(20), 205433. doi:10.1103/PhysRevB.79.205433

Parida, B., Choi, J., Lim, G., Kim, K., & Kim, K. (2013). Enhanced Visible Light Absorption by 3C-SiC Nanoparticles Embedded in Si Solar Cells by Plasma-Enhanced Chemical Vapor Deposition. *Journal of Nanomaterials, 2013*, 10. doi:10.1155/2013/953790

Patnaik, A., Satapathy, A., Mahapatra, S. S., & Dash, R. R. (2008). A Comparative Study on Different Ceramic Fillers Affecting Mechanical Properties of Glass—Polyester Composites. *Journal of Reinforced Plastics and Composites, 28*(11), 1305-1318. doi:10.1177/0731684407086589

Petroski, K., Poges, S., Monteleone, C., Grady, J., Bhatt, R., & Suib, S. L. (2018). Rapid Chemical Vapor Infiltration of Silicon Carbide Minicomposites at Atmospheric Pressure. *ACS Appl Mater Interfaces, 10*(5), 4986-4992. doi:10.1021/acsami.7b17098

Pimenta, M. A., Dresselhaus, G., Dresselhaus, M. S., Cancado, L. G., Jorio, A., & Saito, R. (2007). Studying disorder in graphite-based systems by Raman spectroscopy. *Phys Chem Chem Phys, 9*(11), 1276-1291. doi:10.1039/b613962k

Sanchez-Marquez, J. A., Fuentes-Ramirez, R., Cano-Rodriguez, I., Gamino-Arroyo, Z., Rubio-Rosas, E., Kenny, J. M., & Rescignano, N. (2015). Membrane Made of Cellulose Acetate with Polyacrylic Acid Reinforced with Carbon Nanotubes and Its Applicability for Chromium Removal. *International Journal of Polymer Science, 2015*. doi:10.1155/2015/320631

Sharma, S. P., & Lakkad, S. C. (2011). Effect of CNTs growth on carbon fibers on the tensile strength of CNTs grown carbon fiber-reinforced polymer matrix composites. *Composites Part a-Applied Science and Manufacturing, 42*(1), 8-15. doi:10.1016/j.compositesa.2010.09.008

Tuinstra, F., & Koenig, J. L. (1970). Raman Spectrum of Graphite. *The Journal of Chemical Physics, 53*(3), 1126-1130. doi:10.1063/1.1674108

Wang, Y., Chen, Z. F., & Yu, S. J. (2016). Ablation behavior and mechanism analysis of C/SiC composites. *Journal of Materials Research and Technology-Jmr&T, 5*(2), 170-182. doi:10.1016/j.jmrt.2015.10.004

Ward, Y., Young, R. J., & Shatwell, R. A. (2004). Application of Raman microscopy to the analysis of silicon carbide monofilaments. *Journal of Materials Science, 39*(22), 6781-6790. doi:10.1023/B:Jmsc.0000045606.60263.27

Xie, H., Fu, K., Yang, C. P., Yao, Y. G., Rao, J. C., Zhou, Y. B., . . . Hu, L. B. (2018). Necklace-Like Silicon Carbide and Carbon Nanocomposites Formed by Steady Joule Heating. *Small Methods, 2*(4), 1700371. doi:10.1002/smtd.201700371

Xie, W., Mirza, Z., Mobus, G., & Zhang, S. W. (2012). Novel Synthesis and Characterization of High Quality Silicon Carbide Coatings on Carbon Fibers. *Journal of the American Ceramic Society, 95*(6), 1878-1882. doi:10.1111/j.1551-2916.2012.05153.x

Xu, B. S., Zhou, S. B., Hong, C. Q., Han, J. C., & Zhang, X. H. (2016). Mechanical enhancement of lightweight ZrB2-modified carbon-bonded carbon fiber composites with self-grown carbon nanotubes. *Carbon, 102*, 487-493. doi:10.1016/j.carbon.2016.02.077

Xu, Z. L., Zhang, B., & Kim, J. K. (2014). Electrospun carbon nanofiber anodes containing monodispersed Si nanoparticles and graphene oxide with exceptional high rate capacities. *Nano Energy, 6*, 27-35. doi:10.1016/j.nanoen.2014.03.003

Ye, C., Ran, G., Zhou, W., Qu, Y., Yan, X., Cheng, Q., & Li, N. (2017). The Preparation and Microstructure of Nanocrystal 3C-SiC/ZrO(2) Bilayer Films. *Nanomaterials (Basel), 7*(12), 408. doi:10.3390/nano7120408

Zhang, K., Feldner, A., & Fischer, S. (2011). FT Raman spectroscopic investigation of cellulose acetate. *Cellulose, 18*(4), 995-1003. doi:10.1007/s10570-011-9545-8

Zhang, Q. H., Liu, J. W., Sager, R., Dai, L. M., & Baur, J. (2009). Hierarchical composites of carbon nanotubes on carbon fiber: influence of growth condition on fiber tensile properties. *Composites Science and Technology, 69*(5), 594-601. doi:10.1016/j.compscitech.2008.12.002

Zhang, Y. F., Han, X. D., Zheng, K., Zhang, Z., Zhang, X. N., Fu, J. Y., . . . Wang, Z. L. (2007). Direct observation of super-plasticity of beta-SiC nanowires at low temperature. *Advanced Functional Materials, 17*(17), 3435-3440. doi:10.1002/adfm.200700162

Chapter 5 Electrospun CA fibres with ferrocene powder

5.1 Introduction

Carbon fibre composites are considered to be the most important class of composite materials because they are high strength compared to conventional materials, which allows them to be widely applied in a variety of industries such as aerospace, automotive, construction, and marine (Agarwal, Broutman, & Chandrashekhara, 2017). The performance of these composite materials depends not only on the properties of the fibre and matrix, but also on the interface between them; Good interfacial adhesion provides composites with structural integrity and efficient load transfer between the fibre and matrix (Zhang *et al.*, 2009). Interfacial adhesion can be typically enhanced by increasing the fibre surface area, therefore better stress transfer occurs. With high surface area per unit volume, electrospun cellulose-based carbon nanofibres (CNFs) are good candidates for the production of carbon fibre composites (Bhardwaj & Kundu, 2010). These CNFs have competitive mechanical properties compared to the traditional carbon microfibre-based composites (Deng, Young, Kinloch, Zhu*, et al.*, 2013). Carbon nanotubes (CNTs) are promising materials for the reinforcement of interlaminar regions of composites due to their nanoscale diameter, high aspect ratios and desirable mechanical, electrical, and thermal properties (Thostenson *et al.*, 2002). With proper design, CNTs could be incorporated with carbon fibres to create a hierarchical structure to achieve enhanced mechanical properties of composites (Sharma & Lakkad, 2011). One of the common approaches used to grow CNTs on carbon fibres is a floating catalyst chemical vapour deposition (CVD) method (Zhang *et al.*, 2009). Using this method however makes the in situ size control of CNTs difficult since the

catalyst nanoparticles are dispersed unevenly in the reaction zone (Kunadian *et al.*, 2009). In contrast, to grow CNTs more evenly on the surface of CNFs, catalyst materials have been previously embedded into the electrospun CNFs prior to the CVD process (Hou & Reneker, 2004), (Chuilin, Qiaohui, Xiang-Fa, Darrell, & Haoqing, 2008). There has not been any study to date that involves the combination of catalysts and nanofibrous cellulose into a single composite for the growth of CNTs.

In this Chapter, ferrocene was used as a catalyst, and was encapsulated into cellulose fibres via electrospinning. CNTs were then grown on these electrospun cellulose fibres by CVD. SEM was used to characterise the morphological features of the fibres. Raman spectroscopy was used to examine the structural features of CNFs and CNF/CNTs. Stress transfer properties of CNFs and CNF/CNTs were also assessed by an in situ Raman spectroscopic study of the deformation of CNF/polymer and CNF/CNTs/polymer composites.

5.2 Experimental methods

Cellulose Acetate (CA) at a concentration of 20 wt.% was dissolved in a mixed solution of acetone and N,N-dimethylacetamide (DMAc) (2:1 w/w). Ferrocene ($Fe(C_5H_5)_2$) was then added to the CA/acetone/DMAc mixture at concentrations of 2 wt.% and 4 wt.%. The whole solution was stirred via a magnetic mixer overnight before performing electrospinning.

Electrospinning was carried out using the mixed CA/acetone/DMAc/ferrocene solution with a spinning voltage of 14 kV (a 16 kV for comparison) a solution flow rate of 1 mL h^{-1} and a needle tip-to-collector distance of 14 cm. Randomly

oriented CA/ferrocene nanofibrous mats were produced by electrospinning for 3 h, and were collected onto an aluminium foil collector. The collected mats were removed from the aluminium foil, and then deacetylated in a 0.05 M NaOH aqueous solution for 48 h to allow CA fibres to regenerate into pure cellulose. This fibrous mat was then rinsed and dried in air.

Stabilization and carbonization were completed in a high-temperature tube furnace. Stabilization was firstly carried out for the regenerated cellulose/ferrocene by increasing the furnace from room temperature to 240 °C at a heating rate of 5 °C min^{-1} in air, followed by a steady state for 60 minutes. The stabilized fibres were then carbonized by heating from 240 to 900 °C at a rate of 10 °C min^{-1}, followed by keeping at the final maximum temperature (900 °C) for 180 minutes. Keeping the temperature at 900 °C, styrene, as a carbon source to provide carbon atoms of CNTs, was supplied to the hot zone by a syringe and a flexible tube, facilitated by a pump running at a flow rate at 0.0254 cm^3 h^{-1} for 25 minutes.

Samples were then removed from this process. Composite beam-bending samples were produced, as described in Chapter 4. The procedure for the in situ Raman spectroscopy/bending experiments, but specifically now using the CF900/CNTs samples produced with 2 wt.% and 4 wt.% ferrocene, was described in Chapter 4.

5.3 Characterisation of fibres

A scanning electron microscope (SEM) (HITACHI S3200N SEM-EDS) with a voltage of 20 kV was utilized to observe the morphologies of the electrospun CA,

carbon fibres and the CNTs. Raman spectroscopy was utilized to characterise the CA/2 wt.% ferrocene, CA/4 wt.% ferrocene, regenerated cellulose/2 wt.% ferrocene, regenerated cellulose/4 wt.% ferrocene, CNFs and CVD grown samples. Spectra were obtained using a 532 nm laser coupled to a Renishaw RM1000 spectrometer. A Leica CCD detector was used to record the spectral output. The laser spot size was ~1-2 μm, and the power was ~1 mW when the laser was focused on the sample using a 50× objective microscope lens. Thermogravimetric analysis (TGA) was performed by heating regenerated cellulose with 2 wt.% and 4 wt.% ferrocene at a heating rate of 10 °C min^{-1} from room temperature to 800 °C in the air.

5.4 Results and discussion

5.4.1 SEM images and size distributions of electrospun CA/ferrocene

The SEM images shown in Figures 5.1a-c indicate that there is no obvious change in the morphology by varying ferrocene contents and applied electrospinning voltages.

Figures 5.2a and b show the diameter distributions for the CA fibres produced with 2 wt.% and 4 wt.% ferrocene at a voltage of 14 kV. These fibres exhibit average diameters of 0.958 ± 0.468 μm and 1.191 ± 0.691 μm, respectively. This suggests that the diameter is not significantly affected by changing the ferrocene content in the CA fibres. When increasing the voltage from 14 kV to 16 kV, the diameter of the fibres exhibits a small increase to 1.135 ± 0.570 μm.

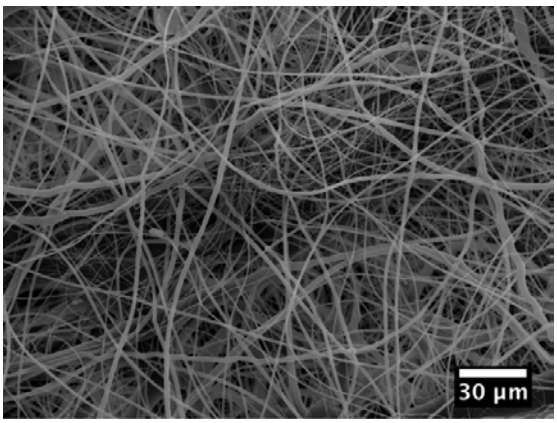

(a)

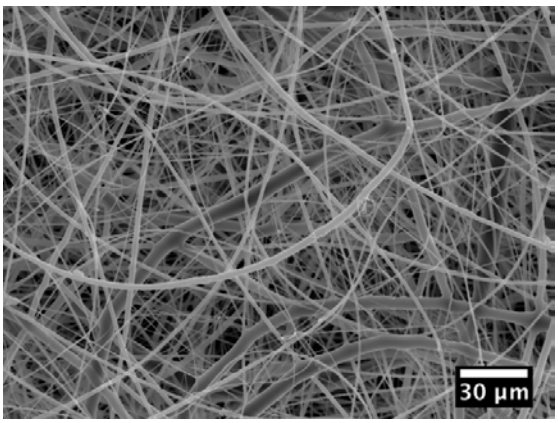

(b)

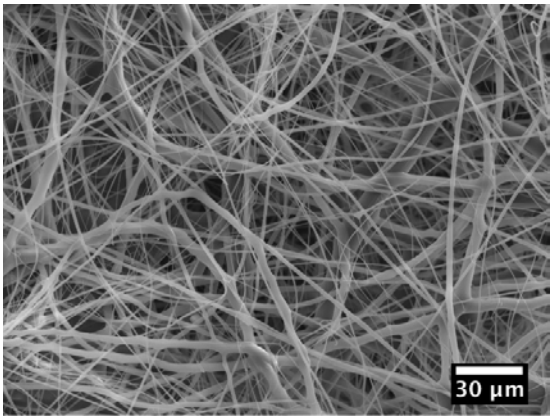

(c)

Figure 5.1 Typical SEM images of (a) CA fibres with 2 wt.% ferrocene, 14 kV and (b) CA fibres with 4 wt.% ferrocene, 14 kV (c) CA fibres at a voltage of 16 kV with 4 wt.% ferrocene.

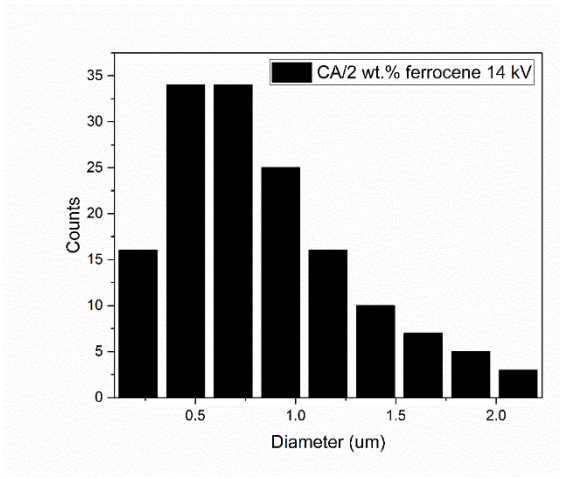

(a)

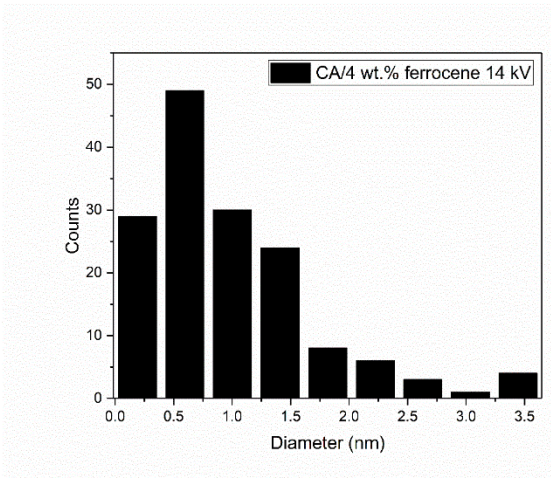

(b)

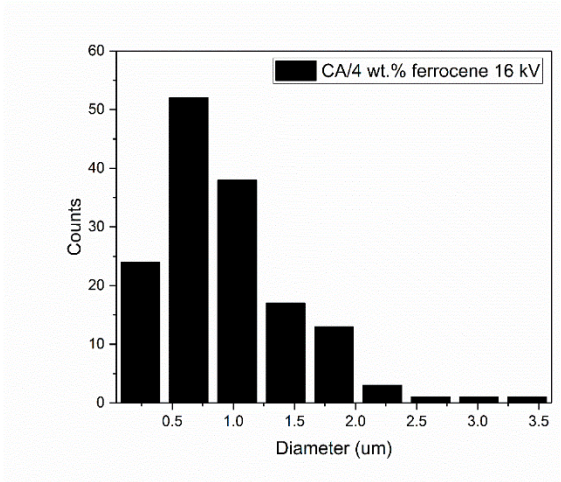

(c)

Figure 5.2 Diameter distributions for electrospun fibres; (a) CA/2 wt.% ferrocene at 14 kV; (b) CA/4 wt.% ferrocene at 14 kV; (c) CA/4 wt.% ferrocene at 16 kV.

5.4.2 Morphology of CNF/CNTs

Two important factors that influence the CNT yield are catalyst concentration and carbonization time. The CNT yield during CVD by two different ferrocene concentrations at 2 wt.% and 4 wt.% are compared with the same styrene flow rate of 0.0254 cm^3 h^{-1} for 3 h of carbonization at 900 °C. It is noted that the Fe nanoparticles act as the catalyst for the growth of CNTs during the CVD process by decomposition of ferrocene during carbonization. At a temperature higher than

500 °C, ferrocene decomposes spontaneously following the chemical reaction (Barreiro *et al.*, 2006)

$$Fe(C_5H_5)_2 \rightarrow Fe + H_2 + CH_4 + C_5H_6 + ... \quad (7.1)$$

This means at a temperature of 900 °C, Fe particles co-exist with different kinds of hydrocarbons in the reaction zone of the CVD furnace (Leonhardt *et al.*, 2006). Figure 5.3a shows that a limited number of CNTs have grown on the surface of the CF900 sample, with a 2 wt.% concentration of ferrocene. A significantly increased CNT yield is achieved with an increase to 4 wt.% of ferrocene, shown in Figure 5.3b. The CNTs are also observed to have mixed with amorphous carbon.

To investigate the influence of carbonization time on the CNT yield, two carbonization times, 0.5 h and 3 h, have been used for comparison with a fixed ferrocene concentration of 4 wt.%, a styrene flow rate of 0.0254 $cm^3\ h^{-1}$ and a temperature of 900 °C. As can be seen from Figures 5.3b and c, a significant increase of CNTs is observed by increasing the carbonization time from 0.5 h to 3 h. It is more difficult to grow CNTs using only styrene and ferrocene, compared to the floating catalyst CVD process that has been demonstrated in Chapter 3, in which H_2 is also used to maintain the reduction atmosphere. This approach requires longer carbonization times to decompose ferrocene into Fe nanoparticles than for the floating catalyst method. The absence of CNTs when using shorter carbonization times also suggests that the decomposition process of ferrocene needs to continuously absorb thermal energy.

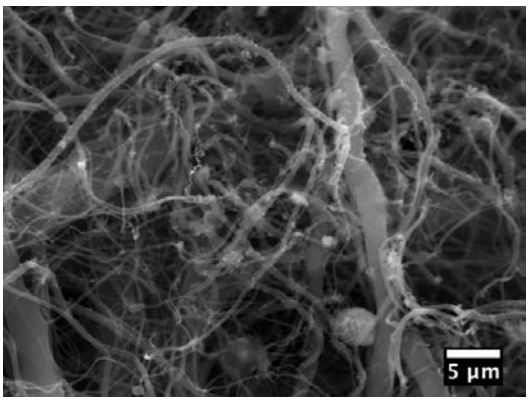

(a)

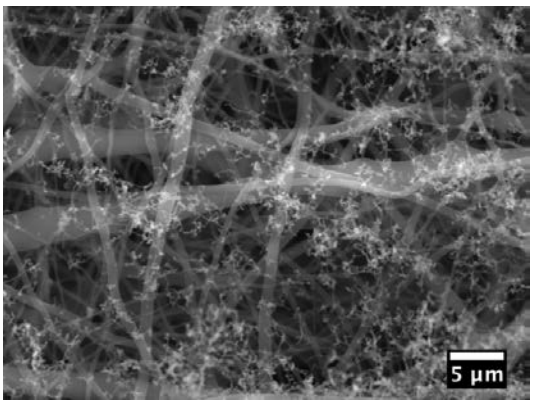

(b)

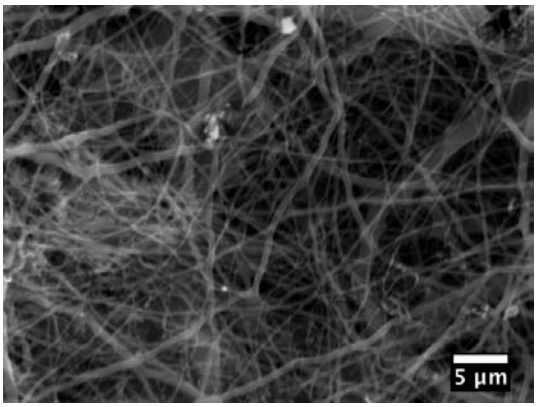

(c)

Figure 5.3 Typical SEM images of (a) the CNF/CNTs produced by 2 wt.% ferrocene and a styrene flow rate of 0.0254 cm^3 h^{-1} for 3 h; (b) the CNF/CNTs produced by 4 wt.% ferrocene and a styrene flow rate of 0.0254 cm^3 h^{-1} for 3 h; (c) CNFs produced by 4 wt.% ferrocene and a styrene flow rate of 0.0254 cm^3 h^{-1} for 0.5 h.

5.4.3 Raman spectroscopy of CA/ferrocene and regenerated cellulose/ferrocene

Raman spectra from CA/ferrocene, regenerated cellulose/ferrocene, and the fibres after CVD treatment have been obtained. The Raman spectra obtained from CA/ferrocene fibres exhibit an intense band located at ~1112 cm^{-1}, shown in Figure 5.4. This band corresponds to the breathing mode of the

cyclopentadienyl ring (Kocsis, Kaptas, Botos, Pekker, & Kamaras, 2011). This band is one of the characteristic features within the Raman spectra of ferrocene. After deacetylation, an intense band appears at ~1095 cm^{-1}, which is attributed to the C-O ring and glycosidic stretching modes (Deng, Young, Kinloch, Zhu, *et al.*, 2013). The presence of this band indicates the formation of cellulose after deacytalation. As this band, characteristic of cellulose, is so close to the ferrocene band located at ~1106 cm^{-1}, it is impossible to conclude if there is any residual ferrocene present in the regenerated cellulose/ferrocene fibres.

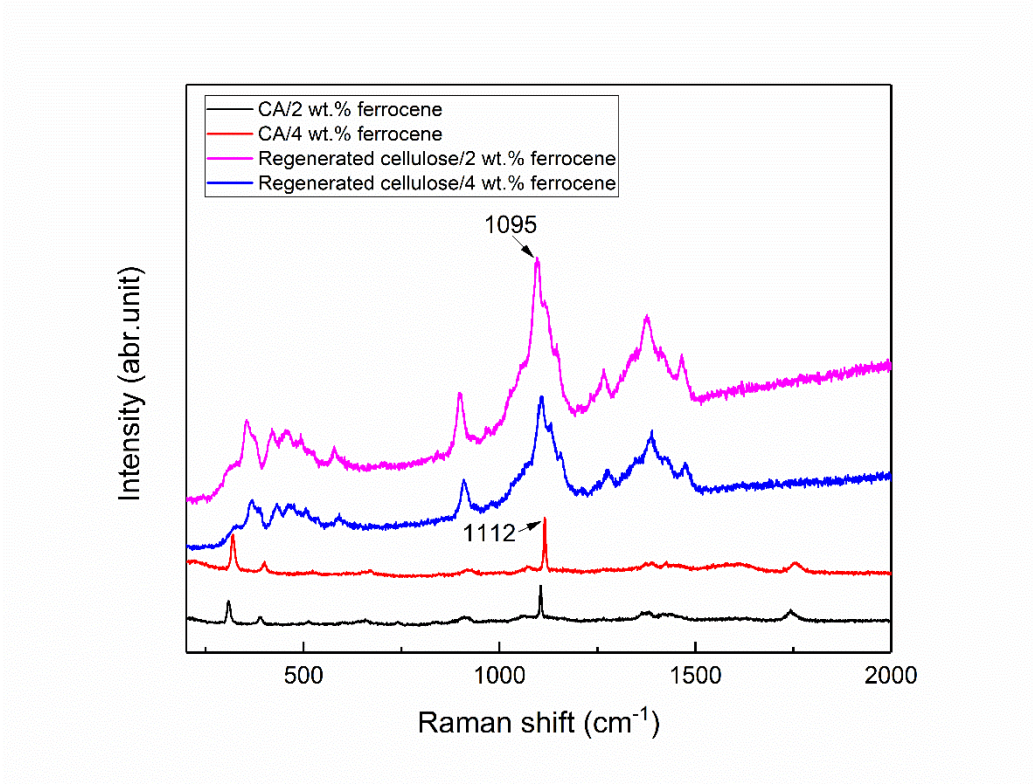

Figure 5.4 Typical Raman spectra for CA/2 wt.% ferrocene, CA/4 wt.% ferrocene, regenerated cellulose/2 wt.% ferrocene, and regenerated cellulose/4 wt.% ferrocene.

5.4.4 TGA analysis of regenerated cellulose/ferrocene

TGA was performed by heating the regenerated cellulose/2 wt.% ferrocene and regenerated cellulose/4 wt.% ferrocene samples from room temperature to 800 °C. The remaining weight percentages from regenerated cellulose with 2 wt.% ferrocene and 4 wt.% ferrocene was 0.8 wt.% and 1.4 wt.%, respectively. The final product after the heating process is thought to be Fe_2O_3. Thus, the weight percent of ferrocene is deduced to be 1.9 wt.% and 3.3 wt.% in the regenerated cellulose/2 wt.% ferrocene and regenerated cellulose/4 wt.% ferrocene samples, respectively. This indicates that the presence of ferrocene is reduced during the deacetylation process. It is thought that during this process, a small amount of ferrocene is physically removed by the water during rinsing.

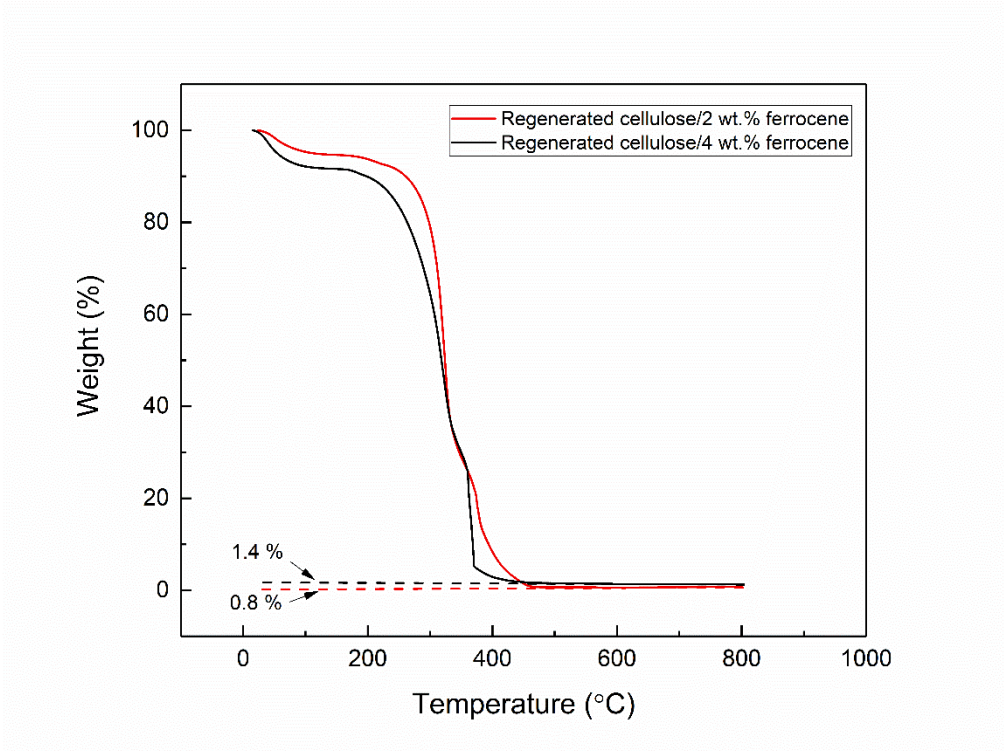

Figure 5.5 TGA of regenerated cellulose with 2 wt.% and 4 wt.% ferrocene.

5.4.5 Structural feature of CNF/CNTs characterised by Raman spectroscopy.

The structural evolution after carbonization and CVD processing of the regenerated cellulose/ferrocene samples was also characterised using Raman spectroscopy, as shown in Figure 5.6. Two obvious bands were observed to be located at ~1350 cm^{-1} and ~1590 cm^{-1}, which correspond to the D band and G bands, respectively. Two bands located at ~482 cm^{-1} and ~583 cm^{-1} are related to an α-Fe_2O_3 structure (Cheng *et al.*, 2015). The α-Fe_2O_3 structure is formed by the oxidation of Fe nanoparticles in air. There is a band that is located at ~1104 cm^{-1} corresponding to ferrocene. These ferrocenes are believed to be inside the CNFs and do not decompose completely during the carbonization and CVD processes. It is noted that the band located at ~2337 cm^{-1} is related to the Raman mode of the N_2 gas present in the air surrounding the sample (Pimenta *et al.*, 2007; Zappielo *et al.*, 2016). The intensity ratio of D and G bands (I_D/I_G) increases from 0.97 ± 0.04 to 1.04 ± 0.03 when increasing the ferrocene content from 2 wt.% to 4 wt.%. The I_D/I_G is in the L_a < 2 nm region for the CF900/CNTs/2 wt.% ferrocene and CF900/CNTs/4 wt.% ferrocene. The relationship between I_D/I_G and L_a, therefore, obtained for L_a < 2 nm is

$$I_D/I_G = 0.0062\, L_a^2 \qquad (5.1)$$

Thus, the value of L_a for the CF900/CNTs/4 wt.% ferrocene is greater than that for the CF900/CNTs/2 wt.% ferrocene sample In theory, a carbon fibre with a higher crystalline planar size L_a exhibits an improved graphitization degree and increased grain size, which results in stronger sp^2 carbon bonds and in turn improved mechanical properties and electrical resistivity (Pimenta *et al.*, 2007).

As can be seen from Table 5.1, the full width at half maximum (FWHM) of both the D and G bands for the CF900/CNTs sample with 2 wt.% ferrocene is larger than that of CF900/CNTs with 4 wt.% ferrocene. According to Ferrari (2007), a narrowing band width reflects lower disorder, which indicates that a higher ferrocene content leads to a higher crystalline structure of the CF900/CNTs.

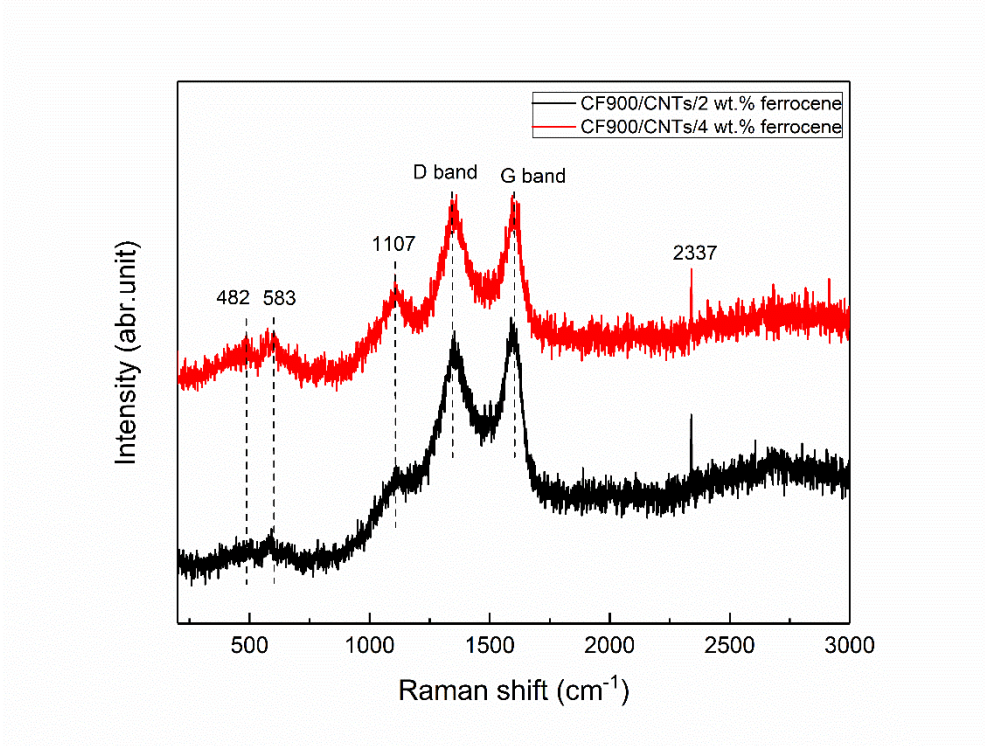

Figure 5.6 Typical Raman spectra for the CF900/CNTs sample with 2 wt.% and 4 wt.% ferrocene.

Table 5.1 Raman band position, I_D/I_G, and FWHM for the CF900/CNTs sample with 2 wt.% and 4 wt.% ferrocene.

		FWHM (cm^{-1})	
Sample	I_D/I_G	D-band	G-band
CF900/CNTs/2 wt.% ferrocene	0.97 ± 0.04	200.1 ± 9.3	139.7 ± 6.4
CF900/CNTs/4 wt.% ferrocene	1.04 ± 0.03	150.1 ± 2.9	95.0 ± 2.3

The stress transfer properties of the CF900/CNTs samples with 2 wt.% and 4 wt.% ferrocene were also assessed by an in situ Raman spectroscopic study. The deformation of CNF/CNTs/2 wt.% ferrocene/polymer and CNF/CNTs/4 wt.% ferrocene/polymer composites was performed in 4-point bending. It can be seen from Figure 5.7 that there is no clear shift in the data, suggesting that there is little stress-transfer taking place. From these data it is assumed that, the crystallinity of the CF900/CNTs is not that well developed, and that because the CNT yield is low using this method, little stress-transfer takes place.

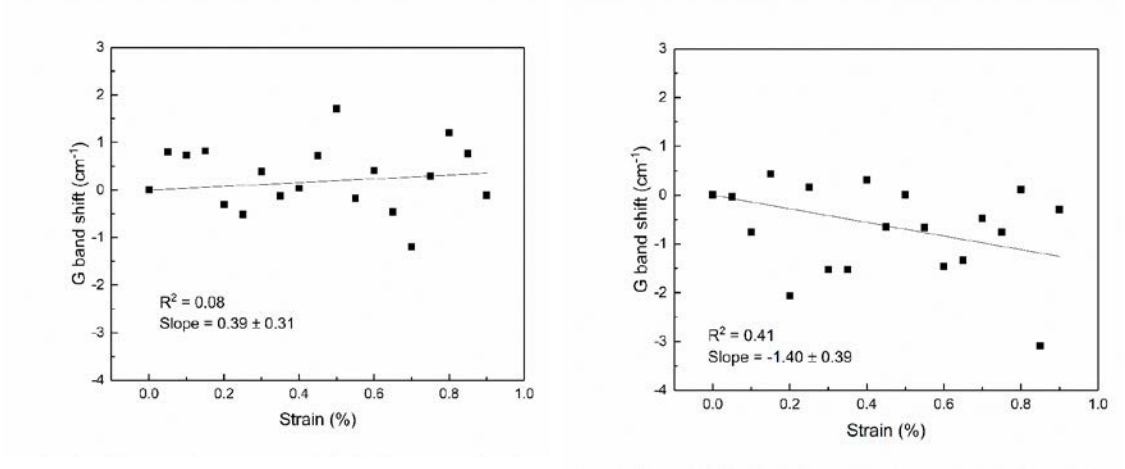

(a) (b)

Figure 5.7 Typical Raman shifts of the position of the G band versus strain for (a) CF900/CNTs/ 2 wt.% ferrocene and (b) CF900/CNTs/4 wt.% ferrocene.

5.5 Conclusions

This Chapter described the production of CF900/CNTs samples by direct incorporation of ferrocene as a catalyst precursor into an electrospun fibre. The morphology of the electrospun fibres and CF900/CNTs were characterised by SEM. The size distribution of CA fibres was compared with different electrospinning voltages and ferrocene contents. It is found that there is no

obvious change in the morphology and distribution between 2 wt.% and 4 wt.% ferrocene. Raman spectroscopy indicated an improved crystallinity of the CF900/CNTs sample with a 4 wt.% ferrocene content compared to a 2 wt.% content. Due to the low CNT yield using this method, no linear fitting was obtained in the in situ Raman spectroscopic study of the deformation of the CNF/CNT composites.

5.6 References

Agarwal, B. D., Broutman, L. J., & Chandrashekhara, K. (2017). *Analysis and performance of fiber composites*: John Wiley & Sons.

Barreiro, A., Hampel, S., Rummeli, M. H., Kramberger, C., Gruneis, A., Biedermann, K., . . . Pichler, T. (2006). Thermal decomposition of ferrocene as a method for production of single-walled carbon nanotubes without additional carbon sources. *J Phys Chem B, 110*(42), 20973-20977. doi:10.1021/jp0636571

Bhardwaj, N., & Kundu, S. C. (2010). Electrospinning: a fascinating fiber fabrication technique. *Biotechnol Adv, 28*(3), 325-347. doi:10.1016/j.biotechadv.2010.01.004

Cheng, X., Gui, X., Lin, Z., Zheng, Y., Liu, M., Zhan, R., . . . Tang, Z. (2015). Three-dimensional α-Fe2O3/carbon nanotube sponges as flexible supercapacitor electrodes. *Journal of Materials Chemistry A, 3*(42), 20927-20934. doi:10.1039/C5TA03635F

Chuilin, L., Qiaohui, G., Xiang-Fa, W., Darrell, H. R., & Haoqing, H. (2008). Growth of carbon nanostructures on carbonized electrospun nanofibers with palladium nanoparticles. *Nanotechnology, 19*(19), 195303. doi:10.1088/0957-4484/19/19/195303

Deng, L. B., Young, R. J., Kinloch, I. A., Zhu, Y. Q., & Eichhorn, S. J. (2013). Carbon nanofibres produced from electrospun cellulose nanofibres. *Carbon, 58*, 66-75. doi:10.1016/j.carbon.2013.02.032

Ferrari, A. C. (2007). Raman spectroscopy of graphene and graphite: Disorder, electron-phonon coupling, doping and nonadiabatic effects. *Solid State Communications, 143*(1-2), 47-57. doi:10.1016/j.ssc.2007.03.052

Hou, H. Q., & Reneker, D. H. (2004). Carbon nanotubes on carbon nanofibers: A novel structure based on electrospun polymer nanofibers. *Advanced Materials, 16*(1), 69-+. doi:10.1002/adma.200306205

Kocsis, D., Kaptas, D., Botos, A., Pekker, A., & Kamaras, K. (2011). Ferrocene encapsulation in carbon nanotubes: Various methods of filling and investigation. *Physica Status Solidi B-Basic Solid State Physics, 248*(11), 2512-2515. doi:10.1002/pssb.201100160

Kunadian, I., Andrews, R., Qian, D. L., & Menguc, M. P. (2009). Growth kinetics of MWCNTs synthesized by a continuous-feed CVD method. *Carbon, 47*(2), 384-395. doi:10.1016/j.carbon.2008.10.022

Leonhardt, A., Hampel, S., Muller, C., Monch, I., Koseva, R., Ritschel, M., . . . Buchner, B. (2006). Synthesis, properties, and applications of ferromagnetic-filled carbon nanotubes. *Chemical Vapor Deposition, 12*(6), 380-387. doi:10.1002/cvde.200506441

Pimenta, M. A., Dresselhaus, G., Dresselhaus, M. S., Cancado, L. G., Jorio, A., & Saito, R. (2007). Studying disorder in graphite-based systems by Raman spectroscopy. *Phys Chem Chem Phys, 9*(11), 1276-1291. doi:10.1039/b613962k

Sharma, S. P., & Lakkad, S. C. (2011). Effect of CNTs growth on carbon fibers on the tensile strength of CNTs grown carbon fiber-reinforced polymer

matrix composites. *Composites Part a-Applied Science and Manufacturing, 42*(1), 8-15. doi:10.1016/j.compositesa.2010.09.008

Thostenson, E. T., Li, W. Z., Wang, D. Z., Ren, Z. F., & Chou, T. W. (2002). Carbon nanotube/carbon fiber hybrid multiscale composites. *Journal of Applied Physics, 91*(9), 6034-6037. doi:10.1063/1.1466880

Zappielo, C. D., Nanicuacua, D. M., dos Santos, W. N. L., da Silva, D. L. F., Dall'Antonia, L. H., de Oliveira, F. M., . . . Tarley, C. R. T. (2016). Solid Phase Extraction to On-Line Preconcentrate Trace Cadmium Using Chemically Modified Nano-Carbon Black with 3-Mercaptopropyltrimethoxysilane. *Journal of the Brazilian Chemical Society, 27*(10), 1715-1726. doi:10.5935/0103-5053.20160052

Zhang, Q. H., Liu, J. W., Sager, R., Dai, L. M., & Baur, J. (2009). Hierarchical composites of carbon nanotubes on carbon fiber: influence of growth condition on fiber tensile properties. *Composites Science and Technology, 69*(5), 594-601. doi:10.1016/j.compscitech.2008.12.002

Chapter 6 Structural Supercapacitors Using a Solid Resin Electrolyte with Carbonized Electrospun Cellulose/Carbon Nanotube Electrodes

6.1 Introduction

Supercapacitors are energy storage devices that have high power densities and long lifetimes compared with batteries (Gonzalez *et al.*, 2016). Charge storage in supercapacitors takes advantage of the electrostatic field that forms at the electrolyte/electrode interface (Salanne *et al.*, 2016). Novel strategies to fabricate so-called multifunctional structural supercapacitors have been of interest in recent years (Deka *et al.*, 2017). Structural supercapacitors generally make use of an electrode, a solid electrolyte and a separator that simultaneously resist mechanical stresses and store electrochemical energy (Deka *et al.*, 2017). Among the materials used for electrodes in structural supercapacitors, carbon fibres are one of the best candidates, since they combine both conductive and high mechanical properties (stiffness, strength) for reinforcing matrix electrolytes (Qian, Diao*, et al.*, 2013).

Recently, electrospinning has been applied to prepare nanofibres for electrocapacitive applications (Zhang *et al.*, 2016). This approach can be used to spin precursor materials, which when thermally treated can be converted to carbon nanofibre (CNF)-based electrodes (Deng, Young, Kinloch, Zhu*, et al.*, 2013). These electrodes can be used for supercapacitors, due to their high surface area to volume ratios, desirable porosity, and excellent mechanical properties (Deng, Young, Kinloch, Abdelkader*, et al.*, 2013). We have recently

shown that carbon nanotubes (CNTs) can be grown on the surface of carbon fibres, produced by an electrospinning method, improving the electrocapacitive performance (Li *et al.*, 2017). Growing CNTs on the surface of the carbon fibres could also be an effective approach to enhance the interfacial strength of a structural supercapacitor, as has been shown to be the case with traditional composite materials (Jin, Young, & Eichhorn, 2014a, 2014b).

Stress transfer ability between carbon fibres and matrix is one of the most important interfacial properties in composites. An interface with high stress transfer efficiency allows a great amount of applied stress to be transferred to the reinforcing phase. The stress transfer depends on the interfacial shear stress between the fibre and the matrix (Schadler *et al.*, 1998). Qian *et al.* have evaluated the in-plane shear properties of carbon aerogel modified carbon fibre fabric-based structural supercapacitors using the ASTM standard D3518 (Qian, Kucernak*, et al.*, 2013). Over the years Raman spectroscopy has been successfully applied to evaluate mechanical properties of carbon materials by the observation of the shift in the position of characteristic bands when the materials are deformed (Papageorgiou *et al.*, 2017). This technique was initially developed by Young and co-workers for the deformation of carbon fibres (Huang & Young, 1995). Since then, it has been applied to investigate the mechanical properties of other carbon materials such as CNTs (Prabhakaran *et al.*, 2007) and graphene (Mohiuddin, Lombardo, Nair, Bonetti, Savini, Jalil, Bonini, Basko, Galiotis, Marzari*, et al.*, 2009). The Raman shift arises from the change of vibrational frequencies of the normal modes when deformation is applied (Schadler *et al.*, 1998). It is believed that higher stress transfer from the matrix to the carbon fibres results in a larger Raman band shift (Xu *et al.*, 2012). Raman spectroscopy also

has been reported as a technique to estimate the mechanical stiffness of CNFs produced from electrospun precursors (Deng, Young, Kinloch, Zhu*, et al.*, 2013).

In the present study, a structural supercapacitor is produced by a hierarchical construction of CNFs. These CNFs are decorated with CNTs for use as electrode materials. These electrodes are combined with poly(ethylene glycol) diglycidyl ether (PEGDGE), which acts as both a solid polymer electrolyte and a matrix material. Raman spectroscopy is used to assess the mechanical properties of these fibres, and their appropriateness for a structural supercapacitor.

6.2 Experimental methods

6.2.1 Production of structural supercapacitors

Electrodes were prepared by carbonization of electrospun de-acetylated cellulose acetate fibres at a temperature of 900 °C, followed by CVD to generate CNTs, and finally a KOH activation of their surface. A full description of the production of these fibres from the cellulose acetate precursor is contained within a previous publication (Li *et al.*, 2017). Plain carbon fibres and CNTs decorated filaments are subsequently denoted as CF900 and CF900/CNTs, respectively. Carbon fibres produced at temperatures of 1500 °C and 2000 °C are denoted as CF1500 and CF2000, and their respective CNTs decorated samples as CF1500/CNTs and CF2000/CNTs.

1-ethyl-3-methylimidazolium bis(trifluoromethylsulfonyl) imide (EMITFSI, purity ⩾98%), PEGDGE (Mn ~ 500), and Triethylenetetramine (TETA) were purchased from Sigma-Aldrich (Dorset, UK). Solid electrolyte was prepared by mixing 10 wt.% EMITFSI as an ionic liquid in an 82.6 wt.% PEGDGE-based epoxy resin, followed

by magnetic stirring for 5 min. TETA at 7.4 wt.% was used as a hardener, and added to the mixed PEGDGE/EMITFSI solution, followed by manually stirring for 12 min until a homogeneous solution was obtained. The mixed PEGDGE/EMITFSI/TETA solution of 0.25 ml was then deposited onto a 13 × 13 mm^2 Whatman glass fibre separator. Activated CF900 or CF900/CNTs fibrous networks were weighed (to 2.2 mg), and then deposited on each side of the separator. Two copper tape current collectors were cut into 45 mm × 10 mm × 0.3 mm shapes and firmly attached on both sides of the electrode layers. The supercapacitors were then placed into an oven at 80 °C for curing. The curing durations were 2 h and 24 h for comparison, during which the supercapacitors were pressed under a load of 10 kg to fasten them. A schematic of a structural supercapacitor produced using this method is shown in Figure 6.1.

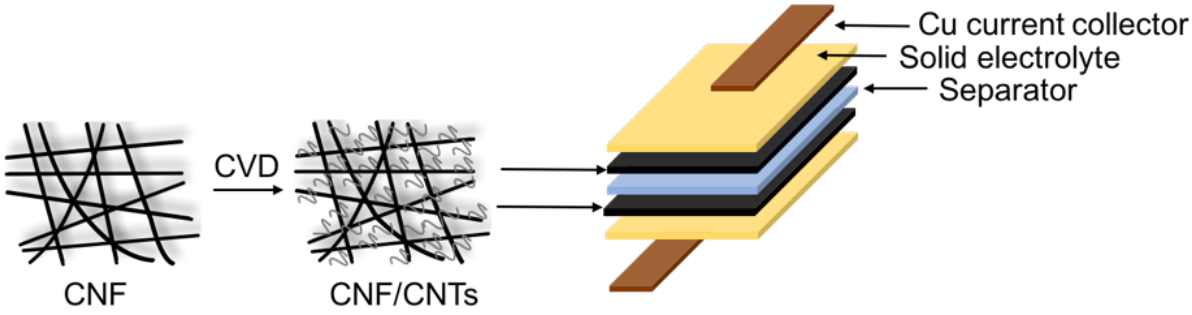

Figure 6.1 Schematic of a structural supercapacitor based on CNF/CNTs electrodes, a glass fibre separator and a solid electrolyte.

6.2.2 Preparation of in situ deformation samples

For in situ Raman spectroscopy studies, a 5 mm × 5 mm square sample of the CF900 or CF900/CNTs material was placed centrally on a 70 mm × 22 mm × 1.5 mm PMMA beam. Two drops (0.25 mL) of the PEGDGE/EMITFSI/TETA resin were deposited on top of the samples. The PMMA beam with this resin was heat

cured in an oven at 80 °C for 2 h and 24 h. The samples were then removed from the oven and cooled in air.

CF1500, CF1500/CNTs, CF2000 and CF2000/CNTs samples were fabricated for mechanical properties characterisation. Instead of making structural supercapacitors using the solid electrolyte, PMMA/CNF/PMMA or PMMA/CNF/CNTs/PMMA composites were prepared for in situ Raman spectroscopy/bending tests. CF1500, CF1500/CNTs, CF2000 or CF2000/CNTs samples were placed centrally on PMMA beams. Two drops (0.25 mL) of 0.1 g ml^{-1} PMMA/acetone solution were then deposited over this sample and dried at room temperature for 1 h.

6.3 Characterisation of materials

A scanning electron microscope (SEM) (HITACHI S3200N SEM-EDS) with a voltage of 20 kV was used to observe the morphologies of the CNFs and the CNF/CNTs. The specific surface area was calculated by the Brunauer-Emmett-Teller (BET) method using a *Micromeritics ASAP 2020 device*. The micropore volume (V_{micro}) and micropore area (S_{micro}) were obtained by using the t-plot method, while the mesopore volume (V_{meso}) and mesopore area (S_{meso}) were estimated by the Barrett-Joyner-Halenda (BJH) method. The total pore volume (V_{tot}) was measured by the nitrogen adsorption volume at the highest relative pressure. Pore size distribution was determined by the Non-local Density Functional Theory (NLDFT).

Galvanostatic charge and discharge (GCD) curves were obtained at a current density of 38 μA cm^{-2} after 2 h of curing. Electrochemical impedance spectra (EIS)

were obtained at a constant perturbation amplitude of 5 mV within a frequency range 0.01 Hz to 10^6 Hz after both 2 h and 24 h of curing.

A Renishaw RM1000 Raman spectrometer coupled to an Ar laser (λ = 532 nm), and a Leica CC detector, recorded spectra from the samples during in situ deformation of the samples. The laser spot size was ~1 - 2 μm, and the focused power was ~1 mW when using a 50× objective lens. Exposure times to collect spectra between strain increments were 30 s. A strain gauge (type CEA-06-240UZ-120, Vishay Micro-Measurements) was attached to the surface of the PMMA beam using cyanoacrylate adhesive. Two wires were soldered to each copper tab of the strain gauge, which were connected to a transducer. A four-point bending rig was used to deform the samples in tension. Raman spectra were recorded in 0.05% strain intervals up to 0.9% strain.

6.4 Results and discussion

6.4.1 Morphology and Porosity Characterisation of CNFs and CNF/CNTs

Figure 6.2a and b show the morphologies of CF900 and CF900/CNTs, respectively. CNTs were observed at the circumferential surfaces of CF900. No other carbon impurities were observed after CVD, in agreement with a previous study (Andrews *et al.*, 2002). The absorption-desorption isotherms for these materials, and their respective surface areas have been previously reported; surface area was found to grow from 712 m^2 g^{-1} to 1211 m^2 g^{-1} after growth of CNTs on CNFs (Li *et al.*, 2017).

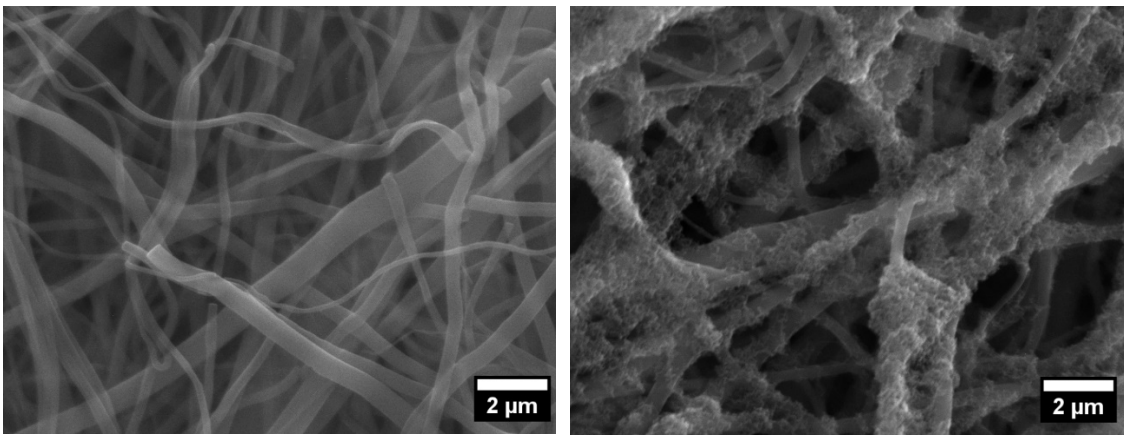

(a) (b)

Figure 6.2 Typical SEM images of (a) CNFs and (b) CNF/CNTs samples.

6.4.2 Galvanostatic charge and discharge tests

GCD curves for the CF900 and CF900/CNTs electrodes at a current density of 19 µA cm^{-2} after curing for 2 h are reported in Figure 6.3. The specific capacitances of CF900 and CF900/CNTs electrodes are calculated to be 0.23 ± 0.01 mF cm^{-2} (175 ± 4 mF g^{-1} or 29 ± 1 mF cm^{-3}) and 0.84 ± 0.01 mF cm^{-2} (643 ± 10 mF g^{-1} or 105 ± 2 mF cm^{-3}), respectively. The values of the capacitance are higher than the multiwall CNTs impregnated carbon fibre-based electrodes (125 mF g^{-1}) reported in a recent study (Hudak *et al.*, 2017) and higher compared with the specific capacitance (52 mF g^{-1}) for activated carbon fibre electrodes (Shirshova *et al.*, 2013). The large IR drop (a rapid voltage change at the initial stage of the *discharge)* for both GCD curves indicates that there is large equivalent series resistance (R_S) in the capacitors.

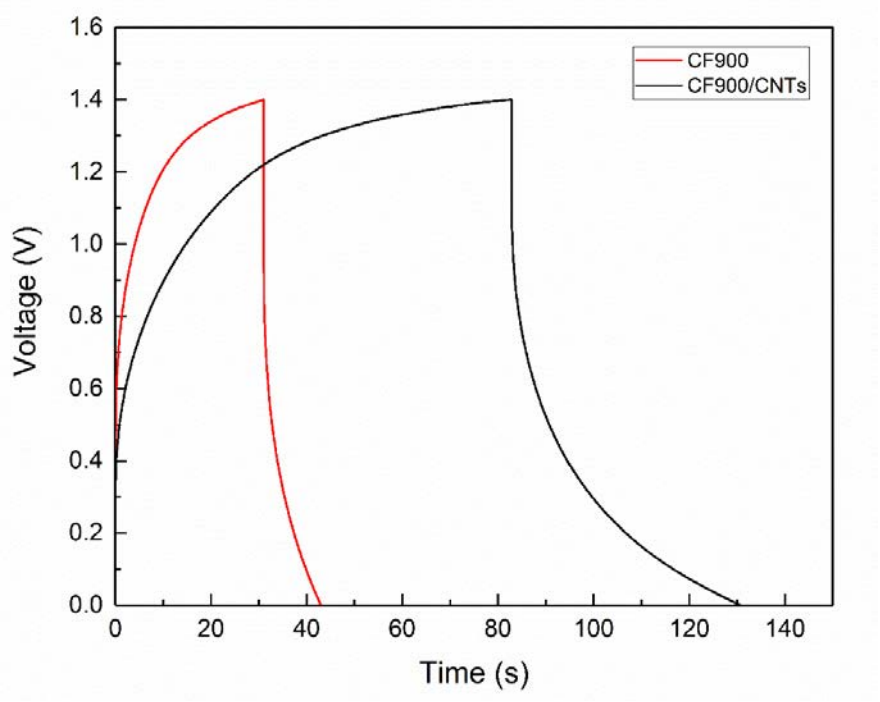

Figure 6.3 GCD curves for CF900 and CF900/CNTs after curing 2 h.

6.4.3 EIS testing of the supercapacitor electrodes

EIS measurements were performed to evaluate the resistive properties of the capacitors, as shown in Figure 6.4. The EIS data between 1 Hz to 10^6 Hz were fitted using Zview software based on an equivalent circuit model (inset of Figure 6.4). The equivalent series resistance (R_S) was then obtained as the intercept of the real axis within the high-frequency region of the Nyquist plot. The R_S value is the total resistance of the electrode, electrolyte, and the current collector. As can be seen from Table 6.1, the R_S value for the CF900 electrode (535 ± 27 Ω) is higher compared to CF900/CNTs (470 ± 21 Ω) after a curing time of 24 h. A higher R_S value is also observed for CF900 after a curing time of 2 h. This indicates that the growth of CNTs increases the electron transport properties of the electrodes. Other than the gel electrolyte itself, this gives rise to a relatively large R_S for all structural capacitors; the use of copper collectors may also be a source of

resistance. However, the values of R_s and R_{ct} are significantly lower than reported in recent work in which the structural supercapacitors were made by the same PEGDGE electrolyte/10 wt.% EMITFSI with monolithic carbon aerogel modified carbon fabric electrodes (Qian, Kucernak*, et al.*, 2013). This shows the CF900 and CF900/CNTs electrodes are competitive in terms of their capacitive performance.

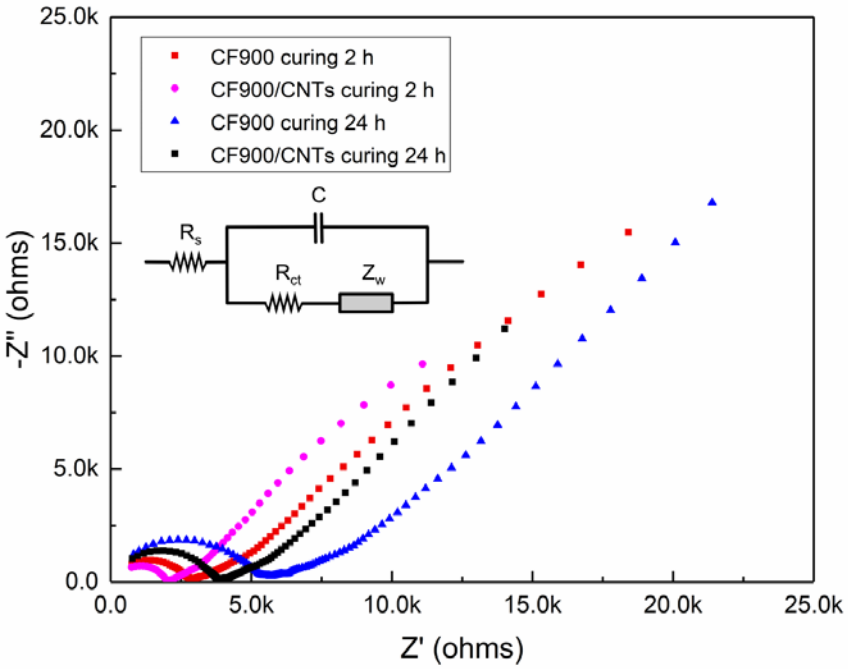

Figure 6.4 Typical EIS curves for CF900 and CF900/CNTs electrodes after curing for 2 h and 24 h. The inset is the equivalent electrical circuit model.

Table 6.1 The values of R_s and R_{ct} for CF900 and CF900/CNTs after curing for 2 h and 24 h.

	R_s (2h) Ω	R_{ct} (2h) Ω	R_s (24h) Ω	R_{ct} (24) Ω
CF900	482 ± 19	2014 ± 24	535 ± 27	3502 ± 100
CF900/CNTs	451 ± 13	1471 ± 13	470 ± 21	2909 ± 33

The middle to the high-frequency region of the Nyquist plot, in which the R_{ct} value is obtained from the diameter of the semicircle, illustrates the charge transfer resistance that occurs at the interface between the electrode and electrolyte. The R_{ct} value results from the movement of charge complexes close to the Helmholtz plane (Hung *et al.*, 2009). As shown in Table 6.1, smaller semicircles are observed for CF900/CNTs electrodes after both curing times of 2 h and 24 h. This demonstrates that these electrodes have lower interfacial resistance, with better charge transfer behavior than the CF900 electrodes. In addition, the R_{ct} values for both CF900 and CF900/CNTs electrodes increase after 24 h of curing in comparison to 2 h. This indicates that enhanced curing leads to a reduced charge transfer behavior. This is thought to be because as the electrolyte becomes more solid, it hinders the charge mobility at the interface between the electrolyte and the electrodes.

The 45° region in the Nyquist plot is known as the Warburg region; the slope of this portion of the curve is called the Warburg resistance (Z_w) and is a result of the frequency dependence of ion diffusion/transport in the electrolyte (Li *et al.*, 2015). In addition, the behaviour of the diffusion of ions in the electrolyte can be characterised by the slope of a regression to the linear region at low-frequency; up to 0.01 Hz in the present work. Normally the vertical line represents the formation of an ideal capacitor. However, the straight lines of all the electrodes have a slope of approximately 45°, showing what could be both kinetic and diffusion-controlled behaviour. Moreover, there is no obvious change in the slope for both CF900 and CF900/CNTs samples (for both the 2 h and 24 h curing times), indicating the growth of CNTs does not significantly affect the diffusion of the ions.

6.4.4 Structural features of the electrodes characterised by Raman spectroscopy

Typical Raman spectra obtained from all samples are presented in Figure 6.5. These spectra were fitted using two Lorentzian curves to determine the position of the G band, and the intensities of the D and G bands. The intensity ratio of the D and G band (I_D/I_G) with carbonization temperature is reported in Figure 6.6. These data show that the I_D/I_G ratio is in the order of CF900 < CF1500 < CF2000.

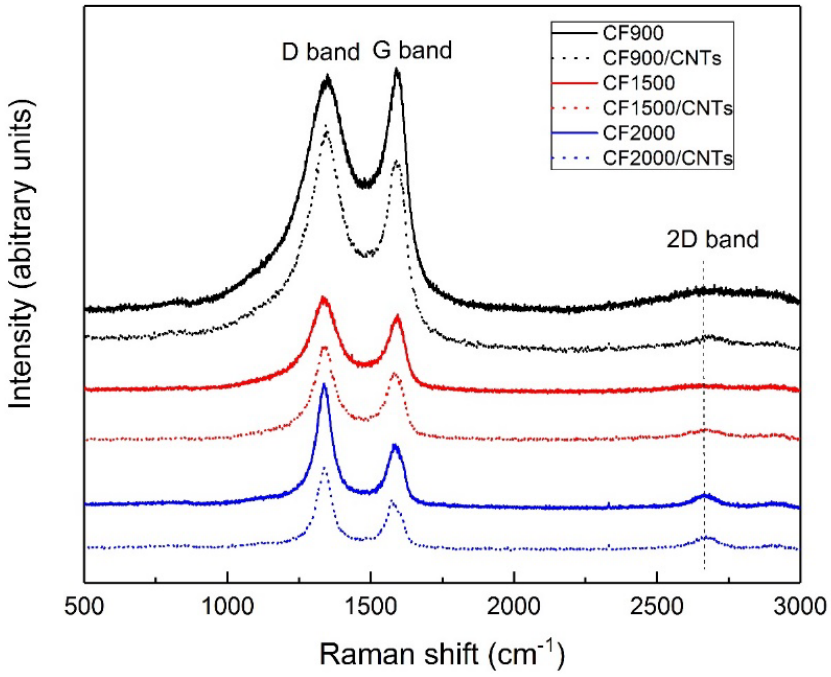

Figure 6.5 Typical Raman spectra for CF900, CF900/CNTs, CF1500, CF1500/CNTs, CF2000 and CF2000/CNTs samples.

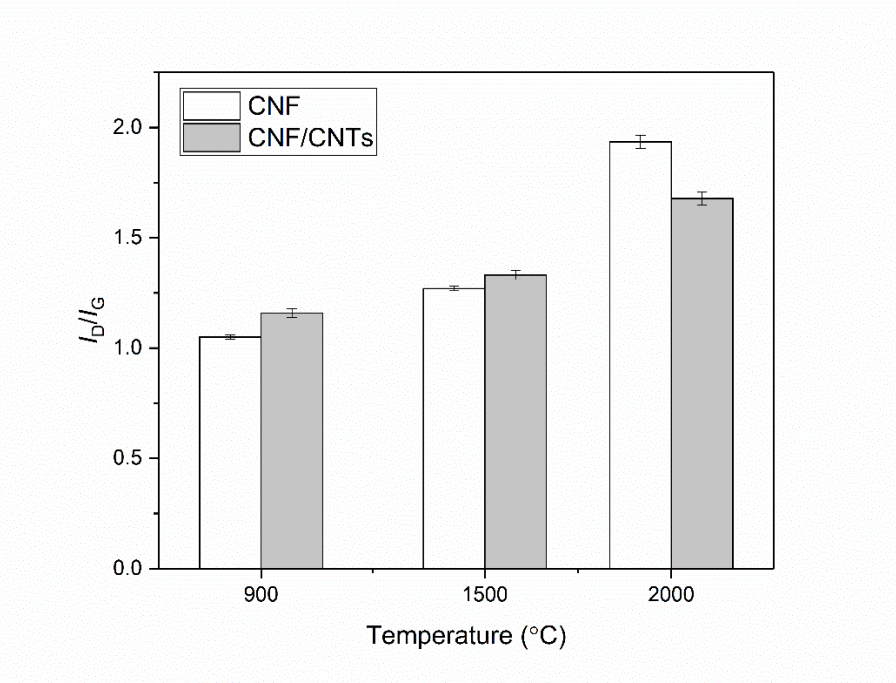

Figure 6.6 Intensity ratio of D band and G band, I_D/I_G, for CNFs and CNF/CNTs. Error bars represent standard errors obtained from Lorentz fittings in Origin software.

From previous work by Kong *et al.* (2012), graphitization cannot be achieved at temperatures below ~1600 °C, therefore the crystallite size is not expected to be as large as for a fully graphitized structure (L_a > 2 nm) for the CF900 and CF1500 samples. The relationship between I_D/I_G and L_a, therefore, obtained for L_a < 2 nm is (Ferrari & Robertson, 2000; Li *et al.*, 2017; Matthews *et al.*, 1999)

$$I_D/I_G = 0.0062\, L_a^2 \qquad (6.1)$$

In contrast, the crystallite size of CF2000 is thought to be larger than 2 nm. The evolution of disorder is typically quantified using the Tuinstra–Koenig equation (Tuinstra & Koenig, 1970) described by the equation

$$I_D/I_G = 49.5\,\text{Å}/L_a \qquad (6.2)$$

Therefore, the L_a values for the CF900, CF1500, and CF2000 electrodes are found to be 1.3 ± 0.01 nm, 1.43 ± 0.01nm and 2.56 ± 0.04 nm, respectively. In theory, a carbon fibre with a higher lateral crystal size L_a indicates a high degree of graphitization, and thereby an increased grain size results in stronger sp^2 carbon bonds which in turn improves mechanical properties and electrical resistivity (Pimenta *et al.*, 2007). The I_D/I_G value, however, decreases from 1.94 ± 0.03 to 1.68 ± 0.03 for CF2000 with the growth of CNTs, in accordance with an increase in the L_a value from 2.56 ± 0.04 nm to 2.95 ± 0.05 nm according to Equation 6.2. This increase indicates an improved degree of graphitization after the growth of CNTs on the CF2000 sample. Moreover, a 2D Raman band is noted at ~2700 cm^{-1} for the spectrum obtained from the CF900/CNTs, CF1500/CNTs, CF2000, and CF2000/CNTs samples. This band is absent for the CF900 and CF1500 samples, indicating that the 2D band is derived either from the CNTs on the surfaces of CF900 and CF1500, or also the highly graphitized fibres produced at higher temperatures (>1600 °C). It is noted that the 2D Raman band is also observed for the CF2000 sample, indicating that a graphitized structure is well developed at 2000 °C. The I_{2D}/I_D ratios have been recorded for the CF900/CNTs, CF1500/CNTs, and CF2000/CNTs samples, and found to be 0.053 (0.001), 0.093 (0.002) and 0.149 (0.003) (errors are negligible and quoted in brackets), respectively. The I_{2D}/I_D increases with an increase of the carbonization temperature, suggesting a reduction in structural defects (McKee & Vecchio, 2006). It is also noted that the I_{2D}/I_D ratio increases when the growth of CNTs occurs on the CF2000 sample; from 0.096 (0.002) to 0.149 (0.003) (errors are negligible and quoted in brackets). This suggests that the growth of CNTs increases the crystallinity of the CF2000 sample.

6.4.5 In situ deformation studies

The presence of a shift in the G-band for a deformed composite sample would indicate a stress-transfer taking place between the resin and the fibres. No obvious Raman shifts were observed for CF900, CF900/CNTs, CF1500, and CF1500/CNTs (Figure 6.7a-d). This is due to the fact that the graphitic structures are not well-developed at carbonization temperatures up to 1500 °C (Kong *et al.*, 2012). Beyond these temperatures, it is thought that a more well-developed and graphitized structure is formed, leading to higher mechanical properties of the fibres, and thereby better stress-transfer properties.

Shifts in the position of the G band were however observed for the CF2000 and CF2000/CNTs samples (Figure 6.8), indicating that stress has transferred between the matrix and the fibres. Shift rates with respect to strain ($\mathrm{d}(\Delta\nu)/\mathrm{d}\varepsilon$) of -4.5 and -8.4 cm^{-1} $\%^{-1}$ are found for CF2000 and CF2000/CNTs respectively. Young's modulus of the fibres can be estimated using the equation 2.15. The value of stress sensitivity of the Raman band shift for the G-band emanating from carbon fibres and graphene has been found to be -3.1 cm^{-1}/GPa (Frank *et al.*, 2011) The moduli for CF2000 and CF2000/CNTs are therefore estimated to be ~145 GPa and ~271 GPa respectively. These moduli are comparable to other electrospun cellulose-based carbon fibres (~100 GPa; (Deng, Young, Kinloch, Zhu*, et al.*, 2013)). Given this stress-transfer from the matrix to the fibres, and that they have intrinsically high mechanical stiffness, these materials are thought to be suitable for structural supercapacitors.

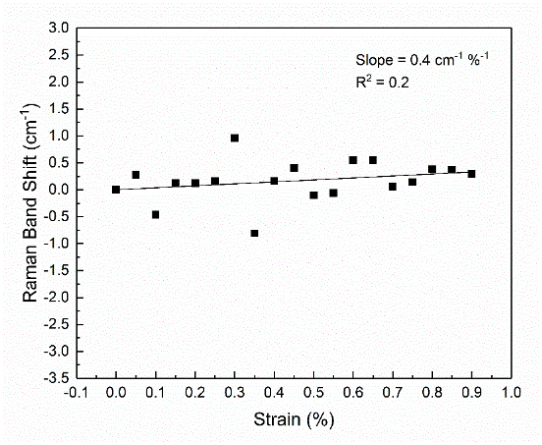

(a)

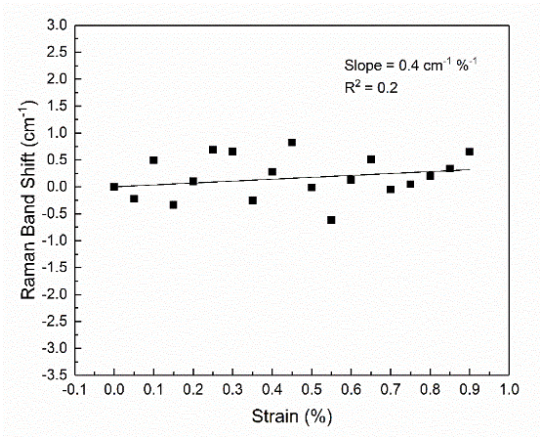

(b)

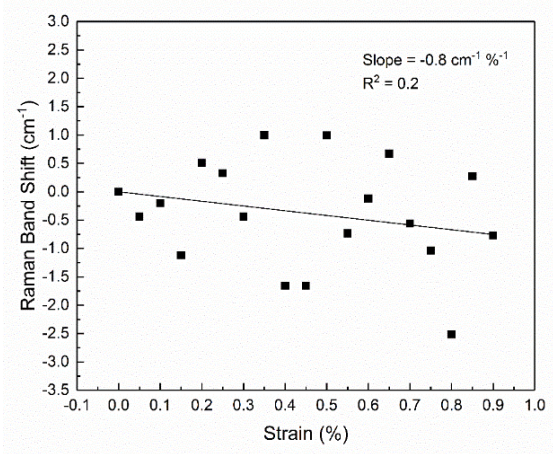

(c)

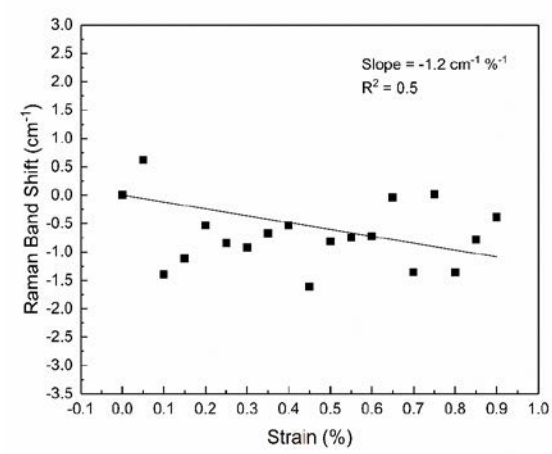

(d)

Figure 6.7 Typical plots of Raman band shift versus strain for (a) CF900, and (b) CF900/CNTs, (c) CF1500, and (d) CF1500/CNTs samples, with linear regressions to the data (black line).

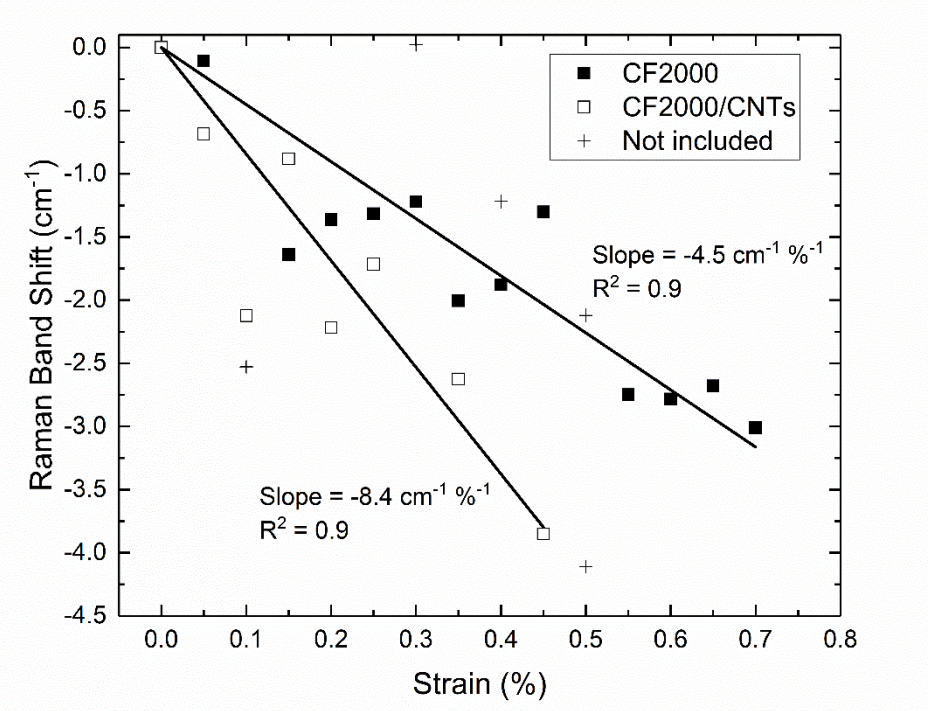

Figure 6.8 Shift in the position of the G-band as a function of strain for CF2000 and CF2000/CNTs samples. + - data not included in the fit.

6.5 Conclusions

Structural supercapacitors have been fabricated by using CNF decorated with CNTs as electrodes. A solid resin (PEGDGE) and an ionic liquid (EMITFSI) electrolyte were used. Capacitive properties of these devices have been measured. CF900/CNTs electrode-based capacitors exhibited a higher capacitive performance than CF900 electrodes (cf. 0.23 ± 0.01 and 0.84 ± 0.01 mF cm^{-2}). There was a decrease in this performance with increased curing time of the resin, from 2 h to 24 h, due to a lack of charge carrier mobility in the latter samples. An in situ Raman spectroscopic study was used to investigate the stress transfer between a resin and the CNFs and CNF/CNTs. Shifts were observed for the CF2000 and CF2000/CNTs samples. These shifts were then used to estimate the moduli of these samples, which were found to be ~145 GPa and ~271 GPa,

respectively. This result indicates that these electrospun cellulose-based CNFs have the potential as electrodes for the fabrication of structural supercapacitors.

6.6 References

Andrews, R., Jacques, D., Qian, D., & Rantell, T. (2002). Multiwall carbon nanotubes: synthesis and application. *Acc Chem Res, 35*(12), 1008-1017. doi:10.1021/ar010151m

Deka, B. K., Hazarika, A., Kim, J., Park, Y. B., & Park, H. W. (2017). Recent development and challenges of multifunctional structural supercapacitors for automotive industries. *International Journal of Energy Research, 41*(10), 1397-1411. doi:10.1002/er.3707

Deng, L., Young, R. J., Kinloch, I. A., Abdelkader, A. M., Holmes, S. M., De Haro-Del Rio, D. A., & Eichhorn, S. J. (2013). Supercapacitance from cellulose and carbon nanotube nanocomposite fibers. *ACS Appl Mater Interfaces, 5*(20), 9983-9990. doi:10.1021/am403622v

Deng, L. B., Young, R. J., Kinloch, I. A., Zhu, Y. Q., & Eichhorn, S. J. (2013). Carbon nanofibres produced from electrospun cellulose nanofibres. *Carbon, 58*, 66-75. doi:10.1016/j.carbon.2013.02.032

Ferrari, A. C., & Robertson, J. (2000). Interpretation of Raman spectra of disordered and amorphous carbon. *Physical Review B, 61*(20), 14095-14107. doi:10.1103/PhysRevB.61.14095

Frank, O., Tsoukleri, G., Riaz, I., Papagelis, K., Parthenios, J., Ferrari, A. C., . . . Galiotis, C. (2011). Development of a universal stress sensor for graphene and carbon fibres. *Nature Communications, 2*. doi:10.1038/ncomms1247

Gonzalez, A., Goikolea, E., Barrena, J. A., & Mysyk, R. (2016). Review on supercapacitors: Technologies and materials. *Renewable & Sustainable Energy Reviews, 58*, 1189-1206. doi:10.1016/j.rser.2015.12.249

Huang, Y., & Young, R. J. (1995). Effect of Fiber Microstructure Upon the Modulus of Pan-and Pitch-Based Carbon-Fibers. *Carbon, 33*(2), 97-107. doi:10.1016/0008-6223(94)00109-D

Hudak, N. S., Schlichting, A. D., & Eisenbeiser, K. (2017). Structural Supercapacitors with Enhanced Performance Using Carbon Nanotubes and Polyaniline. *Journal of the Electrochemical Society, 164*(4), A691-A700. doi:10.1149/2.0721704jes

Hung, K. S., Masarapu, C., Ko, T. H., & Wei, B. Q. (2009). Wide-temperature range operation supercapacitors from nanostructured activated carbon fabric. *Journal of Power Sources, 193*(2), 944-949. doi:10.1016/j.jpowsour.2009.01.083

Jin, S.-Y., Young, R. J., & Eichhorn, S. J. (2014a). Controlling and mapping interfacial stress transfer in fragmented hybrid carbon fibre–carbon nanotube composites. *Composites Science and Technology, 100*, 121-127. doi:10.1016/j.compscitech.2014.05.034

Jin, S.-Y., Young, R. J., & Eichhorn, S. J. (2014b). Hybrid carbon fibre–carbon nanotube composite interfaces. *Composites Science and Technology, 95*, 114-120. doi:10.1016/j.compscitech.2014.02.015

Kong, K., Deng, L. B., Kinloch, I. A., Young, R. J., & Eichhorn, S. J. (2012). Production of carbon fibres from a pyrolysed and graphitised liquid crystalline cellulose fibre precursor. *Journal of Materials Science, 47*(14), 5402-5410. doi:10.1007/s10853-012-6426-y

Li, Q., Deng, L. B., Kim, J. K., Zhu, Y. Q. Q., Holmes, S. M., Perez-Page, M., & Eichhorn, S. J. (2017). Growth of Carbon Nanotubes on Electrospun Cellulose Fibers for High Performance Supercapacitors. *Journal of the Electrochemical Society, 164*(13), A3220-A3228. doi:10.1149/2.1181713jes

Li, Y., Zhang, Q., Zhang, J., Jin, L., Zhao, X., & Xu, T. (2015). A top-down approach for fabricating free-standing bio-carbon supercapacitor electrodes with a hierarchical structure. *Sci Rep, 5*, 14155. doi:10.1038/srep14155

Matthews, M. J., Pimenta, M. A., Dresselhaus, G., Dresselhaus, M. S., & Endo, M. (1999). Origin of dispersive effects of the Raman D band in carbon materials. *Physical Review B, 59*(10), R6585-R6588. doi:10.1103/PhysRevB.59.R6585

McKee, G. S., & Vecchio, K. S. (2006). Thermogravimetric analysis of synthesis variation effects on CVD generated multiwalled carbon nanotubes. *J Phys Chem B, 110*(3), 1179-1186. doi:10.1021/jp054265h

Mohiuddin, T. M. G., Lombardo, A., Nair, R. R., Bonetti, A., Savini, G., Jalil, R., . . . Ferrari, A. C. (2009). Uniaxial strain in graphene by Raman spectroscopy:Gpeak splitting, Grüneisen parameters, and sample orientation. *Physical Review B, 79*(20), 205433. doi:10.1103/PhysRevB.79.205433

Papageorgiou, D. G., Kinloch, I. A., & Young, R. J. (2017). Mechanical properties of graphene and graphene-based nanocomposites. *Progress in Materials Science, 90*, 75-127. doi:10.1016/j.pmatsci.2017.07.004

Pimenta, M. A., Dresselhaus, G., Dresselhaus, M. S., Cancado, L. G., Jorio, A., & Saito, R. (2007). Studying disorder in graphite-based systems by Raman

spectroscopy. *Phys Chem Chem Phys, 9*(11), 1276-1291. doi:10.1039/b613962k

Prabhakaran, K., Stephen, J. E., & Robert, J. Y. (2007). Deformation of isolated single-wall carbon nanotubes in electrospun polymer nanofibres. *Nanotechnology, 18*(23), 235707. doi:10.1088/0957-4484/18/23/235707

Qian, H., Diao, H., Shirshova, N., Greenhalgh, E. S., Steinke, J. G., Shaffer, M. S., & Bismarck, A. (2013). Activation of structural carbon fibres for potential applications in multifunctional structural supercapacitors. *J Colloid Interface Sci, 395*, 241-248. doi:10.1016/j.jcis.2012.12.015

Qian, H., Kucernak, A. R., Greenhalgh, E. S., Bismarck, A., & Shaffer, M. S. (2013). Multifunctional structural supercapacitor composites based on carbon aerogel modified high performance carbon fiber fabric. *ACS Appl Mater Interfaces, 5*(13), 6113-6122. doi:10.1021/am400947j

Salanne, M., Rotenberg, B., Naoi, K., Kaneko, K., Taberna, P. L., Grey, C. P., . . . Simon, P. (2016). Efficient storage mechanisms for building better supercapacitors. *Nature Energy, 1*, 16070. doi:10.1038/Nenergy.2016.70

Schadler, L. S., Giannaris, S. C., & Ajayan, P. M. (1998). Load transfer in carbon nanotube epoxy composites. *Applied Physics Letters, 73*(26), 3842-3844. doi:10.1063/1.122911

Shirshova, N., Qian, H., Shaffer, M. S. P., Steinke, J. H. G., Greenhalgh, E. S., Curtis, P. T., . . . Bismarck, A. (2013). Structural composite supercapacitors. *Composites Part a-Applied Science and Manufacturing, 46*, 96-107. doi:10.1016/j.compositesa.2012.10.007

Tuinstra, F., & Koenig, J. L. (1970). Raman Spectrum of Graphite. *The Journal of Chemical Physics, 53*(3), 1126-1130. doi:10.1063/1.1674108

Xu, P., Loomis, J., Bradshaw, R. D., & Panchapakesan, B. (2012). Load transfer and mechanical properties of chemically reduced graphene reinforcements in polymer composites. *Nanotechnology, 23*(50), 505713. doi:10.1088/0957-4484/23/50/505713

Zhang, B. A., Kang, F. Y., Tarascon, J. M., & Kim, J. K. (2016). Recent advances in electrospun carbon nanofibers and their application in electrochemical energy storage. *Progress in Materials Science, 76*, 319-380. doi:10.1016/j.pmatsci.2015.08.002

Chapter 7 Conclusions and suggestions for future work

7.1 Conclusions

An investigation of hierarchical cellulose derived carbon nanofibres for the fabrication of high-performance supercapacitors, carbon fibre composites, and structural supercapacitors has been reported. Carbon nanotubes (CNTs) have been successfully grown on the surface of carbon nanofibers (CNFs) using a floating catalyst chemical vapour deposition (CVD) technique. An insight into the growth mechanisms of these CNTs on the carbon nanofibres was obtained by observing their morphologies. The CNF electrodes exhibited a competitive capacitive performance. Improvements in the capacitive performance for CNFs were demonstrated after the growth of CNTs. In current study, a relatively easy and cheap approach has been applied to grow CNTs. This is due to the fact that the floating catalytic CVD process is a one-step method to produce CNTs, which allows this method to scale-up and commercialize the CNTs' production in industry based furnace. Some strategies can be done to improve the performance by optimizing parameters of electrospinning, carbonization and activation temperature, and removing impurities in CNFs/CNTs. The stress transfer properties of SiC nanoparticles reinforced CNF/CNTs fibres in a polymer resin composite were evaluated by using an in situ Raman spectroscopic method. A novel approach for the growth CNTs onto CNFs has also been explored, e.g. growing CNTs directly from ferrocene catalysts embedded in electrospun cellulose fibres. In addition, the capacitive and stress transfer properties of the plain CNFs and CNF/CNTs electrodes were evaluated for structural supercapacitors.

7.1.1 CNF/CNTs electrodes for supercapacitors

Hierarchical cellulose-based CNF/CNTs composite fibres were produced by growing CNTs on the surface of electrospun CNFs using a floating catalyst CVD process; ferrocene as a catalyst and styrene as a carbon source were directly fed into a CVD furnace. This is believed to be a one-step way to produce CNTs. In a two-step CVD process where catalysts are pre-deposited onto CNFs, the diameter of these catalysts and CNTs are controllable. However, the in situ size control of CNTs becomes much more difficult in a floating catalyst CVD process as the catalyst nanoparticles are dispersed unevenly in the reaction zone (Kunadian *et al.*, 2009), resulting in different diameters and morphologies of the grown CNTs. Mechanisms of growing CNTs on CNFs were then revealed by observing different morphologies of CNTs. There were five types of CNTs observed within the TEM. Type 1 and 2 CNTs had catalytic nanoparticles located on the tip of the tube end. Whether the catalytic nanoparticles are encapsulated by the graphitic cap, or left as an open end, depends on the shape of the catalytic nanoparticles during the process of the growing CNTs. Type 3 CNTs showed that a catalyst was elongated at the tip of the CNT when compared to Types 1 and 2. This type of CNT was thought to follow a 'vapor-liquid-solid (VLS)' mechanism. The CNTs growth, however, may follow a new mechanism because the existence of hydrogen also contributes to a change in the melting point of Fe by building up a ternary phase diagram. A Type 4 CNT showed a catalyst on the tip was adjacent to another catalytic nanoparticle. A so-called secondary growth was thought to take place if the open-ended side of the CNTs in the free space of CVD reaction zone reaches the closed cap of an already grown CNT. A type 5 CNT showed a round catalyst is encapsulated in the middle of a MWCNT with several graphitized layers attached to it. The growth mechanism proposed for this type of CNTs

where a smaller catalyst has been deposited on the larger one at the end of a CNT in the 'tip grow mode'. Different types of CNT growth have shown that there is not only one mechanism taking place during the floating catalytic CVD process. Difficulties arise in estimating the CNT growth mode; namely the in situ monitoring of the phase change of the catalyst particle during the nanotube growth under typical CVD conditions. Observations by TEM are normally made after the CNTs growth, which can give only limited information on the particle behaviour during the process itself. Moreover, the catalyst particles can undergo reshaping and phase transformations during cooling when the synthesis is arrested (Moshkalev & Verissimo, 2007).

A CVD temperature of 800 °C has been shown to be optimal to grow pure CNTs without the formation of amorphous carbons. Only amorphous carbons were observed at a CVD temperature of 900 °C. It was also demonstrated that the most suitable temperature window is 750 - 825 °C for the growth of pure CNTs in a floating catalyst CVD process. The specific capacitance for samples with grown CNTs on the surface achieved a value 37 F g^{-1} (43 mF cm^{-2}) at a current density 0.25 A g^{-1}, an increase of 15% compared to the neat CNF counterpart. The growth of CNTs improves the electrochemical performance by lowering the equivalent series resistance (R_s), charge transfer resistance (R_{ct}), and Warburg resistance (Z_w) of the electrodes. The lowered resistances result in increases in electron transport and mobility of ions for CNTs grown electrodes, and therefore better electrochemical performance. The improvements of the electrochemical performance are also thought to be because the growth of CNTs enlarges the reactive sites through enhanced surface area and porosity. Accordingly, the Brunauer-Emmett-Teller (BET) specific surface area increases from 712 m^2 g^{-1}

to 1211 m^2 g^{-1}, while the pore volume increases from 0.31 to 0.53 m^3 g^{-1} after the growth of CNTs. There is some evidence that the growth of CNTs on the CNFs also leads to a higher degree of overall crystallinity to improve the conductivity of CNFs; the increase in the overall crystallinity has been demonstrated by Raman spectroscopic analysis. The full width at half maximum (FWHM) of the D band in CNFs sharply decreases from 160.0 ± 5.1 to 92.4 ± 3.6 cm^{-1} after growth of the CNTs. A narrowing peak width reflects lower disorder, which indicates that the growth of CNTs leads to a more highly crystalline structure, and therefore an improved conductivity.

7.1.2 CNF/SiC/CNTs composite fibres

CNF/SiC and CNF/SiC/CNTs composite fibres were fabricated by embedding SiC nanoparticles into a cellulose precursor during an electrospinning process, and for the latter samples using a CVD technique. Raman spectroscopy shows that the CNF/SiC/CNTs samples have a higher crystallinity than the CNF/SiC samples when comparing the I_D/I_G ratios, and the FWHM of the D and G bands. The I_D/I_G ratio increases after the growth of CNTs; from 1.19 ± 0.02 to 1.31 ± 0.02, indicating a larger value of the lateral size of the crystals (L_a) for this sample. The FWHM of both the D and G bands in CNF/SiC sharply decreases from 250.8 ± 3.0 to 149.1 ± 1.3 cm^{-1} and 99.4 ± 2.0 to 69.3 ± 1.1 cm^{-1}, respectively. This decrease is thought to occur because of the presence of the well-ordered carbon structure of the CNTs. The I_D/I_G versus L_a for the CNF/SiC/CNTs has been compared with the data from previously published work (Deng, Young, Kinloch, Zhu*, et al.*, 2013; Kong *et al.*, 2012; Zickler, Smarsly, Gierlinger, Peterlik, & Paris, 2006). The relationship between L_a, measured by X-ray diffraction, and the area ratio I_D/I_G for different carbon fibre sources (pyrolyzed wood, PAN and pitch-

based) derived carbon fibre is presented in Figure 7.1 (Zickler *et al.*, 2006). It can be seen that the maximum of the I_D/I_G ratio for the work of Zickler *et al.* (2006) is located at $L_a \approx 2$ nm, consistent with the value reported by Ferrari and Robertson (2000). The value of this maximum is different from the models used for this work because different Raman laser excitations were applied. The I_D/I_G ratio for the CNF/SiC/CNTs is found to be 1.31 ± 0.02; this sample could fit a model for either an $L_a > 2$ nm or $L_a < 2$ nm (see double-pointed arrow in Figure 7.1). In addition, it is noted that the value of the I_D/I_G ratio for the CNF/SiC/CNTs sample is higher than for CNF2200 and CF2500 (Deng, Young, Kinloch, Zhu*, et al.*, 2013; Kong *et al.*, 2012). This is because the latter two samples fit the model for a $L_a > 2$ nm. This higher value of I_D/I_G ratio for CNF/SiC/CNTs corresponds to a lower L_a, regardless of which model ($L_a > 2$ nm or $L_a < 2$ nm) is used. The Young's modulus for the CNF/SiC/CNTs is however higher than CNF2200 and CF2500 fibres. This suggests that the growth of CNTs improves the stiffness overall, even competitive with highly graphitized CNFs. It is worthwhile noting that higher temperatures could still improve the modulus further. The Young's modulus of carbon materials depends not only on the crystalline size, but also on the degree of preferred orientation and crystalline shape (Li, Wang, & Wang, 2007). So, these properties could have an effect on the modulus values obtained.

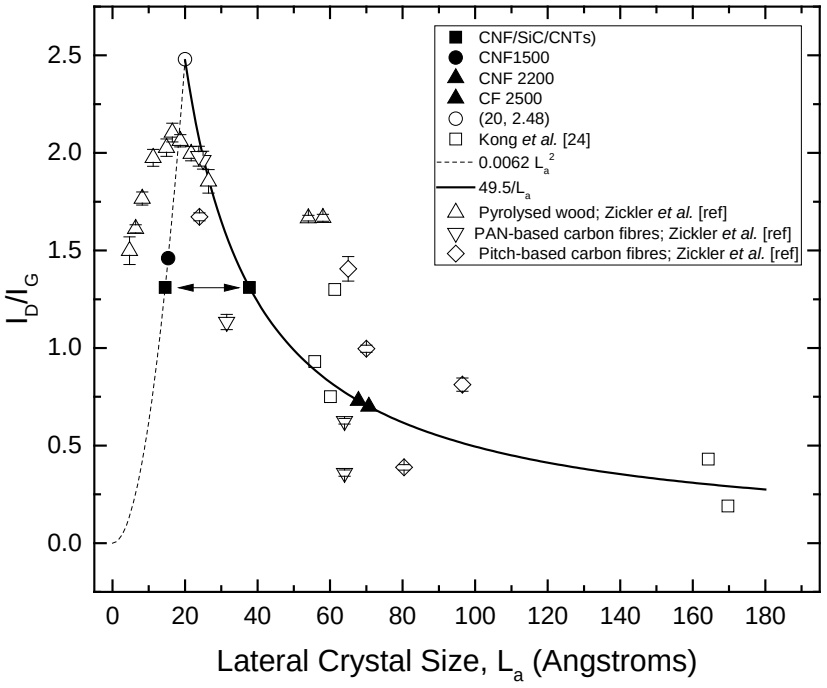

Figure 7.1 L_a *versus* I_D/I_G for CNF/SiC/CNTs compared to data from published work (Deng, Young, Kinloch, Zhu*, et al.*, 2013; Kong *et al.*, 2012; Zickler *et al.*, 2006). The solid line represents the equation $I_D/I_G = 49.5/L_a$, and the dashed line is the relationship $I_D/I_G = 0.0062\ L_a^2$. A double pointed arrow refers to the alternative positions for the I_D/I_G ration for CNF/SiC/CNTs.

A linear downshift in the position of the 2D Raman band for CNF/SiC/CNTs with the application of tensile deformation was observed. From the slope of this shift, an elastic modulus of the CNF/SiC/CNTs was estimated. This was found to be 208 ± 26 GPa. This value is comparable to commercial T650 and IM-7 CFs (200 GPa; (Zhang *et al.*, 2009)), indicating that the CNF/SiC/CNTs composite fibres have high stiffnesses. The modulus of the CNF/SiC/CNTs fibres is also higher than that for the plain CNFs produced at 1500 °C (60 GPa) and 2200 °C (100 GPa), that were obtained using similar methodology (Deng, Young, Kinloch, Zhu*, et al.*, 2013). The modulus of the composite CNF/SiC/CNTs nanofibres is however much lower than pure individual multi-walled CNTs (1.7 - 2.4 TPa)

(Lourie & Wagner, 1998), which may arise from the presence of the less crystalline CNF fibres. No obvious G band shifts were found for both CNFs and CNF/SiC; the influences on mechanical performance after the embedding of SiC nanoparticles into CNFs could not be revealed. It is noted that no zone center transverse optical phonon (TO) bands from the SiC nanoparticles are observed from the samples prepared for the Raman spectroscopic study. This is either because the CNTs have fully covered the CNF/SiC surface, or that bands from the SiC overlap with those from PMMA. Therefore, load sharing between the SiC nanoparticles and the CNFs cannot be estimated using this approach.

7.1.3 Growth of CNTs on cellulose/ferrocene fibres

The CNF/CNTs were produced by direct incorporation of ferrocene as a catalyst precursor into electrospun fibres. The size distribution of CA fibres was compared with different electrospinning voltages and ferrocene contents. The crystallinity of the CNF/CNTs sample with a 4 wt.% ferrocene content was compared to a 2 wt.% content using Raman spectroscopy. It was found that the crystallinity increased with an increased ferrocene content from 2 wt.% to 4 wt.%. This implies that the CNF/CNTs samples with 4 wt.% ferrocene has an increased grain size, which results in stronger sp^2 carbon bonds and in turn improved mechanical properties and electrical resistivity. No linear fitting was however obtained in the in situ Raman spectroscopic study of the deformation of the CNF/CNT composites. This is due to the low CNT yield using this method.

7.1.4 Structural supercapacitors using CNF/CNTs

Structural supercapacitors have been fabricated by using CNFs decorated with CNTs as electrodes, a solid resin (PEGDGE), and an ionic liquid (EMITFSI)

electrolyte. CF900/CNTs electrode-based supercapacitors exhibited a higher capacitive performance than CF900 electrodes. The specific capacitances of CF900 and CF900/CNTs electrodes are calculated to be 0.23 ± 0.01 mF cm^{-2} (175 ± 4 mF g^{-1} or 29 ± 1 mF cm^{-3}) and 0.84 ± 0.01 mF cm^{-2} (643 ± 10 mF g^{-1} or 105 ± 2 mF cm^{-3}), respectively. The values of the capacitance are higher than the multiwall CNTs impregnated carbon fibre-based electrodes (125 mF g^{-1}) reported in a recent study (Hudak *et al.*, 2017) and higher compared with the specific capacitance (52 mF g^{-1}) for activated carbon fibre electrodes (Shirshova *et al.*, 2013).

It is important to note that the individual functionalities of a structural supercapacitor (mechanical and electrocapacitive performance) do not need to be better than the mono-functionality provided by conventional materials, but a compromise should be considered to achieve the system mass savings and energy efficiencies required (Qian, Diao*, et al.*, 2013). The capacitive performance is not 'state-of-the-art', mainly because of the high resistance of the electrolyte matrix. The equivalent series resistance (R_s) is 470 ± 21 Ω for the 24 h curing time. Despite this, the capacitances of CNF/CNT electrode materials are still comparable with other recent studies (Javaid *et al.*, 2016; Qian, Kucernak*, et al.*, 2013). It is also believed that to maximise the mechanical properties of the composite, a stiff matrix is required to give sufficient stress-transfer to the fibres. The matrix stiffness typically increases with an increase in the degree of cross-linking (Gonzalez, Vilatela, Molina-Aldareguia, Lopes, & LLorca, 2017). This stiffening of the matrix, for one structural supercapacitor containing polymer electrolytes, will then reduce the mobility of the ions, and therefore reduce conductivity. In this sense these two properties work against each other. Javaid

et al. reported the increase of EMITFSI concentration results in increased ionic conductivity but decreased compression strength of PEGDGE electrolytes (Javaid *et al.*, 2016). Therefore, in real applications, the concentration of ILs in the electrolyte matrix should be adjusted to balance the multifunctionality of the structural supercapacitor. The increased R_s at 24 h compared to 2 h of curing of the electrolyte matrix suggested that the higher degree of cross-linking is not beneficial for the electrocapacitive performance.

An in situ Raman spectroscopic study was used to investigate the stress transfer between a resin and the CNFs and CNF/CNTs. Shifts in the position of G band were observed for the CF2000 and CF2000/CNTs samples in an in situ Raman spectroscopic study. These shifts were then used to estimate the moduli of these samples, which were found to be ~145 GPa and ~271 GPa, respectively. These moduli are comparable to other electrospun cellulose-based carbon fibres (~100 GPa; (Deng, Young, Kinloch, Zhu*, et al.*, 2013)). Standard tensile tests were not carried out to verify/complement the in situ Raman study for the CNFs and CNF/CNTs. This is because of the samples are small and brittle because of the electrospinning rig used, and the inherent mechanical properties of carbon fibres. Despite this, these electrospun carbon fibre electrodes can still be applied for the fabrication of micro-supercapacitors and nano-supercapacitors, for which traditional mechanical testing approaches are invalid. In this sense, the Raman/deformation test is believed to be the best way to test small sample sizes. Moreover, in comparison to the standard mechanical testing methods used to evaluate interfacial shear stress, the in situ Raman/deformation test also offers a non-destructive way to obtain the stiffness of the carbon-based materials. This

also allows the method to be potentially used in inspecting the structural supercapacitors by converting the Raman shifts into stress (Frank *et al.*, 2011).

7.2 Suggestions for future work

Since good capacitive performance, in comparison to other work, has been demonstrated by using the carbonized electrospun cellulose fibres, consideration should be given to scaling up the production of the fibres. The challenge for scalability of the process lies in the electrospinning process itself, which has a relatively low production rate. However, scaled-up electrospinning processes, such as needless electrospinning (Teo & Ramakrishna, 2006) and multi-needle electrospinning (Persano, Camposeo, Tekmen, & Pisignano, 2013) could be applied in future work.

The present work has demonstrated an improvement of both mechanical and capacitive properties for supercapacitors by growing CNTs on CNFs. To further assess the influence of CNTs on the performance of composites or supercapacitors, various CNT contents in the sample could be obtained for a comparison. This could be achieved by controlling the CVD temperature, the duration times and the speed of feeding the catalysts/carbon source to the reaction site. In addition, the concentration of Argon and H_2 is also adjustable to alter the CNT content.

No shifts in the Raman bands for deformed carbonized cellulose/ferrocene nanofibres were observed. It is thought that this was due to the low yield of CNTs and the low carbon crystallinity of the obtained CNFs. To enhance the stiffness of the CNF/CNTs composite fibres in future work, strategies will be focused on

optimising the CVD parameters to increase the purity and yield of CNTs, and increasing the carbonization temperatures to improve the crystallinity of CNFs.

It is thought that some load sharing might occur between SiC nanoparticles and the CNFs in the CNF/SiC composite fibres. The assessment of this load sharing would be useful for a better understanding the influence of SiC nanoparticles on the mechanical properties of the CNFs. No characteristic Raman bands for the SiC particles were observed from the samples produced in this study. This is either because the CNTs have fully covered the CNF/SiC surface, or that Raman bands from the SiC overlap with those from PMMA. Increasing the SiC content in the electrospun CNFs would be one way to allow increase the intensity of these bands, thereby allowing detection using the Raman spectrometer; the upper limit of the SiC nanoparticles in cellulose is affected by viscosity of the obtained SiC/cellulose suspension, applied voltages, etc. It can be also achieved by using an alternative polymer resin to prepare the deformation samples.

As for the structural supercapacitors, new electrodes and electrolyte matrices that can achieve both high mechanical and electrical properties are yet to be discovered. Polymers such as polyethylene glycol (PEG) (Snyder, Gienger, & Wetzel, 2015), polyethylene-oxide (PEO) (Westover *et al.*, 2014), or a diglycidylether of bisphenol-A (DGEBA) (Javaid *et al.*, 2013) will be used as matrices electrolyte or mixed with the electrolyte for current study to balance the multifunctionality of the structural supercapacitors. In addition, various carbon-based materials such as graphene (Gao *et al.*, 2013), and carbon aerogel (Qian, Kucernak*, et al.*, 2013) could also be incorporated with electrospun CNFs to produce supercapacitors and carbon fibre composites. The graphene has potential to build up large ion accessible surface areas with proper designed layering

and stacking configurations to further improve supercapacitor performance (Tan & Lee, 2013). The CAG-modification for carbon fibre has been demonstrated to be an effective approach to improve the electrochemical surface area, and to reinforce the polymer matrix surrounding the primary fibres (Qian, Kucernak*, et al.*, 2013).

7.3 References

Deng, L. B., Young, R. J., Kinloch, I. A., Zhu, Y. Q., & Eichhorn, S. J. (2013). Carbon nanofibres produced from electrospun cellulose nanofibres. *Carbon, 58*, 66-75. doi:10.1016/j.carbon.2013.02.032

Ferrari, A. C., & Robertson, J. (2000). Interpretation of Raman spectra of disordered and amorphous carbon. *Physical Review B, 61*(20), 14095-14107. doi:10.1103/PhysRevB.61.14095

Frank, O., Tsoukleri, G., Riaz, I., Papagelis, K., Parthenios, J., Ferrari, A. C., . . . Galiotis, C. (2011). Development of a universal stress sensor for graphene and carbon fibres. *Nature Communications, 2*. doi:10.1038/ncomms1247

Gao, Y., Zhou, Y. S., Xiong, W., Jiang, L. J., Mahjouri-samani, M., Thirugnanam, P., . . . Lu, Y. F. (2013). Transparent, flexible, and solid-state supercapacitors based on graphene electrodes. *APL Materials, 1*(1), 012101. doi:10.1063/1.4808242

Gonzalez, C., Vilatela, J. J., Molina-Aldareguia, J. M., Lopes, C. S., & LLorca, J. (2017). Structural composites for multifunctional applications: Current challenges and future trends. *Progress in Materials Science, 89*, 194-251. doi:10.1016/j.pmatsci.2017.04.005

Hudak, N. S., Schlichting, A. D., & Eisenbeiser, K. (2017). Structural Supercapacitors with Enhanced Performance Using Carbon Nanotubes

and Polyaniline. *Journal of the Electrochemical Society, 164*(4), A691-A700. doi:10.1149/2.0721704jes

Javaid, A., Ho, K. K. C., Bismarck, A., Shaffer, M. S. P., Steinke, J. H. G., & Greenhalgh, E. S. (2013). Multifunctional structural supercapacitors for electrical energy storage applications. *Journal of Composite Materials, 48*(12), 1409-1416. doi:10.1177/0021998313487239

Javaid, A., Ho, K. K. C., Bismarck, A., Steinke, J. H. G., Shaffer, M. S. P., & Greenhalgh, E. S. (2016). Carbon fibre-reinforced poly(ethylene glycol) diglycidylether based multifunctional structural supercapacitor composites for electrical energy storage applications. *Journal of Composite Materials, 50*(16), 2155-2163. doi:10.1177/0021998315602324

Kong, K., Deng, L. B., Kinloch, I. A., Young, R. J., & Eichhorn, S. J. (2012). Production of carbon fibres from a pyrolysed and graphitised liquid crystalline cellulose fibre precursor. *Journal of Materials Science, 47*(14), 5402-5410. doi:10.1007/s10853-012-6426-y

Kunadian, I., Andrews, R., Qian, D. L., & Menguc, M. P. (2009). Growth kinetics of MWCNTs synthesized by a continuous-feed CVD method. *Carbon, 47*(2), 384-395. doi:10.1016/j.carbon.2008.10.022

Li, D. F., Wang, H. J., & Wang, X. K. (2007). Effect of microstructure on the modulus of PAN-based carbon fibers during high temperature treatment and hot stretching graphitization. *Journal of Materials Science, 42*(12), 4642-4649. doi:10.1007/s10853-006-0519-4

Lourie, O., & Wagner, H. D. (1998). Evaluation of Young's modulus of carbon nanotubes by micro-Raman spectroscopy. *Journal of Materials Research, 13*(9), 2418-2422. doi:10.1557/Jmr.1998.0336

Moshkalev, S. A., & Verissimo, C. (2007). Nucleation and growth of carbon nanotubes in catalytic chemical vapor deposition. *Journal of Applied Physics, 102*(4), 044303. doi:10.1063/1.2769354

Persano, L., Camposeo, A., Tekmen, C., & Pisignano, D. (2013). Industrial Upscaling of Electrospinning and Applications of Polymer Nanofibers: A Review. *Macromolecular Materials and Engineering, 298*(5), 504-520. doi:10.1002/mame.201200290

Qian, H., Diao, H., Shirshova, N., Greenhalgh, E. S., Steinke, J. G., Shaffer, M. S., & Bismarck, A. (2013). Activation of structural carbon fibres for potential applications in multifunctional structural supercapacitors. *J Colloid Interface Sci, 395*, 241-248. doi:10.1016/j.jcis.2012.12.015

Qian, H., Kucernak, A. R., Greenhalgh, E. S., Bismarck, A., & Shaffer, M. S. (2013). Multifunctional structural supercapacitor composites based on carbon aerogel modified high performance carbon fiber fabric. *ACS Appl Mater Interfaces, 5*(13), 6113-6122. doi:10.1021/am400947j

Shirshova, N., Qian, H., Shaffer, M. S. P., Steinke, J. H. G., Greenhalgh, E. S., Curtis, P. T., . . . Bismarck, A. (2013). Structural composite supercapacitors. *Composites Part a-Applied Science and Manufacturing, 46*, 96-107. doi:10.1016/j.compositesa.2012.10.007

Snyder, J. F., Gienger, E. B., & Wetzel, E. D. (2015). Performance metrics for structural composites with electrochemical multifunctionality. *Journal of Composite Materials, 49*(15), 1835-1848. doi:10.1177/0021998314568167

Tan, Y. B., & Lee, J. M. (2013). Graphene for supercapacitor applications. *Journal of Materials Chemistry A, 1*(47), 14814-14843. doi:10.1039/c3ta12193c

Teo, W. E., & Ramakrishna, S. (2006). A review on electrospinning design and nanofibre assemblies. *Nanotechnology, 17*(14), R89-R106. doi:10.1088/0957-4484/17/14/R01

Westover, A. S., Shabab, F. N., Tian, J. W., Bernath, S., Oakes, L., Erwin, W. R., . . . Pint, C. L. (2014). Stretching Ion Conducting Polymer Electrolytes: In-Situ Correlation of Mechanical, Ionic Transport, and Optical Properties. *Journal of The Electrochemical Society, 161*(6), E112-E117. doi:10.1149/2.035406jes

Zhang, Q. H., Liu, J. W., Sager, R., Dai, L. M., & Baur, J. (2009). Hierarchical composites of carbon nanotubes on carbon fiber: influence of growth condition on fiber tensile properties. *Composites Science and Technology, 69*(5), 594-601. doi:10.1016/j.compscitech.2008.12.002

Zickler, G. A., Smarsly, B., Gierlinger, N., Peterlik, H., & Paris, O. (2006). A reconsideration of the relationship between the crystallite size La of carbons determined by X-ray diffraction and Raman spectroscopy. *Carbon, 44*(15), 3239-3246. doi:10.1016/j.carbon.2006.06.029